ANTIPHASE DYNAMICS IN SOLID STATE LASERS WITH FABRY-PEROT CAVITY

by

Laurentiu Stamatescu

A thesis submitted for the degree of

Doctor of Philosophy

in

The University of Adelaide

Department of Physics and Mathematical Physics

May, 2003

This work contains no material which has been accepted for the award of any other degree or diploma in any University or other tertiary institution and, to the best of my knowledge and belief, contains no material previously published or written by another person, except where due reference has been made in the text.

I give consent to this copy of my thesis, when deposited in the University Library, being available for loan and photocopying.

SIGNED: ....
DATE: ..27.11.2003.....

Supervisor: Dr. M. W. Hamilton

Acknowledgements

I would like to thank my supervisor, Dr. Murray W. Hamilton, for the guidance, support and patience offered during my time at the University of Adelaide and thereafter. I believe that he reached a good balance between pointing the project in the right direction and then giving me enough freedom to develop it as I saw fit. I hope that my sometimes less than straightforward approach to solving problems did not frustrate him too much.

I would also like to thank the other members of the Optics group, Prof. Jesper Munch and Dr. Peter Veitch, for advice and encouragement at various stages of the project.

My interaction with Prof. Paul Mandel from the Université Libre de Bruxelles before, during and after his visit to the University of Adelaide was both challenging and very helpful. The articles written by him and his collaborators, being more analytic than the approach taken by us, constituted a great resource and reference point for our work.

I received excellent support from the staff of the Physics Department. It is my pleasure to thank John Smith and Mike Shorthose for their help with the construction of the electronic devices, the staff in the mechanical workshop who taught me how to use the machines and other people in the Department who helped me in various ways.

The fellow students in the Optics group were a great source of information, encouragement and help. Special mentions go to Kerry Corbett for the numerous discussions regarding methods of tackling the analysis and modelling of lasers and to Tim Hill for taking over an experiment that was very far from being perfect.

The Australian Research Council deserves recognition for funding this project under the Small Grants scheme and the University of Adelaide for providing excellent facilities and material support.

I would like to acknowledge the solid scientific foundation offered by my teachers at all levels of schooling in Romania and I wish I had taken full advantage of their generous offer.

Finally, I would like to thank my mother and my father for their moral and material support throughout my previous studies and my spouse and children for their continuous encouragement and support during this prolonged effort.

Abstract

The intensities of the longitudinal modes produced by a homogeneously broadened laser with Fabry-Perot cavity are coupled through the population inversion and behave like an array of coupled harmonic oscillators. This coupled array has several normal modes of oscillation, each being characterised by a resonant frequency and a certain phase relationship between the intensities of the optical modes. When the laser is excited, the total intensity responds strongly only at the highest frequency, the lower resonant frequencies being either absent or strongly attenuated. This phenomenon, named antiphase dynamics, implies that the low frequency variations in the individual mode intensities are such that their superposition in the total intensity almost cancels out.

We modelled our end pumped laser by extending the classical model of Tang Statz deMars to non-uniform pump along the active medium. With this model we have been able to account for the anomalous threshold behaviour of the laser, where modes with lower gain can surpass modes with higher gain as the pump power is increased.

We explore the antiphase dynamics in our laser by modulating the pump power and measuring the transfer functions from this input to various outputs (individual longitudinal modes or total intensity). Since antiphase dynamics is primarily a phase locking mechanism, we consider not only the magnitude but also the phase of the transfer functions. In particular, expressing the transfer functions in the pole-residue form, we compare the predictive power of the two models with the experiment, showing that the end pumped model can account for more observed features.

Another possibility to investigate the antiphase and to gain a better understanding of the laser is to study its response when excited by various sources of noise. We limit ourselves to the Tang Statz deMars equations subject to internal (quantum) noise and calculate the power spectra of the longitudinal modes and of the total intensity. We also calculate cross-spectra between pairs of longitudinal modes, the phase of which can shed light on the antiphase mechanism. We finally demonstrate that power- and cross-spectra can be measured relatively easily, transforming the noise from an experimental difficulty into a probing tool.

Table of Contents

Chapter 1 Introduction

1.1 Reasons for Studying Antiphase Dynamics

The study of linear systems has a long history and it certainly represents a success story in the development of human knowledge. Its mathematical apparatus is firmly developed and the applications are wide ranging. However, not the same thing can be said about the non-linear science, despite its closer resemblance to reality in the vast majority of cases. Its development was slow and marked by the formidable difficulty of the task. The manifestations of the non-linear systems range from the relatively simple behaviour of the limit cycles to the wildly different chaotic states. While there are already a number of techniques available for the analysis of non-linear systems (like embedding, mutual information, fractal dimensions, Poincaré sections, Lyapunov spectrum etc.), they are still limited in applicability and predictive power compared to the linear counterparts [1]. Nevertheless, the interest in developing tools for non-linear systems is high and non-linear dynamics is an active research field.

For both linear and non-linear systems, noise represents an interesting type of stimulus. The response of the linear deterministic systems to noise calls for a non-deterministic description, more akin to the language required by non-linear systems. This statistical description in terms of distribution functions, auto- and cross-correlation functions and power spectra characterises adequately linear systems with noisy inputs. For the non-linear systems however, the statistical description is still useful but not complete and new terminology and methods have been devised. The non-linear systems can respond very differently to apparently similar types of noise; for example, they can differentiate between random processes with the same rms value and the same spectrum (or auto-correlation function) because they are sensitive to the higher order correlation functions of the input. Some non-linear systems (autonomous systems) can generate irregular (noise-like) signals by themselves, a feature the linear systems can never exhibit.

This project was initially aimed at the study of the effect of noise on systems characterised by non-linear dynamic equations. A good example of such a system is a laser, since it is well described by the non-linear rate equations and is relatively easy to construct and operate. It also has a broad range of applications making such a study worthwhile. Therefore, the project started with the construction of a low power single-mode Nd:YAG laser and, in parallel, with the investigation of methods suitable for the analysis of non-linear systems.

When the laser became operational, it turned out that it only had a very limited range of pump power above threshold where it could work in a single longitudinal mode. For reasonable levels of output power and stability, the laser exhibited operation on up to 11-12 longitudinal modes. Multimode operation complicated the theoretical analysis of the laser significantly, since the dimension of the dynamic system was at least twice the number of longitudinal modes plus one. Validation of new theoretical results through experiments on such a system, taking into account the realities of mechanical and electronic stability, was highly questionable. It was also felt that a non-linear study of the laser should be preceded by a thorough linear analysis, where the effects of inter-mode interaction are well understood.

Initial experiments and a survey of the literature on the subject of multimode lasers have shown that such systems can exhibit an interesting type of behaviour, called antiphase dynamics. This phenomenon is a particular case of phase locking and it is not restricted to this type of lasers: it can also appear in globally coupled map lattices [2], networks of electrically coupled cells [3], Josephson junction arrays [4, 5], in lasers with intra-cavity second harmonic generation [6] etc. In the case of the laser, it manifests itself as a type of collective dynamics of the intensities of the longitudinal modes; when the laser is excited with step functions or broadband noise (be it internal or external) or is modulated with sine waves, the intensities of the longitudinal modes oscillate quite strongly at certain resonant frequencies, while the total intensity oscillates very little.

A simplified explanation for this conduct could be based on the energy balance in the laser: since all laser modes compete for the energy supplied via the population inversion, if the intensities of some modes increase, the intensities of the other modes must decrease to balance the constant input energy rate and the total intensity remains almost constant. However, such an explanation does not give any indication on what type of antiphase exists or the values of the resonant frequencies; the in-phase oscillation at the highest resonant frequency (the relaxation oscillations frequency) cannot be accounted for either. Models for the laser had to be developed and investigated in order to obtain detailed information and this has become the goal of the project.

1.2 Development of the Project

The initial modelling of the laser was done with paraxial ray tracing for the design of the cavity and global rate equations for the power balance. These calculations proved to be sufficient for the engineering side of the project, allowing the construction of the laser to proceed. Suitable laser diodes were selected for pumping the laser and current and temperature controllers were designed and built. The third iteration of the laser cavity design was successful and the laser started operating with good beam quality and efficiency close to the calculated value. The first indication that the laser was multimode came from a measurement of the free spectral range with a fast photodiode. The spectrum of the photodiode (as observed on an RF spectrum analyser) had a fine structure that could be only explained by assuming that there were several longitudinal modes. This was confirmed when a Fabry-Perot with appropriate free spectral range and mirror coatings was used to visualise the spectrum of the laser.

Once it was clear that the laser was a much more complicated system than initially envisioned, it was necessary to find a suitable model. A survey of the literature showed that the most popular model for this type of lasers was that introduced by Tang, Statz and deMars [7]. Their model properly represented the essential physics of the problem, while also offering a good balance between simplicity and accuracy. Based on a linearised version of this model, it was possible to determine theoretically the transfer functions of the laser when the pump power was modulated (the input) and the individual modes or the total intensity were observed (the output). An interesting result of the transfer function calculations was the fact that they confirmed the existence of antiphase dynamics even in the linearised model and predicted the type of antiphase. Measurements done on the system were in relatively good qualitative agreement with the theoretical prediction and the results have been published in [8].

Encouraged by the success of the transfer functions method, we looked at ways of obtaining better agreement with the measurements. It was quite clear that the most important difference between our laser and the Tang Statz deMars model was in the type of pumping. The Tang Statz deMars model assumes a uniform pump, while our laser was end pumped and, due to the exponential absorption of the pump radiation, the population inversion had a decaying profile along the axis of the cavity. By modifying the model to incorporate this type of longitudinal non-uniformity, we arrived at a new set of differential equations that we called the Tang Statz deMars equations with exponential decay.

Based on this new model, the threshold behaviour of the laser was investigated analytically and the first difference from the uniform pump case appeared: modes with different gains no longer followed a strict ordering of intensities as the pump was increased from threshold to a certain maximum value. The experimental work on the dependence of the modal intensities on the pump strength confirmed the theoretical prediction: modes with lower gain can have higher intensities than modes with higher gain. We had an attempt at publishing an article regarding this model and its experimental confirmation, but one of the referees found the article too mathematical and the submission was rejected.

The second confirmation of the model came when the transfer functions method has been revisited to make use of the new set of equations. Previously, the transfer functions based on the Tang Statz deMars equations indicated a rigid ordering of the phases of the modes required to obtain antiphase dynamics. In the case of the transfer functions based on the new model, this rigid ordering has been eliminated, bringing the theory one step closer to the behaviour of the real laser.

One of the main difficulties in the measurement of the transfer functions of the laser was the noise present in the system. Averaging was used to minimise the effect of the noise, but the more averaging was used, the more the drift of the laser became a problem. It is known that white noise can be used as an input for determining transfer functions very efficiently. However, in our case the problem was that neither the source nor the type of the noise was known. An experiment where the cross-spectrum of two modes has been measured indicated that the phase of the cross-spectrum appeared very similar to the phase of the transfer functions. This experiment suggested that the noise could be changed from a nuisance into an excellent probing tool for the dynamics of the system. Having a good model for the laser meant that we could finally tackle the problem of laser behaviour in the presence of noise. Again, the model was linearised and the mathematical apparatus was developed to predict the modal noise power- and cross-spectra, depending on where the noise entered the system.

Most of the numerical modelling described in this thesis was done using the free software Scilab [9]. Some of the results of this work have been published, either as articles in journals or as conference contributions. A list of publications is included in Appendix 1.

1.3 Structure of the Thesis

The historical perspective presented here has shown that the development of the project was not in a linear progression. This is often the case when theoretical and experimental work are pursued together: experiments require re-thinking of the theoretical models, new models suggest new experiments. However, the chronological order is not necessarily the best way to present the results of the investigation. Logical ordering of the presentation is preferable and this is how the material is presented here.

The next chapter describes the design, construction and typical parameters of our laser. These elements are the required input for the laser models while the particular architecture of the laser (end pumped) has motivated the development of a new model. In Chapter 2 we also present the building blocks for the experimental set-ups. The way these blocks are combined and elements that are specific to each experiment are described in the respective chapters.

In Chapter 3 we introduce several models for the laser and calculate their steady state solutions. The first model refers to a single-mode laser where no longitudinal effects are present. It serves to introduce the rate equations and to justify some of the calculations used in Chapter 2 for the construction of the laser. The next model, applicable to a uniformly pumped multimode laser with Fabry-Perot cavity, is that of Tang Statz and deMars [7]. Finally, the Tang Statz deMars model is modified to include the exponential absorption of the pump. These last two models are used to predict the threshold behaviour of the laser (i.e. the dependence of the modal intensities on the pump power level) and the experiment at the end of the chapter shows convincingly that the latter model comes closest to the measurements.

Once the laser has been modelled and its steady state determined, it was possible to study the response of the laser to modulation. This is the objective of Chapter 4, where the transfer functions are investigated both theoretically and experimentally. Both representations of the transfer function are used (pole-zero and the partial fraction decomposition) and their connection with antiphase dynamics and the choice of the model is discussed.

The tools developed for the transfer functions are further advanced and applied to calculating the response of the laser to noise in Chapter 5. The noise can be either internally generated by the laser itself (shot noise) or externally applied to the laser (through the pump, for example). Although the only case considered is that of internally generated white noise and the system is linearised, the results are of interest. The chapter concludes with a discussion of the experimental techniques required for the determination of power- and cross-spectra.

The final chapter of the thesis summarises both the few achievements of the work undertaken here and the numerous new questions and possible future directions for this project. It is a pleasure to know that the efforts invested in this project are being successfully continued [10] and that they have stimulated creative collaboration with colleagues in the field [11].

Chapter 2 **Experimental System Description**

2.1 Introduction

This chapter presents the experimental system used in testing the models developed in the course of this thesis. Its role is to describe the elements of the system, to explain the rationales behind the design decisions and to provide the numerical values necessary in subsequent calculations. Starting from this common base, several experimental set-ups have been constructed. These particular set-ups will be described in detail in each of the following chapters, in the context of model validation and in relation to the purpose of the measurement. However, the emphasis there will be mainly on the measurement methodology and data processing, since most of the 'hardware' associated with the experiments is presented here.

A significant body of literature has been consulted before and during the construction of the laser. Some of the more important references are [12], [13], [14]; others will be listed where appropriate. It should be mentioned that it took many iterations of the various parts of the system to get to the present configuration; it is also fair to say that the system is far from being perfect, but it proved to be adequate enough to answer several burning questions and to generate many more.

The experimental set-up can be divided into three systems: the pump system, the Nd:YAG laser and the detection system (Figure 2-1).

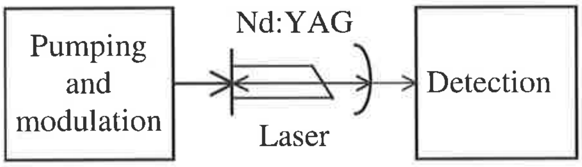

Figure 2-1 System block diagram

It is obvious that there is a strong interaction among these three systems and that the design phase has involved many compromises. However, for the simplicity of exposition, when describing one system it is assumed that all numerical values pertaining to the other systems are already known.

2.2 Pump System

The role of the pump system is two-fold: on one hand it has to supply optical power to the Nd:YAG laser to make it work and, on the other hand, it has to allow the modulation of the laser. In order to fulfil its obligations, the pump system has to deliver at the front facet of the Nd:YAG laser a beam with appropriate wavelength, shape and temporal evolution.

This is achieved by combining a number of sub-systems that have to provide several desirable characteristics of the overall system:

- high throughput;
- intensity and wavelength control;
- good collimation and focusing;
- good isolation;
- linear modulation.

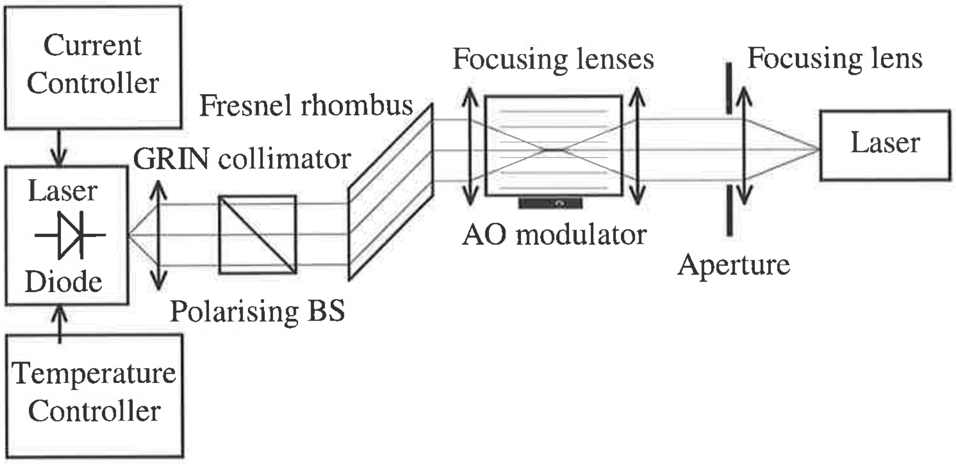

Figure 2-2 Pump system block diagram

A graphical depiction of the pump system is shown in Figure 2-2. It consists of a laser diode, which is current and temperature controlled, followed by a collimator that transforms the highly divergent beam of the laser diode into a parallel beam with elliptical cross-section. The beam passes through the optical isolator and the acousto-optic modulator and it is finally focused down by the focusing lens into the Nd:YAG rod.

2.2.1 Current Control

The current supplied to the laser diode has to be carefully controlled for proper operation. The most important requirements for the current controller are listed below:

- no ripples, to avoid unwanted modulation of the pump power;
- no turn-on or turn-off spikes, to protect the laser diode;
- the absolute value of the current has to be kept constant for large variations in the supply voltage or temperature;
- low noise.

The solution chosen to meet the first two requirements was to use a rechargeable battery as the power supply, instead of the conventional combination transformer, rectifier, and regulator. Although periodical recharging of the battery is required, the absence of ripples and spikes coming from the power supply line and the ease of implementing an effective transient suppression were decisive factors in adopting this solution. As the voltage of the battery decreases steadily during the operation, the current controller uses feedback to maintain the desired value of the current. The use of a MOSFET pass transistor instead of a bipolar one allows achieving very low noise operation.

Table 2-1 Current controller specifications

Characteristic	Typical value	Comments
Maximum supply voltage	13.5 V	limited by dissipation
Minimum supply voltage	11.5 V	limited by saturation
Current	0-100 mA	set by 10 turn potentiometer
Current noise density	50.1 pA/√Hz	at $I_0 = 100$ mA

The schematic diagram of the current controller is presented in Appendix A2.1, together with a description of the circuit and design considerations. In the Table 2-1we list the principal characteristics of the current controller specifically designed and constructed for the LT017MD laser diode.

2.2.2 Temperature Control

As the wavelength of the light emitted by the laser diode changes with the temperature of the semiconductor crystal (about 0.23 nm /°C [16]), it is important to have a good control of the temperature, both to be able to select a wavelength that matches the absorption of the Nd:YAG crystal and to maintain the selected wavelength when the ambient temperature changes [15].

The electronic side of the temperature controller constructed for the LT017MD laser diode is a modified version of the classical PID (proportional-integrator-differentiator) control system, with the differentiator stage omitted. This system uses a thermistor as the sensing element and a pair of thermoelectric coolers (Peltier cells or heat pumps) as the effector element. The design considerations for the temperature controller (both electronic and mechanical) are presented in the Appendix A2.2. The following table presents the main characteristics of the temperature controller.

Table 2-2 Temperature controller specifications

Characteristic	Typical value	Comments
Power supply	240 V AC	
Front panel display supply	9 V DC	alkaline battery
Thermistor type	10 kΩ	Betaterm
Thermoelectric cooler type	MI1064 (4 V, 5.3 A)	Marlow Industries
Minimum temperature	0°C	
Maximum temperature	60°C	

2.2.3 Laser Diode

The Nd:YAG laser is pumped by a 40 mW single-stripe, single-mode (both transverse and longitudinal) GaAlAs laser diode (LT017MD from Sharp [16]). The relatively large output power of the diode is obtained by decreasing the reflectivity of the front facet and increasing the reflectivity of the back facet of the diode with appropriate coatings. The diode is packaged in a TO-9 can with an anti-reflection coated window and integral monitor photodiode.

The principal characteristics of the laser diode are summarised in Table 2-3.

Table 2-3 LT017MD laser diode characteristics @ 25 °C

Characteristic	Typical value	Comments
Operating wavelength, λ	810 nm	typical
Nominal optical power	40 mW	max. 50 mW
Threshold current, I_{th}	65 mA	typical
Nominal current	110 mA	@40 mW
Divergence (parallel)	8 degrees	FWHM
Divergence (perpendicular)	25 degrees	FWHM
Monitor photo-current	0.4 µA/mW	typical

From the divergence angles we can estimate the waist of the beam within the laser diode to be approximately $\omega_{parallel} = 1.1\ \mu m$ and $\omega_{perpendicular} = 0.38\ \mu m$. The optical power of the laser diode has been measured with a thermopile and the graph is shown in Figure 2-3.

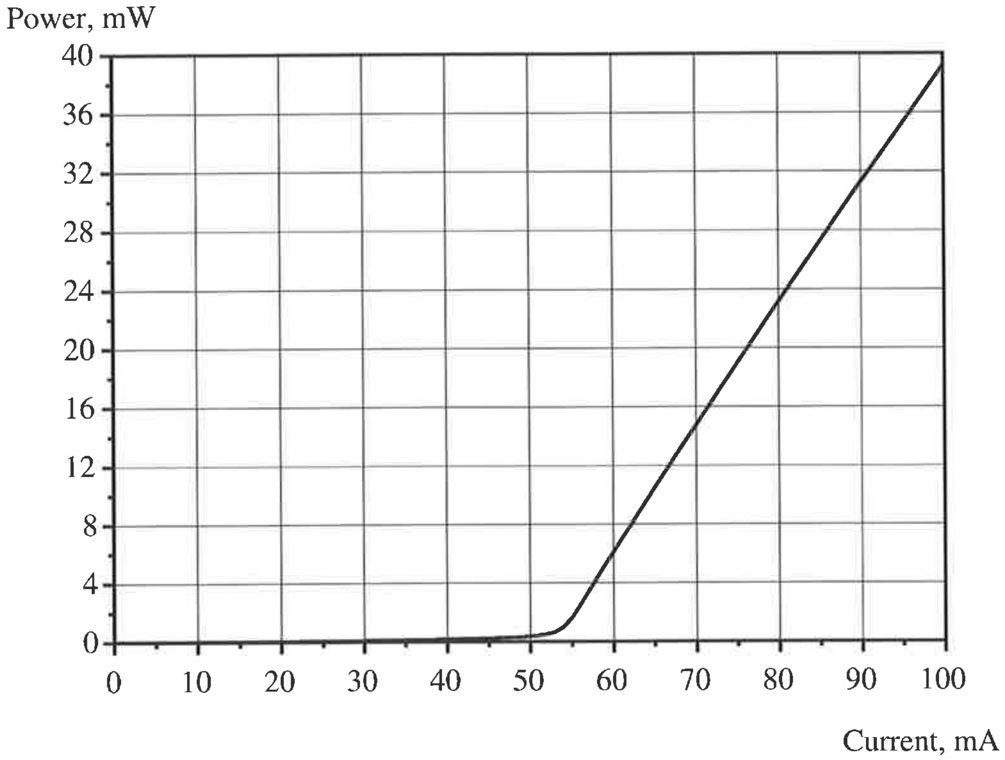

Figure 2-3 Laser diode optical power output versus forward current

The threshold current for the laser diode operation is $I_{th} = 52.30\ mA$ and the dependence of the optical power on the current above threshold is given by:

$$P = aI + b, \tag{2-1}$$

where the slope is $a = 0.826\ mW / mA$ and the zero intercept is $b = -43.2\ mW$. The measured wavelength of the diode is 807 nm.

2.2.4 Collimation and Focusing

While the light emitted by the laser diode is in the form of a divergent beam, the Nd:YAG laser requires a pump beam that satisfies the mode matching condition. This condition means that at any point along the axis of the laser, the pump beam has to have a size (in the transverse direction) smaller than or equal to the size of the laser mode of the cavity. If this condition is not fulfilled, some of the pump energy will not make any contribution to the desired transverse laser mode (TEM_{00}) and will result in high fluorescence losses. Even worse, this energy could provide enough gain for the higher order transverse modes to start lasing.

Using only one lens to transform a divergent beam into a convergent one is difficult and it is also inconvenient due to the need to insert other elements into the pump beam (isolator, modulator etc). Therefore, the best option is to transform the divergent beam of the laser diode into a parallel one using a collimating lens and, at the other end, to focus the beam down to the desired size.

The collimation of the beam is done with a GRIN lens collimator of $f_1 = 3.7\,mm$ focal distance (model 06 GLC 009 from Melles Griot [17]). It produces a parallel beam with a semi-axis of about 1.34 mm in one direction and 0.44 mm in the other.

The configuration employed in the focusing of the pump beam has been modelled with the computer program Paraxia [18], which uses ABCD matrices to determine the propagation of Gaussian beams through optical elements [19]. The elements used to implement this configuration are a plano-convex singlet for focusing and the laser rod. The plano-convex singlet has a focal distance $f_2 = 25\,mm$ (model 06 LXP 003 from Melles Griot) and is positioned at about 22 mm in front of the coated end of the Nd:YAG rod. The shape of the focused beam of the laser diode is elliptical and its waist is $4.8\,\mu m$ mm in one direction and $14.4\,\mu m$ in the orthogonal direction. The laser cavity is positioned such that the waist is located inside the Nd:YAG rod and the size of the beam at the entry into the rod is about the same as the size of the laser mode.

Given the importance of the mode matching condition for achieving low threshold, the size of the pump beam had to be measured to insure that the focusing is close to the predicted value. There are standard techniques for measuring the size of a laser beam, like the scanning knife-edge [20]. However, given the size of the beam used in this application and the low accuracy required, a technique based on the use of a charge-coupled device (CCD) camera seemed more appropriate. The method developed was a modification of the techniques presented in [21]:

- The attenuated beam was focused directly onto the CCD sensor and the TV signal was displayed on the digital oscilloscope.
- The trigger point was set as high as possible to acquire the TV line corresponding to the cross-section with the highest amplitude.
- Using the cursors, the time difference between the points at 13.5% of the maximum amplitude was measured.
- Knowing the time required to scan a horizontal line and the horizontal width of the CCD sensor, the size of the beam was calculated.

This method allowed quick measurements and easy adjustments of the optical elements. For the laser diode beam, the waist in one direction was determined to be about $24\,\mu m$, a value sufficiently close to the value calculated above ($14.4\,\mu m$). It was not possible to make reliable measurements in the other direction, as the pixel size of the CCD sensor was about $9\,\mu m$.

2.2.5 Optical Isolation

It is well known that laser diodes suffer from the destabilising influence of even minute amounts of optical feedback [22], [23]. In the case of an end pumped laser, optical feedback is unavoidable because the pump beam must be normal to the end of the laser rod. This end is optically polished and coated with a dielectric stack which constitutes one of the mirrors of the Nd:YAG laser cavity. This mirror is highly reflective for the 1064 nm wavelength of the

Nd:YAG laser and about 33% reflective for the 807 nm wavelength of the laser diode. Therefore, in conjunction with the collimation and focusing lenses, quite a large proportion of the reflected light is sent back into the laser diode, causing unstable operation and potential for damage to the diode facets. The latter can happen when the alignment is sufficiently good to allow operation in external cavity regime, which substantially reduces the threshold current of the laser diode.

As a side note, this mode of operation for the laser diode is relatively easy to obtain and we have achieved a very low threshold current for the laser diode (about 35 mA). However, when we tried to modulate the injection current with a sine wave, the output power varied in steps due to mode jumping between the closely packed modes of the long external cavity, making this mode of operation completely unusable [24].

Insertion of an optical isolator can alleviate these problems by allowing the light to pass from the laser diode to the Nd:YAG laser, but reflecting away the light coming back. The action of the isolator is very effective in the case of the laser diode because the emitted light is already polarised, so there is no power loss apart from the Fresnel reflection losses (about 8.75% due to inappropriate anti-reflection coatings of the rhombus).

The isolator used in the pump system comprised a polarising cube beamsplitter (03 PBS 063 from Melles Griot) and a Fresnel rhombus (of unknown origin) as a retarding device. Its operation is fairly straightforward: the polarising beamsplitter is aligned with the polarisation axis of the laser diode such that maximum transmission is achieved. The polarisation of the beam is then transformed by the Fresnel rhombus from linear to circular at the first pass and from circular to linear at the second pass. However, the polarisation axis of the back-reflected light is rotated by 90 degrees and the polarising beamsplitter deflects it sideways.

The isolator exhibited an insertion loss of about 0.8dB (8.74%) and 24 dB of isolation. The isolation is not very large, but in line with the calculations based on the characteristics of the constructive elements. This isolation, combined with a small amount of misalignment, proved to be sufficient for stable operation of the laser diode.

2.2.6 Modulation

In the initial experiments the Nd:YAG laser was modulated through direct modulation of the laser diode current. While this method is simple and has good bandwidth, it also has the problem that it stimulates the mode-hopping behaviour of the laser diode. When the laser diode jumps between two adjacent longitudinal modes there is a small change in the output power; also, since the two modes have slightly different wavelengths, they are absorbed differently in the Nd:YAG material. This means that superposed on the desired modulation there is an additional effect due to mode hopping. For this reason, the direct modulation was abandoned in favour of external modulation. Moreover, the stability of the laser diode was constantly monitored with the built-in photodiode and an oscilloscope for evidence of mode hopping.

The modulation of the pump beam is achieved through the use of an acousto-optic modulator. This device (type N23080, produced by NEOS [25]) consists of a modulator (tellurium dioxide crystal) acoustically coupled to a piezo-electric transducer (lithium niobate) and an impedance matching network (see Table 2-4). When an RF signal with appropriate frequency is applied to the input connector, it produces ultrasonic vibrations in the piezo-electric transducer. These vibrations are coupled into the modulator and establish a diffraction grating whose strength is dependent on the intensity of the RF drive. If the beam of light is focused down on this diffraction grating at Bragg angle, it will be diffracted and the energy will be distributed among various orders of diffraction. The more RF is applied to the acousto-optic modulator, the less optical power remains into the zeroth order of diffraction (undiffracted light). Therefore, the acousto-optic modulator introduces a 180° phase shift between the modulating signal and the pump power. The relationship between the input RF power and the optical power left in the undiffracted beam is non-linear, but for low levels of RF drive there is almost linear proportionality.

Table 2-4 Acousto-optic modulator specifications

Characteristic	Typical value	Comments
Diffraction efficiency	86%	At $\lambda = 632.8\ nm$
Deflection angle	15.2 mrad	At $\lambda = 807.5\ nm$
Spectral range	440-850 nm	
Nominal RF frequency	80 MHz	40 MHz bandwidth
Maximum RF power	0.9 W	

In experiments the acousto-optic modulator was driven by an RF signal generator set to 80 MHz, followed by a 1W RF amplifier (model 1zh produced by Minicircuits). The RF generators used were either a Hewlet-Packard RF generator model 8640B, with a modulation bandwidth of 60 kHz, or a Rhode-Schwartz model SMT03 RF generator with a modulation bandwidth of 100kHz. Although the reduction in the magnitude of the modulation transfer function above the cut-off frequency is gradual, it introduces a significant phase shift between the electronic input and the optical output. This is a serious limitation of the modulation system since the phase shift is evident well below the cut-off frequency and complicates the interpretation of the measurements.

2.3 Nd:YAG Laser

The Nd:YAG laser was specifically built for the experimental study of the non-linear equations governing its operation. Therefore, the main design criteria were single-mode operation (both transversal and longitudinal) and good dynamic range of power above threshold, while the output power and the efficiency of the laser were of second importance. In principle, single-mode operation could be attained by shortening the laser cavity (to increase inter-mode separation) and by narrowing the effective gain curve through the use of frequency selective elements. For a number of reasons we decided not to use intra-cavity elements and accept multimode operation. Given a certain optical power available for pump, the dynamic range requirement can be met by reducing the losses of the cavity (including transmission loss which means low output power) and by concentrating the available pump power into a small volume of the active medium. Thus, the design of the laser involved iterative calculations for both the power balance and cavity design and the final results are described below.

2.3.1 Nd:YAG Properties

The active medium of the laser used in this study is yttrium aluminium garnet doped with neodymium ($Y_3Al_5O_{12}:Nd^{3+}$ or Nd:YAG). This is a commonly used type of solid state laser material, due to a combination of favourable properties [12], [26], [27], [28].

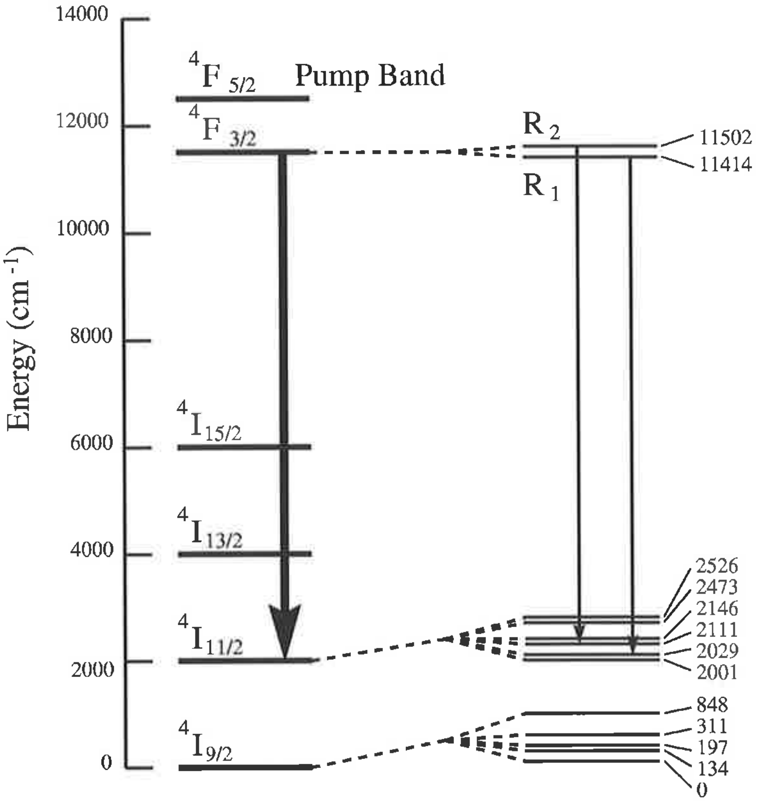

Figure 2-4 The energy diagram of the Nd^{+3} in YAG

The host crystal (YAG) has good mechanical, optical and thermal properties. Due to the cubic structure the fluorescent linewidth is narrow, resulting in high gain and therefore low lasing threshold. There is no charge compensation required when the Nd^{3+} substitutes for the Y^{3+}, but the radii of the two ions differ by about 3% and this limits the concentration of neodymium to less than about 1.25%. The Nd:YAG laser is a four-level system, with a simplified energy levels diagram shown in Figure 2-4 [12], [26]. The pumping is from the ground state to the $^4F_{5/2}$ level, at a wavelength of $\lambda_p = 807.5\ \text{nm}$. The quantum efficiency of the pumping is given by:

$$\eta_Q = \frac{h\nu}{h\nu_p}, \tag{2-2}$$

limiting the slope efficiency of the laser to 75.88%.

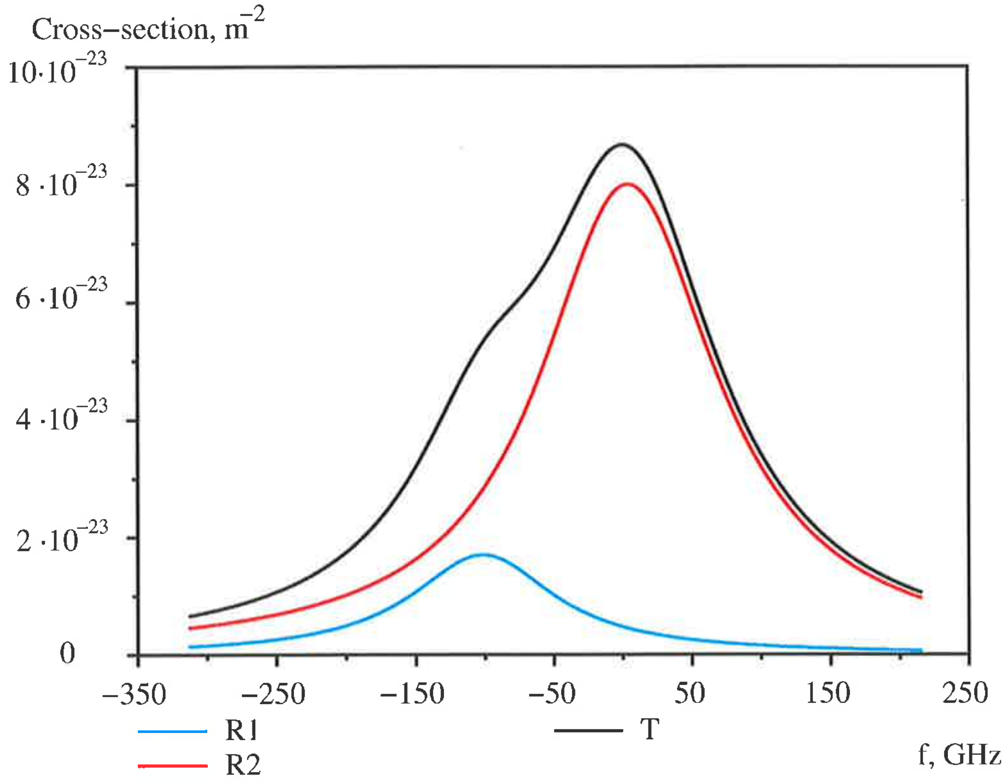

Figure 2-5 Cross-section of the 1064 nm Nd:YAG line

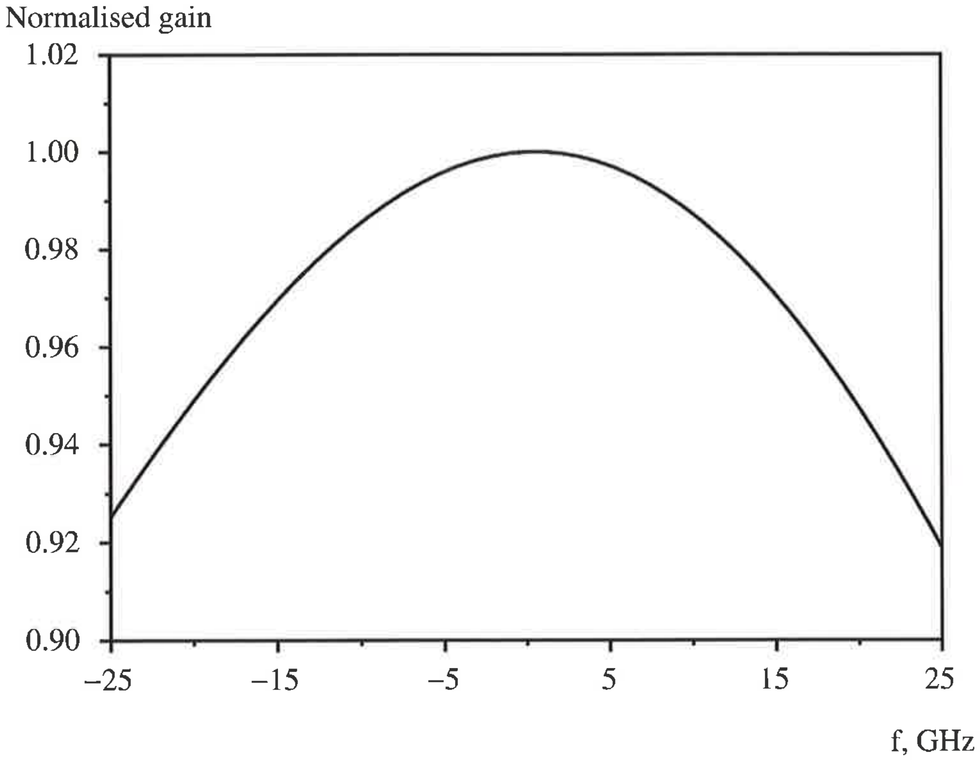

Figure 2-6 Detailed view of the centre of the gain curve

As seen in Figure 2-5, the 1064 nm laser line of Nd:YAG consists of two Lorentzian lines that partially overlap [26]. The lasing transition starts on the R_2 level of the $^4F_{3/2}$ manifold, and ends on the Y_3 level of the $^4I_{1/2}$. This level is sufficiently high above the ground state, that thermal excitation is completely negligible. Assuming short relaxation time among the emitting states, the level R2 is in thermal equilibrium with the level R_1. The Boltzmann factor is given by:

$$\frac{N_2}{N_1} = \exp\left(\frac{E_{R_2} - E_{R_1}}{kT}\right) \tag{2-3}$$

and at room temperature this is about 0.68. One important consequence of this situation, illustrated in Figure 2-6, is that the gain curve of the material is slightly asymmetric, influencing the threshold behaviour of the laser.

The most important optical properties of the Nd:YAG material are listed in Table 2-5.

Table 2-5 Nd:YAG optical properties

Characteristic	Typical value	Comments
Laser wavelength	1.0641µm	
Laser linewidth	0.45 nm 0.59 nm 0.6 nm	[12] [28]
Emission cross-section (effective value for the R_2 level of the $^4F_{3/2}$ manifold)	$2.8\ 10^{-23}\ m^2$ $2.7\ 10^{-23}\ m^2$ $3.4\ 10^{-23}\ m^2$	[12] [28] [15]
Scattering coefficient	$0.2\ m^{-1}$	[12]
Pump wavelength	0.8075 µm	
Pump linewidth	0.9 nm	
Absorption coefficient at the pump wavelength	$1200\ m^{-1}$ $1830\ m^{-1}$ $900\ m^{-1}$ $600\ m^{-1}$	1.0% Nd [15] 1.1% Nd [26] 1.1% Nd [28] [46]
Refractive index	1.8163 1.76	At 1.0641µm At 0.8075 µm
Fluorescence decay time	230 µs	

2.3.2 Power Balance

If we assume that the laser operates in a steady state condition and consider a packet of photons starting at some point in the cavity, we expect their number to remain constant after a round trip. This can be expressed in the form of the following equation [12]:

$$R_1 R_2 \exp 2(g - \alpha) l_{YAG} = 1 . \tag{2-4}$$

Here R_1 and R_2 are the reflectivities of the mirrors, g and α are respectively the gain and the loss per unit length in the active medium and l_{YAG} is the length of the active medium (see Figure 2-7). This formula tells us that the gain of the active medium must compensate both the losses of the mirrors and the absorption and scattering in the laser rod.

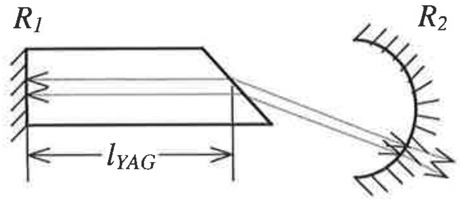

Figure 2-7 Optical cavity diagram

By taking the natural logarithm of both sides of (2-4) we get:

$$2gl_{YAG} = 2\alpha l_{YAG} - \ln R_1 - \ln R_2 . \tag{2-5}$$

Given that the reflectivities of the mirrors are quite high, the logarithms can be approximated as $\ln R_1 \approx R_1 - 1 = -L_m$ and $\ln R_2 \approx R_2 - 1 = -T$. Here L_m represents the loss of the back mirror and T represents the transmission of the spherical mirror (output coupler). Thus, the balance of power in the cavity can be written as:

$$G = L + T , \tag{2-6}$$

where $G = 2gl_{YAG}$ is the round trip gain of the cavity and the losses in the active medium ($2\alpha l_{YAG}$) and at the back mirror (L_m) have been combined in a single loss term L.

The gain per unit length of the active medium is the product of the stimulated emission cross-section σ and the population inversion density N: $g = \sigma N$. As we shall see in the next chapter, at threshold the population inversion density is given by the product of the fluorescence decay time τ_f and the threshold pump rate density W_{th}: $N_{th} = \tau_f W_{th}$ – see (3-12). Hence, at threshold we have:

$$G = 2\sigma\tau_f W_{th} l_{YAG} . \tag{2-7}$$

The threshold pump rate density represents the number of Nd^{3+} ions brought to the upper lasing level per unit volume and per second and can be calculated as follows. The number of pump photons absorbed in the laser rod per second at threshold is $\eta_p P_{th} / h\nu_p$, where η_p is the pumping efficiency, P_{th} is the laser diode optical power required to reach the threshold and $h\nu_p$ is the energy of a pump photon. Assuming mode matching (perfect overlap between the laser mode and the pump beam), each photon absorbed in the rod will excite a Nd^{3+} ion to the pump band, ready to contribute to the laser action. The references consulted imply or assume that the transition from the pump band ($^4F_{5/2}$) to the upper laser level ($^4F_{3/2}$) occur with negligible or no losses. Therefore, dividing the above mentioned number to the volume V of the lasing region gives the threshold pump rate density:

$$W_{th} = \frac{\eta_p P_{th}}{h\nu_p V} . \tag{2-8}$$

Finally, the incident power required to reach the threshold can be obtained by combining relations (2-6), (2-7) and (2-8) and writing the volume of the lasing region as the product between the area of the elliptical mode and the length of the rod $V = \pi\omega_a\omega_b l_{YAG}$ (see 2.3.3):

$$P_{th} = \frac{\pi \omega_a \omega_b hc(T+L)}{2\sigma\tau_f \lambda_p \eta_p}.$$

(2-9)

In the reference [13] the formula for the gain G is refined by calculating the effective overlap between the laser mode (of waist ω) and the pump mode (of waist ω_p) along the axis of the cavity. The calculation uses as a weighing factor the absorption of the pump beam in the rod (expressed through the absorption cross-section σ_p and the Nd^{3+} ion density N_{Nd}). If we rearrange this formula to explicit the threshold pump power we obtain:

$$P_{th} = \frac{\pi \left[\sigma_p N_{Nd} \int_0^{l_{YAG}} \frac{\exp(-\sigma_p N_{Nd} z)}{\left[\omega^2(z) + \omega_p^2(z)\right]/2} dz \right]^{-1} hc(T+L)}{2\sigma\tau_f \lambda_p \eta_p}.$$

(2-10)

While this formula has not been used to determine the threshold incident power, it is useful as it highlights the importance of mode matching.

The pump power required to reach the threshold can be estimated using appropriate numerical values for the right hand side of (2-9):

- $\omega_a = 65.1\,\mu m$, $\omega_b = 115.5\,\mu m$ (from 2.3.3);
- $T = 1 - R_2 = 0.01$, where R_2 is the reflectivity of the output coupler (from 2.3.4);
- $L = 1 - R_1 + 2\alpha l_{YAG} = 0.0043 + 0.004 = 0.0083$, where R_1 is the reflectivity of the coated end of the laser rod (from 2.3.4) and α is the scattering coefficient of the active material (from Table 2-5);
- $\sigma, \tau_f, \lambda_p$ have the values listed in Table 2-5 (where multiple values are listed, the first one is being used);
- $\eta_p = T_i \cdot T_m = 0.605$, where $T_i = 0.913$ is the transmission of the isolator (see 2.2.5) and $T_m = 0.663$ is the transmission of the coated end of the laser rod (from 2.3.4).

Given the uncertainty of some of the numerical values (like σ, T, η_p) the result of the calculation should be considered with considerable caution:

$$P_{th} = 13.65\,mW.$$

(2-11)

2.3.3 Cavity Design

The optical cavity of the laser employs a plane mirror deposited directly on one end of the Nd:YAG rod and a spherical mirror. The main requirements for the cavity are:

- it must be stable;
- the size of the mode at the plane mirror should be as small as possible;
- the optical length of the cavity should be as small as possible.

The first requirement is necessary for continuous operation at low power, the second for minimising the threshold power and the third for increasing the separation (and therefore the competition) between longitudinal modes [29]. The configuration chosen for our resonator is very close to hemi-confocal. A symmetrical confocal cavity has two identical spherical mirrors separated by a distance equal to their radius of curvature (or a distance equal to the sum of their focal distances). If a plane mirror is introduced halfway between the two spherical mirrors as shown in the Figure 2-8, the field in the cavity reflects back on itself. This configuration has good stability properties and gives an almost constant spot size within the rod.

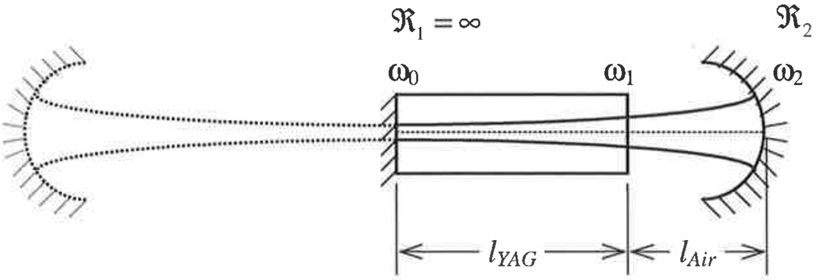

Figure 2-8 Hemi-confocal optical cavity diagram

The higher transverse modes of the cavity can be avoided through careful optical alignment; therefore we are only concerned with the TEM$_{00}$ Gaussian mode. For this case, the general formulae for the spot size $\omega(z)$ and radius of curvature of the wavefront $\Re(z)$ at some point z on the optical axis are:

$$\omega(z) = \omega_0 \left[1 + \left(\frac{\lambda z}{\pi \omega_0^2} \right)^2 \right]^{1/2}, \tag{2-12}$$

$$\Re(z) = z \left[1 + \left(\frac{\pi \omega_0^2}{\lambda z} \right)^2 \right]. \tag{2-13}$$

Here λ is the wavelength of the laser mode in air and ω_0 is the waist at the plane mirror ($z = 0$). At the other end of the cavity ($z = L_{cav}$, where L_{cav} is the length of the cavity) the radius of curvature of the wavefront must match the radius of curvature of the spherical mirror:

$$\Re(L_{cav}) = \Re_2 . \tag{2-14}$$

As far as the ray propagation is concerned, the length of the cavity is given by [30]:

$$L_{cav} = \frac{l_{YAG}}{n_{YAG}} + l_{air}, \tag{2-15}$$

where n is the refractive index of Nd:YAG. It is interesting to note that the formula for L_{cav} is quite different from the one for the optical length L_{optic} as defined by (3-80).

Applying condition (2-14) to the formula (2-13) yields:

$$\omega_0^2 = \frac{\lambda}{\pi} [L_{cav}(\Re_2 - L_{cav})]^{1/2} . \tag{2-16}$$

For our laser $\Re_2 = 25\,mm$, $L_{cav} = 12.5\,mm$ and $\lambda = 1.064\,\mu m$, giving a waist size of $\omega_0 = 65\,\mu m$.

A laser cavity with symmetry about the optical axis does not have a preferred orientation for the polarisation of the electromagnetic field. Therefore, in such a cavity two orthogonally polarised sets of longitudinal modes exist, with their orientation dictated by the small anisotropy inherently present in the cavity (mainly in the active medium). Cutting the internal end of the laser rod at Brewster angle forces the polarisation of each mode to be in the same direction (horizontal), so that in the subsequent modelling we do not have to include the possibility of polarisation instability and switching [31], [32]. This not only forced the existence of a unique polarisation of the lasing modes, but also avoided the need for anti-reflection coatings at that end.

The analysis of the laser cavity is complicated by the presence of the Brewster angle. While the initial design neglected this detail without introducing too much error, subsequent analysis based on the computer programme Paraxia [18] permitted to fully understand the effects of the Brewster angle. Thus, the modelling has shown that the eigen-mode of the laser cavity is elliptical and the waist in one direction remains as calculated above ($\omega_a = 65.1\,\mu m$), while in the other direction the waist is $\omega_b = 115.5\,\mu m$. Since the pump beam is also elliptical, it is possible to adjust the orientation of the laser diode such that the ellipses are aligned and take advantage for mode matching.

2.3.4 Mechanical Construction

In construction the laser is quite simple: it consists of a laser rod and an output-coupling mirror. There is an aluminium frame holding the laser rod in a 'V' groove and the mirror mount. The frame itself sits on a five-axis positioner in front of the focusing lens of the pump system. The laser rod is glued to the aluminium frame and, since the yttrium aluminium garnet (YAG) synthetic crystal has good thermal conductivity, this insures good thermal coupling of the active zone to the ambient.

The rod was cut at Brewster angle at one end and both ends were optically polished. Optical measurements done at AWA Industries have shown that the quality of the polished surfaces was very good (see Table 2-6 Laser rod specifications). The perpendicular end was coated with a dielectric stack mirror highly reflective at the operating wavelength ($\lambda = 1064\,nm$) and transmissive at the pump wavelength ($\lambda = 807\,nm$). Several measurements have been done at Adelaide University and at DSTO to check the characteristics of the dielectric stack at both pump and laser wavelengths and the results are shown in the table below:

Table 2-6 Laser rod specifications

Characteristic	Typical value	Comments
Nd concentration	1.1%	Atomic
Rod length	10 mm	l_{YAG} (on axis)
Brewster angle	61°12'	$n_{YAG} \cong 1.82$
Surface quality (RMS)	0.013λ	At $\lambda = 546\,nm$
Surface quality (PV)	0.085λ	At $\lambda = 546\,nm$
Mirror reflectivity	99.57%	At $\lambda = 1064\,nm$
Mirror transmission	66.3%	At $\lambda = 807\,nm$

The spherical mirror is an output coupler type PR1-1064-99-0537-0.025CC from CVI Laser Corporation. It has a radius of curvature of 0.025 m and coatings optimised for 1064 nm with a nominal reflectivity of 99% ±0.5% on the concave side and a maximum transmission loss of 0.25% on the flat side. The mirror is positioned at about $l_{air} = 7\ mm$ from the exit point of the beam from the laser rod. It is mounted on a piezo-electric ring which, in turn, is attached to the mirror mount. This arrangement permits small adjustments of the laser cavity length to either compensate for thermal drift or to apply the dither necessary for the lock-in amplifier.

2.4 Detection System

All the experiments performed with the Nd:YAG laser involved measurements of the total intensity and / or the intensities of individual longitudinal modes. While measuring total intensity is fairly easy, measuring individual modes is considerably more difficult.

First, the longitudinal mode to be measured has to be separated from the beam emerging at the output coupler. The separation is done with a Fabry-Perot filter with adjustable pass-band position (centre frequency). The pass-band of the Fabry-Perot has to be sufficiently narrow so the mode being measured is not contaminated with contributions from other modes.

Because the Fabry-Perot reflects back all the light outside its pass-band, there must be a certain degree of isolation between the laser and the Fabry-Perot. If there is no isolation or if the isolation is not sufficiently good, the light reflected back into the cavity will perturb the operation of the laser to the point where it becomes a completely different system (laser with external feedback or even extended/multiple cavity laser).

Also, since the length of the laser cavity is not actively controlled by a servo system, there is drift in the frequencies of the modes, making it necessary to lock the Fabry-Perot cavity to the mode being measured. Locking requires either one cavity or the other (i.e. the laser or the Fabry-Perot) to be frequency modulated with a low frequency dither. This dither signal has the potential to perturb the measurements as well, so its amplitude must be kept as low as possible.

Finally, the light is transformed into electric signals with the help of various types of photodiode-amplifier combinations. They are required to be linear, have enough bandwidth and be able to cope with a large dynamic range. The electric signals are further processed by direct digitisation with A/D boards or applied to specialised instruments (spectrum analyser, digital oscilloscope etc.).

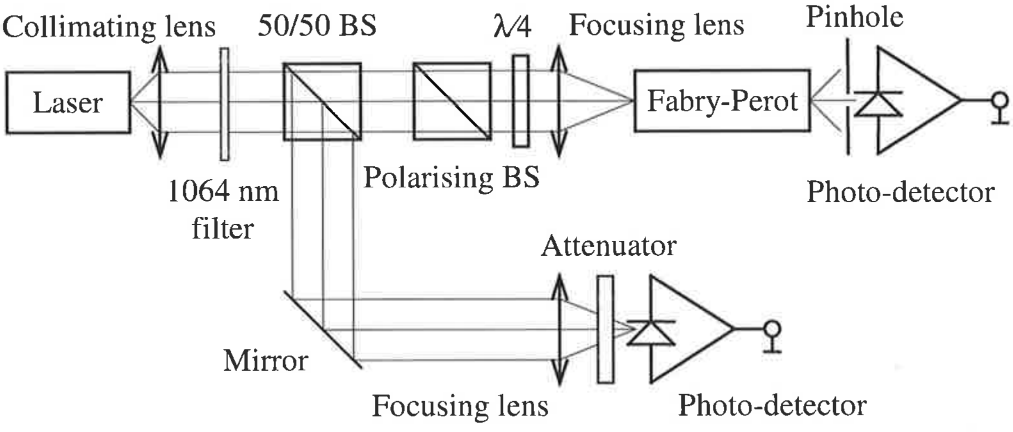

Figure 2-9 Detection system block diagram

An example of a possible configuration of the detection system is depicted in Figure 2-9. Here the laser beam is collimated and split into two beams of equal intensity by the non-polarising 50/50 beamsplitter. One of the beams is passed through an isolator constructed from a polarising beamsplitter and a quarter wave plate and focused onto the input aperture of the Fabry-Perot filter. The intensity of the longitudinal mode of the laser selected at the output of the Fabry-Perot is detected by one of the photo-detectors. The other beam is possibly attenuated and applied to the other photo-detector. This arrangement can be used for measuring transfer functions of individual modes and total intensity or cross-spectrum of noise between individual modes and total intensity.

2.4.1 Fabry-Perot Filters

The Fabry-Perot filters are used in the detection system to obtain the spectrum of the laser or to select individual longitudinal modes. These filters are very similar in construction to the laser cavity: two high reflectivity mirrors with a common optical axis. The separation between mirrors can be varied over a very small range with the help of a piezo-electric transducer and this action permits the adjustment of the filter's pass-band position. For the experimental set-ups used in this work two types of filters have been used: a commercial spherical mirror Fabry-Perot and a 'home-made' plane mirror Fabry-Perot.

The spherical mirror Fabry-Perot is a model SA-10 confocal spectrum analyser (produced by TecOptics) with the characteristics listed in the Table 2-7.

Table 2-7 SA-10 spectrum analyser specifications

Characteristic	Typical value	Comments
Free spectral range	10 GHz	Cavity length 7.5 mm
Mirror reflectivity	99.7%	Soft coatings
Finesse	268	Measured
Scan range	0.8 μm	Per 1000 V
Detector	Ge photodiode	High dark current
Spacer expansion coeff.	0.8-2.0 10^{-6} °C^{-1}	Invar 36

Since the separation between successive longitudinal modes of the laser is 6.15 GHz and the laser usually operates on more than 2 modes, some modes are folded back into the 10 GHz free spectral range of the filter. Although this folding complicates the identification of the modes, the high finesse and the excellent thermal stability of this Fabry-Perot have made it the filter of choice for most of the experiments. It is important to note that the Fabry-Perot requires an aperture in front of the photodiode to prevent the simultaneous detection of more than one mode at a time. The size of the aperture is a compromise between resolution and throughput and the theoretical treatment of the spherical Fabry-Perot in [33] includes a justification for the appropriate selection of this size.

The plan mirror Fabry-Perot was constructed with two plane mirrors with 99% and 95% reflectivity at 1064 nm, which gave a reflectivity finesse of about 100. However, the defect finesse (due to misalignment and lack of planeity) reduced the overall finesse considerably, so the resolution was just enough to separate each mode. One of the mirrors was mounted on a piezo-electric stack to allow either the scanning of the spectrum or the selection of a particular mode. This filter has been mainly used in experiments where simultaneous observation of two individual modes was necessary.

2.4.2 Optical Isolation

In the simplest form, some degree of isolation between the laser and the Fabry-Perot interferometer can be achieved by purposely mis-aligning the axis of the Fabry-Perot in respect to the laser. However, with this rudimentary method it is quite difficult to control the degree of isolation and the throughput of the filter decreases fairly rapidly with the misalignment angle.

The method of optical isolation chosen for the Nd:YAG laser is similar to the one used for the laser diode, since the light coming out is polarised due to the Brewster angle in the cavity. In this case the isolator consisted of a polarising cube beamsplitter (03 PBS 063 from Melles Griot) and a quarter waveplate (QWPM-1064-0x-4 from CVI Laser Corporation) instead of the Fresnel rhombus. The operation, however, is very similar: the light passes unhampered through the polarising cube beamsplitter since its axis is aligned to the laser. The quarter waveplate transforms the polarisation of the beam from linear to a circular on the first pass and then back from circular to linear for the light coming back. However, the direction of polarisation for the rays reflected back is orthogonal to the polarisation of the laser and the polarising cube beamsplitter deflects these rays sideways.

The degree of isolation offered by this isolator is similar to the other isolator (around 25 dB), since the limiting element is the same – the polarising cube beamsplitter.

2.4.3 Photo-Detectors

The dynamic range of the optical signals received by the photo-detectors is quite large, particularly when considering measurements of extremely small spectral components superposed on large DC levels. Obtaining a large dynamic range required two conditions: the use of very low noise transimpedance amplifiers (to push down the noise floor) and careful management of the optical power level applied to the photodiode (to keep it just under the saturation level, when possible). This last condition, for example, required the use of attenuators while detecting the total intensity. When detecting individual modes extra amplification had to be provided to compensate for the transmission loss of the Fabry-Perot filters and the fact that individual modes can be quite weak compared to the total intensity.

Ideally, the gain and phase characteristics of the photodiode amplifiers should be accurately known and sufficiently good so they do not affect the measurements. In practice, small variations in the gain or phase shifts could be tolerated and / or eliminated through calibration.

Selecting suitable photodiodes and constructing amplifiers to match each photodiode have achieved most of these requirements. The design and construction of such a photodiode amplifier is described in Appendix A2.3. The characteristics of the photo-detectors varied to some extent from one another, due to the differences between the photodiodes used and the gain required. In all cases their bandwidth was at least 300 kHz and the noise floor was well below the noise level in the presence of the optical signals. All these amplifiers were DC coupled, the only exception being the one constructed for the germanium diode of the spherical Fabry-Perot. This diode had a very large dark current, making the AC coupling mandatory.

2.4.4 Lock-in Techniques

In some of the experiments it was necessary to follow the evolution of a certain longitudinal mode for an extended period of time (for example when measuring transfer functions). Since the cavities of the laser and the Fabry-Perot filter are subject to temperature drift, even if initially the Fabry-Perot is passing the desired mode, after a while the mode is lost. Therefore, for such experiments it is necessary to find a way to lock the Fabry-Perot filter to the laser cavity so they drift together and the mode under investigation is always within the pass-band of the filter.

The technique used in such cases makes use of a lock-in amplifier and is described in the following. We assume that a longitudinal mode of the laser is being passed through the Fabry-Perot and that it is possible to frequency modulate it, for example by modulating the length of the laser cavity. This can be done by applying a sinusoidal voltage to the piezoelectric ring on which the spherical mirror of the laser cavity is mounted. This dither signal is relatively small in amplitude (less then a volt on the piezoelectric ceramic) and has a frequency chosen such that it is situated in a relatively quiet region of the modal intensity spectrum (low noise and far from the regions of interest). The effect of this dither signal on the intensity of light passed by Fabry-Perot filter is shown in Figure 2-10. If the mode is situated to the left of the transmission peak, a shift of the mode frequency to the right and then to the left produces an increase followed by a decrease of the passed intensity (left-hand side graph). If the mode is situated to the right of the transmission peak, a shift of the mode frequency to the right and then to the left produces a decrease followed by an increase of the passed intensity (right-hand side graph).

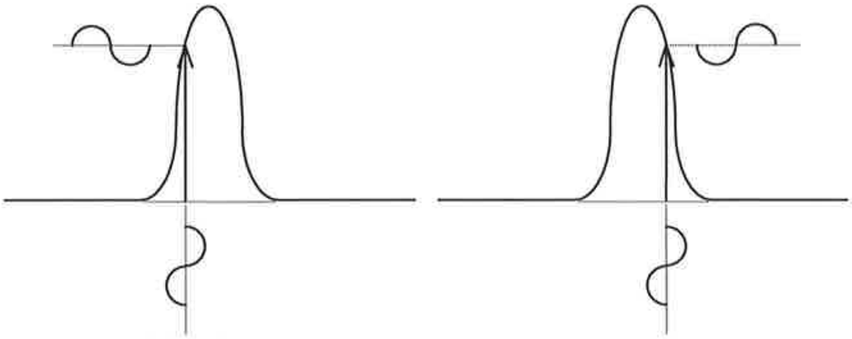

Figure 2-10 Effect of dither on a mode offset from the centre of the Fabry-Perot pass-band

Thus, if the longitudinal mode of the laser is frequency modulated with the dither signal, the Fabry-Perot filter transforms this frequency modulation into an amplitude modulation. The detected intensity is in phase or in antiphase with the driving signal, depending on the position of the laser mode frequency with respect to the peak of the pass-band of the Fabry-Perot. If the position of the laser mode coincides with the top of the Fabry-Perot peak, then the detected signal appears as in Figure 2-11.

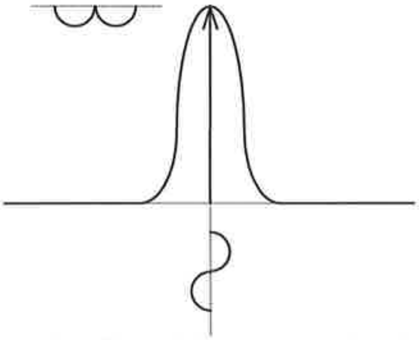

Figure 2-11 Effect of dither on a mode at the centre of the Fabry-Perot pass-band

When the frequency of the mode is shifted to the left or to the right, the passed intensity decreases in both cases and the frequency of the detected signal is twice the original frequency of the dither. At the frequency of the dither however, there is no detected signal, which is consistent with the change of phase between the two positions of the mode shown in Figure 2-10.

As a matter of convenience, the practical implementation of this technique is done using a lock-in amplifier, as shown in Figure 2-12. This instrument consists of a very low noise amplifier, a phase locked loop and a synchronous demodulator followed by low pass filtering and display. The dither signal is applied to the laser cavity and to the reference input of the lock-in amplifier. The laser beam is passed through the Fabry-Perot filter and transformed into an electric signal by the photo-detector, which is then applied to the signal input of the lock-in amplifier.

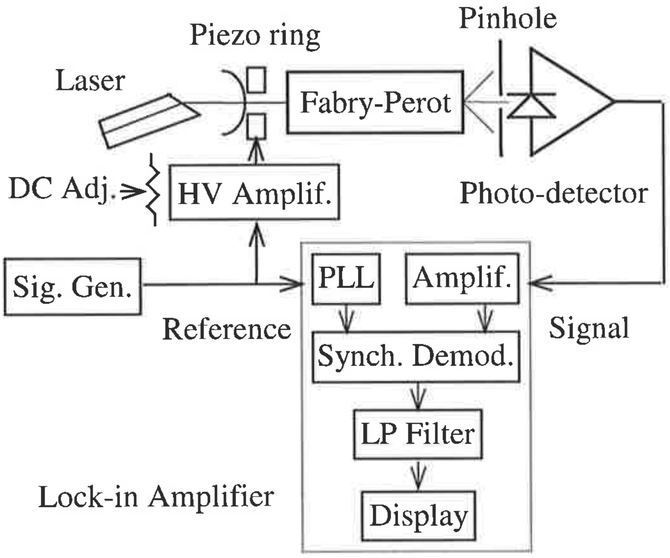

Figure 2-12 Open-loop application of the lock-in amplifier

The synchronous demodulation in conjunction with the low-pass filtering permits the detection of a minute amount of signal at the dither frequency, even in the presence of large amounts of noise and unrelated signals. Being a coherent technique, it also detects the phase of the input signal with respect to the reference channel and this can be used to indicate the situation where the frequency of the laser mode coincides with the peak of the Fabry-Perot pass-band.

Normally, the output from the lock-in amplifier can be fed back into the high voltage amplifier to create a closed loop system. In our case this proved not to be necessary, since the drift was relatively small during the measurements. Thus, the lock-in was only used to indicate the relative positions of the laser mode and the Fabry-Perot pass-band. It should also be noted that we could have applied the dither to the Fabry-Perot filter instead of the laser cavity, but this has become apparent after the measurements have been taken. The lock-in amplifiers used in this work were the SR510 (single output channel) and SR830 DSP (dual output channel) form Stanford Research Systems.

2.5 Laser Alignment and Measured Performance

The alignment of the laser cavity was initially done with the seeder of a high power Q-switched Nd:YAG laser. The seeder is a high quality CW Nd:YAG laser offering single-mode oscillation (axial and transversal), high stability, low divergence. In the first stage, the seeder was used as a light source of appropriate wavelength while the cavity of our laser was scanned like a Fabry-Perot spectrum analyser (using the piezo-electric ring). The cavity was monitored with a CCD camera for a sudden increase in luminosity, indicating the resonant condition. In the second stage, the seeder was substituted with the 807 nm laser diode and the five-axis positioner was adjusted until the laser started to operate. In the third stage, the CCD camera monitored the output of the Nd:YAG laser for the presence of the transverse modes and the five-axis positioner was further adjusted to achieve TEM_{00} operation. At the beginning of the third stage, the laser oscillated in up to 9 to 12 transverse modes (TEM_{33} or TEM_{34}); as the alignment was improved, the number of transverse modes decreased until only the TEM_{00} mode remained. In all stages, the CCD camera was fitted with a low-pass filter, so that the ambient light and / or the pump radiation were not obscuring the 1064 nm radiation.

Once the laser was aligned and started to operate, the first experiment performed was a measurement of the output power versus the laser diode temperature. The result is shown in Figure 2-13; based on this result, in all subsequent experiments the temperature was maintained in the vicinity of 24°C, with only small adjustments when required to prevent the laser diode from mode-hopping.

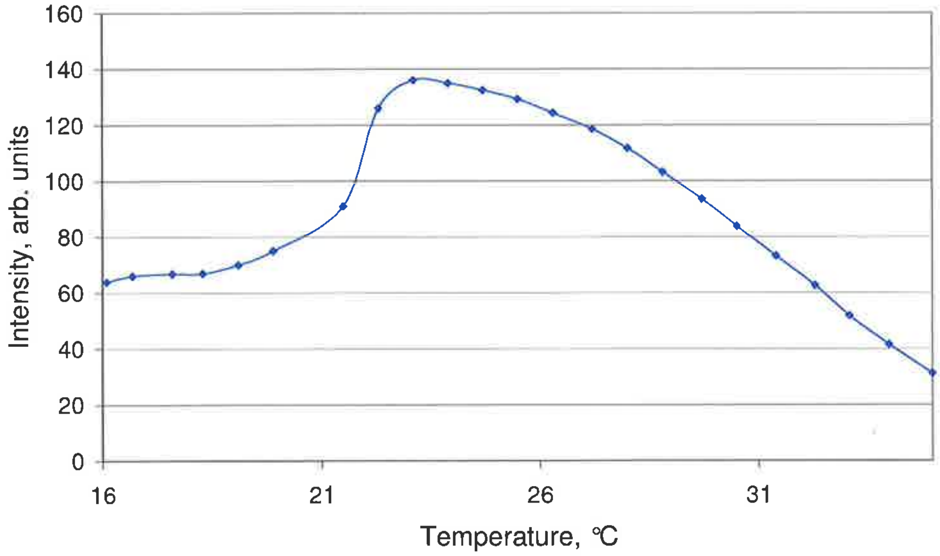

Figure 2-13 Nd:YAG laser optical power as function of the laser diode temperature

The next experiment performed was a measurement of the Nd:YAG laser output power versus laser diode current (shown in Figure 2-14), to assess the validity of the power balance calculations. Above the threshold, the output optical power of the Nd:YAG laser has an almost linear dependence on the laser diode current:

$$P = mI + n \tag{2-17}$$

with a slope of $m = 5.56 \cdot 10^{-2}\ mW/mA$ and a zero intercept of $n = -3.994\ mW$. The laser diode current for the threshold of the Nd:YAG laser was $I_{th} = 69.8\ mA$, corresponding to an input optical power of $P_{th} = 14.5\ \text{mW}$.

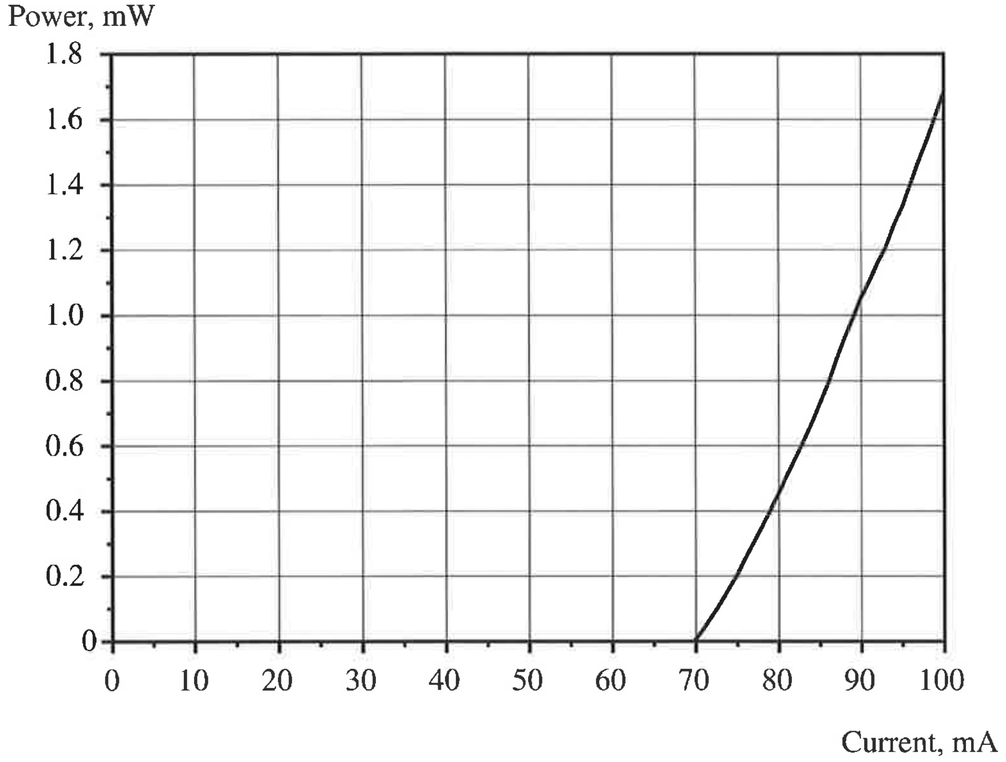

Figure 2-14 Nd:YAG laser optical power as function of the laser diode current

The measured value of the threshold pump power appeared to compare quite well ($\cong 6\%$) with the calculated value given by (2-11). However, successive measurements gave a range of values for the laser diode current required to start the Nd:YAG laser: from as low as $I_{th} = 64.4\,mA$ to as high as $I_{th} = 83.1\,mA$. If we assume that (2-1) is correct, this corresponds to a threshold pump power ranging from $P_{th} = 9.17$ mW to $P_{th} = 25.44$ mW. This spread was due to a number of causes, like the aging of the optical components and the introduction of the AOM, but most importantly to varying degrees of laser cavity alignment.

Further characterisation of the laser was achieved by measuring the total intensity noise spectrum with an extremely fast photodiode, amplifier and an RF spectrum analyser. The spectrum showed a cluster of peaks at a frequency of $f_l = 6.1715\,GHz$. This measurement suggested multimode operation and allowed a precise measurement of the optical length of the cavity:

$$L_{optic} = \frac{c}{2f_l}. \tag{2-18}$$

The length determined this way, $L_{optic} = 24.33\,mm$, agrees reasonably well with the length calculated from (3-80), $L_{optic} = 25.16\,mm$, using the values listed in the Table 2-5 (for n_{YAG}) and in the section 2.3.4 (for l_{YAG}, l_{air}).

The same noise spectrum, measured with a lower frequency photodiode / amplifier, displayed a peak at a frequency of the order of tens to hundreds of kHz, known as the relaxation oscillations frequency [34]. Measuring the position of the peak for different pump levels allows the determination of the cavity decay time τ_c and thus the total cavity loss ($T + L$).

It is shown in [35], [36] that for a single-mode laser the relaxation oscillations frequency is related to the normalised pump power w through the formula:

$$f_{RO} = \frac{1}{2\pi}\left[\frac{(w-1)}{\tau_f \tau_c} - \left(\frac{w}{2\tau_f}\right)^2\right]^{1/2}.$$

When the normalised pump level is such that the term proportional to the square of the pump is negligible, this relation can be approximated with:

$$f_{RO}^2 \cong \frac{w-1}{4\pi^2 \tau_f \tau_c}. \tag{2-19}$$

The graph in Figure 2-15 is an example of plotting the measurements according to this formula and fitting a straight line to them (small adjustments to the threshold pump level were required to obtain the equality of the two coefficients). Using for τ_f the value from Table 2-5, we obtain for the cavity decay time the value $\tau_c = 6.94\,ns$. A discussion regarding the applicability of the formula to the multimode laser follows in the sections 4.4.3 and 4.5.3.

The total cavity loss is related to the cavity decay time through the formula [12]:

$$T + L = \frac{2L_{optic}}{c\tau_c}. \tag{2-20}$$

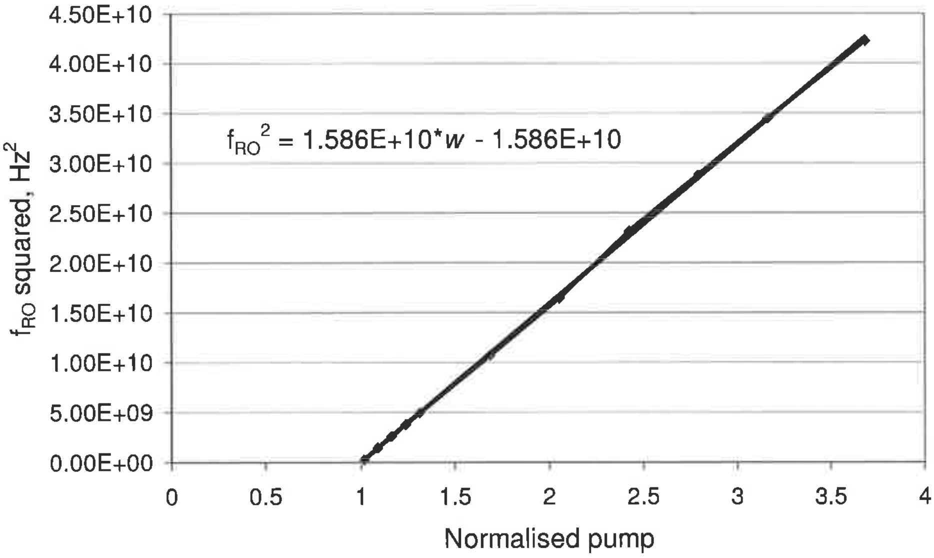

Figure 2-15 Relationship between the relaxation oscillations frequency and the pump level

For the measurement mentioned above, the losses of the cavity amount to $T + L = 0.0234$, a value relatively close to the one used for power balance calculations ($T + L = 0.0183$).

2.6 Conclusions

The characteristics of the laser constructed for the purpose of this study have been described above and the agreement between the calculations and the measurements is as good as one could expect from the uncertainty of the numerical values and the limited degree of sophistication used in modelling.

Designing and constructing the laser and the auxiliary systems was a great learning experience. At the same time, having a good understanding how the laser operates and the critical design parameters gave more confidence in the validity of models and measurements done with this system. It also allowed critical evaluation and rejection of directions not worth pursuing. For example, in principle one could measure the light emitted laterally by the laser due to fluorescence and thus monitor the population inversion (N). Correlating this measurement with the light emitted axially (proportional to the number of photons in the cavity modes, P), it would be possible to obtain a phase diagram in N-P coordinates. Embedding techniques applied to the time series thus obtained would allow gaining valuable insight into the dynamics of the laser. Unfortunately, the N measurement is significantly contaminated with laser light (P) scattered by the laser rod. Trying to remove the correlation proved to be difficult, so the whole idea of using the phase state diagram had to be abandoned.

The numerical values for some of the laser parameters have changed over time (e.g cavity decay time or threshold level). In such cases, the values determined at the time of the experiment were those used in calculations.

Chapter 3 Laser Modelling and Steady State

3.1 Introduction

Many lasers with gain provided by a single electronic transition of the active species operate on several longitudinal modes of the cavity, due to either inhomogeneous broadening or strong spatial hole burning. In such lasers it is expected, and usually observed, that above threshold the intensities of the different cavity modes are more or less proportional to the gain at their respective frequencies. The mode with the highest gain is the first to reach the threshold as the pumping rate is increased, and this first mode remains the most intense as the pump rate is further increased and other modes with lower gain begin to oscillate. However, this behaviour is not universal and our laser is a good example of this fact. In order to explain such behaviour, we introduce a model for a laser with homogeneous broadening and spatial hole burning, showing that, under certain circumstances, modes that have a higher lasing threshold due to lower gain can become more intense than the first mode to oscillate. In the next chapter we show that this model can also qualitatively account for certain characteristics of the measured transfer functions of the modulated laser.

Similar behaviour has been reported for a laser system where lasing on several transitions of the active Nd^{3+} ion can occur a little above threshold, but some of the lasing lines die off as the pump rate is increased further beyond threshold [37]. The laser in question used the crystal $LiNdP_4O_{12}$ (LNP) in which the Nd^{3+} ion is present in a much greater concentration (~30%) than is possible in crystals such as YAG where the Nd^{3+} is a dopant species (~1% replacement of Y). In that experiment there was a single longitudinal cavity mode under the gain profile of each electronic transition of the Nd^{3+} ions, except for one transition that had two modes under its gain profile. Here we consider the case of a Nd:YAG laser where only a single gain profile is relevant, though multiple longitudinal modes fit within it.

The classic model of Tang Statz deMars [7] captures many important features of the solid state lasers. As expected however, when the laser does not satisfy the assumptions of the original model, its behaviour departs from the model's predictions. In particular, the Tang Statz deMars model assumes that the pumping rate is uniform along the length of the gain medium, which fills the laser cavity. In the case of a solid state laser pumped by a laser diode at one end of the cavity, this assumption does not hold. We will show here that an extension of the standard Tang Statz deMars model, which allows for a pump rate that varies exponentially along the laser medium, can account qualitatively for the experimentally observed behaviour.

3.2 Rate Equations for the Single-Mode Laser

In this section we introduce the Langevin rate equations for the single-mode laser, to serve as the starting point for further development in this and next chapters. In the latter sections of this chapter we extend the equations to multimode operation and consider the spatial dependence of the independent variables, while ignoring the random forcing. In Chapter 5 we reintroduce the stochastic terms and consider their effect on the quasi-linear model of the multimode laser with spatial hole burning.

3.2.1 The Rate Equations

The rate equations follow from the quantum mechanical equations for the electro-magnetic field and atoms, interacting with each other and in contact with appropriate reservoirs [38], [39]. The Nd:YAG laser belongs to the B class of lasers, which are characterised by rapid de-phasing of the atomic polarisation. This allows the adiabatic elimination of the latter, reducing the equations to the evolution of the electric field and the populations of various atomic levels. If the knowledge of the electric field phase is not of interest, then either the photon number or the field intensity can replace the electric field. These two variables have identical evolution equations but different statistics, as it will be described in Chapter 5. For a lightly pumped four level laser the depletion of the ground state can be neglected and only the upper laser level atomic population (N_2) has independent variation [39].

Following [39], [34], and using similar notations, the rate equations of a four level single-mode laser can be expressed as follows:

$$\frac{\mathrm{d}N_2(t)}{\mathrm{d}t} = W(t) - \Gamma_2 N_2(t) - \pi[1 + P(t)]N_2(t) + r(t) \tag{3-1}$$

$$\frac{\mathrm{d}P(t)}{\mathrm{d}t} = \pi[1 + P(t)]N(t) - \gamma P(t) + s(t), \tag{3-2}$$

where the meaning of the symbols employed is defined in Table 3-1.

The first equation shows that the population inversion increases due to the pumping and decreases due to both the decay and the stimulated emission. The second equation shows that the photon number increases due to the stimulated emission and to that part of the spontaneous emission that is coupled into the lasing mode and decreases due to losses in the cavity. Each equation also includes a stochastic driving term, *r(t)* and *s(t)*, respectively, introduced here but only considered in Chapter 5.

The constants used in the rate equations (3-1) and (3-2) are related to the Nd:YAG material properties and the optical cavity parameters (introduced in Chapter 2) through the following relations:

$$\frac{1}{\tau_f} = \Gamma_2 + \pi, \quad \frac{1}{\tau_c} = \gamma, \quad \frac{c\sigma}{V} = \pi. \tag{3-3}$$

Table 3-1 Names of the symbols used in equations

N_2	Population inversion	P	Photon number
W	Pump rate	π	Mode rate
Γ_2	Level 2 decay rate	γ	Cavity decay rate
r	Population inversion noise source	s	Photon number noise source
τ_f	Fluorescence decay time	τ_c	Cavity decay time
V	Lasing region volume	σ	Emission cross-section

3.2.2 The Steady State Solutions

In steady state the population inversion and the photon number are constant, so the time derivatives in the rate equations (3-1) and (3-2) vanish and we get the following simultaneous equations:

$$\overline{W} = \Gamma_2 \overline{N}_2 + \pi\left(1+\overline{P}\right)\overline{N}_2 \tag{3-4}$$

$$\pi\left(1+\overline{P}\right)\overline{N}_2 = \gamma\overline{P}\,. \tag{3-5}$$

From these equations we obtain:

$$\overline{P} = \frac{\overline{W} - \gamma\left(1+\frac{\Gamma_2}{\pi}\right) + \sqrt{\left[\overline{W} - \gamma\left(1+\frac{\Gamma_2}{\pi}\right)\right]^2 + 4\gamma\overline{W}}}{2\gamma} \tag{3-6}$$

$$\overline{N}_2 = \frac{\gamma\overline{P}}{\pi\left(1+\overline{P}\right)}\,. \tag{3-7}$$

If we define the threshold pump rate as:

$$\overline{W}_{th} = \gamma\left(1+\frac{\Gamma_2}{\pi}\right) = \frac{1}{\pi\tau_f\tau_c}\,, \tag{3-8}$$

then we obtain the following values for the photon number and population inversion at threshold:

$$\overline{P}_{th} = \sqrt{1+\frac{\Gamma_2}{\pi}} = \frac{1}{\sqrt{\pi\tau_f}} \tag{3-9}$$

$$\overline{N}_{2,th} = \frac{\gamma}{\pi}\frac{\sqrt{1+\frac{\Gamma_2}{\pi}}}{1+\sqrt{1+\frac{\Gamma_2}{\pi}}} = \frac{1}{\pi\tau_c\left(1+\sqrt{\pi\tau_f}\right)}\,. \tag{3-10}$$

It is illustrative to calculate the threshold values of the pump rate, population inversion and photon number for typical parameters of the laser ($\tau_f = 230\,\mu s$, $\tau_c = 1.71\,ns$, $\pi = 12.7\cdot10^{-6}\,s^{-1}$):

$$W_{th} = 1.999\cdot10^{17},\ N_{2,th} = 4.59663\cdot10^{13},\ P_{th} = 18479\,.$$

For a pump level twice the threshold value we have:

$$W = 3.997\cdot10^{17},\ N_2 = 4.59688\cdot10^{13},\ P = 3.415\cdot10^{8},$$

showing the small change in the number of inverted atoms above the threshold and, in contrast, the significant change in the photon number. The large dynamic range of the average photon number is also evident in the graphical representation of (3-6), depicted in Figure 3-1.

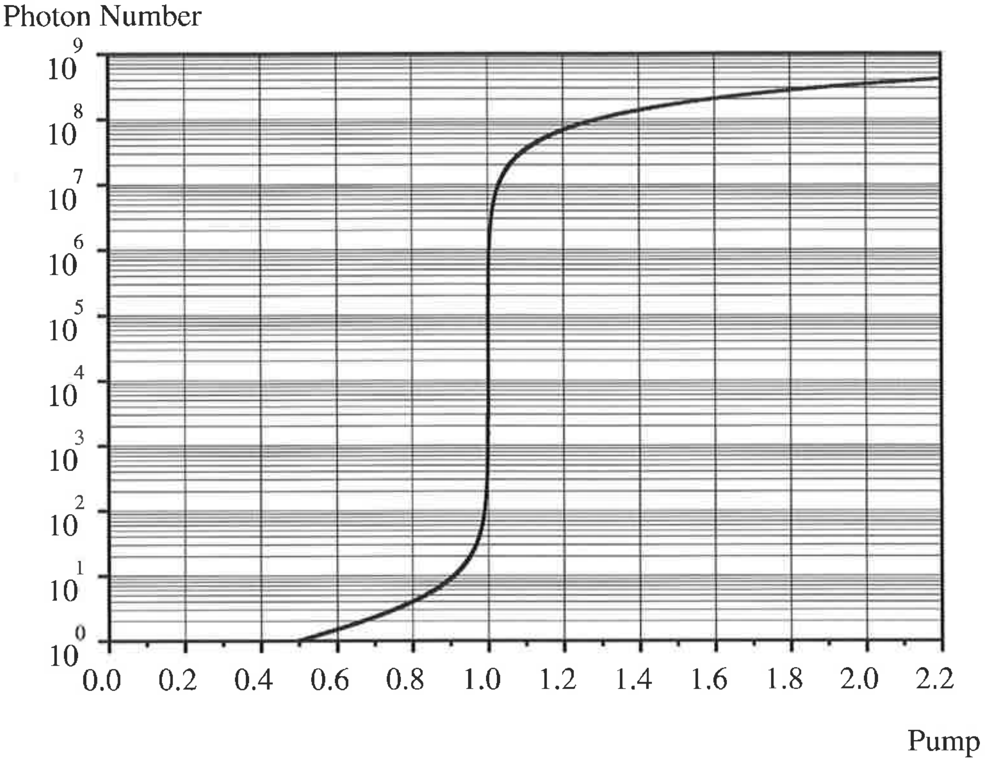

Figure 3-1 Threshold behaviour of the single-mode laser

In order to cover the regions both below and above the threshold, we used a logarithmic scale for the vertical axis. The horizontal axis is in linear scale and makes use of the normalised value of the pump rate, which is described in the next section.

3.2.3 Normalisation of the Rate Equations

The rate equations can be brought into a more convenient form by using appropriate normalisation factors. For the pump rate and the population inversion the appropriate factors are their threshold values (3-8) and (3-10). Given the numerical values of the laser parameters mentioned above, the threshold value of the population inversion can be simplified to:

$$N_{2,th} \cong \frac{1}{\pi \tau_c}, \tag{3-11}$$

the relative difference between (3-10) and (3-11) being of the order of $5.4 \cdot 10^{-5}$. With this simplification, we can write the following relation between the threshold values of the pump rate and the population inversion:

$$W_{th} = \frac{N_{2,th}}{\tau_f}. \tag{3-12}$$

If we define $n = \dfrac{N_2}{N_{2,th}}$ and $w = \dfrac{W}{W_{th}}$, the rate equations can be written as:

$$\frac{\mathrm{d}n}{\mathrm{d}t} = \frac{w}{\tau_f} - \frac{n}{\tau_f} - \pi P n \tag{3-13}$$

$$\frac{\mathrm{d}P}{\mathrm{d}t} = \frac{nP}{\tau_c} - \frac{P}{\tau_c} + \frac{n}{\tau_c}. \tag{3-14}$$

At this point it is useful to define the intensity of the electric field in the resonator as:

$$I = \frac{cPh\nu}{V} \tag{3-15}$$

and to normalise it to the saturation intensity I_s. The latter is the value of the intensity in the resonator for which the gain decreases to half of the small signal gain, or the stimulated emission rate equals the fluorescence decay rate ($\pi P_s n = \dfrac{n}{\tau_f}$) in (3-13):

$$I_s = \frac{h\nu}{\sigma\tau_f}. \tag{3-16}$$

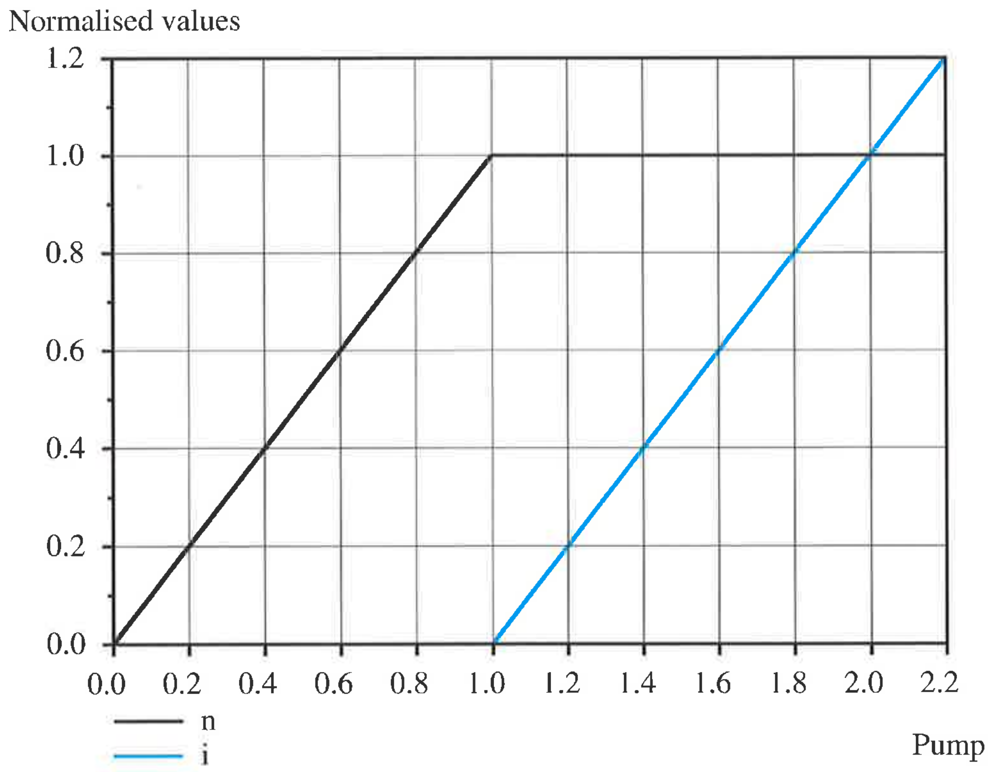

Figure 3-2 Steady state solutions of the single-mode laser

Introducing the normalised value of the intensity: $i=\frac{I}{I_s}$, we finally obtain the normalised rate equations:

$$\frac{\mathrm{d}n}{\mathrm{d}t}=\frac{1}{\tau_f}(w-n-ni) \tag{3-17}$$

$$\frac{\mathrm{d}i}{\mathrm{d}t}=\frac{1}{\tau_c}(ni-i+\pi\tau_f n). \tag{3-18}$$

The last term in (3-18) represents the spontaneous emission and, while it is essential for the start-up of the laser, its contribution above the threshold is very small and can be neglected. We show in Figure 3-2 the steady state solutions of the normalised rate equations as functions of the normalised pump level. The figure shows that above the threshold, to a high degree of accuracy, the normalised population inversion is clamped to 1 and the intensity increases linearly with the pump power.

3.3 Rate Equations for the Uniformly Pumped Multimode Laser

In a dielectric solid state laser the diffusion of the energy stored in inverted atoms is quite small. Therefore, in order to be able to model such a laser correctly, one has to take into account the spatial distribution of the field in the cavity and its effect on the population inversion. This is particularly important for the Fabry-Perot resonators with low losses, where the standing wave nature of the field leads to strong non-uniformities along the axis of the resonator.

3.3.1 Standing Waves in a Fabry-Perot Resonator

In a Fabry-Perot type resonator the electromagnetic field consists of two counter-propagating waves, each of them travelling from one mirror to the other. For a cavity optimised for high output power, the reflectivity of the output coupler is chosen to be rather low (Figure 3-3a). Therefore, the intensity of the incident wave (I_+) drops at the plane of the output coupler, but it is subsequently amplified as it passes through the active medium. On the other hand, if the cavity is optimised for low lasing threshold, the reflectivities of both mirrors must be rather high (Figure 3-3b). Consequently, the intensities of the two counter-propagating waves (I_+ and I_-) are nearly constant along the cavity axis and a strong standing wave pattern develops. The large variations of the electric field due to this pattern are responsible for the spatial hole burning in dielectric solid state lasers.

Our laser was designed for low lasing threshold, so we have chosen high reflectivity dielectric mirrors (99.5% for the end mirror and 99% for the output coupler). This means that it definitely falls into the latter case and the model we develop must take into account the small-scale ($\sim\lambda/2$) variation of the resultant intensity.

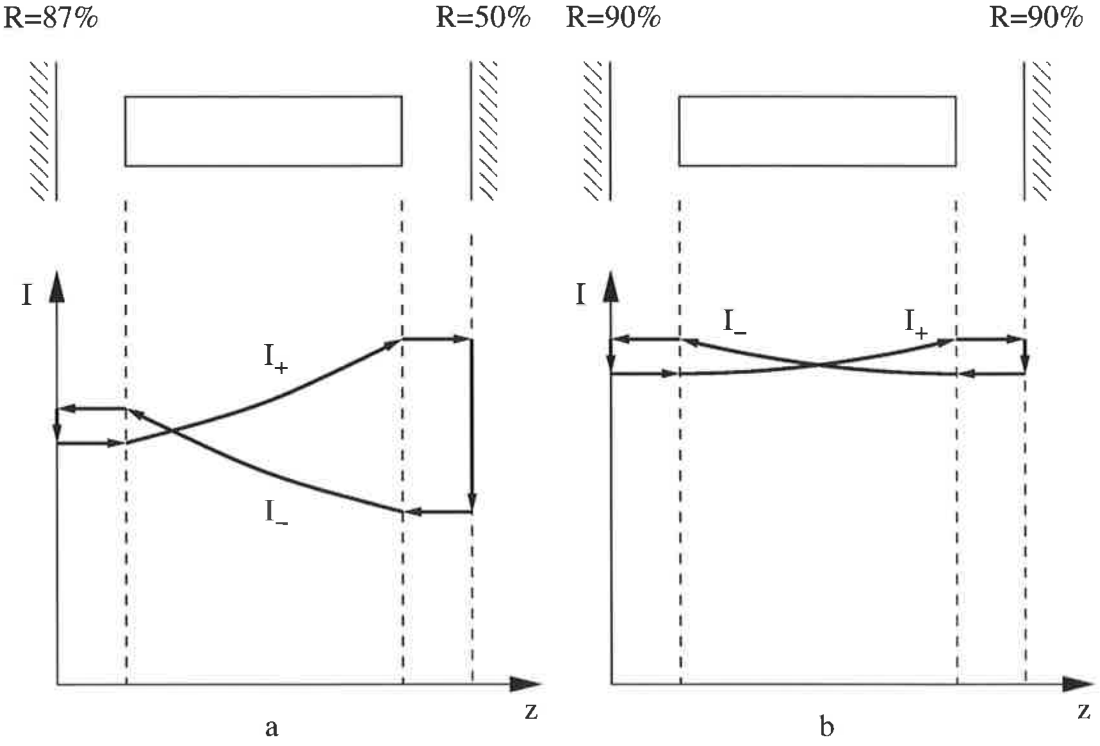

Figure 3-3 Comparison between a cavity optimised for high output power and a cavity optimised for low threshold

Based on these arguments, we will assume a plane-plane resonator of length *L* with no losses (empty cavity with 100% reflective mirrors). Although our laser uses dielectric mirrors, to simplify the calculations we will assume that we have perfectly conductive metallic mirrors.

The expressions for the electric fields in the cavity are given by:

$$E_+(z,t) = E_0(t)\sin\left[2\pi\left(\frac{t}{T}-\frac{z}{\lambda}\right)\right] \tag{3-19}$$

for the wave moving in the positive direction of the *z* axis and:

$$E_-(z,t) = E_0(t)\sin\left[2\pi\left(\frac{t}{T}-\frac{2L-z}{\lambda}\right)+\pi\right] \tag{3-20}$$

for the wave reflected by the second mirror and moving in the opposite direction. These equations take into account the phase change occurring at the mirrors and assume the amplitude of the electric field to be a slowly varying function of time. The resultant field at any point in the cavity is given by the relation:

$$E(z,t) = E_+(z,t) + E_-(z,t) \tag{3-21}$$

or:

$$E(z,t) = 2E_0(t)\sin\left[2\pi\left(\frac{t}{T}-\frac{L}{\lambda}\right)+\frac{\pi}{2}\right]\cdot\cos\left[2\pi\left(\frac{L-z}{\lambda}\right)-\frac{\pi}{2}\right]. \tag{3-22}$$

The boundary conditions for metallic mirrors require the electric field to be zero at the plane of the mirrors at any time. While the above expression satisfies this condition automatically at $z=L$, from the condition at $z=0$ we obtain:

$$L=\frac{m\lambda}{2}. \tag{3-23}$$

With this condition the expression for the total electric field becomes:

$$E(z,t)=-2E_0(t)\cos\omega t\cdot\sin kz, \tag{3-24}$$

where $k=\frac{2\pi}{\lambda}$ is the wave vector. As we are using the rate equations that deal with the intensities rather than the fields, the corresponding expression for the total intensity is:

$$I(z,t)=\sqrt{\frac{\varepsilon_0}{\mu_0}}\left\langle E^2(z,t)\right\rangle_t, \tag{3-25}$$

where the brackets $\langle\;\rangle_t$ refer to the average over a few cycles of the electric field. Substituting the above formula for the electric field, we obtain:

$$I(z,t)=\sqrt{\frac{\varepsilon_0}{\mu_0}}4E_0{}^2(t)\left\langle\cos^2\omega t\right\rangle_t\sin^2 kz \tag{3-26}$$

or

$$I(z,t)=\sqrt{\frac{\varepsilon_0}{\mu_0}}2E_0{}^2(t)\sin^2 kz. \tag{3-27}$$

If we define $I_0(t)=\sqrt{\frac{\varepsilon_0}{\mu_0}}E_0{}^2(t)$, then the intensity of the field in the resonator can be written as:

$$I(z,t)=I_0(t)(1-\cos 2kz). \tag{3-28}$$

3.3.2 Tang Statz deMars Equations

A dielectric solid state laser with a Fabry-Perot type cavity can be conveniently modelled by the Tang Statz deMars equations [7]. These equations take into account the spatial hole burning due to the standing wave nature of the light in the cavity. In the following, the original deduction is presented with the notations introduced in the normalised rate equation above.

The model assumes a cavity completely filled with the gain medium and pumped such that the pump power does not vary along the length of the cavity. If the reflectivity of the end mirrors is high enough, the intensity of the electric field of any longitudinal mode in the cavity is given by the normalised version of equation (3-28):

$$i_j(z,t) = i_j(t)(1 - \cos 2k_j z),$$

(3-29)

where the wave vectors $k_j = \dfrac{2\pi}{\lambda_j}$ are such that:

$$L_{optic} = \frac{m_j \lambda_j}{2}, \ m_j >> 1.$$

(3-30)

Here $L_{optic} = nL$ is the optical length of the cavity and n is the refractive index of the active medium at the lasing wavelength.

In the following we extend the normalised rate equations (3-17) and (3-18) without spontaneous emission to the multimode case. If we also take into account the longitudinal variation of the intensity of the electric field and of the population inversion, these equations become:

$$\frac{\mathrm{d}n(z,t)}{\mathrm{d}t} = \frac{1}{\tau_f}\left[w(t)/L_{optic} - n(z,t) - \sum_{i=1}^{N} g_i n(z,t) i_i(t)(1 - \cos 2k_i z) \right]$$

(3-31)

$$\frac{\mathrm{d}i_j(t)}{\mathrm{d}t} = \frac{1}{\tau_c}\left[g_j i_j(t) \int_0^{L_{optic}} n(z,t)(1 - \cos 2k_j z) dz - i_j(t) \right], \ j = 1 \ldots N.$$

(3-32)

In these equations we consider that each mode is characterised by a gain g_j, normalised with respect to the centre of the gain curve – see (3-53) and (3-54).

While the equation (3-31) is local, i.e. it refers to what happens in a narrow slice normal to the axis of the cavity, the set of equations (3-32) is global, in the sense that they only describe the temporal variation of the modal intensities. The spatial dependence of the modal intensities is known and given by (3-29). In steady state the time derivatives are zero, so (3-31) gives:

$$n(z) = \frac{w/L_{optic}}{1 + \sum_{i=1}^{N} g_i i_i (1 - \cos 2k_i z)}.$$

(3-33)

If the pump level is not too high above the threshold level, this equation can be approximated by:

$$n(z) \approx \frac{w}{L_{optic}}\left[1 - \sum_{i=1}^{N} g_i i_i (1 - \cos 2k_i z) \right].$$

(3-34)

For the time-varying situation, the above approximation of the steady state suggests that $n(z,t)$ could be written as:

$$n(z,t) = \frac{n_0(t)}{L_{optic}} + \sum_{i=1}^{N} \frac{n_i(t)}{L_{optic}} \cos 2k_i z.$$

(3-35)

Viewed another way, this approximation consists in using only the first term of the Fourier expansion of the population inversion density in respect to the mode intensities. By substituting this expression into the normalised rate equations, we obtain:

$$\frac{\mathrm{d}\,n_0(t)}{\mathrm{d}\,t}+\sum_{i=1}^{N}\frac{\mathrm{d}\,n_i(t)}{\mathrm{d}\,t}\cos(2k_i z)=\frac{1}{\tau_f}\left\{w(t)-n_0(t)-\sum_{i=1}^{N}n_i(t)\cos(2k_i z)-\right.$$
$$\left.-\sum_{k=1}^{N}g_k\left[n_0(t)+\sum_{i=1}^{N}n_i(t)\cos(2k_i z)\right]i_k(t)(1-\cos 2k_k z)\right\}$$

(3-36)

$$\frac{\mathrm{d}\,i_j(t)}{\mathrm{d}\,t}=\frac{1}{\tau_c}\left[g_j i_j(t)\frac{n_0(t)}{L_{optic}}\int_0^{L_{optic}}(1-\cos 2k_j z)dz+\right.$$
$$\left.+g_j i_j(t)\sum_{k=1}^{N}\frac{n_k(t)}{L_{optic}}\int_0^{L_{optic}}\cos 2k_k z(1-\cos 2k_j z)dz-i_j(t)\right].$$

(3-37)

In Appendix A3.1, we have shown details of the calculations required to obtain the Tang Statz deMars equations:

$$\frac{dn_0}{dt}=\frac{1}{\tau_f}\left[w_0-n_0-\sum_{k=1}^{N}g_k(n_0-1/2n_k)i_k\right]$$

(3-38)

$$\frac{dn_j}{dt}=\frac{1}{\tau_f}\left[g_j n_0 i_j-n_j\left(1+\sum_{k=1}^{N}g_k i_k\right)\right],\quad j=1\ldots N$$

(3-39)

$$\frac{di_j}{dt}=\frac{1}{\tau_c}\left[g_j(n_0-1/2n_j)-1\right]i_j,\quad j=1\ldots N.$$

(3-40)

3.3.3 Steady State Solutions for the Tang Statz deMars Equations

The equations derived above can be solved without difficulty for steady state solutions [40]. In this case, the time derivatives of the population inversion components and the intensities of the modes vanish:

$$w_0-n_0{}^0-\sum_{k=1}^{N}g_k\left(n_0{}^0-1/2n_k{}^0\right)i_k{}^0=0$$

(3-41)

$$g_j n_0{}^0 i_j{}^0-n_j{}^0\left(1+\sum_{k=1}^{N}g_k i_k{}^0\right)=0,\quad j=1\ldots N$$

(3-42)

$$g_j\left(n_0{}^0-1/2n_j{}^0\right)-1=0,\quad j=1\ldots N.$$

(3-43)

From the equations (3-43) we can express the components of the population inversion:

$$n_j^{\,0} = 2\left(n_0^{\,0} - 1/g_j\right). \tag{3-44}$$

The equations (3-42) can be summed over the values of *j* to give:

$$n_0^{\,0}\sum_{j=1}^{N} g_j i_j^{\,0} = \sum_{j=1}^{N} n_j^{\,0}\left(1 + \sum_{k=1}^{N} g_k i_k^{\,0}\right) \tag{3-45}$$

and so:

$$\sum_{k=1}^{N} g_k i_k^{\,0} = \frac{\sum_{j=1}^{N} n_j^{\,0}}{n_0^{\,0} - \sum_{j=1}^{N} n_j^{\,0}}. \tag{3-46}$$

This sum can be calculated by substituting the components of the population inversion determined in (3-44); if we use it in the equations (3-42) again, we can express the intensities of the modes as functions of the average of the population inversion:

$$i_j^{\,0} = \frac{n_0^{\,0} - 1/g_j}{g_j\left[\sum_{k=1}^{N} 1/g_k - n_0^{\,0}(N - 1/2)\right]}. \tag{3-47}$$

We can use the expressions for $n_j^{\,0}$ and $i_j^{\,0}$ in the first equation and get:

$$w_0 = n_0^{\,0} + \frac{n_0^{\,0}\sum_{k=1}^{N} 1/g_k - \sum_{k=1}^{N} 1/g_k^2}{\sum_{k=1}^{N} 1/g_k - (N - 1/2)n_0^{\,0}}. \tag{3-48}$$

This is a quadratic equation in $n_0^{\,0}$, and the acceptable solution is:

$$n_0 = \frac{w_0}{2} + \frac{\sum_{k=1}^{N} 1/g_k}{N - 1/2} - \frac{\sqrt{w_0^2(N - 1/2)^2 + 4\left(\sum_{k=1}^{N} 1/g_k\right)^2 - 4(N - 1/2)\sum_{k=1}^{N} 1/g_k^2}}{2(N - 1/2)}. \tag{3-49}$$

Using the substitutions:

$$S_1 = \sum_{k=1}^{N} 1/g_k, \qquad S_2 = \sum_{k=1}^{N} 1/g_k^{\,2},$$

the solutions for the steady state can be written as:

$$n_0^{\,0} = \frac{w_0}{2} + \frac{S_1}{N - 1/2} - \sqrt{\frac{w_0^{\,2}(N - 1/2)^2 + 4S_1^{\,2} - 4S_2(N - 1/2)}{2(N - 1/2)}} \tag{3-50}$$

$$n_j^{\,0} = 2\left(n_0^{\,0} - 1/g_j\right)$$

(3-51)

$$i_j^{\,0} = \frac{n_0^{\,0} - 1/g_j}{g_j\left[S_1 - n_0^{\,0}(N - 1/2)\right]}.$$

(3-52)

3.3.4 Threshold Behaviour of the Tang Statz deMars Equations

It is apparent from the above equations that the threshold for each individual mode and the steady state values of the modal intensities depend on the values of the relative gains g_j. Although we have previously shown that the emission line of Nd:YAG consists of two partially overlapping lines, in the following we will consider a simpler profile given by only one Lorentzian line:

$$g_j = \frac{1}{1 + \left(\frac{\nu_j - \nu_0}{\Delta\nu}\right)^2}, \quad j = 1 \ldots N.$$

(3-53)

We allow the highest gain mode to be offset from the centre of the line ν_0 by a fraction of the mode spacing $\delta\nu$:

$$\nu_j = \nu_0 + \left[(-1)^{(j-1)} \operatorname{int}\left(\frac{2j+1}{4}\right) + offset\right]\delta\nu, \quad 0 \le offset \le 0.5.$$

(3-54)

The numbering is such that mode 1 is the first to reach threshold and the others appear alternatively on the left and on the right of the gain profile. We have introduced the dimensionless variable *offset* because the position of the comb of the modes changes due to the thermal drift of the cavity.

In Figure 3-4 we plot the average and the components of the population inversion as a function of the pump level for an $offset = 0.2$. Unlike the case of the single-mode laser, the average population inversion is not clamped to the threshold value any more. This is due to the fact that the population inversion located at the nodes of the standing wave is not being used for lasing and it only decays through spontaneous emission. As the pump level increases above the threshold, this unused population inversion continues to increase and, on average, the population inversion becomes significantly higher then the threshold value. Of course, this means higher losses and a lower total intensity then that obtainable from a laser without spatial hole burning, for the same level of pump power. It is also interesting to note that the graph of total intensity versus pump power (shown in Figure 3-5) is linear to a very good approximation, despite the fact that the individual modal intensities do not have a linear variation.

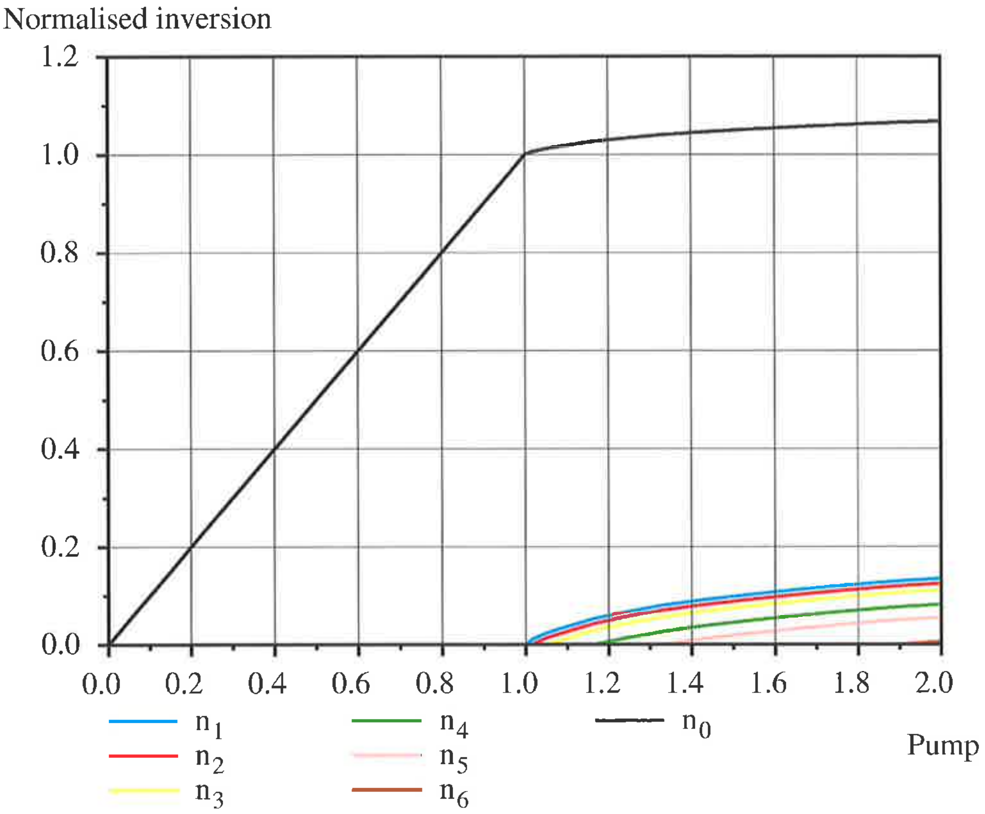

Figure 3-4 Population inversion average (n_0) and components ($n_1 - n_6$) for uniform pumping

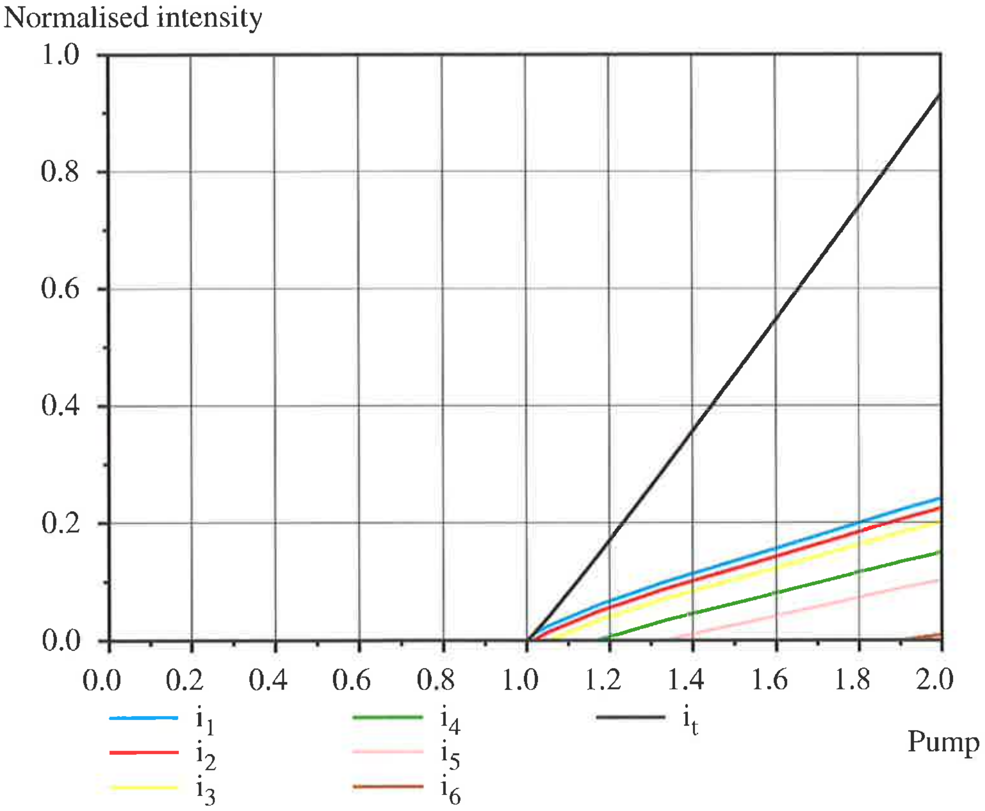

Figure 3-5 Total intensity (i_t) and modal intensities ($i_1 - i_6$) for uniform pumping

In Figure 3-6 and Figure 3-7 we present an enlarged view of the population inversion components and modal intensities respectively in the vicinity of the threshold.

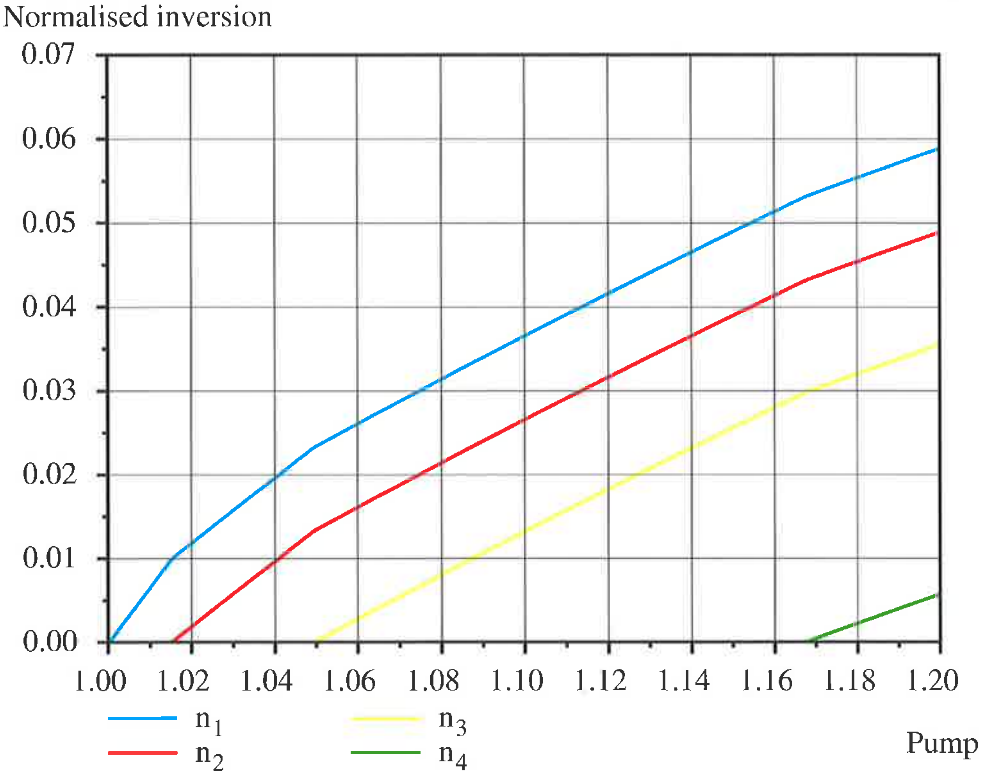

Figure 3-6 Detailed view of the population inversion components at threshold for uniform pumping

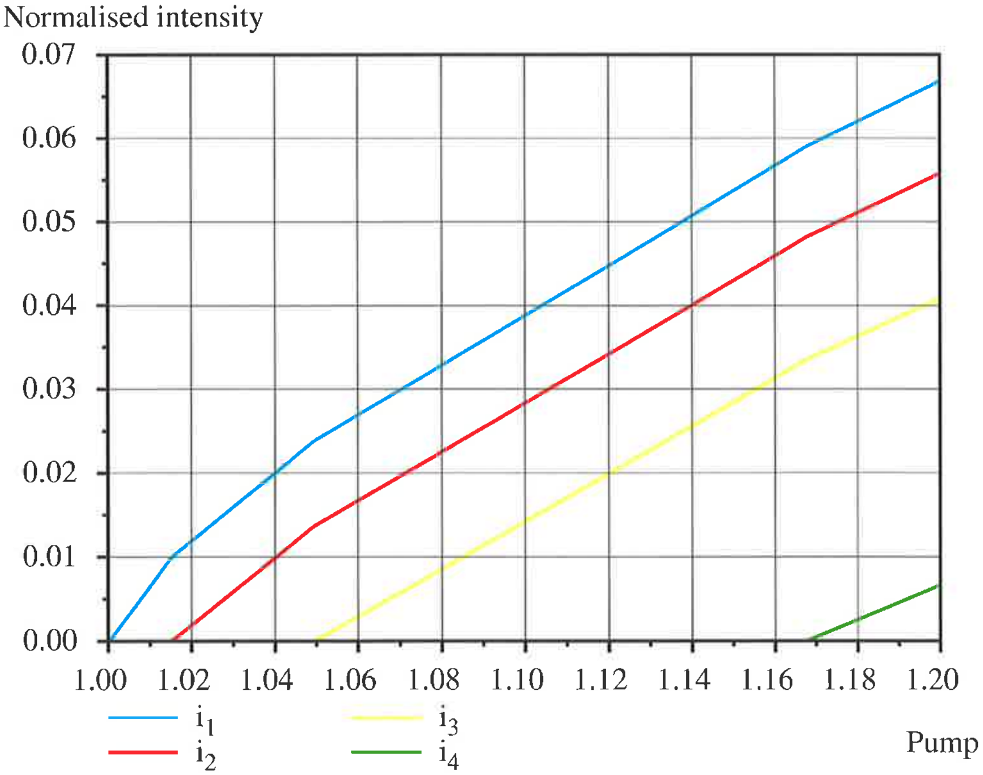

Figure 3-7 Detailed view of the modal intensities at threshold for uniform pumping

It is clear that the emergence of a new mode changes the slope of the graphs for both the components of the population inversion and the intensities of the modes, while the average of the population inversion and the total modal intensity have a smooth variation. It is also apparent that the ordering of the modes is the same as the ordering of the gains g_j, irrespective of the pump level.

3.4 Rate Equations for the End Pumped Multimode Laser

There are two important differences between the Tang Statz deMars model [7] and practical end pumped lasers. In the model it is assumed that the active material fills the cavity and that the pump power is absorbed uniformly along the axis of the active material. The consequences of removing these two restrictions for a variety of lasers have been analysed by many authors. For the homogeneously broadened multimode lasers with Fabry-Perot cavity described by the rate equations, the models presented in [41], [42] and, more recently, in [43] are examples of extensions of the Tang Statz deMars equations to cover non-uniform gain. A comparison between the equations derived in [41] and [42] is presented in [44]. The model [43] is a generalisation of our model, including both the incomplete filling of the cavity and exponentially absorbed pump.

3.4.1 Tang Statz deMars Equations with Exponential Decay

Our model assumes a laser pumped optically from one end. In this geometry, the cavity usually consists of a low transmission output coupler and a piece of gain medium with a mirror deposited on one end. This end mirror is generally highly transmissive for the pump radiation and highly reflective at the lasing wavelength. If we consider the pump rate to vary exponentially along the axis of the cavity due to the absorption of the pump radiation into the active medium, we can write the linear density of the absorbed pump rate as:

$$w(z,t) = w(t)\mu \exp(-\mu z). \tag{3-55}$$

The gain medium is assumed to be long enough to absorb most of the pump power and, for simplicity, we can consider that it fills the cavity. This assumption is quite justified because the contribution of the missing end of the rod would be negligible anyway, due to the non-uniform distribution of the gain. Therefore:

$$w(L_{optic}, t) \approx 0 \tag{3-56}$$

and thus:

$$\int_0^{L_{optic}} w(z,t)dz \approx w(t). \tag{3-57}$$

If we take into account the longitudinal variation of the intensity of the electric field and that of the population inversion, the normalised rate equations without spontaneous emission become:

$$\frac{\mathrm{d}n(z,t)}{\mathrm{d}t}=\frac{1}{\tau_f}\left[w(z,t)-n(z,t)-\sum_{i=1}^{N}g_i n(z,t)i_i(t)(1-\cos 2k_i z)\right]$$

(3-58)

$$\frac{\mathrm{d}i_j(t)}{\mathrm{d}t}=\frac{1}{\tau_c}\left[g_j i_j(t)\int_0^{L_{optic}}n(z,t)(1-\cos 2k_j z)dz-i_j(t)\right].$$

(3-59)

Following the same arguments as in the deduction of the Tang Statz deMars equations, we get for the steady state solution:

$$n(z)=\frac{w_0\mu\exp(-\mu z)}{1+\sum_{i=1}^{N}g_i i_i(1-\cos 2k_i z)}.$$

(3-60)

Again, if the pump level is not too high above the threshold level, this equation can be approximated by:

$$n(z)\approx w_0\mu\exp(-\mu z)\left[1-\sum_{i=1}^{N}g_i i_i(1-\cos 2k_i z)\right].$$

(3-61)

For the time-varying situation, the above approximation of the steady state suggests that $n(z,t)$ could be written as:

$$n(z,t)=n_0(t)\mu\exp(-\mu z)+\sum_{i=1}^{N}n_i(t)\mu\cos(2k_i z)\exp(-\mu z).$$

(3-62)

This expression can be substituted into the normalised rate equations and by dividing both sides of the first equation with $\mu\exp(-\mu z)$ we obtain:

$$\frac{\mathrm{d}n_0(t)}{\mathrm{d}t}+\sum_{i=1}^{N}\frac{\mathrm{d}n_i(t)}{\mathrm{d}t}\cos(2k_i z)=\frac{1}{\tau_f}\left\{w(t)-n_0(t)-\sum_{i=1}^{N}n_i(t)\cos(2k_i z)-\right.$$
$$\left.-\sum_{k=1}^{N}g_k\left[n_0(t)+\sum_{i=1}^{N}n_i(t)\cos(2k_i z)\right]i_k(t)(1-\cos 2k_k z)\right\}$$

(3-63)

$$\frac{\mathrm{d}i_j(t)}{\mathrm{d}t}=\frac{1}{\tau_c}\left[g_j i_j(t)n_0(t)\mu\int_0^{L_{optic}}(1-\cos 2k_j z)\exp(-\mu z)dz+\right.$$
$$\left.+g_j i_j(t)\sum_{k=0}^{N}n_k(t)\mu\int_0^{L_{optic}}\cos(2k_k z)(1-\cos 2k_j z)\exp(-\mu z)dz-i_j(t)\right].$$

(3-64)

In Appendix A3.2 we have shown details of the calculations required to obtain the Tang Statz deMars equations with exponential decay:

$$\frac{dn_0}{dt} = \frac{1}{\tau_f}\left[w_0 - n_0 - \sum_{k=1}^{N} g_k (n_0 - 1/2\, n_k) i_k\right]$$

(3-65)

$$\frac{dn_j}{dt} = \frac{1}{\tau_f}\left[g_j n_0 i_j - n_j\left(1 + \sum_{k=1}^{N} g_k i_k\right)\right], \quad j = 1 \ldots N$$

(3-66)

$$\frac{\mathrm{d}i_j}{\mathrm{d}t} = \frac{1}{\tau_c}\left\{g_j\left[n_0 - 1/2\sum_{k=1}^{N} n_k \frac{\mu^2 L_{optic}^2}{\mu^2 L_{optic}^2 + 4\pi^2 (m_k - m_j)^2}\right] - 1\right\} i_j, \quad j = 1 \ldots N.$$

(3-67)

3.4.2 Steady State Solutions for the Tang Statz deMars Equations with Exponential Decay

Finding the steady state solutions in the case of exponentially decaying pump is slightly more involved compared to the case of uniform pump. As before, we obtain a system of simultaneous equations by equating the time derivatives to zero:

$$w_0 - n_0 - \sum_{k=1}^{N} g_k (n_0 - 1/2\, n_k) i_k = 0$$

(3-68)

$$g_j n_0 i_j - n_j\left(1 + \sum_{k=1}^{N} g_k i_k\right) = 0, \quad j = 1 \ldots N$$

(3-69)

$$g_j\left[n_0 - 1/2\sum_{k=1}^{N} n_k \frac{\mu^2 L_{optic}^2}{\mu^2 L_{optic}^2 + 4\pi^2 (m_k - m_j)^2}\right] - 1 = 0, \quad j = 1 \ldots N.$$

(3-70)

The equations (3-70) can be simplified if we introduce the notation:

$$\alpha_{j,k} = \frac{\mu^2 L_{optic}^2}{\mu^2 L_{optic}^2 + 4\pi^2 (m_k - m_j)^2}, \quad j,k = 1 \ldots N$$

(3-71)

so we obtain:

$$\sum_{k=1}^{N} \alpha_{j,k} n_k = 2n_0 - 2/g_j, \quad j = 1 \ldots N.$$

(3-72)

These equations could be solved numerically to yield n_j, if we consider n_0 as a parameter:

$$n_j = a_j n_0 + b_j, \quad j = 1 \ldots N.$$

(3-73)

The equations (3-69) can be summed, similarly to the case of the Tang Statz deMars equations, over the values of *j* to give:

$$\sum_{k=1}^{N} g_k i_k = \frac{\sum_{j=1}^{N} n_j}{n_0 - \sum_{j=1}^{N} n_j}$$

(3-74)

and so:

$$i_j = \frac{n_j}{g_j\left(n_0 - \sum_{k=1}^{N} n_k\right)}, \quad j = 1 \ldots N\,.$$

(3-75)

Using the above results in the equation (3-68) we get:

$$w_0 - n_0 - \frac{n_0 \sum_{k=1}^{N} n_k}{n_0 - \sum_{j=1}^{N} n_j} + \frac{1}{2}\sum_{k=1}^{N} \frac{n_k^2}{n_0 - \sum_{j=1}^{N} n_j} = 0\,.$$

(3-76)

If we substitute n_j given by (3-73) in the equation above, we obtain a quadratic equation for n_0:

$$n_0^2\left(\sum_{j=1}^{N} a_j^2 - 2\right) + 2n_0\left(\sum_{j=1}^{N} a_j b_j + w_0 - w_0\sum_{j=1}^{N} a_j\right) + \sum_{j=1}^{N} b_j^2 - 2w_0\sum_{j=1}^{N} b_j = 0\,.$$

(3-77)

Once we solve this equation, we can determine n_0 and, from (3-73) and (3-75), n_j and i_j.

3.4.3 Threshold Behaviour for the Tang Statz deMars Equations with Exponential Decay

In the case of the Tang Statz deMars equations with exponential decay, there are two parameters that influence the threshold behaviour of the laser: the offset of the modes of the cavity with respect to the centre of the emission line and the coefficient of absorption of the medium μ. The latter depends on the concentration of the active ion (Nd^{3+}) in the host crystal and the tuning of the laser diode to the absorption peak of the Nd:YAG. If we use instead of μ the dimensionless absorption parameter:

$$q = \frac{2\pi}{\mu L_{optic}},$$

(3-78)

the equation (3-71) can be written as:

$$\alpha_{j,k} = \frac{1}{1 + q^2\left(m_k - m_j\right)^2}, \quad j,k = 1 \ldots N\,.$$

(3-79)

In choosing values of q for the model we have the problem that different values of μ exist in the literature. One value of the peak linear absorption coefficient of the Nd^{3+} at 808nm is $\mu = 900\ m^{-1}$ [28] for the typical Nd concentration of 1.1% that we used. This is similar to another value for the peak absorption coefficient $\mu = 800\ m^{-1}$ [45]. Another value of μ from the literature is $\mu = 333\ m^{-1}$ [46]. It should be noted that the *effective* absorption coefficient would also depend on the linewidth and exact operating wavelength of the laser diode used as a pump source. For our laser we have $L_{optic} = 2.5cm$, giving $q = 0.317$ and $q = 0.754$ for the values $\mu = 800\ m^{-1}$ and $\mu = 333\ m^{-1}$ respectively. As we show explicitly below, the predicted behaviour does depend fairly strongly on q and thus, from a practical point of view, on the detuning of the pump laser from the Nd^{3+} absorption peak at 808nm. For the sake of comparison with the experiment, the optical length is calculated taking into account the geometry of the laser:

$$L_{optic} = n_{YAG} l_{YAG} + l_{air} . \tag{3-80}$$

A value of $q = 1$ corresponds to the absorption of over 99.8% of the incident power into the rod and this justifies the assumption made earlier on about the active medium filling the cavity. For this value of q and for an *offset=0.2* we plot the population inversion average and components in Figure 3-8, while in Figure 3-9 we plot the total intensity and modal intensities. We note that, similar to the uniform pump case, the average population inversion and the total intensity have a smooth variation as the pump power is increased.

In Figure 3-10 and Figure 3-11 we plot the components of the population inversion and in the intensities of the modes alone. If we compare these graphs with those in Figure 3-6 and Figure 3-7, we can see that here the main mode and the second one have, for some values of the pump parameter, the same intensity, despite the difference in gain between the two.

This effect becomes even more visible if we assume a higher value for the absorption coefficient μ or, equivalently, a smaller value of q. The Figure 3-12 and Figure 3-13 are the equivalent of the Figure 3-9 and Figure 3-10, but here *q=0.85*.

It is quite clear from the details shown in Figure 3-14 and Figure 3-15 that the intensities of the modes no longer respect the ordering given by the gains g_j.

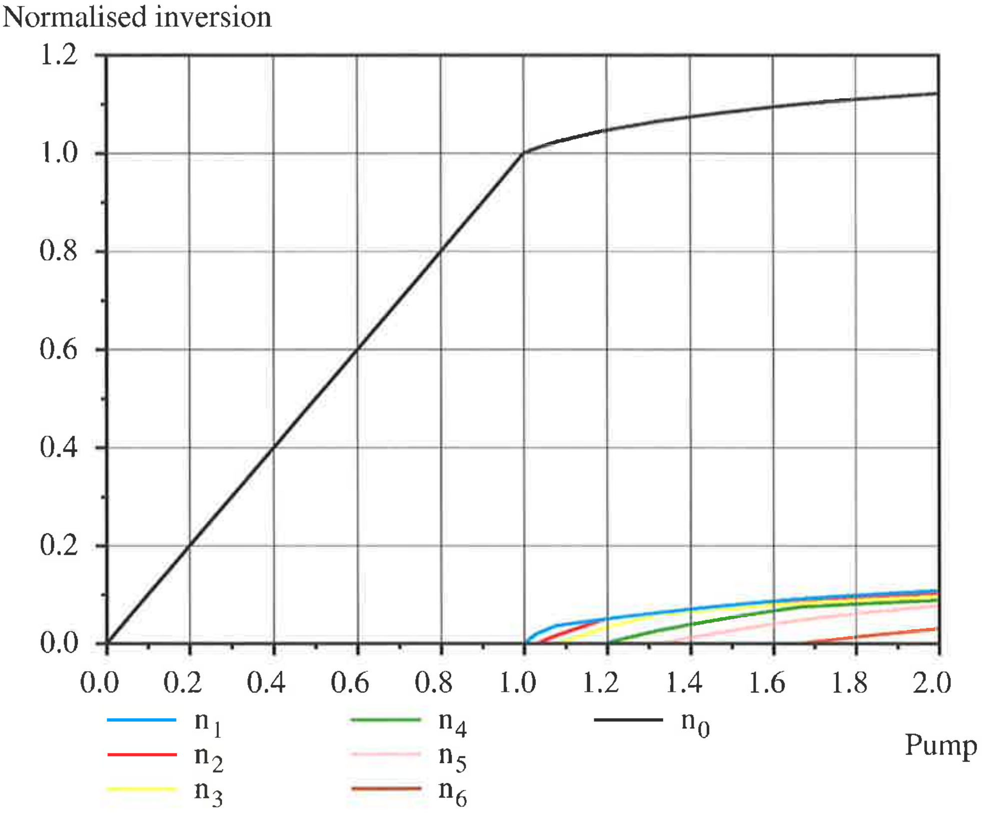

Figure 3-8 Population inversion average (n_0) and components ($n_1 – n_6$) for end pumping (q =1)

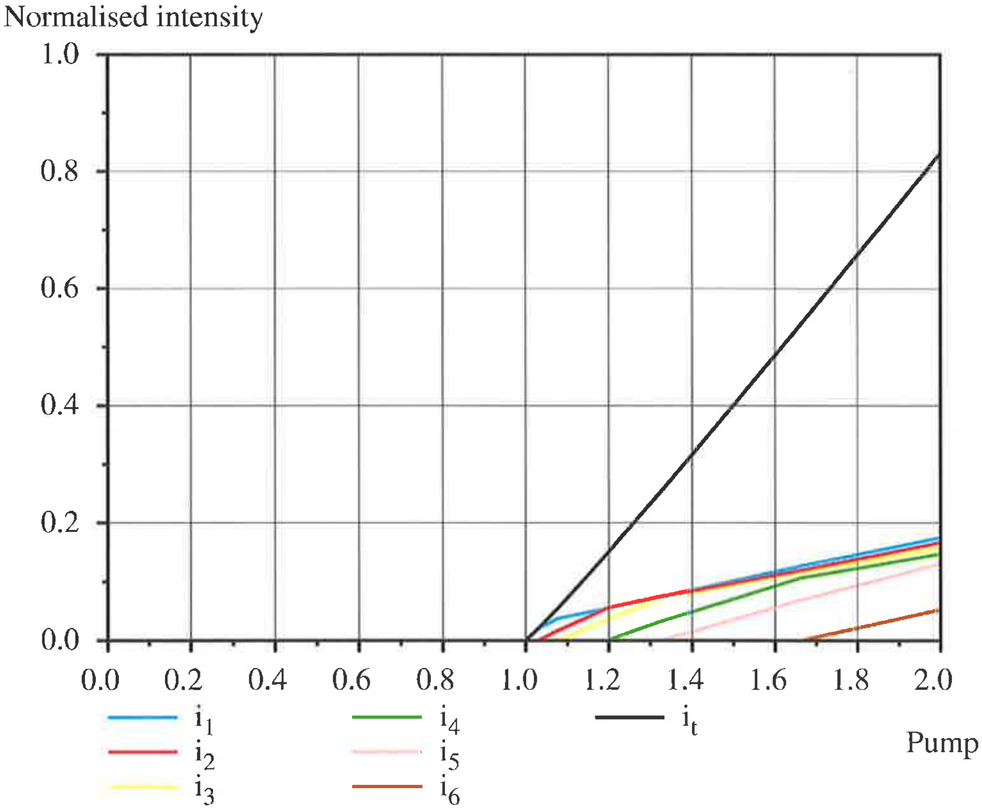

Figure 3-9 Total intensity (i_t) and modal intensities ($i_1 – i_6$) for end pumping (q =1)

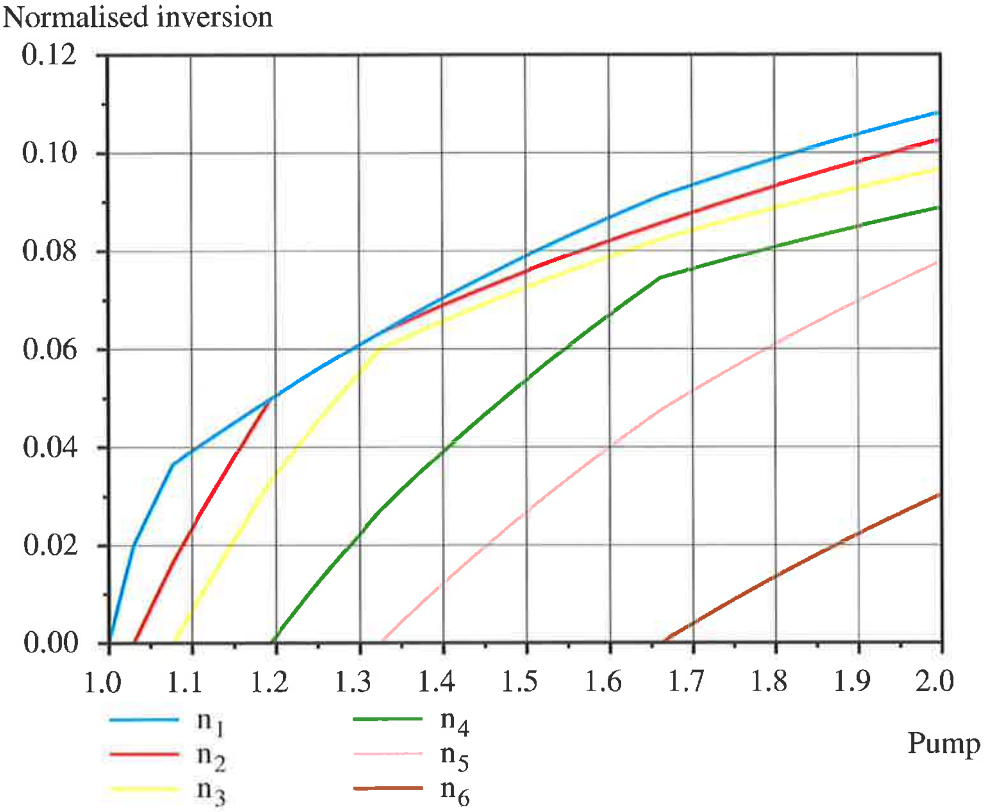

Figure 3-10 Detailed view of the population inversion components for end pumping (q =1)

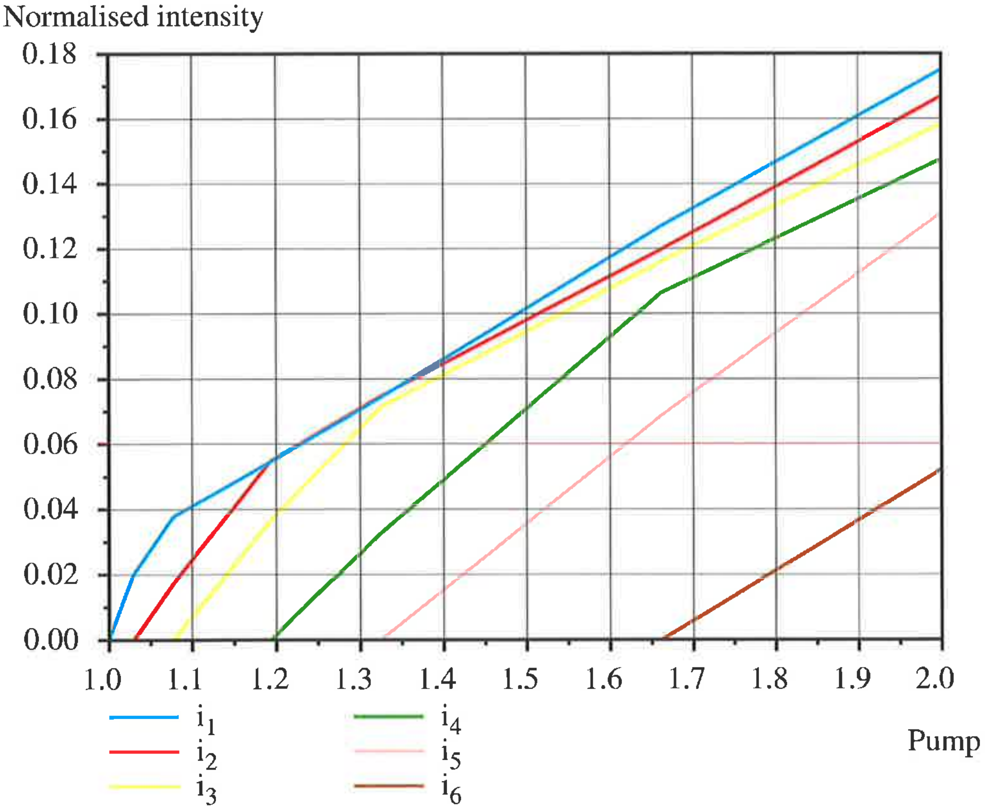

Figure 3-11 Detailed view of the modal intensities for end pumping (q =1)

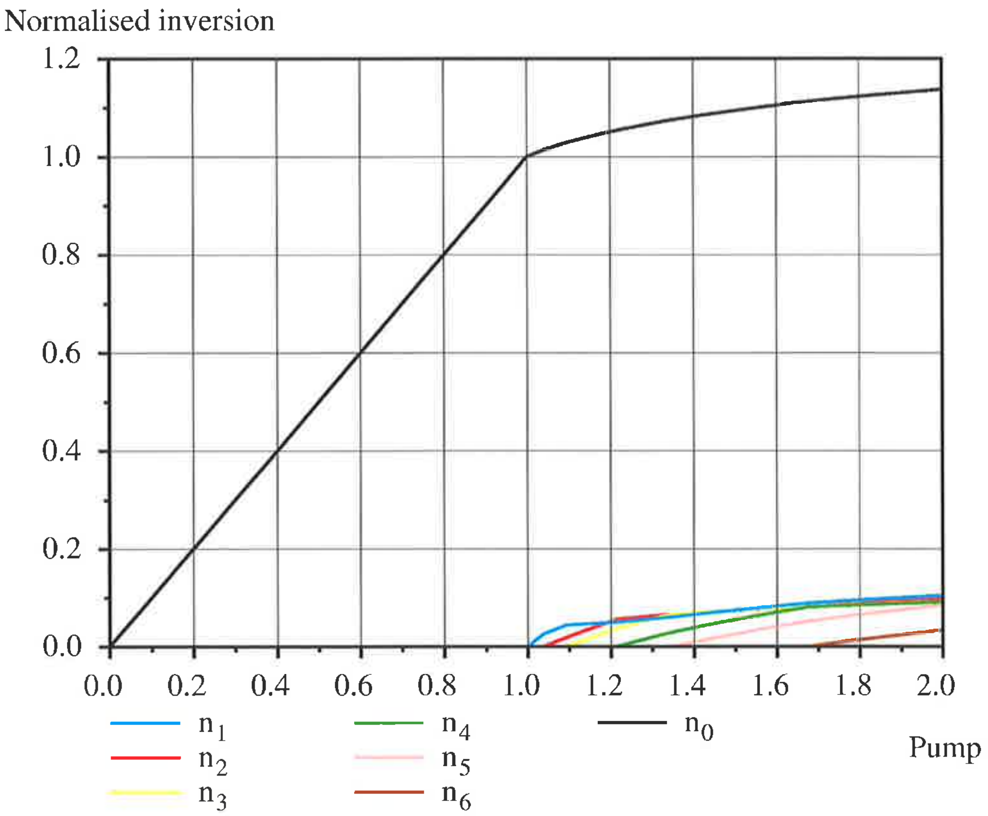

Figure 3-12 Population inversion average (n_0) and components ($n_1 - n_6$) for end pumping (q =0.85)

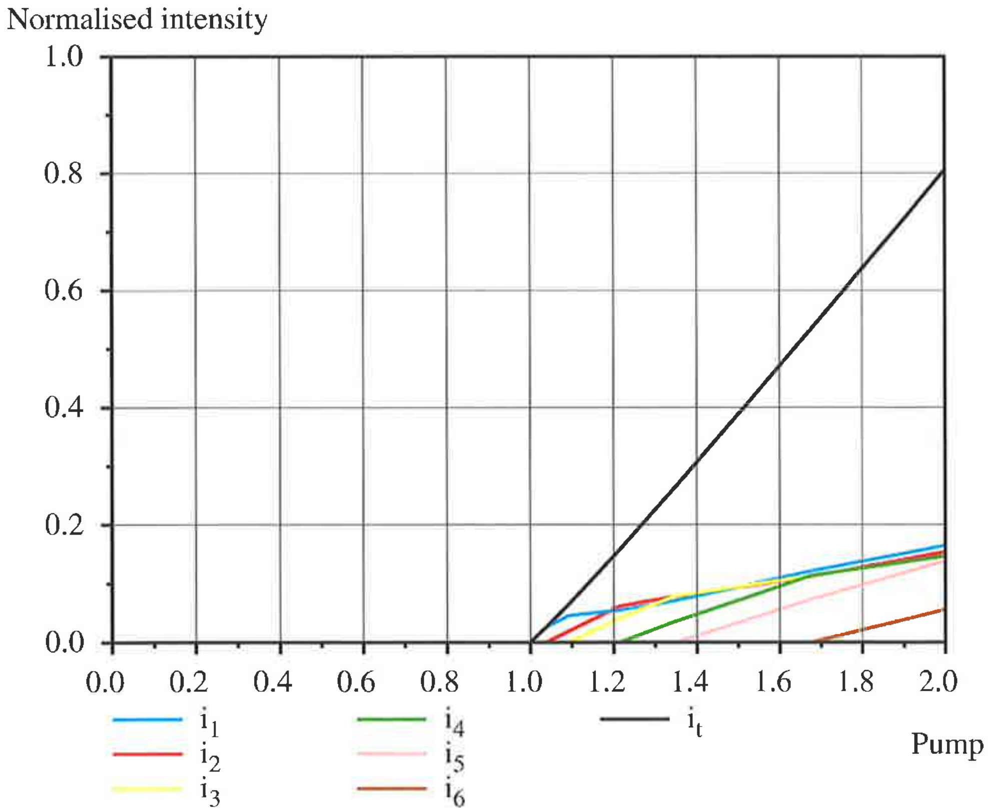

Figure 3-13 Total intensity (i_t) and modal intensities ($i_1 - i_6$) for end pumping (q =0.85)

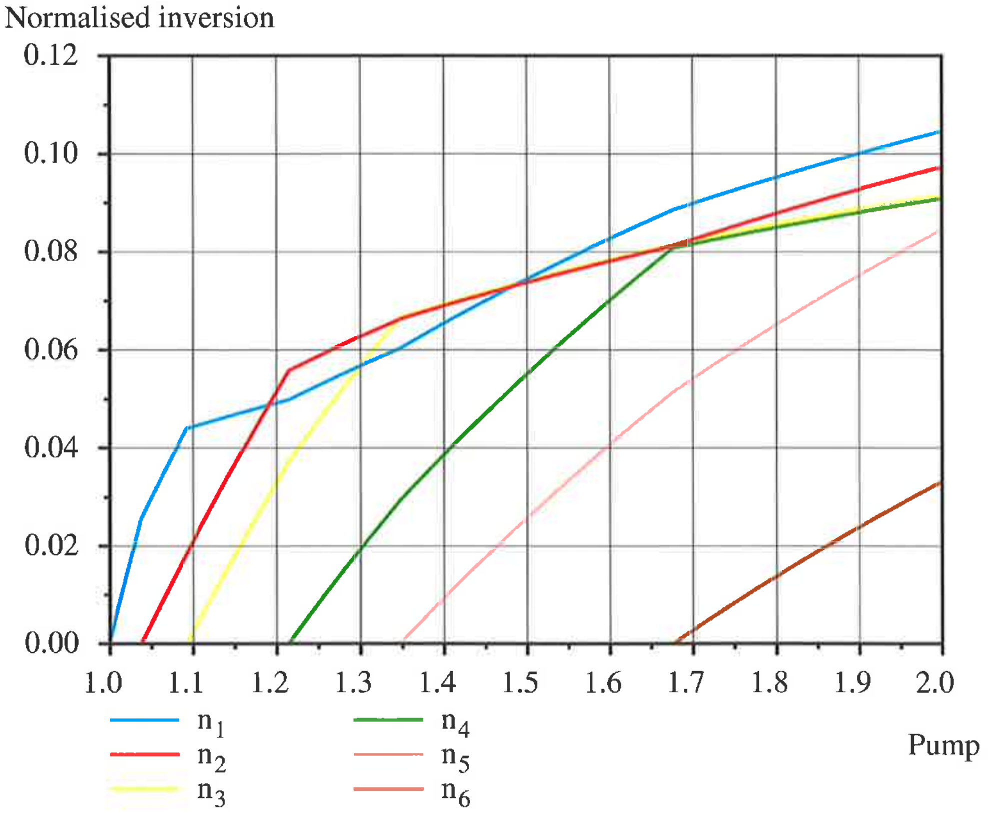

Figure 3-14 Detailed view of the population inversion components for end pumping (q =0.85)

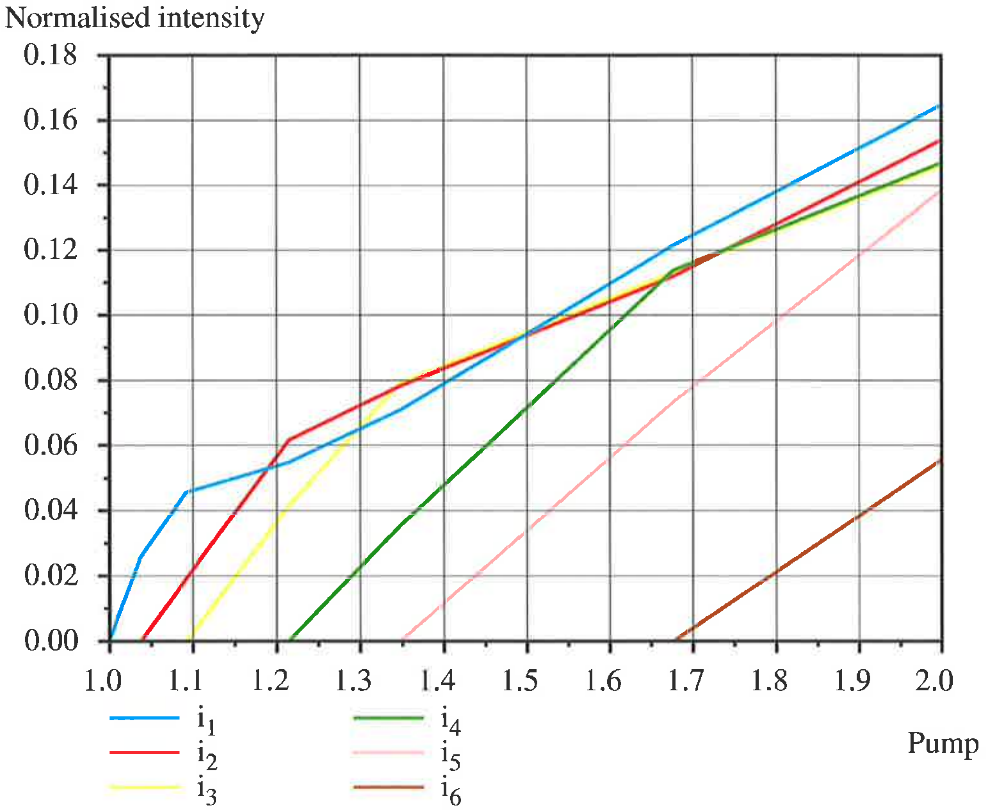

Figure 3-15 Detailed view of the modal intensities for end pumping (q =0.85)

3.5 Experimental Work

The Tang Statz deMars model and the predictions that follow from it are supported by an impressive number of experiments. We saw in the previous section that modifying the model to take into account the effects of the axial non-uniformity caused by end pumping produces qualitatively different threshold behaviour. The question is: will an experiment performed on a real end pumped laser confirm this behaviour? This is the purpose of the experimental investigation described in the following.

3.5.1 Experimental Set-ups

Two experimental set-ups have been used to investigate the dependence of the individual longitudinal mode intensities on the pump level. The first set-up was quite simple, the pump level being modified by manually changing the current of the laser diode. The main drawback of this arrangement was the fact that it took a significant amount of time to acquire a set of data (e.g. about 40 minutes for the set discussed below). This meant that the modes of the laser could drift with respect to the gain curve of Nd:YAG and change one of the critical parameters of the experiment (the offset). Given that the thermal isolation of the laser cavity from the ambient could not be easily achieved, the temperature control of the cavity was ruled out. Instead, we tried to speed-up the measurements and opted for a completely automated system that replaced the manual steps involved in changing the laser diode current and recording of the spectra. This second set-up necessitated an acousto-optic modulator to adjust the pump power and a LabView program running on the computer to control the experiment.

The manual set-up is illustrated in the Figure 3-16. The pump power sent into the Nd:YAG laser was controlled through direct adjustment of the current supplied to the diode laser and monitored with the built-in photodiode. The output of the Nd:YAG laser was analysed with the spherical Fabry-Perot filter used in scanning mode (as a spectrum analyser). There was some deliberate misalignment between the Fabry-Perot and the laser in order to reduce the selective feedback from the former into the later. The triangular high voltage ramp applied to the piezoelectric actuators of the optical spectrum analyser had a frequency of 5.5 Hz and an amplitude of 400 V_{pp}; this way it was possible to cover about 20 GHz (two free spectral ranges) and thus detect each longitudinal mode twice.

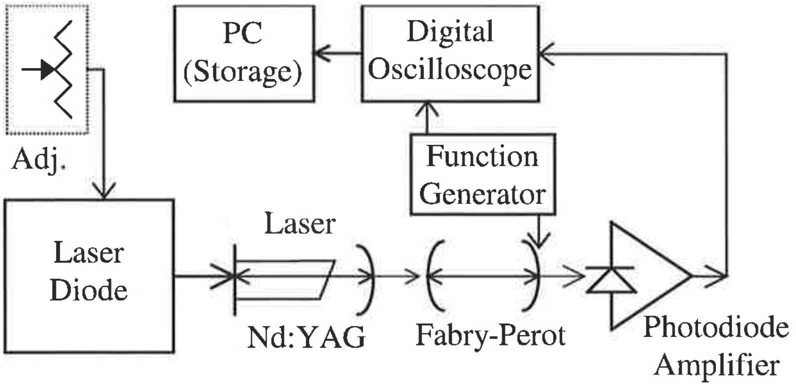

Figure 3-16 Experimental set-up with manual control of the pump power

The output of the optical spectrum analyser was detected with a Si photodiode followed by a DC coupled amplifier. The resulting spectra were averaged and recorded on a digital oscilloscope synchronised with the ramp applied to the optical spectrum analyser.

The automated set-up is quite similar to the manual one, as far as the measurement functionality is concerned. The difference is in the way the input power is varied and the acquired data is stored. As shown in Figure 3-17, the PC running the LabView program controls the RF generator (Rhode-Schwartz SMT03) via a GPIB interface. The higher the output of the RF generator, the less is the amount of light not diffracted by the AOM and thus reaching the laser. The digital oscilloscope is also controlled via the GPIB interface, making it possible to transfer the spectra into the LabView program for storage.

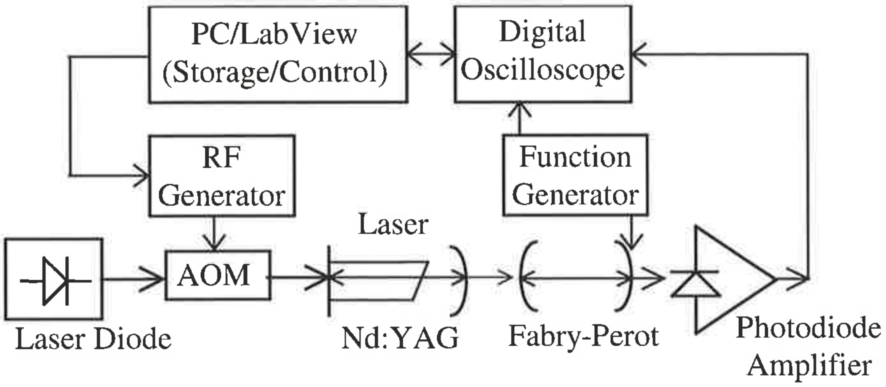

Figure 3-17 Experimental set-up with automated control of the pump power

It turned out that while there was an improvement in the number of stored spectra per minute, the difference in the acquisition time is not very substantial.

3.5.2 Data Processing

Although the 10 GHz free spectral range of the Fabry-Perot was comparable with the mode spacing of the laser (6.15GHz), it was possible to identify each longitudinal mode without any problems. A typical example of an optical spectrum (drawn in blue), including the identification of the modes and the ramp signal applied to the Fabry-Perot (drawn in red), is presented in Figure 3-18.

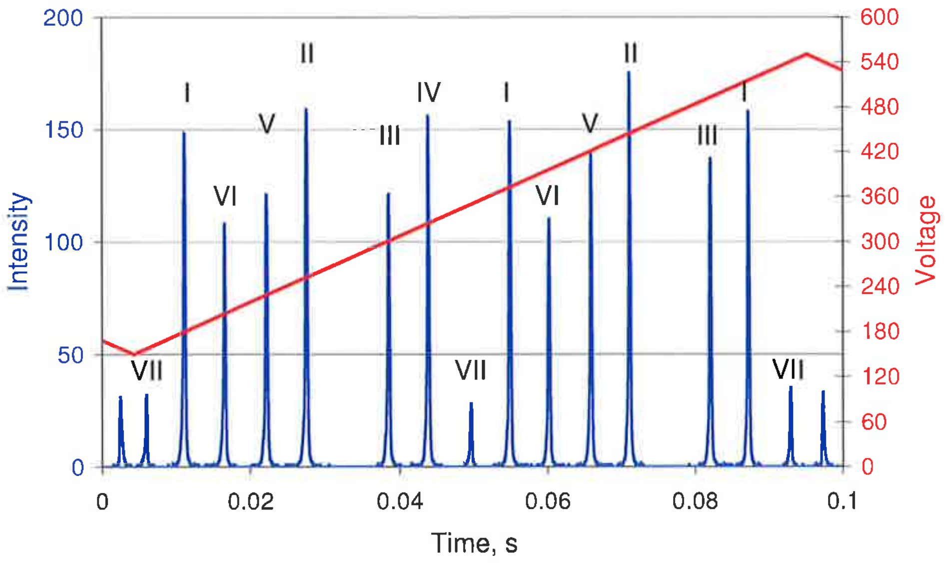

Figure 3-18 The optical spectrum of the Nd:YAG laser, acquired for large input pump power

The processing of the recorded spectra was done in Scilab and involved subtraction of the background, integration of the area under the peaks in the spectrum and compensation for the drift. The background is due to the dark current of the photodiode and to the offset of the electronics. The area under the peaks was considered a more reliable indicator of the intensity of the modes than the maximum value, especially in the conditions of a digitised spectrum. It also helped to remove the effect of the Fabry-Perot alignment changing during the scan.

The drift due to the small changes of the ambient temperature meant that the positions of the peaks changed slightly from one spectrum to the other. This change was relatively easy to track and make sure that the areas of the peaks were attributed to the right modes. However, the drift represented the most serious problem of the experiment, because it changed the gains of the modes during the measurements. The drift and the fluctuations of the modal intensities were the main factors that prevented a quantitative comparison between our theoretical model and the experiment.

3.5.3 Experimental Results

We show the results of two sets of measurements in Figure 3-19, Figure 3-20 and Figure 3-21, Figure 3-22, respectively. They plot the intensities of the longitudinal modes (in arbitrary units) as function of the intensity of the laser diode current. Each set of measurements was done with a different cavity length, corresponding to a different value of the laser cavity detuning with respect to the peak of the gain.

The first set of measurements, obtained with the manual set-up, is shown in Figure 3-19 and Figure 3-20. We can clearly see the anomalous threshold behaviour of the longitudinal modes as the pump input power is increased: modes two, three and four take over the first mode one after the other. The modes are labelled in the same order in which they appear with increasing pump power. Figure 3-19 shows the total laser output intensity, obtained by summing the intensities of the individual modes. The oscillations in the modal intensities are probably due to instabilities excited by optical feedback into the laser from the scanning Fabry-Perot. Comparing these with the total intensity, it is evident that there is a degree of antiphase behaviour in the dynamics [8].

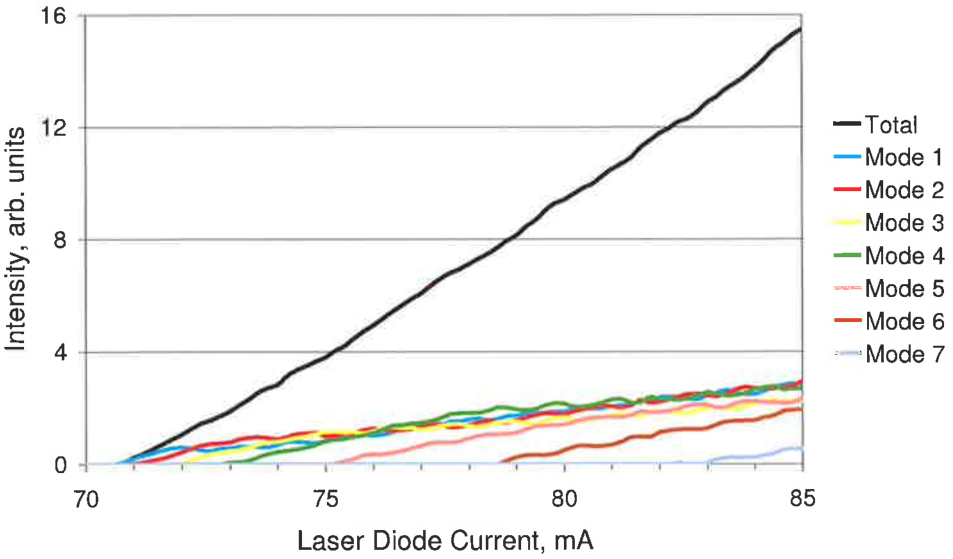

Figure 3-19 Threshold behaviour of the Nd:YAG laser, measured with the manual set-up

However, the "knee" in the intensity of the first mode (close to 72mA input current) is most likely related to the eclipsing of one mode by another. The appearance of these "knees" suggests that the effect is due to mode competition as the new modes begin to oscillate, and this is evident in the numerical modelling described above.

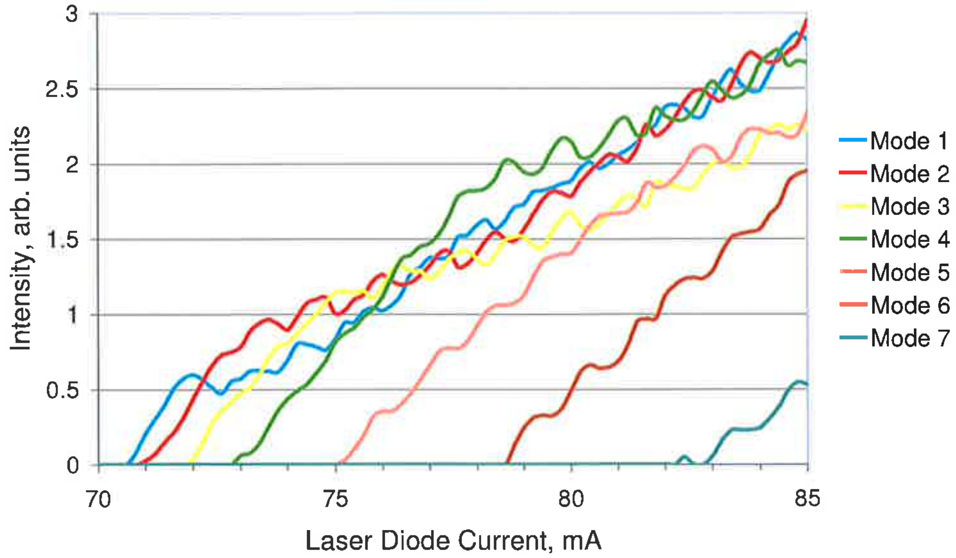

Figure 3-20 Detailed view of the modal intensities, measured with the manual set-up

The second set of measurements, acquired with the automated set-up, is presented in Figure 3-21 and Figure 3-22. The laser cavity is in about the same state as in the previous case, except that the mode comb has a different position with respect to the spectral peak of the gain. Here the behaviour is more like that expected from the Tang Statz deMars equations. However, this does not preclude the end pumped model, as it allows, for the same value of *q*, to have either normal or anomalous ordering, depending on the value of the offset. Again oscillations are seen in the intensities of the individual modes, but not in the total intensity.

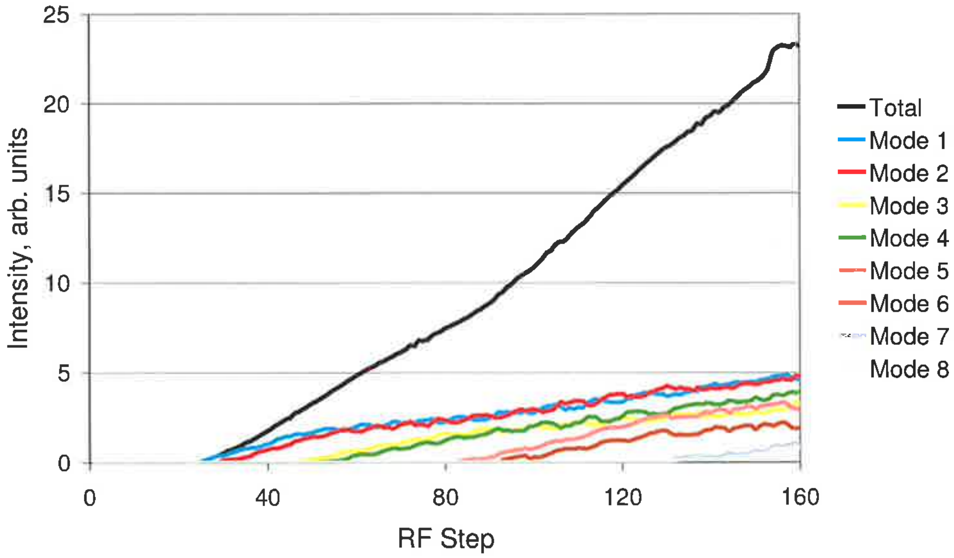

Figure 3-21 Threshold behaviour of the Nd:YAG laser, measured with the automated set-up

It was unfortunate, but none of the measurements done with the automated set-up showed the anomalous behaviour as well as the one done manually and presented above. We observed crossover of modal intensities in some measurements, but for various reasons (usually sudden temperature drift) they were not acceptable for presentation.

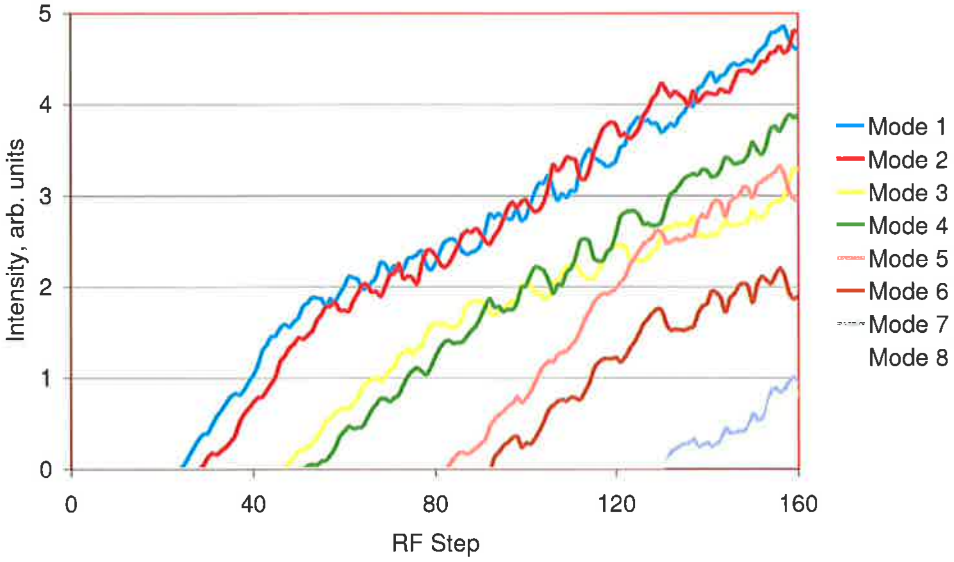

Figure 3-22 Detailed view of the modal intensities, measured with the automated set-up

Calculation as those shown in Figure 3-4 to Figure 3-7 and a multitude of published results indicate that the Tang Statz deMars equations cannot account for the behaviour presented in Figure 3-19 and Figure 3-20. They predict that at all pump levels the laser modes follow the same order in intensities as their gains and their threshold pump powers. Including in the model the exponential decay of the pump in the active medium reconciles the theory and the experiment.

3.6 Conclusion

In this chapter we introduced models for the multimode Nd:YAG laser with Fabry-Perot cavity, in the rate equations framework. We considered the original Tang Statz deMars equations and then modified them to take into account the effects of the axial non-uniformity caused by end pumping. The modified model predicts that the ordering of the longitudinal mode intensities does not strictly follow the modal gains and changes with the pump level. The departure from the calculations based on the Tang Statz deMars equations increases with the absorption coefficient of the pump radiation in the active medium. The experimental data recorded from our laser confirmed the predictions of the end pumped model. This gave us encouragement to further test and compare the new model with that of Tang, Statz and deMars. In the next chapter these two models will form the foundation of the calculations for the laser modulated in the small-signal regime.

Chapter 4 Linear Model

4.1 Introduction

In this chapter we investigate the manifestation of antiphase dynamics in the Nd:YAG laser subject to external low-level sinusoidal modulation. This investigation, which will be continued in the in Chapter 5 with noise replacing external modulation, draws on the modelling of the laser presented in Chapter 3 and the description of the experimental set-up presented in Chapter 2.

Antiphase dynamics is not restricted to lasers with Fabry-Perot cavities; it was observed in a number of systems as mentioned in Chapter 1. An important difference between various systems exhibiting antiphase dynamics is the type of antiphase. In some cases (certain regimes of operation for Josephson junction arrays [4], intra-cavity second harmonic generation [6]) the oscillators have comparable amplitudes and the phases are staggered, with increments of $2\pi/N$ (where N is the number of oscillators). In other cases (globally coupled map lattices [2], large networks of electrically coupled cells [3]) the phases of the oscillators are clustered and the clusters oscillate out of phase. It is known that the multimode lasers with Fabry-Perot cavity belong to the latter type, but the substantiation was rather indirect (inspection of modal waveforms obtained experimentally or through numeric integration of rate equations, universal relations between the peak heights of the modal and total intensity power spectra [47], etc). Since antiphase dynamics is primarily a phase locking phenomenon, we would like to find a way to explicit the phase relationship between the coupled oscillators.

The multimode Nd:YAG laser with Fabry-Perot resonator is a system well suited to the study of antiphase dynamics. When several longitudinal modes of the cavity are operating, their intensities are coupled through the distributed gain produced by the population inversion in the active medium. This particular type of coupling, which is responsible for antiphase dynamics, is caused by the standing wave nature of the electromagnetic field in the resonator [7]. This argument is supported by the fact that lasers with ring resonators, characterised by travelling wave fields, do not exhibit this phenomenon. Although we mention the electromagnetic fields here, it was shown in the previous chapter that the coupling involves only the intensities of the longitudinal modes and not the electric fields themselves. The analysis of the coupled system thus formed indicates that its eigen-frequencies are in the tens of kilohertz region and this makes the experimental analysis feasible. Due to the coupling, the phases of the modal intensities are clustered in such a way that their superposition in the total intensity nearly destroys the response at all but one of the system eigen-frequencies.

There is a significant amount of work, both experimental and theoretical, devoted to the investigation of antiphase dynamics in this system. Some of the references consulted can be loosely classified after the methods used for analysing the problem and / or exciting the system:

- Stability analysis: [40], [47], [48], [49], [50].
- Transient behaviour: [48], [49], [51], [52], [53].
- Pump modulation, low level: [8], [49], [54] and high level: [49], [54].
- Loss modulation: [55], [56], [57].
- Feedback modulation, selective: [58], [59], [60] or not: [60].

- Noise: [48], [51], [52], [53].

In order to investigate the mechanism responsible for antiphase dynamics, we resort to the well-known method of transfer functions. A strong reason for our choice is that this method provides both magnitude and phase information, the phase relating directly to antiphase. Another argument for the transfer function method is that it is applicable to both theoretical and experimental situations and provides a unified language for these two approaches. Among several possibilities, we choose to modulate the pump power applied to the Nd:YAG laser with sinusoidal signals and to analyse the response of the total and modal intensities. The theoretical treatment uses a linearised model to obtain numerically the transfer functions of individual modes and total intensity. The location of the zeros of the transfer functions with respect to the poles provides a simple graphical explanation for the limited response of the total intensity at the lower resonant frequencies. At the same time, the partial fraction decomposition is used for a semi-quantitative analysis of the dynamics of the individual modes, presenting a compelling argument for the clustering type of antiphase dynamics. The experimental results have been processed in pole-zero and pole-residue form, to allow direct comparisons with the theoretical analysis.

This procedure has been succinctly described in [8] using the Tang Statz deMars model for the theoretical analysis. The comparison with the experimental results has pointed out the shortcomings of this model when applied to an end pumped laser. This has prompted the development of the Tang Statz deMars equations with exponential decay.

In the next section we introduce the mathematical formalism required to calculate the transfer functions for a system modulated in the small-signal regime around the steady state. The following two sections apply these ideas to the uniformly pumped laser (Tang Statz deMars equations) and, respectively, to the end pumped laser (Tang Statz deMars equations with exponential decay). The experimental set-up and the processing of the results are described afterwards, followed by a comparative discussion and concluding remarks.

4.2 Longitudinal Modes versus Collective Modes

We note that throughout this chapter the word mode will be used quite frequently with two related but different meanings. One meaning refers to the modes of the laser, i.e. to the eigen-functions of the optical cavity as described in Chapter 3. Since the laser considered here oscillates only on the lowest transverse mode (TEM_{00}), the only distinction between these eigen-functions is given by the longitudinal component, hence the use of the term longitudinal modes. In the same idea, the intensities of these longitudinal modes of the laser are named modal intensities.

The other meaning of the word mode refers to the collective oscillations of the modal intensities. Since the longitudinal modes of the laser are coupled, they behave like an array of coupled oscillators. The resonant frequencies of the coupled system are called collective modes of oscillation and their study is the main objective of this chapter. In some references the collective modes are described as the normal modes of oscillation of the system.

4.3 Transfer Function Theory

The transfer functions represent one of the basic tools in the control system theory. Their application to the models described in the previous chapter follows the ideas presented in [61] and [62]. The reader familiar with the linear system theory can skip this section.

4.3.1 State-Space Formalism

We assume that the system under consideration can be represented by a set of simultaneous differential equations of first order and, indeed, this is the case for a laser described by the rate equations. If the pump power modulation is explicitly taken into account ($w = mw_0 \sin \omega t$, m being the modulation index), the system of simultaneous differential equations can be written in condensed form as:

$$\frac{d\mathbf{x}}{dt} = \mathbf{F}(\mathbf{x}) + \mathbf{b}w. \tag{4-1}$$

Here **x** and **b** are column vectors representing the state variables of the system and, respectively, the way the input signal is distributed into the system, while **F** represents the dynamics of the system. As shown in the previous chapter, the dimension of the system is *2N+1*, where *N* is the number of longitudinal modes of the laser.

Without modulation ($w = 0$), one can find the steady state solution $\mathbf{x}^0$ of the equation (4-1) by setting the left hand side of the equation to zero:

$$\mathbf{F}(\mathbf{x}^0) = \mathbf{0}. \tag{4-2}$$

Once the equilibrium point has been found, the non-linear system of equations can be linearised around this point by calculating the stability or the Jacobian matrix of the system:

$$\mathbf{A} = \left(\frac{\partial\, \mathbf{F}(\mathbf{x})}{\partial\, \mathbf{x}}\right)\Bigg|_{\mathbf{x}=\mathbf{x}^0}. \tag{4-3}$$

With the system initially in its steady state, a small perturbation will evolve according to the equation:

$$\frac{d\tilde{\mathbf{x}}}{dt} = \mathbf{A}\tilde{\mathbf{x}}, \tag{4-4}$$

where $\tilde{\mathbf{x}} = \mathbf{x} - \mathbf{x}^0, |\tilde{\mathbf{x}}| << |\mathbf{x}^0|$.

The behaviour of the system is determined by the eigen-values of the matrix **A,** which can be found by solving the characteristic equation:

$$\det(\lambda\mathbf{I} - \mathbf{A}) = 0. \tag{4-5}$$

This polynomial equation has *2N+1* solutions and, because the matrix **A** is real but not symmetric, the eigen-values λ_k are either real or come in complex conjugate pairs. Assuming distinct eigen-values, the temporal response of the system is a combination of exponential functions of the form:

$$\tilde{\mathbf{x}}(t) = \sum_{k=1}^{2N+1} \mathrm{e}^{\lambda_k t}\, \mathbf{K}_k \tilde{\mathbf{x}}(0), \tag{4-6}$$

where $\mathbf{K}_k$ are matrices giving the distribution of the initial conditions $\tilde{\mathbf{x}}(0)$ to each mode $e^{\lambda_k t}$ and to each component of $\tilde{\mathbf{x}}$ [62]. If all eigen-values have negative real parts (stable system), the perturbation $\tilde{\mathbf{x}}$ will decay to zero and the laser will reach the steady state solution $\mathbf{x}^0$. This means that, since we are interested in the long-term response of the laser to sinusoidal modulation, the initial conditions are unimportant and can be set to zero.

If we continuously excite the system by modulating the pump power ($w \neq 0$), we have to add to the linearised system (4-4) the extra term from (4-1), which can be considered as the input of the system:

$$\frac{d\tilde{\mathbf{x}}}{dt} = \mathbf{A}\tilde{\mathbf{x}} + \mathbf{b}w \,. \tag{4-7}$$

The (scalar) output of the system can be any linear combination of the state variables:

$$y = \mathbf{c}^T \tilde{\mathbf{x}} \,. \tag{4-8}$$

The transposed vector $\mathbf{c}^T$ selects which state variables contribute to the output y. It is possible to have several outputs from the system, each of them having a different vector $\mathbf{c}^T$. Such a system, named SIMO (single input, multiple output), will be used to analyse the multimode laser. However, a SIMO system is just a collection of SISO (single input, single output) systems. A block diagram of a linearised SISO system described by the equations (4-7) and (4-8) is presented in Figure 4-1:

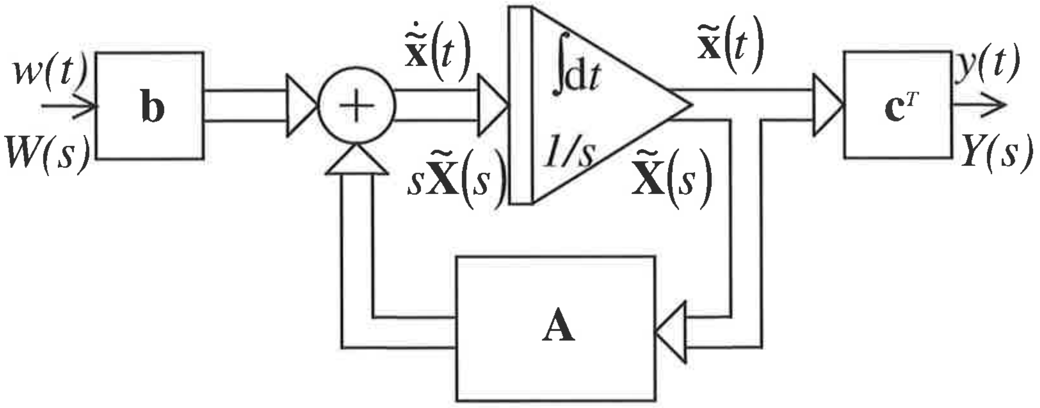

Figure 4-1 Schematic representation of a SISO linear system

In the diagram, the input $\dot{\tilde{\mathbf{x}}}$ of the integrator is the sum of the system input w multiplied by the vector $\mathbf{b}$ and the feedback term $\mathbf{A}\tilde{\mathbf{x}}$. The integrator output $\tilde{\mathbf{x}}$, multiplied by $\mathbf{c}^T$, generates the output of the system y.

To change from differential to algebraic equations, one has to apply the Laplace transform to equations (4-7) and (4-8):

$$\begin{aligned} s\tilde{\mathbf{X}}(s) - \tilde{\mathbf{x}}(0) &= \mathbf{A}\tilde{\mathbf{X}}(s) + \mathbf{b}W(s) \\ Y(s) &= \mathbf{c}^T \tilde{\mathbf{X}}(s) \,. \end{aligned} \tag{4-9}$$

Here we follow the convention of using capital letters for the Laplace transforms of the corresponding time functions (i.e. $\tilde{\mathbf{X}}(s)$ corresponds to $\tilde{\mathbf{x}}(t)$ and so on) and $s = \sigma + j\omega$ is the complex frequency. Referring back to the block diagram in Figure 4-1, we can see that the action of the integrator corresponds to division by s, while the derivation corresponds to multiplication by s.

Assuming zero initial conditions ($\tilde{\mathbf{x}}(0)=0$), we can solve the equation for $\tilde{\mathbf{X}}(s)$ first:

$$(s\mathbf{I}-\mathbf{A})\tilde{\mathbf{X}}(s)=\mathbf{b}W(s)$$

or

$$\tilde{\mathbf{X}}(s)=(s\mathbf{I}-\mathbf{A})^{-1}\mathbf{b}W(s)$$

and then calculate the output of the system as function of the input excitation $W(s)$:

$$Y(s)=\mathbf{c}^T(s\mathbf{I}-\mathbf{A})^{-1}\mathbf{b}W(s). \tag{4-10}$$

4.3.2 Pole-Zero Representation of the Transfer Functions

A transfer function can be defined as the ratio of the output Y to the input W and is a function of the complex frequency s. From (4-10) we get:

$$H(s)=\frac{Y(s)}{W(s)}=\mathbf{c}^T(s\mathbf{I}-\mathbf{A})^{-1}\mathbf{b}. \tag{4-11}$$

Normally, the transfer functions are expressed as a ratio of polynomials of the form:

$$H(s)=\frac{Y(s)}{W(s)}=\frac{\prod_{i=1}^{m}(s-z_i)}{\prod_{j=1}^{n}(s-\lambda_j)}, \tag{4-12}$$

where z_i are the zeros and λ_j are the poles of the transfer function. We can get closer to this representation by formally expressing the matrix inversion involved in (4-11) as:

$$H(s)=\frac{\mathbf{c}^T\,\mathrm{adj}(s\mathbf{I}-\mathbf{A})\mathbf{b}}{\det(s\mathbf{I}-\mathbf{A})},$$

where $\mathrm{adj}(s\mathbf{I}-\mathbf{A})$ stands for the adjoint of the matrix $(s\mathbf{I}-\mathbf{A})$. The denominator of the transfer function is the left hand side of the characteristic equation (4-5). The roots of this equation are the poles or the resonant frequencies of the system. It is important to note that the denominator will be the same, regardless of the combination selected for output (through the vector c^T). This means that all outputs from the system resonate at the same frequencies. The only exception to the rule happens when one or more zeros (roots of the numerator) coincide with one or more poles. In this case, pole-zero cancellations occur and the corresponding resonant frequencies of the system are not visible anymore in that particular output.

The pole-zero form of the transfer function allows us to gain some understanding of the shape of the frequency response (in particular the magnitude plot). As an exercise, let us assume a transfer function given by the poles and the zeros from Table 4-1 and represented in the complex plane in the Figure 4-2.

Table 4-1 Poles and zeros for the example system

Poles		Zeros	
Real	Imag	Real	Imag
-15.50	0.00	-13.50	0.00
-5.50	17.50	-4.50	20.50
-5.50	-17.50	-4.50	-20.50

This transfer function has a real pole, a real zero, a pair of complex poles and a pair of complex zeros. If we consider the magnitude of the transfer function in logarithmic coordinates, then the poles are the places where the function tends to $+\infty$ (peaks), while the zeros are the places where the function tends to $-\infty$ (wells).

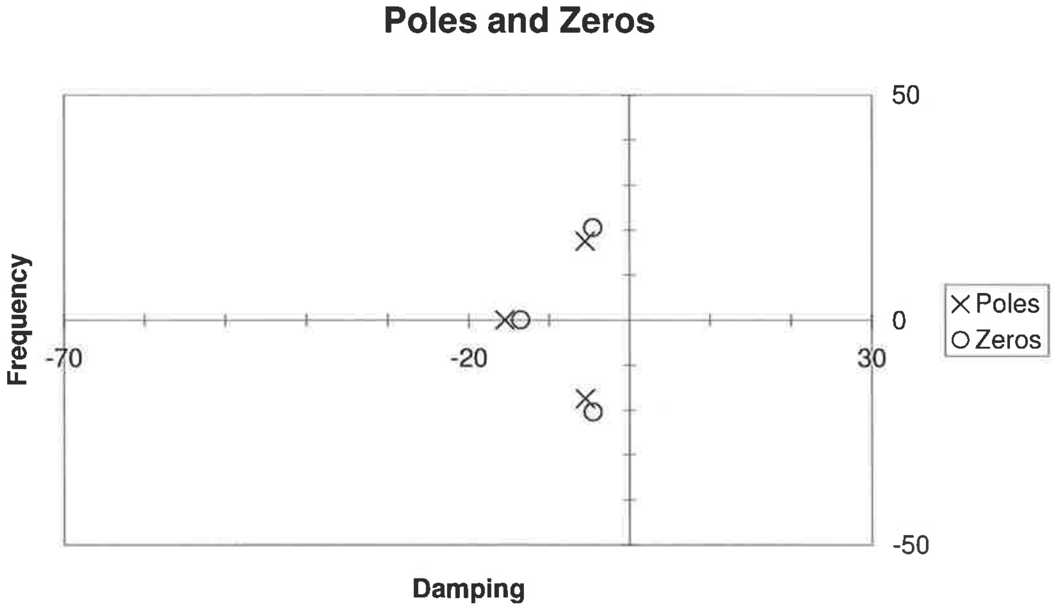

Figure 4-2 Pole-zero diagram for an example system

The Figure 4-3 presents a three dimensional image of the magnitude in dB. The frequency representation is obtained by restricting the complex frequency s to imaginary values: $s = j\omega$. Thus, the magnitude plot of the transfer function's frequency representation is the intersection between the surface representing the magnitude of the transfer function in the whole complex plane and a vertical plane containing the imaginary axis ($\sigma = 0$). This interpretation provides an intuitive way of understanding the effects of the poles and the zeros and how changes in their location alter the magnitude plot.

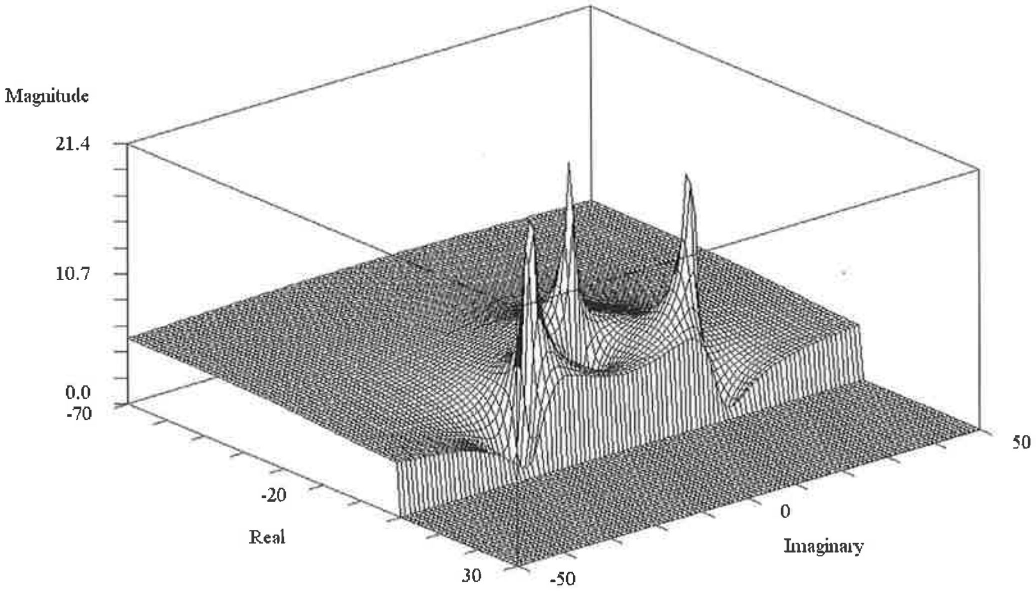

Figure 4-3 Three dimensional view of the magnitude of the example system

4.3.3 Pole-Residue Representation of the Transfer Functions

We can get a different perspective on the behaviour of the system if we express the transfer functions as partial fractions:

$$H(s) = \frac{r_1}{(s-\lambda_1)} + \frac{r_2}{(s-\lambda_2)} + \ldots + \frac{r_{2N+1}}{(s-\lambda_{2N+1})}. \tag{4-13}$$

Each fraction corresponds to one of the natural modes of the system and the numerator r_j (the residue) gives the weight of the respective natural mode in the overall response of the output. In order to get explicit formulae for the residues, we have to determine the eigen-vectors of the matrix **A**:

$$\mathbf{A}\mathbf{v}_k = \lambda_k \mathbf{v}_k \qquad k = 1 \ldots 2N+1.$$

We can assemble these column vectors into a square matrix:

$$\mathbf{V} = \left[\mathbf{v}_1 \; \mathbf{v}_2 \cdots \mathbf{v}_{2N+1}\right], \tag{4-14}$$

which has the property that, when applied to the original matrix **A** as a similarity transformation, it converts the system to diagonal form:

$$\Lambda = \mathbf{V}^{-1}\mathbf{A}\mathbf{V}$$

$$\Lambda = \begin{bmatrix} \lambda_1 \, 0 \cdots 0 \\ 0 \, \lambda_2 \cdots 0 \\ \vdots \\ 0 \, 0 \cdots \lambda_{2N+1} \end{bmatrix}.$$

We can apply the above transformation in the opposite direction to get:

$$\mathbf{A} = \mathbf{V}\Lambda\mathbf{V}^{-1}$$

and substitute this expression into the transfer function expression (4-11). We obtain:

$$H(s) = \frac{Y_t(s)}{W(s)} = \mathbf{c}^T\left(s\mathbf{I} - \mathbf{V}\Lambda\mathbf{V}^{-1}\right)^{-1}\mathbf{b} = \mathbf{c}^T\mathbf{V}(s\mathbf{I} - \Lambda)^{-1}\mathbf{V}^{-1}\mathbf{b}. \tag{4-15}$$

This equation can be represented by the following block diagram:

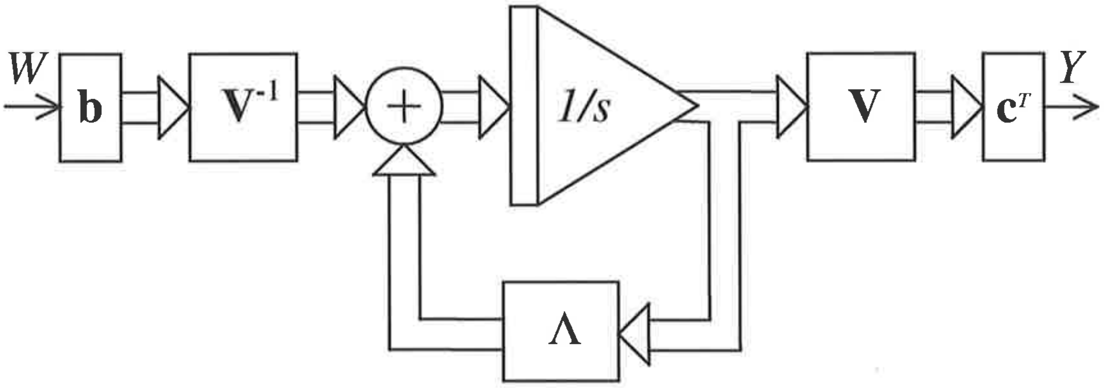

Figure 4-4 Schematic representation of a diagonalised SISO linear system

The factor $(s\mathbf{I} - \Lambda)^{-1}$ can be easily inverted:

$$\Lambda(s) = (s\mathbf{I} - \Lambda)^{-1} = \begin{bmatrix} \frac{1}{s-\lambda_1} 0 \cdots 0 \\ 0 \frac{1}{s-\lambda_2} \cdots 0 \\ \vdots \\ 0\,0 \cdots \frac{1}{s-\lambda_{2N+1}} \end{bmatrix}.$$

If we define the input distribution vector as:

$$\mathbf{e} = \mathbf{V}^{-1}\mathbf{b} = \begin{bmatrix} e_1 \\ e_2 \\ \vdots \\ e_{2N+1} \end{bmatrix}, \tag{4-16}$$

then its elements will give the distribution of input excitation to each of the normal modes of the system. Next, we need a similar vector that gives the contribution of each normal mode to the output of the system:

$$\mathbf{h}^T = \mathbf{c}^T\mathbf{V} = [h_1\ h_2 \ldots h_{2N+1}]. \tag{4-17}$$

If we substitute the matrix **Λ**(s) and the vectors **e**, **h** back into the transfer function (4-15) we get its partial fraction decomposition in the form (4-13):

$$H(s) = \mathbf{h}^T\Lambda(s)\mathbf{e} = \frac{h_1e_1}{(s-\lambda_1)} + \frac{h_2e_2}{(s-\lambda_2)} + \cdots + \frac{h_{2N+1}e_{2N+1}}{(s-\lambda_{2N+1})}. \tag{4-18}$$

This formula tells us that the visibility of a normal mode in the output of the system is a combined effect of the controllability of the mode, given by **e**, and the observability of the mode, given by **h**. If the system has more than one output, the differences between them are given by the differences in the vectors **h**, since the vector **e** is the same for all outputs.

4.4 Transfer Functions for the Uniformly Pumped Laser

4.4.1 Analytic Calculations

The analysis presented above can be applied to the Tang Statz deMars model without difficulty. The model is described in terms of first order differential equations [equations (3-38) to (3-40)] which can be brought to the form of equation (4-1).

First, we separate the pump power into two components: w_0, representing the steady state value, and w, the time varying part (modulation). The modulation is given by the relation:

$$w = mw_0 \sin \omega t \,, \tag{4-19}$$

where m is the modulation index ($m << 1$). With this separation, the model equations become:

$$\begin{aligned}
\frac{dn_0}{dt} &= \frac{1}{\tau_f}\left[w_0 - n_0 - \sum_{k=1}^{N} g_k \left(n_0 - 1/2\, n_k\right) i_k \right] + \frac{1}{\tau_f} w \\
\frac{dn_j}{dt} &= \frac{1}{\tau_f}\left[g_j n_0 i_j - n_j \left(1 + \sum_{k=1}^{N} g_k i_k \right) \right], \quad j = 1 \ldots N \\
\frac{di_j}{dt} &= \frac{1}{\tau_c}\left[g_j \left(n_0 - 1/2\, n_j\right) - 1 \right] i_j, \quad j = 1 \ldots N .
\end{aligned} \tag{4-20}$$

In the above equations N is the number of oscillating modes, n_0 is the average population inversion and n_j are population inversion components oscillating spatially with the same wavelength as the corresponding laser modes of intensity i_j. The gains of the modes are taken into account through the coefficients g_j, while τ_f and τ_c represent population inversion and cavity decay time respectively.

Then we need to establish the equivalence between the vector **x** of equation (4-1) and the variables of equations (4-20) and to write explicitly the modulation distribution vector, **b**:

$$\mathbf{x} = \begin{bmatrix} n_0 \\ n_1 \\ \vdots \\ n_N \\ i_1 \\ \vdots \\ i_N \end{bmatrix}, \quad \mathbf{b} = \begin{bmatrix} 1/\tau_f \\ 0 \\ \vdots \\ 0 \\ 0 \\ \vdots \\ 0 \end{bmatrix}. \tag{4-21}$$

Because only the first element of the state vector **x** is modulated (n_0), **b** has all elements zero but the first, as indicated above.

The right hand side of equations (4-20), less the modulation term $\mathbf{b}w$ of the first equation, represents the non-linear dynamics of the system $\mathbf{F}$. Having identified $\mathbf{F}$, the next step required is to solve (4-2) for a given pump level w_0 and find the steady state solution $\mathbf{x}^0$ of the system. This has been done in the previous chapter and the solution is given by the relations (3-50) to (3-52).

The Jacobian matrix of the system is obtained by calculating the partial derivatives of $\mathbf{F}$, as indicated by (4-3); the results of these calculations are presented in the Appendix A4.1. The elements of the stability matrix are expressed in terms of the steady state solution $\mathbf{x}^0$; if desired, the substitution can be performed to obtain the matrix elements as functions of the pump level alone. However, the Jacobian matrix represents the terminus point as far as our analytic calculations are concerned; from now on the results will be presented only in numerical form. The reason is that the transfer functions require either the calculation of the matrix inverse $(s\mathbf{I}-\mathbf{A})^{-1}$ or the calculation of the eigen-values and eigen-vectors of the matrix $\mathbf{A}$. Some progress has been reported to date in the case of the laser with equal modal gains [40] or in the case of the 3 modes laser with arbitrary gains ([47]). However, in the general case it is very difficult to obtain analytical results.

Finally, we need to express the output of the system as a linear combination of the type (4-8). In our case, the system has multiple outputs (SIMO); they can be any of the individual longitudinal modes (i_1 to i_N) or the total intensity (i_t):

$$\begin{aligned} y_j &= \mathbf{c}_j^T \tilde{\mathbf{x}} \quad j = 1 \ldots N \\ y_t &= \mathbf{c}_t^T \tilde{\mathbf{x}}. \end{aligned} \tag{4-22}$$

While in the experimental situation we select the desired mode with a Fabry-Perot filter, in the numerical calculations the selection is done using the row vectors $\mathbf{c}_j^T$ ($j = 1 \ldots N$) and $\mathbf{c}_t^T$:

$$\begin{aligned} \mathbf{c}_1^T &= [0\,0 \ldots 0\,1 \ldots 0] \\ &\vdots \\ \mathbf{c}_N^T &= [0\,0 \ldots 0\,0 \ldots 1] \\ \mathbf{c}_t^T &= [0\,0 \ldots 0\,1 \ldots 1]. \end{aligned} \tag{4-23}$$

At this point we have all the elements necessary for determining the transfer functions of the laser: the input distribution vector $\mathbf{b}$, the Jacobian matrix $\mathbf{A}$ and the output selection vectors $\mathbf{c}^T$.

4.4.2 Numeric Calculations

In order to proceed with the numeric investigation of the transfer functions for the Tang Statz deMars equations, we need to set the values of the parameters appearing in the model. Thus, we use $\tau_f = 230\,\mu s$ for the fluorescence time of the Nd:YAG (the value from Table 2-5) and $\tau_c = 3.56\,ns$ for the value of the cavity decay time (measured for the laser alignment existent during transfer function measurements). For the relative gains g_j of the longitudinal modes we use the Lorentzian line given by (3-53) and (3-54), with the same values as in the section 3.3.4 ($\Delta\nu = 135\,\text{GHz}$ and $\delta\nu = 6.15\,\text{GHz}$). The offset of the first mode with respect to the centre of the Lorentzian ($offset = 0.04$) and the pump level ($w_0 = 1.308$) have been adjusted to give best agreement with the experimental results.

With these choices we calculated the steady state values for the population inversion components and the modal intensities. The results (including the relative gains) are listed in Table 4-2; the last row of the table gives the average population inversion and total intensity, respectively:

Table 4-2 Steady state solution for uniform pumping

Mode	n_j^0	p_j^0	g_j
1	0.077027	0.094003	0.999987
2	0.061752	0.075938	0.992408
3	0.059096	0.072767	0.991101
4	0.013273	0.016715	0.969096
5	0.007960	0.010050	0.966607
0/t	1.038527	0.269473	

Having determined the equilibrium point of the system, we can now calculate the elements of the Jacobian matrix **A**. The eigen-values of the matrix **A** are tabulated below in a form more suitable for interpretation ($\lambda = -1/d + j2\pi f$):

Table 4-3 Eigen-values of the system matrix **A** for uniform pumping

Eigen-value	-1/Real part, μs	Imaginary part/2π, kHz
λ_1	$d_0 = 188.1$	
$\lambda_{2,3}$	$d_1 = 364.0$	$f_1 = 13.13$
$\lambda_{4,5}$	$d_2 = 366.5$	$f_2 = 18.01$
$\lambda_{6,7}$	$d_3 = 363.0$	$f_3 = 34.24$
$\lambda_{8,9}$	$d_4 = 363.2$	$f_4 = 37.15$
$\lambda_{10,11}$	$d_5 = 346.1$	$f_5 = 96.08$

4.4.3 The Effect of Pump Level on the Eigen-Values of the Stability Matrix

The pump level influences the stability matrix **A** in two ways. Firstly, the number of operating longitudinal modes, and thus the dimensionality of the system, depend directly on the pump level. Secondly, the elements of the Jacobian are calculated using the steady state solution, which also depends on the pump level. Therefore, it is worthwhile to investigate how the eigen-values change with the pump before studying the transfer functions at a given pump level.

The first eigen-value λ_1 has no imaginary part and it can be shown that it is related to the decay of the population inversion. In Figure 4-5 we have represented the dependence of the reciprocal of this eigen-value, $d_0 = -1/\lambda_1$, on the pump parameter w_0. For values of the pump parameter below the threshold of the first mode, we obtain $d_0 = \tau_f$. As we increase the pump level, the stimulated emission adds to the spontaneous emission and d_0 starts decreasing accordingly. As there is no resonance associated with this eigen-value, it has only a small effect on the transfer functions at very low frequencies (≤ 1kHz).

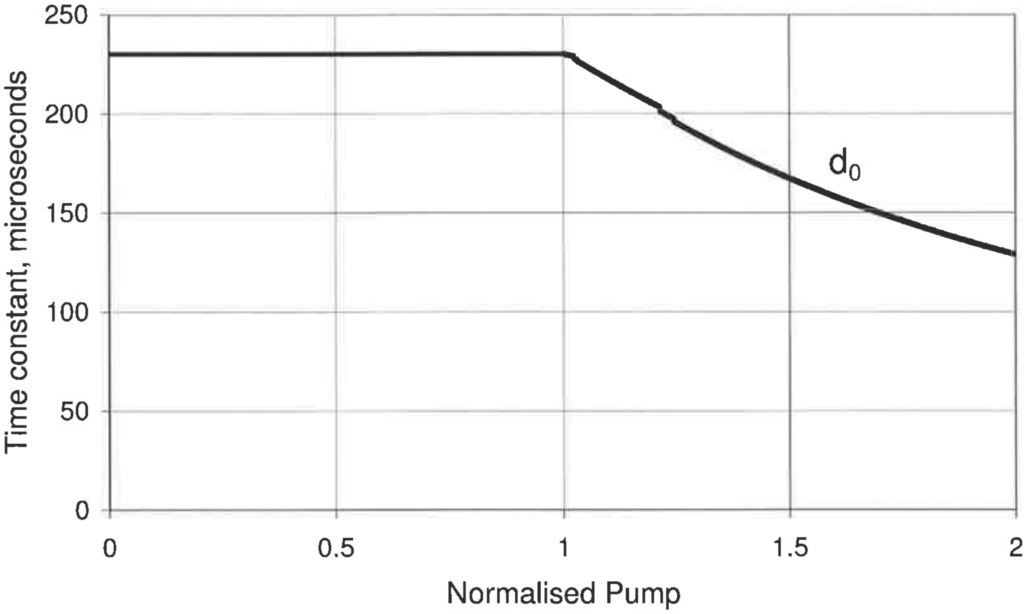

Figure 4-5 Inverse of the real eigen-value versus pump for the uniformly pumped laser

The real parts of the complex eigen-values have a similar dependence on the pump level, as shown in Figure 4-6. As the pump increases, the decay time constants ($d = -1/\mathrm{Re}(\lambda)$) decrease or the absolute values of the real parts ($-\mathrm{Re}(\lambda)$) increase. Thus, the poles move away from the imaginary axis, in the negative direction. However, at the same time the frequencies of the poles ($\mathrm{Im}(\lambda)/2\pi$) increase, so the damping (ζ) of the poles does not change much.

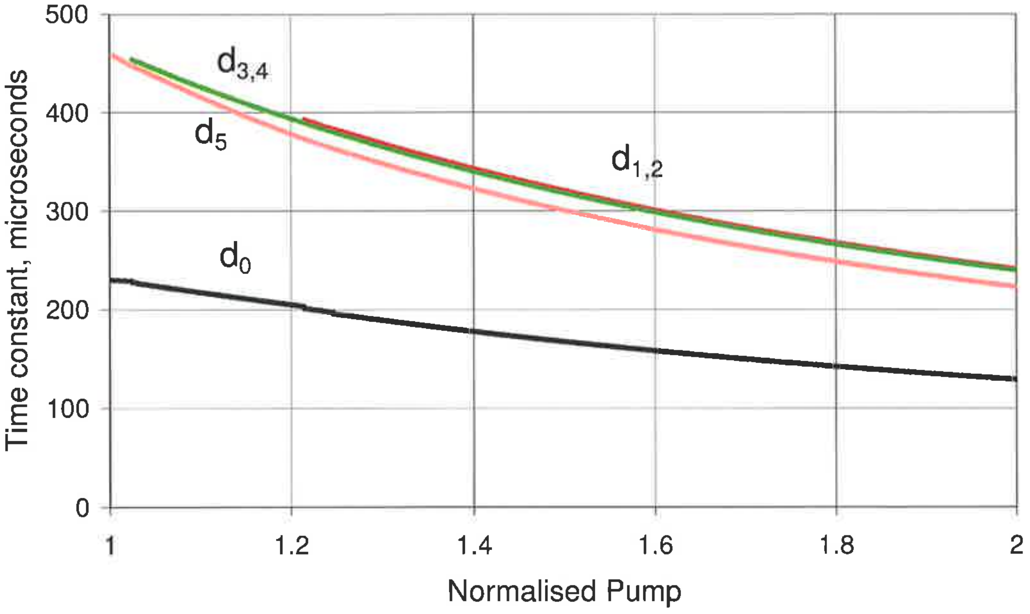

Figure 4-6 Damping of the poles versus pump for the uniformly pumped laser

It was shown in a number of references ([48], [49], [63]) that for the multimode lasers the squares of the pole frequencies scale almost linearly with the excess pump level. By excess pump level we mean the difference between the actual pump level and the pump level at the threshold of the mode that generated the corresponding frequency. Figure 4-7 is a graph showing this relationship.

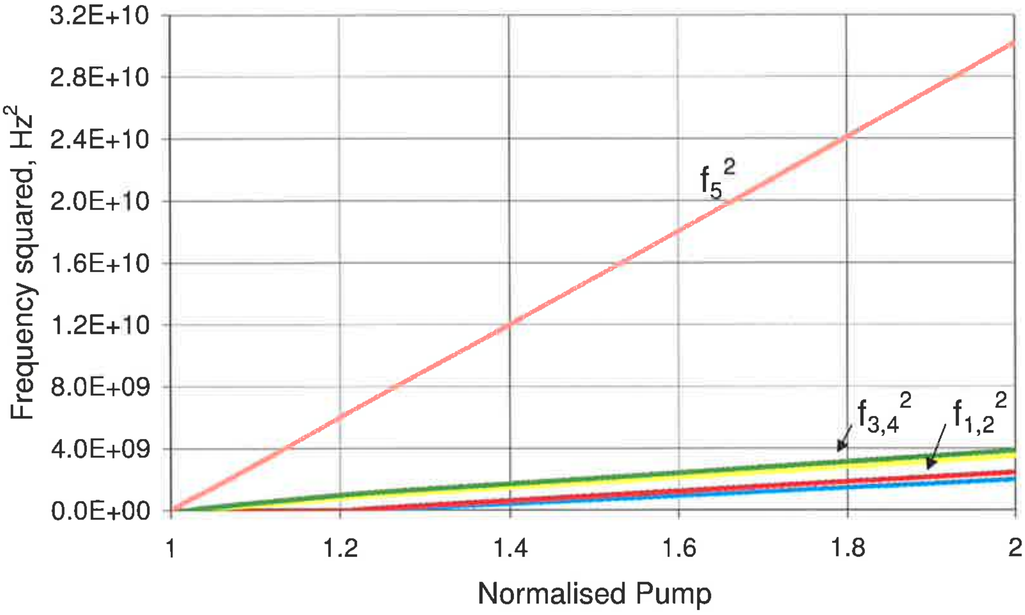

Figure 4-7 Square of the pole frequencies versus pump for the uniformly pumped laser

The linearity is particularly good for the highest frequency (f_5), which corresponds to the classical relaxation oscillation frequency of the single-mode laser [34]. The later approximately scales with the pump level according to the formula (2-19). If this formula is fitted to the data for f_5^2 in Figure 4-7, the value obtained for cavity decay time is $\tau_c = 3.65\,ns$, a value about 2.5% higher than the value used as input for calculations ($\tau_c = 3.56\,ns$). This difference gives an indication for the magnitude of the error made in the calculation of the cavity decay time by applying the single-mode formula (2-19) to the multimode laser.

A rescaled version of the Figure 4-7 is presented in the Figure 4-8, showing that the linearity for the other frequencies is not as good as for f_5 .

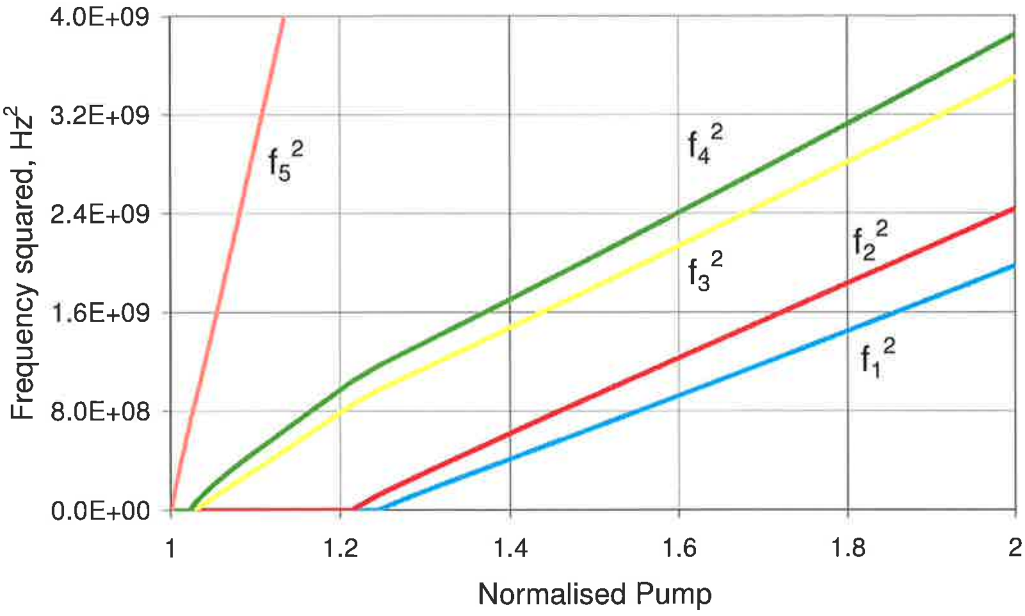

Figure 4-8 Square of the pole frequencies versus pump for the uniformly pumped laser (detail)

4.5 Transfer Functions for the End Pumped Laser

4.5.1 Analytic Calculations

The calculations for the transfer functions of the end pumped laser are very similar to the case of the uniformly pumped laser. The set of differential equations used is that corresponding to the Tang Statz deMars model with exponential decay [equations (3-65) to (3-67)], with the difference that the first equation includes pump modulation:

$$\frac{dn_0}{dt} = \frac{1}{\tau_f}\left[w_0 - n_0 - \sum_{k=1}^{N} g_k\left(n_0 - 1/2\,n_k\right)i_k\right] + \frac{1}{\tau_f}w$$

$$\frac{dn_j}{dt} = \frac{1}{\tau_f}\left[g_j n_0 i_j - n_j\left(1 + \sum_{k=1}^{N} g_k i_k\right)\right], \quad j = 1\ldots N$$

$$\frac{\mathrm{d}i_j}{\mathrm{d}t} = \frac{1}{\tau_c}\left\{g_j\left[n_0 - 1/2\sum_{k=1}^{N} n_k \frac{1}{1 + q^2\left(m_k - m_j\right)^2}\right] - 1\right\}i_j, \quad j = 1\ldots N. \tag{4-24}$$

We use the same expression as in (4-19) for the pump modulation and the same substitutions for the variable **x** and vector **b** (4-21), and for the output selection vectors $\mathbf{c}_j^T$ ($j = 1\ldots N$) and $\mathbf{c}_t^{\mathrm{T}}$ (4-23).

As we already know, the calculations for the steady state solution are more involved for this model than for the uniformly pumped case and do not lend themselves to an easy analytical solution. However, the Jacobian matrix can be derived relatively easily from the equations (4-24), as shown in the Appendix A4.2.

4.5.2 Numeric Calculations

The end pumped model requires the same parameters as the uniformly pumped laser plus the absorption coefficient for the pump radiation. Therefore, we use in the numeric calculations exactly the same values as those used in the section 4.4.2 and choose $\mu = 314.16\,m^{-1}$ for the absorption coefficient. This value corresponds to $q = 0.8$ for the dimensionless absorption parameter defined in (3-78) and was selected because it gave a good resemblance between the calculation results and the measurements.

The steady state solution is given in Table 4-4 and it is worth noting that the intensity of mode 1 is below that of modes 2 and 3, despite the fact that its gain is the highest. The average population inversion is also higher than the value in Table 4-2, showing that the gain clamping is even less effective in the end pumped model compared to the case of uniform pump.

Table 4-4 Steady state solution for end pumping

Mode	n_j^0	p_j^0	g_j
1	0.056291	0.064706	0.999987
2	0.064343	0.074526	0.992408
3	0.064419	0.074712	0.991101
4	0.010147	0.012036	0.969096
5	0.004277	0.005086	0.966607
0/t	1.069441	0.231065	

The eigen-values of the stability matrix corresponding to this steady state solution are listed in the Table 4-5 and they are not very dissimilar to those in the Table 4-3.

Table 4-5 Eigen-values of the system matrix **A** for end pumping

Eigen-value	-1/Real part, μs	Imaginary part/2π, kHz
λ_1	$d_0 = 195.8$	
$\lambda_{2,3}$	$d_1 = 377.2$	$f_1 = 7.16$
$\lambda_{4,5}$	$d_2 = 377.7$	$f_2 = 10.65$
$\lambda_{6,7}$	$d_3 = 375.1$	$f_3 = 18.48$
$\lambda_{8,9}$	$d_4 = 374.2$	$f_4 = 30.28$
$\lambda_{10,11}$	$d_5 = 351.7$	$f_5 = 96.07$

4.5.3 The Effect of Pump Level on the Eigen-Values of the Stability Matrix

As the pump level is increased, both the real and the imaginary parts of the eigen-values of the Jacobian change. The variation of the reciprocal of the real eigen-value is shown in Figure 4-9 and, while similar to the corresponding graph for the uniform pump (Figure 4-5), it displays considerably more variation each time a new longitudinal mode reaches its threshold.

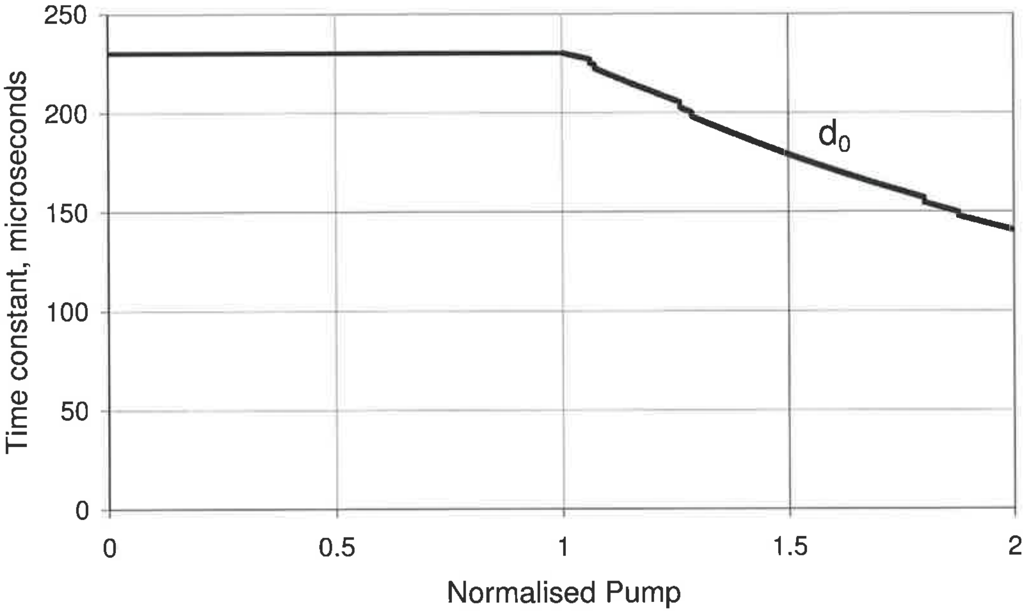

Figure 4-9 Inverse of the real eigen-value versus pump for the end pumped laser

Similarly, the reciprocals of the real parts of the complex eigen-values show a monotonic decrease with increasing pump level (Figure 4-10). The most noticeable difference from the uniform pump situation (Figure 4-6) is the existence of an additional pair of modes above $w \approx 1.8 - 1.9$ (i.e. 7 modes instead of 5). This is surprising since the end pumped model increases the competition between the longitudinal modes, so one would expect fewer not more active modes than the uniform pump model.

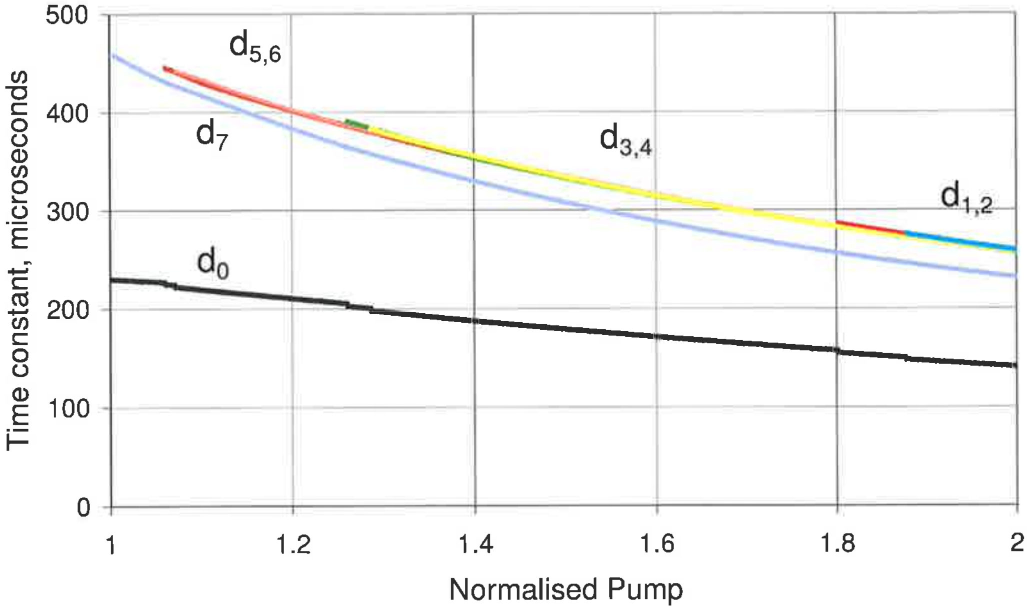

Figure 4-10 Damping of the poles versus pump for the end pumped laser

The linear relationship between the square of the pole frequency and the excess pump level is verified reasonably well for the highest frequency, as shown in Figure 4-11. Fitting a straight line to the f_7^2 data and using the resulting slope in the relation (2-19) to calculate the cavity decay time gives a value of $\tau_c = 3.69\,ns$. This value is about 3.75% higher than the cavity decay time actually used as input for the numeric calculations ($\tau_c = 3.56\,ns$).

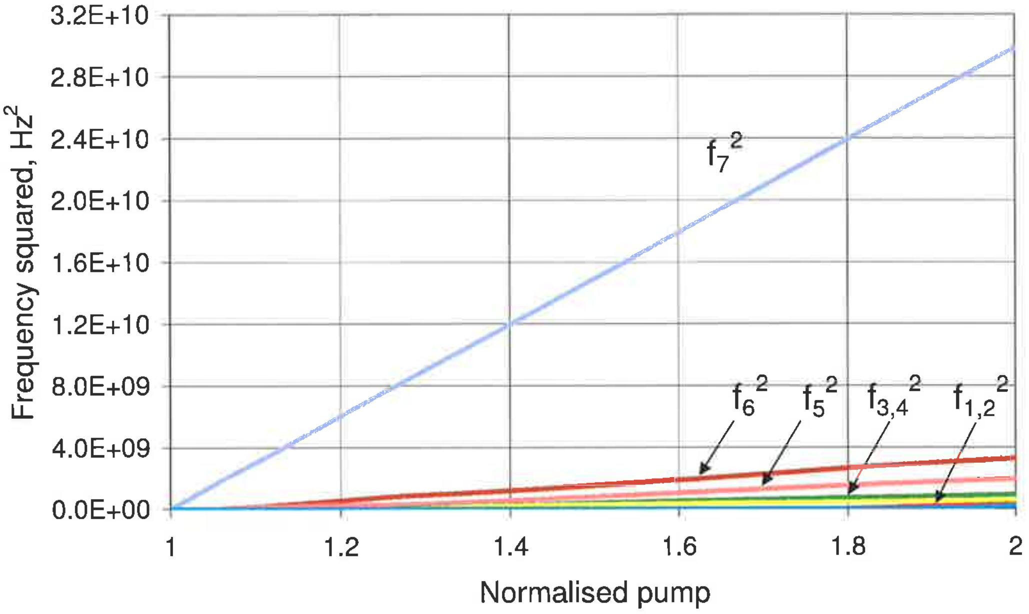

Figure 4-11 Square of the pole frequencies versus pump for the end pumped laser

For the frequencies of the other poles however, the linearity is not so good as it can be seen in Figure 4-12.

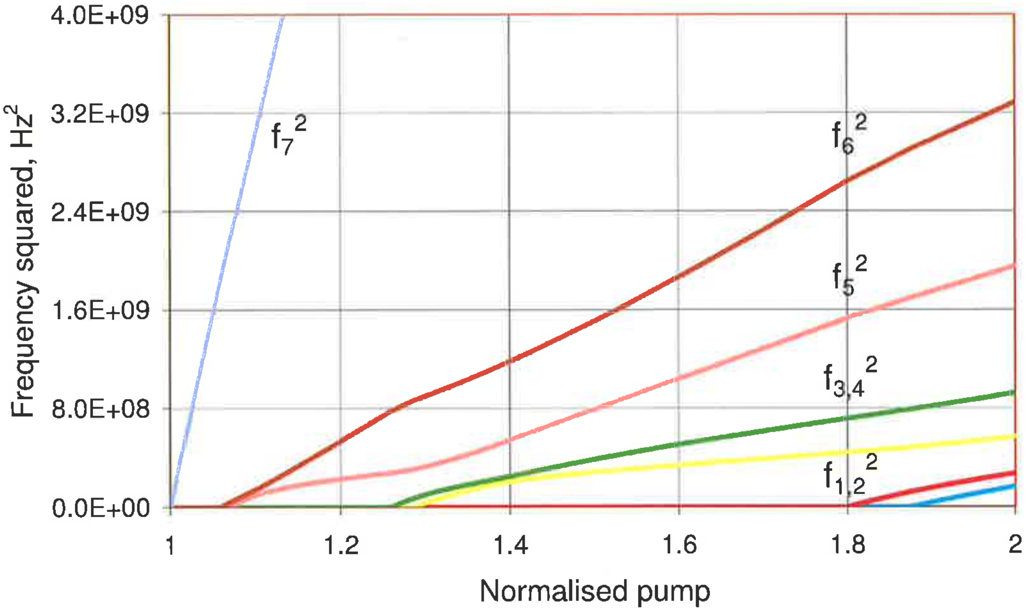

Figure 4-12 Square of the pole frequencies versus pump for the end pumped laser (detail)

4.6 Experimental Determination of the Transfer Functions

In this section we describe the set-up employed for the experimental measurement of the transfer functions of the Nd:YAG laser and the processing of the results. In the previous sections of this chapter the transfer functions were defined with respect to the Nd:YAG laser, i.e. the input of the system was the modulation of the pump power and the outputs were either individual modes or the total intensity. Here, the measured transfer functions were determined with respect to the inputs of the dynamic signal analyser and they included elements other than the laser (as described below), which needed to be either factored out or taken into account.

4.6.1 Experimental Set-up

The experimental set-up for these measurements consisted of some of the building blocks described in Chapter 2 and the block diagram represented in Figure 4-13 shows how they were inter-connected. The set-up had to perform two main tasks:

- to measure the transfer functions;
- to monitor the drift of the laser modes and track them during the measurements.

The measurement of the transfer functions was a fairly lengthy process and it was likely to have changes in the ambient temperature during this time. These temperature changes affected the length of the laser cavity, and thus changed the position of the laser modes with respect to the pass-band of the Fabry-Perot spectrum analyser. In order to monitor this drift, we used the elements shown in the upper side of Figure 4-13 (signal generator, high voltage amplifier, piezoelectric ring, Nd:YAG laser, Fabry-Perot spectrum analyser, photodiode amplifier 1 and lock-in amplifier).

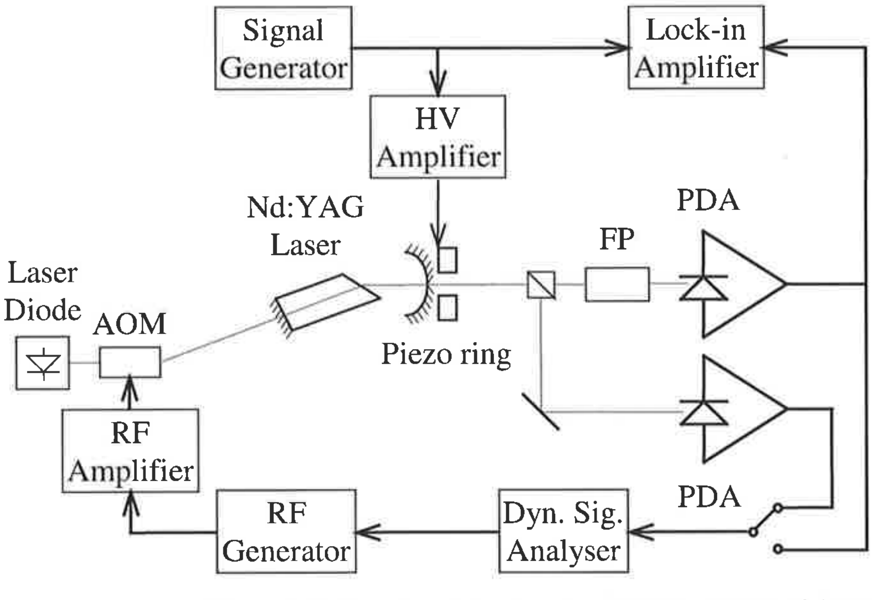

Figure 4-13 Experimental set-up for the measurement of the transfer functions

Using the technique presented in section 2.4.4, the dither produced by the signal generator was applied to both the Nd:YAG laser and the reference input of the lock-in amplifier. The amplitude of the dither was about 100 mV on the piezoelectric ring of the laser mirror and the frequency of the dither was chosen to be 3 kHz, well below the region of interest for the transfer functions. The phase of the lock-in was chosen such that the amplitude of the dither signal measured at the output of the Fabry-Perot spectrum analyser crossed zero when the latter was centred on the desired laser mode. Before each measurement, the high voltage applied to the piezoelectric element of the Fabry-Perot was manually adjusted to find the null of the dither. This insured that the laser mode to be measured was centred with respect to the pass-band of the optical spectrum analyser. During the measurements, the rate of drift was such that the laser took about 20 minutes to traverse the pass-band of the Fabry-Perot, while the measurement time for each transfer function was significantly shorter (about 31 seconds).

The parts of the system involved in the actual measurement of the transfer functions are shown in the lower side of Figure 4-13 (dynamic signal analyser, RF generator, RF amplifier, acousto-optic modulator, Nd:YAG laser, Fabry-Perot spectrum analyser and / or photodiode amplifier). The HP35670A dynamic signal analyser was used to control the measurements. Its internal source generated the sinusoidal signals that were applied to the modulation input of the Hewlet-Packard 8640B RF generator. The amplitude modulated output of the RF generator (80 MHz) was amplified and applied to the acousto-optic modulator, which impressed the modulating signals of the signal analyser's source upon the pump beam of the Nd:YAG laser. The output of the laser was detected with photodiode amplifiers either directly (for total intensity) or through the Fabry-Perot optical filter (for individual modes) and finally measured by the dynamic signal analyser.

The bandwidth of the measurement system was sufficiently wide to cover the chosen frequency span without significant gain changes. Despite the flatness of the gain characteristic, the phase characteristic showed significant changes in the region of interest, which had to be taken into account. The transfer function of the measurement system (which includes all elements described in the paragraph above except the laser) was recorded and the results are shown in Figure 4-14.

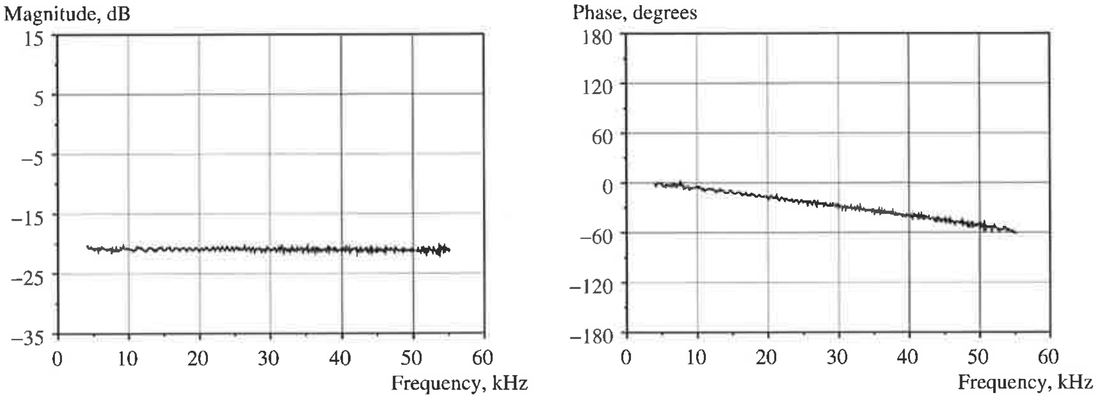

Figure 4-14 The magnitude and the phase of the measurement system transfer function

The HP35670A dynamic signal analyser offers many options for the measurement of the transfer functions; we selected the following:

- Source mode: periodic chirp. This source type does not require windowing (if the acquisition is triggered from the source) and allows the measurements to be taken quickly. It is not the best for non-linear systems, but the alternatives had more significant problems (noise requires windowing and swept sine is too slow for the drift of the laser).
- Frequency span: 4-55.2 kHz. This is the highest frequency range in the two-channel mode and the part of the spectrum that is lost (below 4 kHz) is not of great interest.
- Average mode: 1000 RMS averages, overload rejection on. Due to the large level of intrinsic noise of the laser, it was necessary to average many measurements, while monitoring for overload conditions was required to reject distorted signals.

The measurements were difficult, due to both the drift and the noise of the laser. Almost complete sets of measurements had to be abandoned due to the changes in temperature. The coherence function (which shows how much of the received signal is due to the source) for individual modes was not very good, especially in the vicinity of the zeros of the transfer function. However, the coherence was quite good for the total intensity, showing that most of the noise was cancelled out due to antiphase dynamics. Despite these problems, we were able to take measurements of sufficiently good quality to justify further work on them.

As a side note, the problems caused by the noise actually suggested using it as an alternative to the use of the transfer functions for the study of antiphase dynamics and motivated the work described in the next chapter.

4.6.2 Processing of the Data

Once the measurements of the laser were completed, the data was re-loaded into the signal analyser, one transfer function at a time. For each of them, a pole-zero model was fitted to the measurement, using the curve fit option of the HP35670A dynamic signal analyser [64]. This option allows up to 20 poles and 20 zeros to be included in the model and has two modes of automatic operation: fixed order and maximum order. In the fixed order mode, the complex fitter finds the curve with the given numerator and denominator orders that best fits the data in the least-squares sense. In the maximum order mode, the complex data fitter uses successively higher system orders to search for the best-fit curve. This mode uses the measured coherence of the transfer function to determine when a fit is considered sufficiently good. Both modes accept manually entered poles and zeros, which are kept fixed. They also use the measured coherence of the transfer function to determine the weighing function used in the fitting process. The result of the curve fitting is presented in a pole-zero table and as a synthesised curve overlapped over the measurement.

The procedure followed in the fitting of the transfer functions was the following:

- The noise spectrum (see Figure 4-15 for an example) was used to estimate the parameters of the complex conjugate pair of poles corresponding to the relaxation oscillations. This was required because their location (96 kHz) was too far outside the measured range for transfer functions (4-55.2 kHz). The location of this pair of poles was kept the same for all measured transfer functions.
- The max order fit was used on each transfer function to find the location of the other poles (see Table 4-6).
- The 11 poles thus obtained were marked as fixed and a fixed-order (9) fit was performed for zeros.
- Using the result of the automatic fit as a starting point, the location of the zeros was manually modified until both the amplitude and the phase of fit coincided with the amplitude and the phase of the measurement.
- The fit table was copied into the synthesis table and transformed from the pole-zero format into the pole-residue format. Both formats were saved for interpretation.

With reference to Figure 4-15, it should be noted that the sharp peak at very low frequency is the dither (3 kHz), while the one just above 50 kHz is a spurious signal from the electronic equipment.

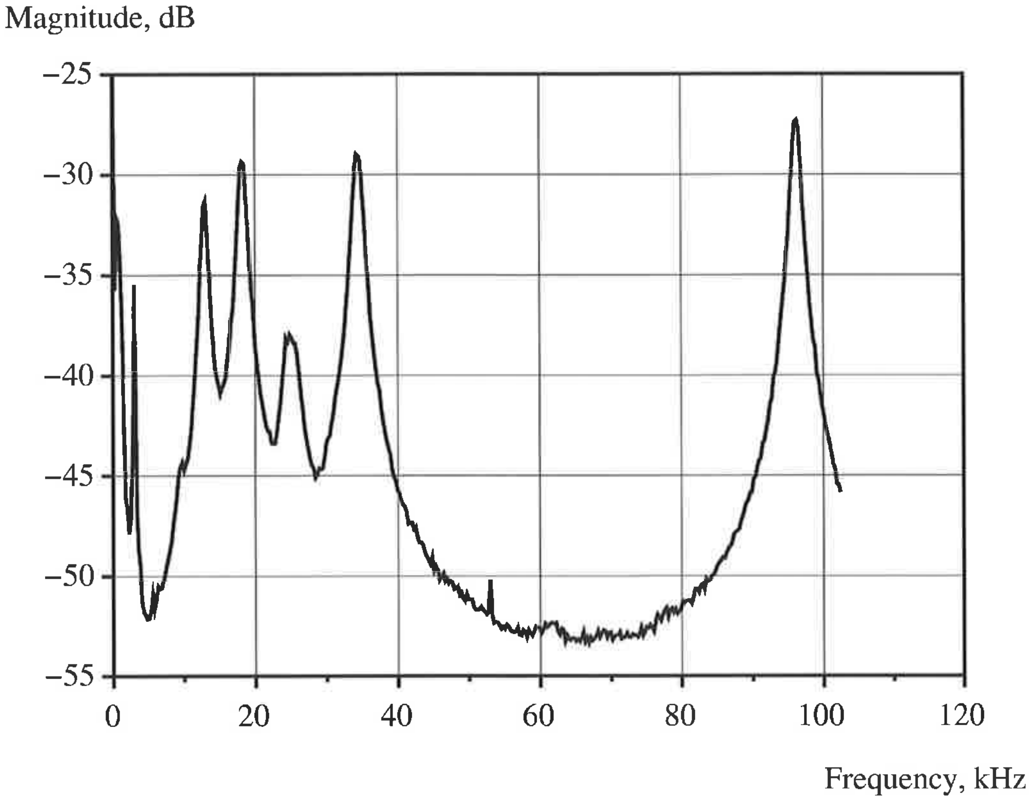

Figure 4-15 Noise spectrum of one of the longitudinal modes

The values shown in Table 4-6 represent average values for the damping and the frequency of the poles. Each transfer function displayed slightly different values, due to the temperature induced drift of the laser modes.

Table 4-6 Average values of the measured poles

Eigen-value	-1/Real part, µs	Imaginary part/2π, kHz
λ_1	$d_0 = 1.50$	
$\lambda_{2,3}$	$d_1 = 297.0$	$f_1 = 13.26$
$\lambda_{4,5}$	$d_2 = 294.0$	$f_2 = 18.60$
$\lambda_{6,7}$	$d_3 = 177.3$	$f_3 = 25.50$
$\lambda_{8,9}$	$d_4 = 222.6$	$f_4 = 34.60$
$\lambda_{10,11}$	$d_5 = 224.8$	$f_5 = 96.06$

An example of measurement (jagged line) and fit (smooth line) for one of the longitudinal modes is shown in Figure 4-16 (magnitude in linear scale) and in Figure 4-17 (phase in degrees).

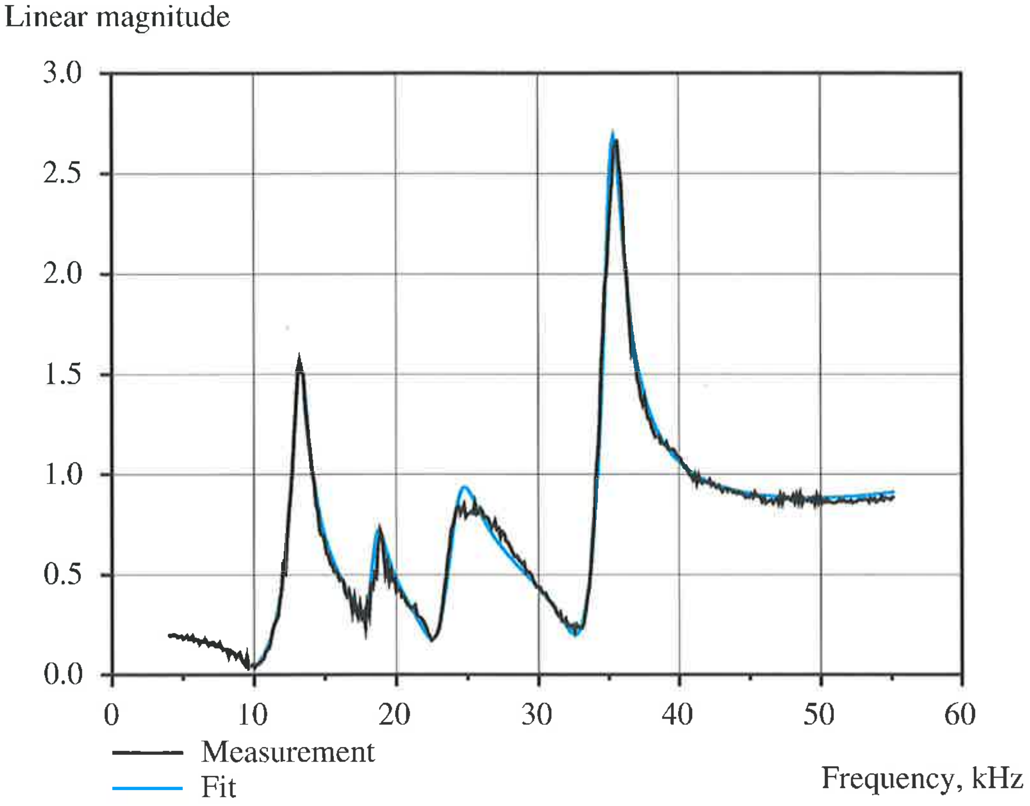

Figure 4-16 Example of measurement and fit for the magnitude of one of the longitudinal modes

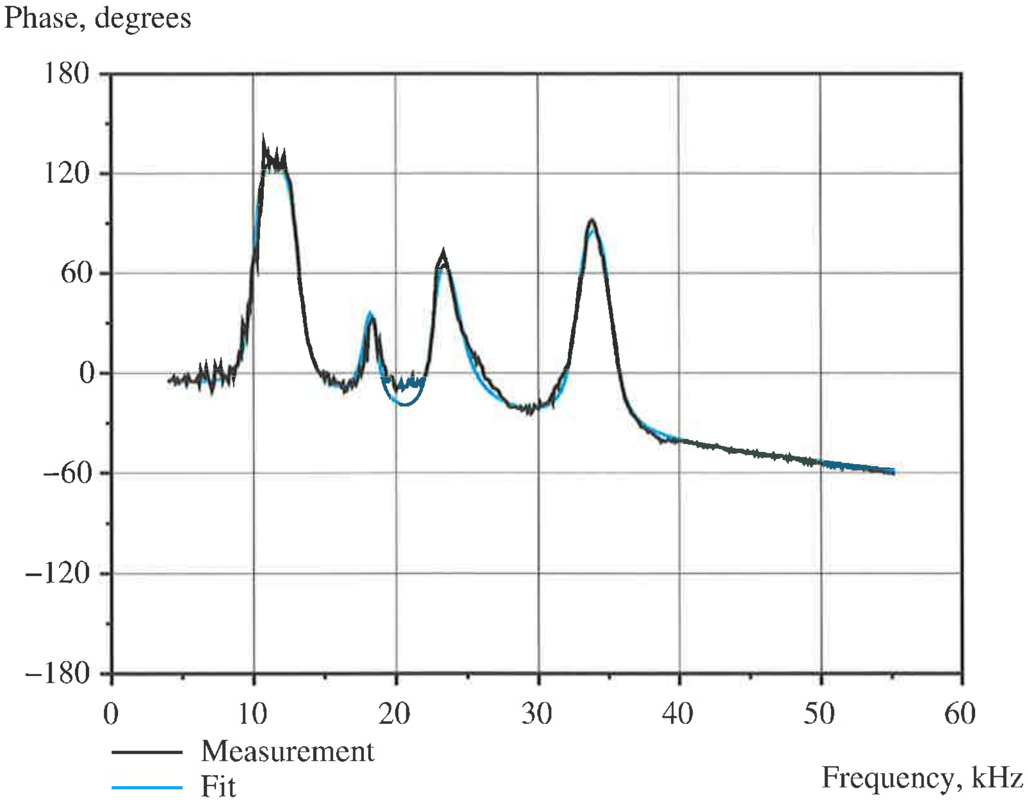

Figure 4-17 Example of measurement and fit for the phase of one of the longitudinal modes

4.7 Comparison of Results

In this section we compare the transfer functions calculated from the two models (uniformly pumped and end pumped) with those experimentally determined. The purpose of the comparison is to test the ability of each model to represent the important features of the real laser. At the same time, we establish the capability of the transfer functions method to shed light on the mechanisms responsible for antiphase dynamics.

4.7.1 Comparison of the Frequency Response Plots

Plotting the magnitude and the phase of the transfer functions versus frequency is a good starting point for interpreting the results. As mentioned above, the experimental transfer functions were only available from 4 kHz to 55.2 kHz, while the theoretical transfer functions were calculated up to 120 kHz, to include the relaxation oscillations resonance. We have chosen this extended frequency range because it gives a complete image of the response of each longitudinal mode or total intensity to pump modulation.

The calculations for the frequency response of the theoretical transfer functions were done in Scilab, following the procedure described in section 4.3. The necessary elements of the linearised system (the input vector **b**, the Jacobian matrix **A** and the output vectors $\mathbf{c}_j^T$ and $\mathbf{c}_t^{\mathrm{T}}$) were calculated in 4.4.2 (for the uniformly pumped model) and in 4.5.2 (for the end pumped model), respectively. Scilab used these elements to directly construct the state-space representation of the transfer functions, which were subsequently transformed into rational fractions (ratios of polynomials in the complex frequency s). Substituting $s = 2\pi jf$ in the rational fractions and giving the frequency f values in the range mentioned above, produced the desired frequency response.

The transfer functions for the longitudinal modes 1 to 5 are given in Figure 4-18 to Figure 4-22, respectively. Each figure shows the magnitude in dB and the unwrapped phase in degrees, for the uniformly pumped model, the end pumped model and the experimental measurement.

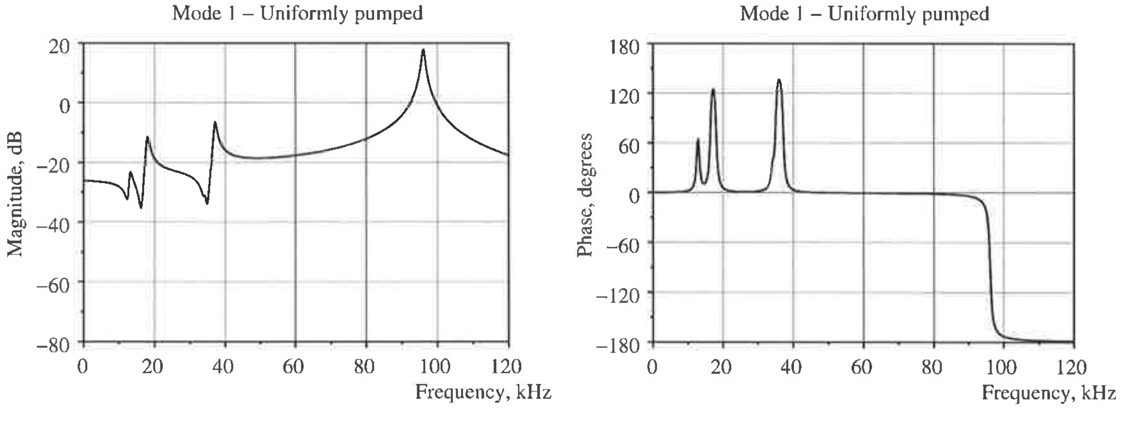

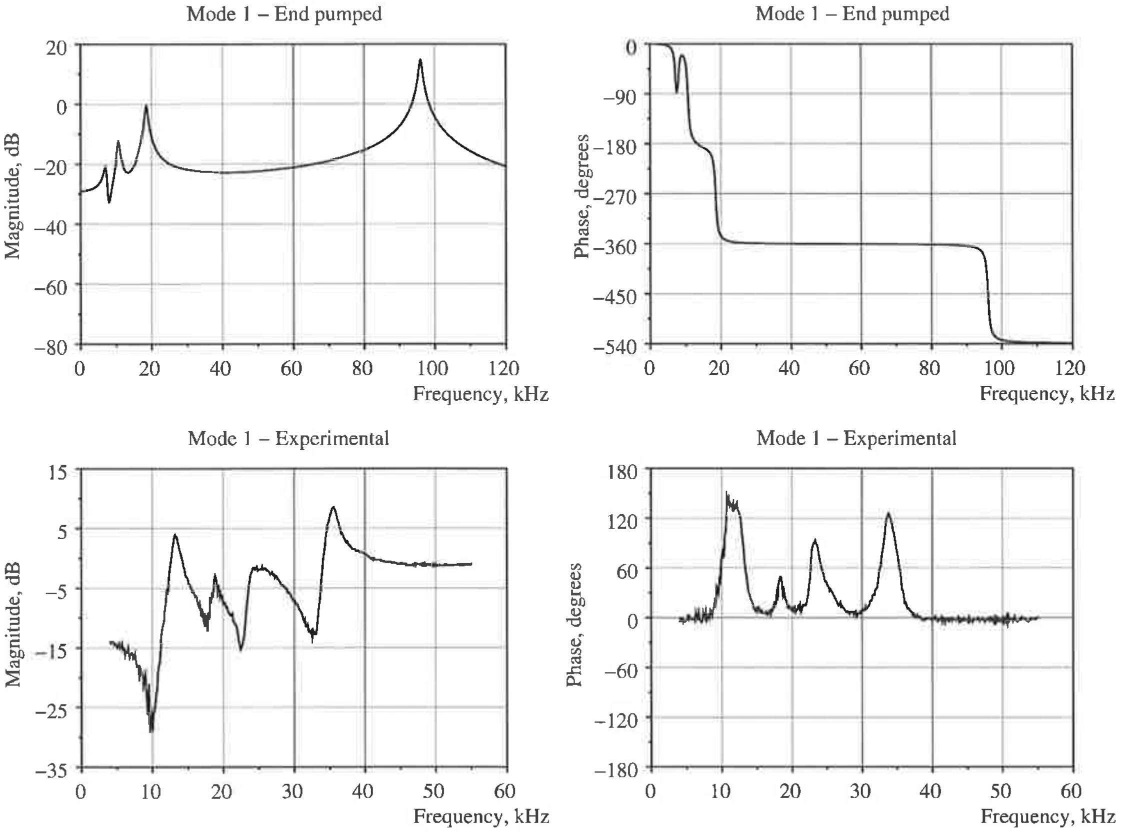

Figure 4-18 Calculated and measured transfer functions for the longitudinal mode 1

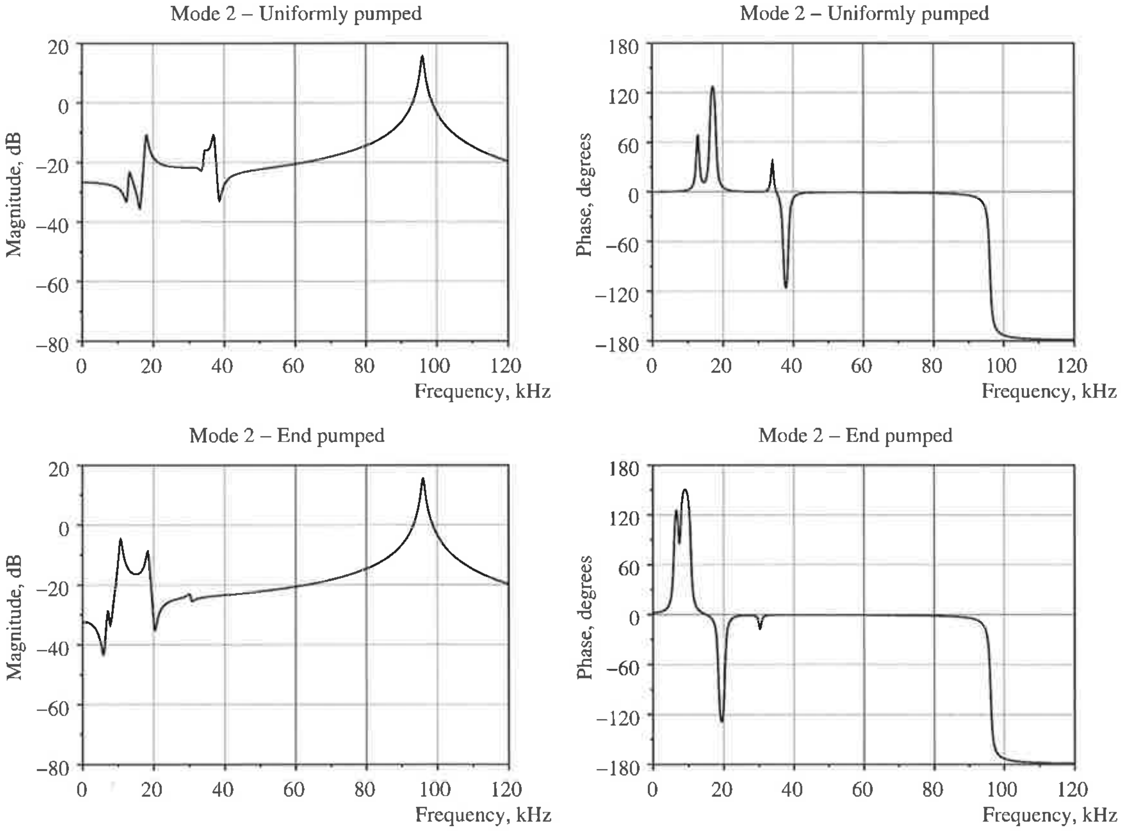

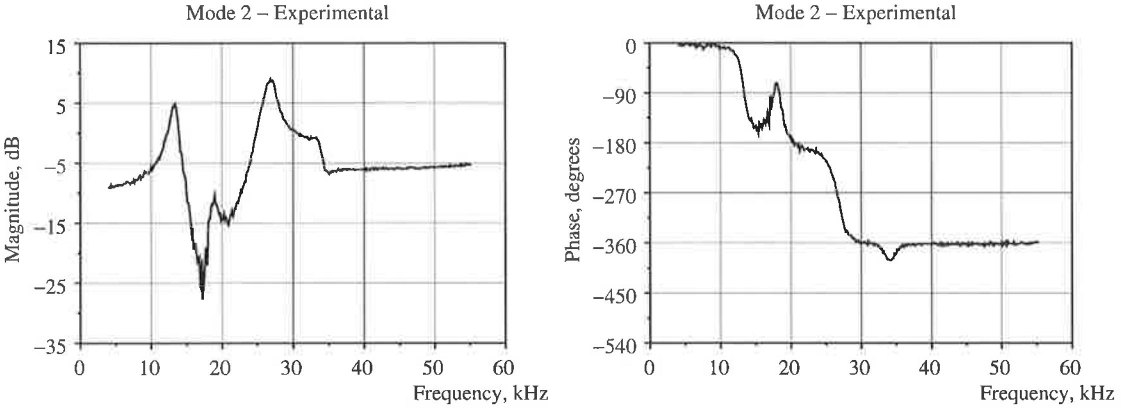

Figure 4-19 Calculated and measured transfer functions for the longitudinal mode 2

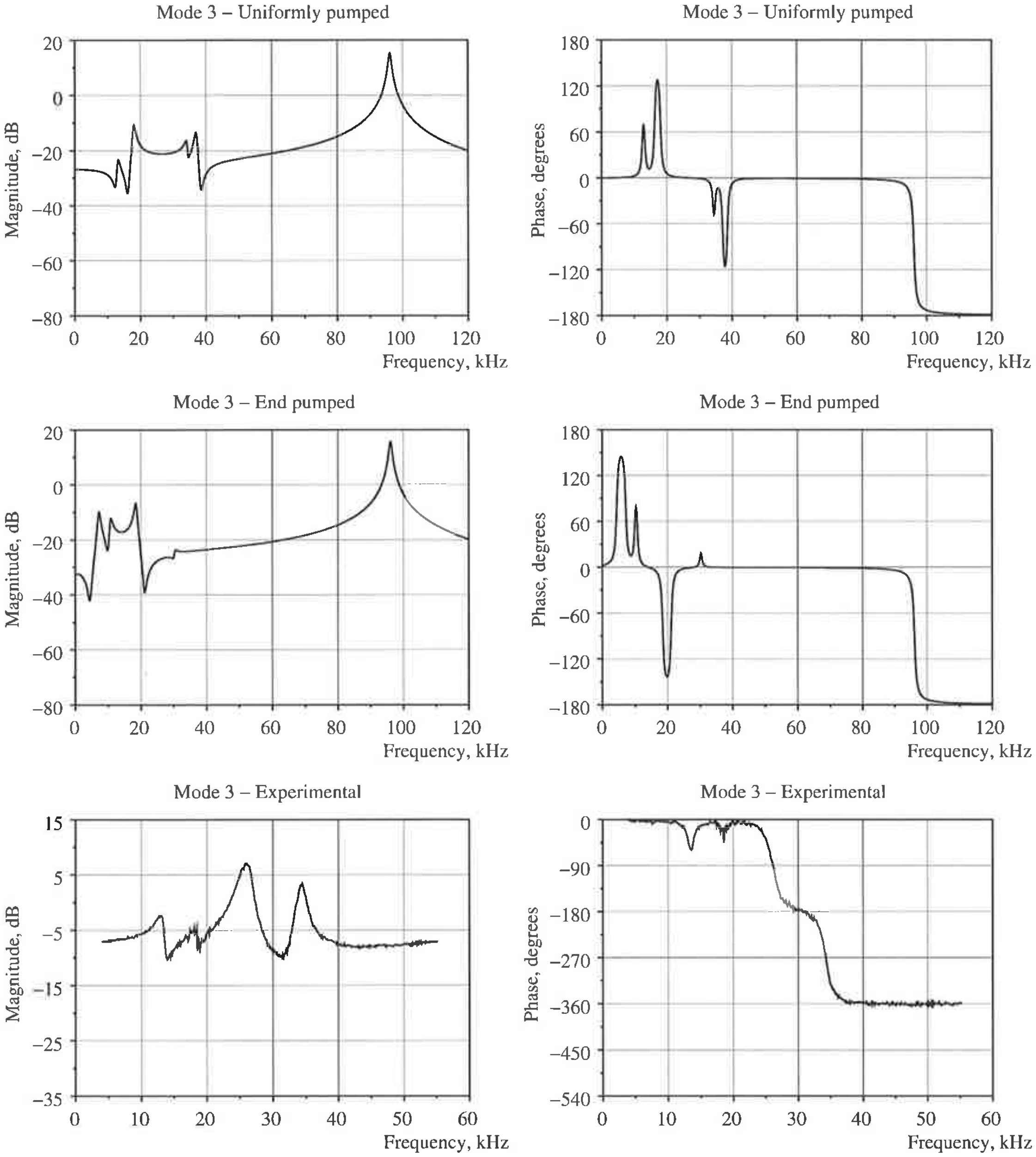

Figure 4-20 Calculated and measured transfer functions for the longitudinal mode 3

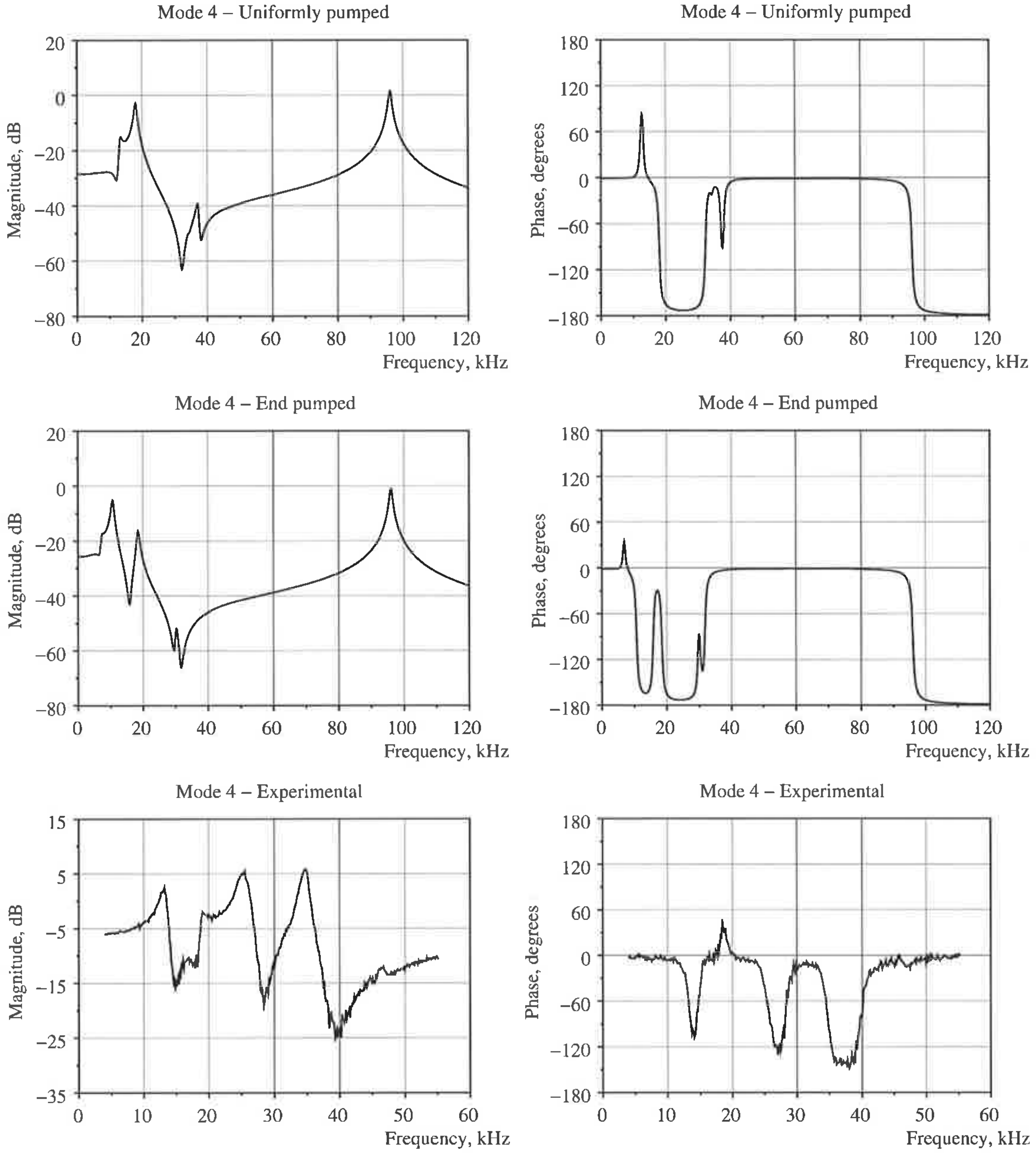

Figure 4-21 Calculated and measured transfer functions for the longitudinal mode 4

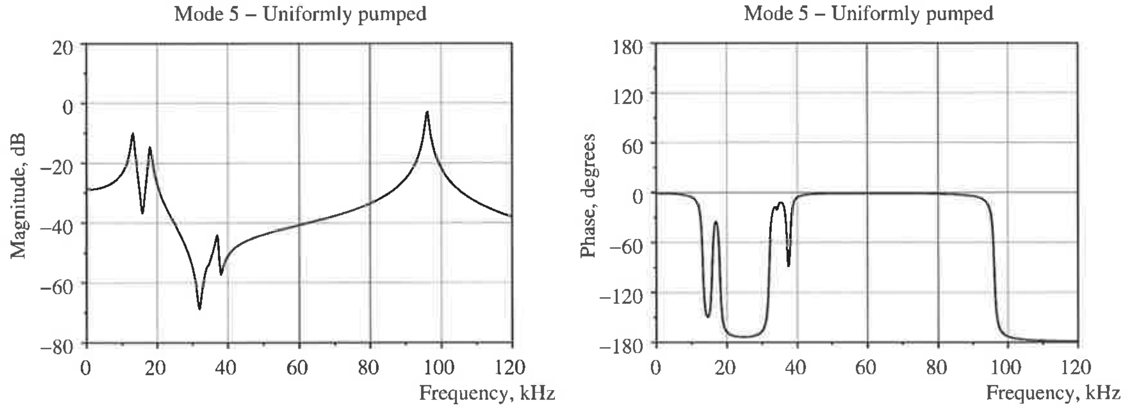

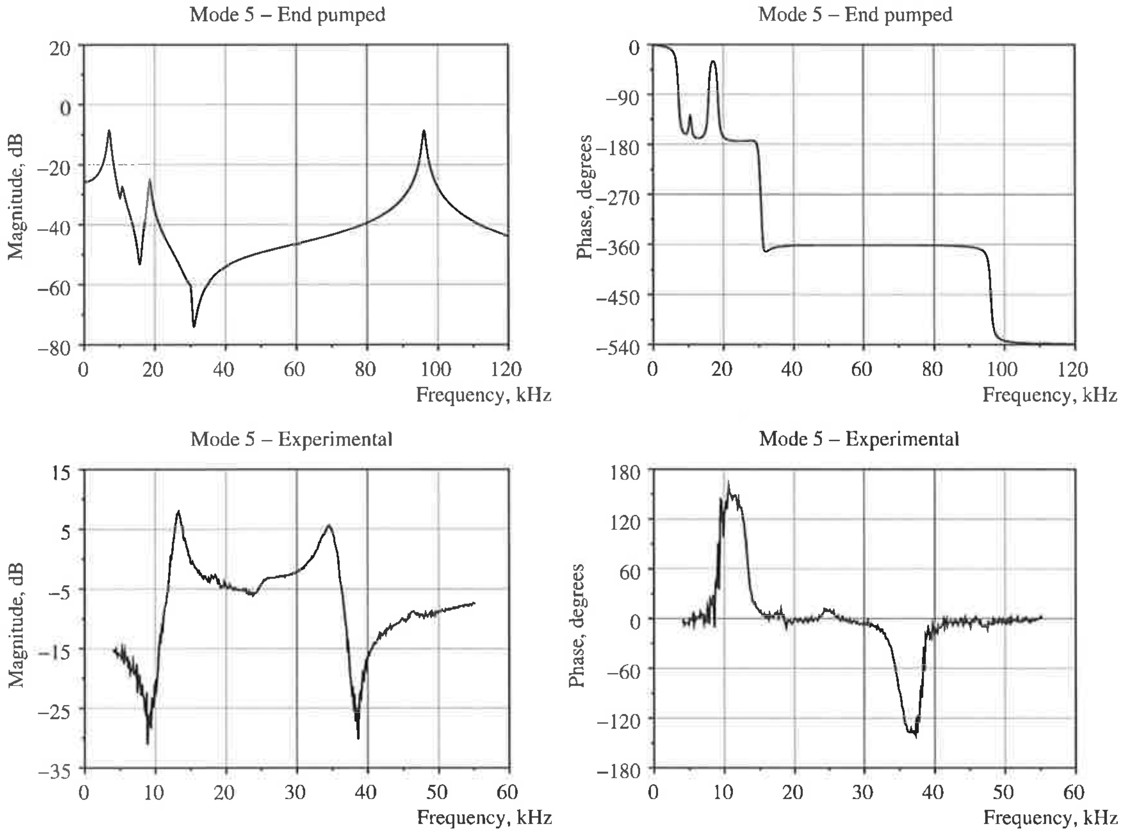

Figure 4-22 Calculated and measured transfer functions for the longitudinal mode 5

The transfer functions for total intensity are shown in Figure 4-23. Given that the experimental measurements were done without the optical spectrum analyser and with a different photodiode amplifier, the scaling for the magnitude is unrelated to that of the previous plots and the phase does not include any correction.

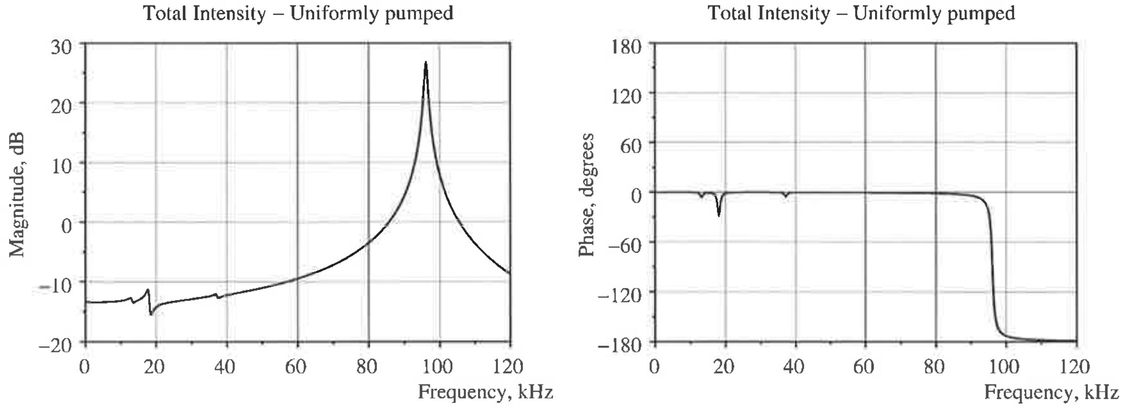

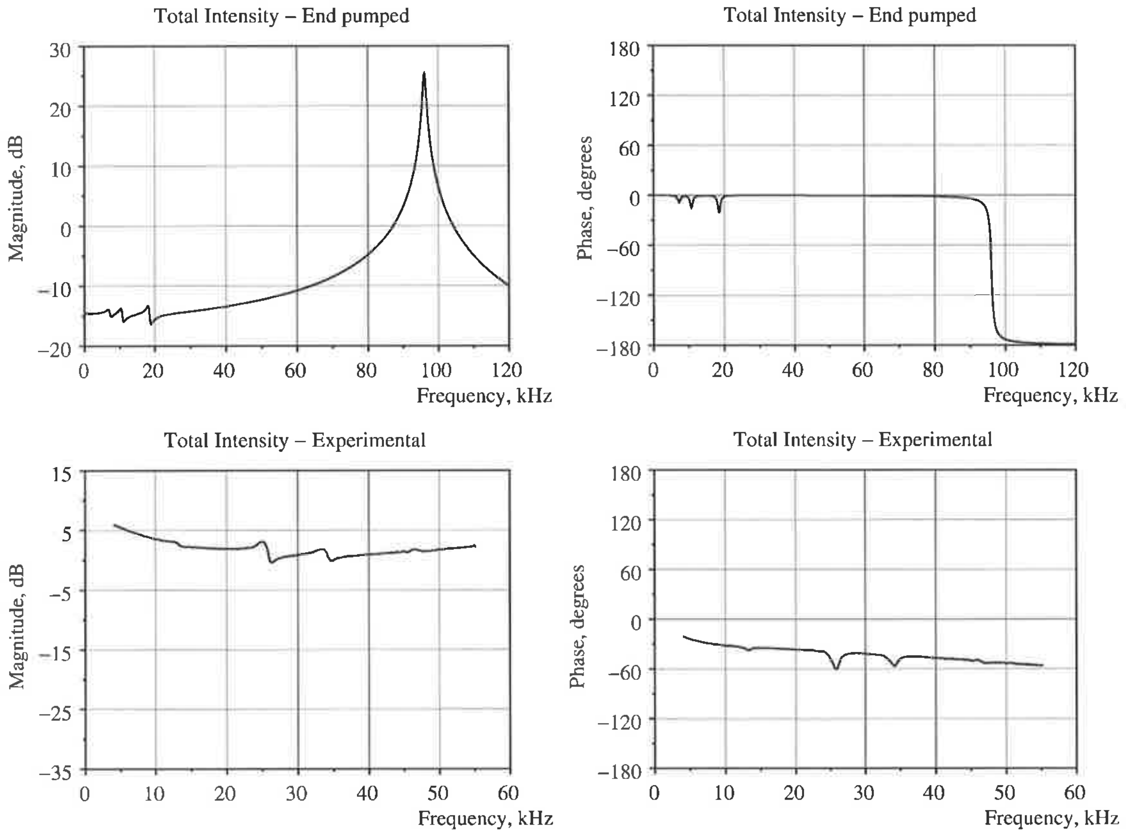

Figure 4-23 Calculated and measured transfer functions for the total intensity

An advantage of the type of comparisons used in this section is that the experimental transfer functions are almost in a 'raw' form (the only post-processing applied to the measurements is the removal of the phase shift introduced by the measurement system). This eliminates the possibility of errors due to the fitting process, but it also restricts the interpretation to general comments regarding the shapes of the curves.

What could be learnt from these plots? There are few obvious things to note first:

- There is evidence of antiphase dynamics in the magnitude plots: while modes 1 to 5 have several peaks in the low frequency zone, the total intensity has a much smoother plot. However, the cancellation of the low frequency motions is not perfect; the total intensity still has remnants of the peaks at low frequency.
- While both the magnitude and phase plots of the calculated transfer functions show some degree of qualitative agreement with the experimental measurements, neither model can aspire for quantitative agreement. For example, there are similarities in the total number of resonant frequencies and the overall shape of the phase curves, but there are also differences in the exact location and size of the peaks and in the detailed phase changes for each longitudinal mode.
- For some longitudinal modes, the total phase change can exceed 180° in the case of the end pumped model (modes 1 and 5) and in the case of the experiment (modes 2 and 3). However, in the case of the uniformly pumped model the change is always restricted to 180°.

There are a few other characteristics worth mentioning:

- The number of low frequency peaks varies from one longitudinal mode to the other. The magnitude plots give no indication why a longitudinal mode would respond to one resonant frequency but not to the other.
- The uniformly pumped model predicts that the low frequency part of the phase plot has a number of 'bumps' corresponding to the resonant frequencies. As we look in succession from mode 5 to mode 1, the orientation of the 'bumps' progressively changes from 'down' to 'up'. Similar conclusions have been drawn in [47] using the same model and in [59] considering the Tang Statz deMars equations with loss modulation. Neither the experiment nor the end pumped model show this rigid ordering (but they do not agree with each other either). This is also implied in the reference [41], where incomplete filling of the laser cavity is considered.

In the next two sections we will try to explain these features in essentially two equivalent ways: by looking at the location of the poles and the zeros of the transfer functions or by working out their partial fraction decomposition.

4.7.2 Comparison of Results in Pole-Zero Form

Determining the poles and the zeros of the numerical transfer functions is quite easy, especially if the transfer functions are in the form of rational fractions (as described in the previous section). The poles of the transfer functions are the eigen-values of the stability matrix **A** and they have been already calculated in section 4.4.2 for the uniformly pumped model (Table 4-3) and in section 4.5.2 for the end pumped model (Table 4-5). The zeros of the transfer functions are the roots of the numerator and Scilab has specialised routines to find them. For the experimental transfer functions, the poles and the zeros have been determined by fitting a pole-zero model to the data, as described in the section 4.6.2.

The diagrams in Figure 4-24 to Figure 4-28 represent the low frequency poles (crosses) and zeros (circles) of the transfer functions corresponding to the 5 longitudinal modes of the laser. The complete diagrams would have included another pair of poles (corresponding to the relaxation oscillations resonance, at ±96 kHz), but this pair has been omitted because it would have made more difficult to see the region of interest (±40 kHz). Each figure presents a diagram from the experimental measurements and one each for the uniformly pumped model and for the end pumped model.

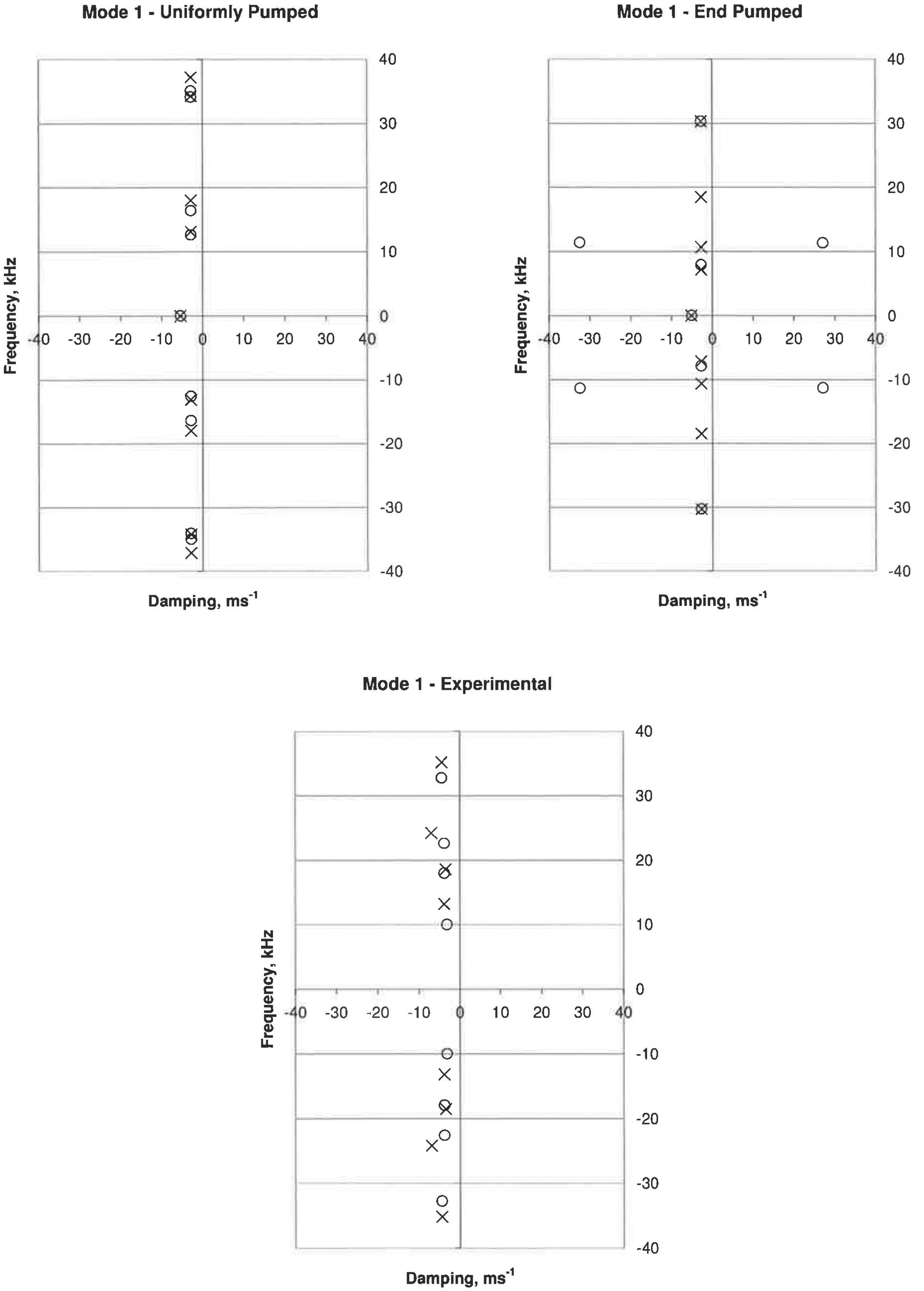

Figure 4-24 Calculated and measured pole-zero diagrams (low-frequency) for the longitudinal mode 1

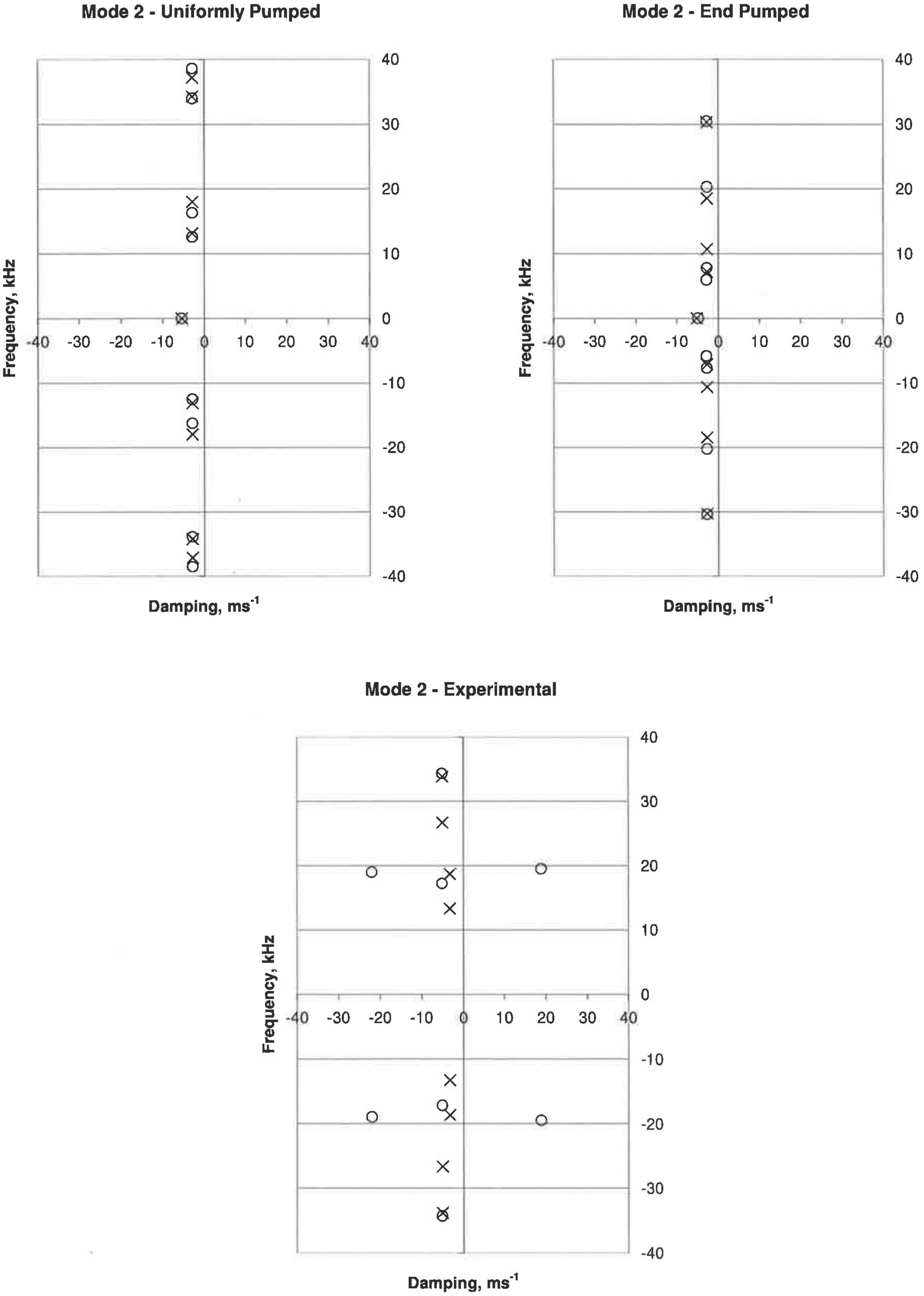

Figure 4-25 Calculated and measured pole-zero diagrams (low-frequency) for the longitudinal mode 2

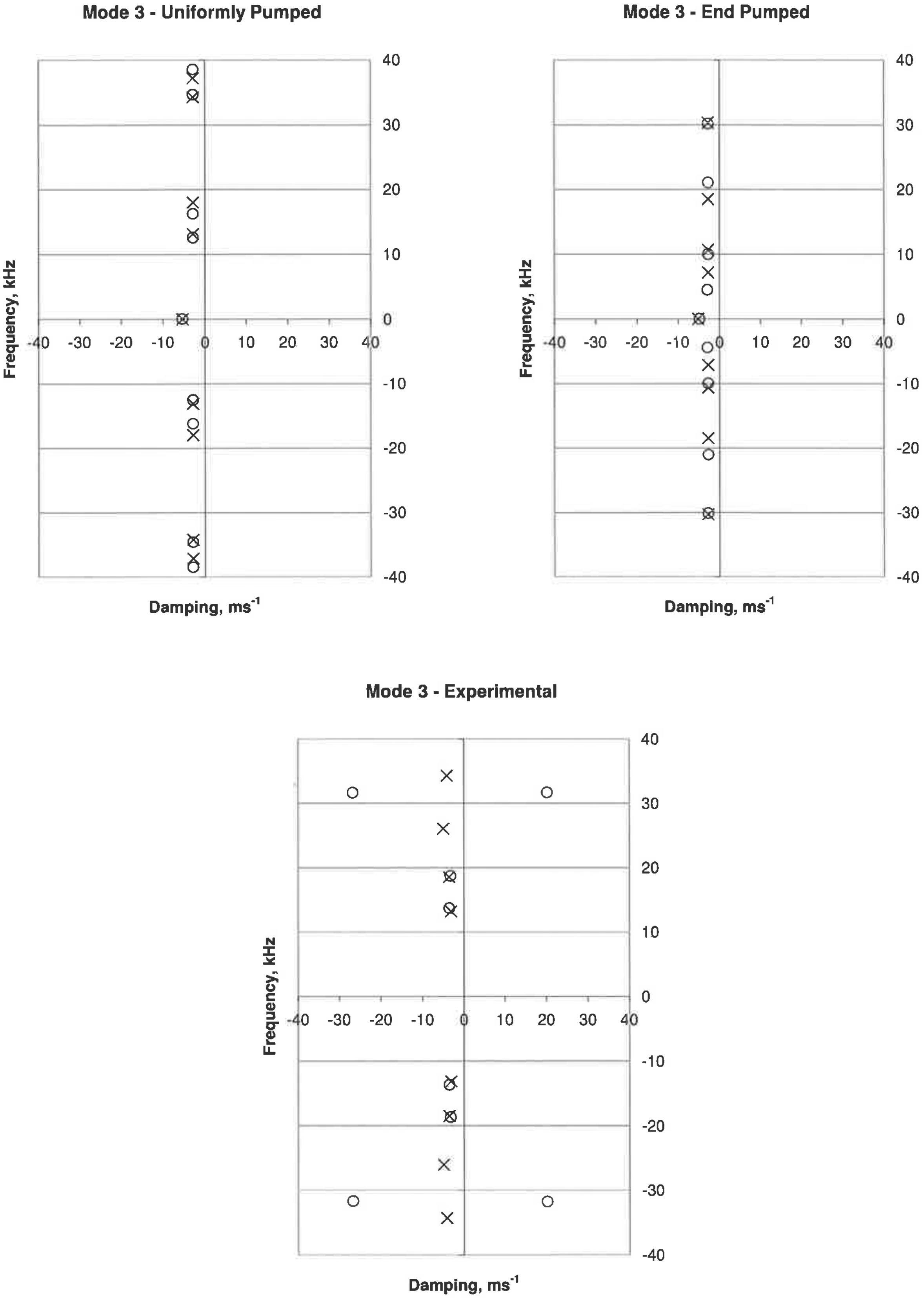

Figure 4-26 Calculated and measured pole-zero diagrams (low-frequency) for the longitudinal mode 3

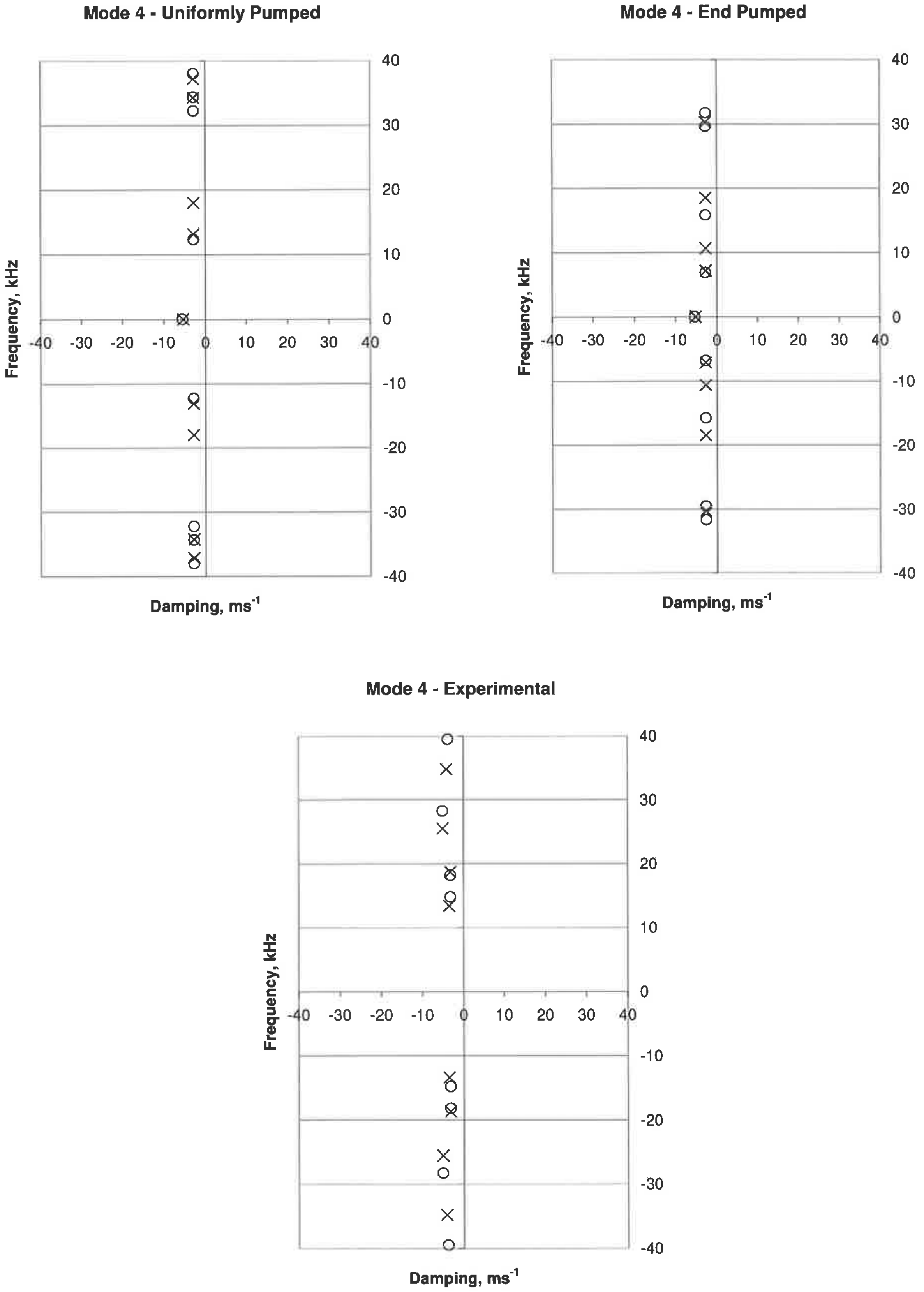

Figure 4-27 Calculated and measured pole-zero diagrams (low-frequency) for the longitudinal mode 4

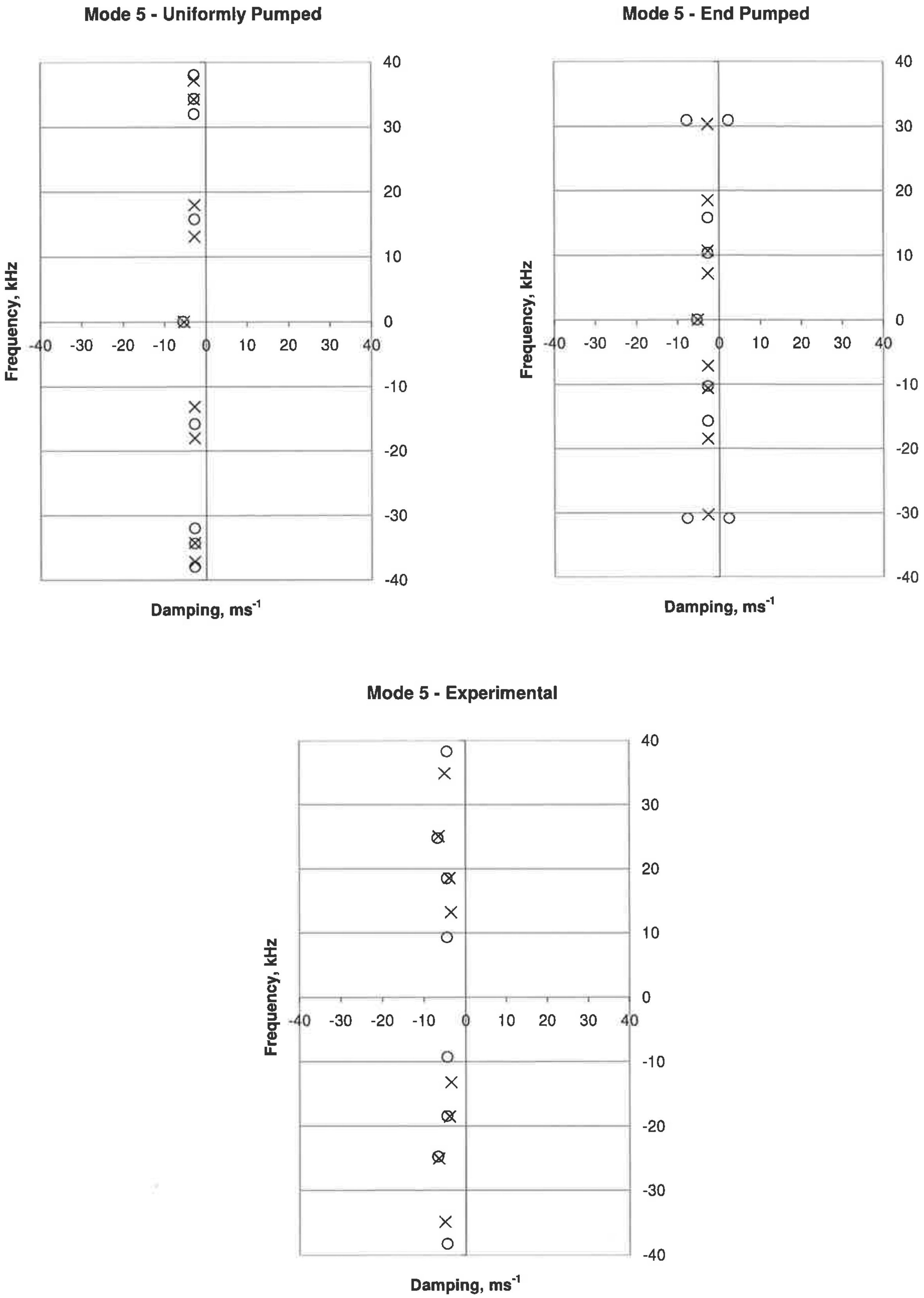

Figure 4-28 Calculated and measured pole-zero diagrams (low-frequency) for the longitudinal mode 5

It should be noted that in the experimental diagrams the positions of the poles change slightly from one longitudinal mode to the other, due to a number of reasons (most likely changes in the operating parameters of the laser due to the drift in temperature and inaccuracies in the fitting process). We prefer to show these variations instead of using the average position of the poles, because otherwise there would be discrepancies between these diagrams and the frequency response plots. We also omitted the real pole and the real zero from the experimental plots due to difficulties in fitting the pair correctly.

For similar reasons, the measured total intensity was not fitted, so only the results of the numerical calculations are shown in Figure 4-29. If we assume that the experimental pole-zero diagram for the total intensity would be similar to the theoretical ones (as would suggest the frequency responses in Figure 4-23), it is quite understandable why the fitting routine could not produce sensible results: due to the pole-zero cancellations.

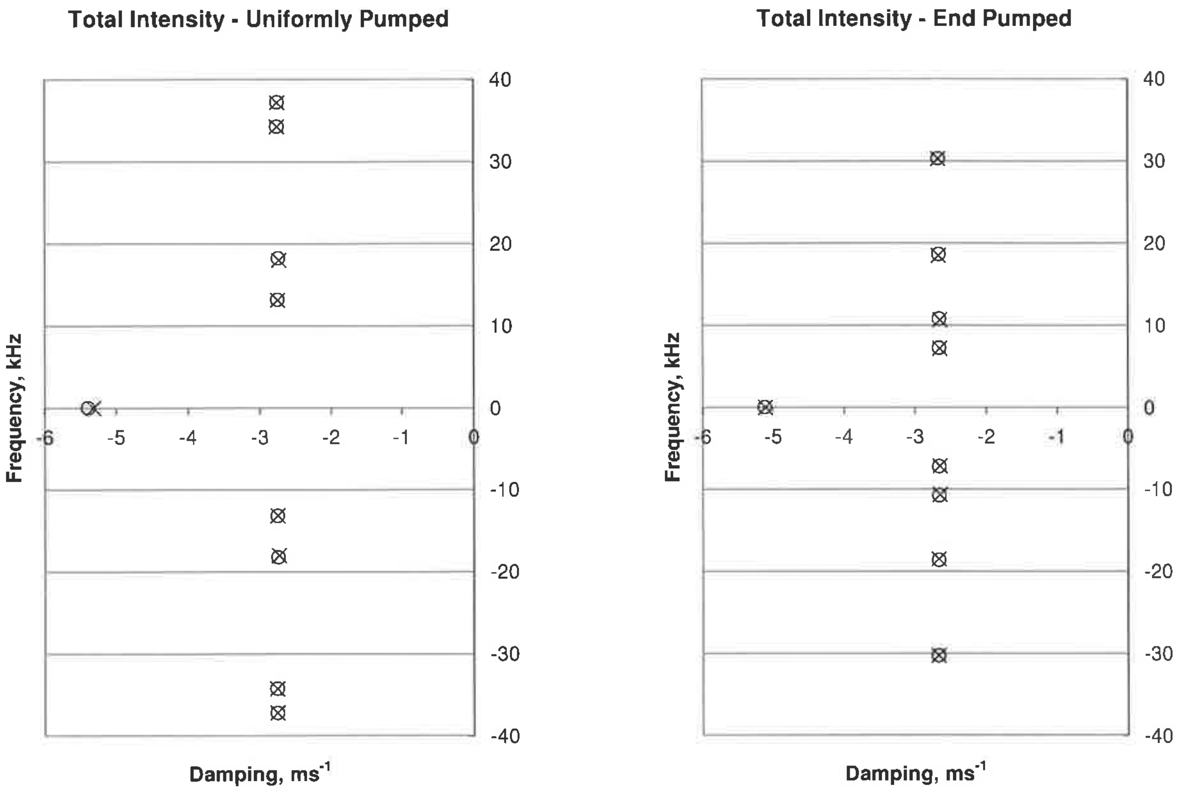

Figure 4-29 Calculated pole-zero diagrams (low-frequency) for the total intensity

Before interpreting the pole-zero diagrams, we would like to illustrate the relationship between them and the frequency response plots, along the lines suggested in section 4.3.2 (see the graphical interpretation presented in Figure 4-2 and Figure 4-3). If we choose as an example the first longitudinal mode, we see that the magnitude of the experimental frequency response shown in Figure 4-18 starts with a minimum at about 10 kHz, followed by a maximum at 13.2 kHz, another minimum at 17.8 kHz and another maximum at 18.8 kHz. This agrees quite well with the pattern existent in the experimental pole-zero diagram of Figure 4-24: a zero at 10 kHz, a pole at 13.2 kHz, another zero at 18 kHz and another pole at 18.6 kHz. We note that the zero at 18 kHz is quite close to the pole at 18.6 kHz, so the corresponding dip and peak are quite shallow compared to the dip and the peak corresponding to the zero at 10 kHz and pole at 13.2 kHz, which are further apart. Another element worth noting is the fact that the maximum around 25 kHz is quite broad, especially its right hand side. The pole-zero diagram explains the broadness of the maximum through the fact that the pole (24.2 kHz) responsible for it is further away from the imaginary axis (more damping). The asymmetry of the maximum is explained by the fact that the pole is further apart from the zero at higher frequency (32.8 kHz) than the zero at lower frequency (22.6 kHz). These considerations apply to all pole-zero diagrams, including those for the calculated transfer functions.

It should be noted that the vertical axis displays the frequency and not the pulsation ω; therefore, estimating distances in the complex plane would require all vertical coordinates to be multiplied by 2π. This means that our pole-zero diagrams are expanded in the horizontal direction and features apparently close together in vertical direction are actually further apart.

We now attempt to explain some of the transfer functions features mentioned in the previous section, using the pole-zero diagrams. The most remarkable of them is the manifestation of antiphase dynamics – the almost featureless response of the total intensity to low frequency modulation, compared to that of the individual longitudinal modes. Given the lack of a pole-zero diagram for the experimental transfer function of the total intensity, we will only use those for the calculated transfer functions. Both models show a striking difference between the pole-zero diagrams for the individual modes (shown in Figure 4-24 to Figure 4-28) and those for the total intensity (shown in Figure 4-29): the zeros of the total intensity diagram are almost perfectly overlapped with the poles, while for the individual modes the overlap is rather infrequent. As mentioned in section 4.3.2, when a zero of the transfer function coincides with a pole the resonance at the pole frequency disappears. Therefore, antiphase dynamics is nothing more than an effect of the pole-zero cancellation; in the absence of analytic calculations we still do not know why it happens, but at least we do know how it happens.

Pole-zero cancellations also explain why some individual longitudinal modes do not respond to certain resonant frequencies. For example, the experimental measurements for the longitudinal mode 5 (see Figure 4-22) show only a couple of peaks at 13.3 kHz and 34.6 kHz. Looking at the corresponding pole-zero diagram (Figure 4-28), we observe that two zeros nearly coincide with the poles at 18.5 kHz and 25.1 kHz, quenching their response. Similar behaviour can be observed both in other experimental measurements and in numeric calculations.

As all zeros of the transfer functions are concentrated in the low frequency part of the spectrum, the pair of poles corresponding to the relaxation oscillations does not have any zeros nearby that could reduce their response. Therefore, all the individual modes and the total intensity have a strong response at this frequency.

As mentioned in the previous section, for some longitudinal modes in the end pumped model and in the experiment the total phase change can exceed 180°. We now correlate the phase of these frequency response plots with the corresponding pole-zero diagrams. Thus, for the end pumped model we compare Figure 4-18 with Figure 4-24 (longitudinal mode 1) and Figure 4-22 with Figure 4-28 (longitudinal mode 5). For the experimental measurements we need to compare Figure 4-19 with Figure 4-25 (longitudinal mode 2) and Figure 4-20 with Figure 4-26 (longitudinal mode 3). All the pole-zero diagrams mentioned above (and none of the others) share one characteristic: they have zeros in the right-hand side of the complex frequency plane. Thus, we conclude that the zeros with positive real parts are responsible for the larger total phase change.

Transfer functions with all the zeros in the left-hand side of the complex frequency plane are called minimum-phase transfer functions, while those with some zeros in the right-hand side of the complex plane are called nonminimum-phase transfer functions. Both types of functions are stable. If all the zeros with positive real parts of a nonminimum-phase transfer function are reflected about the imaginary axis, the magnitude of the frequency response plot remains the same, but the total phase change becomes smaller.

A more detailed discussion of both types of transfer functions is presented in [61]. The graphical methods presented there can be applied to the arrangement of poles and zeros that we have for the end pumped and experimental systems. It can be shown that, as the frequency varies from 0 to ∞, the modes with zeros in the right-hand side of the complex plane will exhibit a total phase change of 540°, compared to 180° for those with all zeros in the left-hand side of the complex plane.

The existence of nonminimum-phase transfer functions for some modes is important if the laser is included in a feedback loop. As these transfer functions exhibit more signal delay compared to the minimum-phase ones, the stability of the loop is more difficult to achieve.

The pole-zero representation of the transfer functions in the complex frequency plane permits a visual interpretation of antiphase dynamics and a qualitative account of this and other features. For a more quantitative account, we turn to the pole-residue representation of the transfer functions.

4.7.3 Comparison of Results in Pole-Residue Form

Expressing the theoretical transfer functions in partial fraction expansions (4-13) requires the calculation of the eigen-vectors of the Jacobian matrix **A**. Once these are obtained and assembled in the matrix **V** according to (4-14), the input distribution vector **e** and the output distribution vectors $\mathbf{h}_i$ and $\mathbf{h}_t$ are found using (4-16) and (4-17), respectively. With these vectors, the residues are calculated according to (4-18), each of them being the product of the corresponding elements of the input and output vectors: $r_i = e_i h_i$. For the experimental transfer functions, the conversion from pole-zero to pole-residue was performed with the routines of the HP35670A dynamic signal analyser.

It was pointed out in section 4.3.2 that the poles (which are the eigen-values λ_i of the stability matrix **A**) are the same for the whole system. Therefore, both total intensity and individual longitudinal modes will have the same resonant frequencies. However, the strength of the response at each resonant frequency is determined by the magnitude of the corresponding residue and they are different for each longitudinal mode (or total intensity). What is more important is the fact that the residues, which are complex numbers, do not show only the strength of the response but also its phase. Comparing the phases of the residues pertaining to the individual longitudinal modes allows us to identify how they combine in the total intensity and thus the type of antiphase.

We calculated and present in Table 4-7 and Table 4-8 the magnitude and the phase of the residues for the uniformly pumped and the end pumped models. Because in both tables the phases are close to either 90° or to -90°, the magnitude is essentially equal to the imaginary component of the residue. It also means that for each collective mode the contributions of the longitudinal modes are either up (+90°) or down (-90°). This shows very clearly that, except for the highest frequency, the phases of the coupled oscillators (the intensities of the longitudinal modes) are clustered and the two clusters are 180° out of phase. As the resultant amplitudes of the clusters are comparable, when they are algebraically added they cancel almost completely, explaining why the total intensity does not have resonant response to modulation in this frequency region. Therefore, antiphase dynamics is nothing more than an effect of residue clusters cancelling at each of the low frequency normal modes. This interpretation for antiphase dynamics complements the pole-zero cancellation presented in the previous section.

Table 4-7 Residues for the uniformly pumped model

Freq.	13.13 kHz		18.01 kHz		34.24 kHz		37.15 kHz		96.08 kHz	
Mode	Mag.	Phase	Mag.	Phase	Mag.	Phase	Mag.	Phase	Mag.	Phase
1	0.128	90.0	0.674	89.9	0.023	90.0	1.247	90.0	22.50	-90.0
2	0.135	89.9	0.735	89.8	0.216	90.0	0.727	-90.0	17.48	-90.0
3	0.136	89.9	0.750	89.8	0.239	-90.0	0.537	-90.0	16.65	-90.0
4	0.381	89.8	1.953	-90.1	0.001	-90.1	0.025	-90.1	3.44	-90.0
5	0.840	-90.1	0.489	-90.2	0.001	-90.1	0.014	-90.1	2.05	-90.0
T	0.061	-89.4	0.283	-89.7	0.003	-89.8	0.057	-89.8	62.13	-90.0

Table 4-8 Residues for the end pumped model

Freq.	7.16 kHz		10.65 kHz		18.48 kHz		30.28 kHz		96.07 kHz	
Mode	Mag.	Phase	Mag.	Phase	Mag.	Phase	Mag.	Phase	Mag.	Phase
1	0.194	-90.2	0.625	-90.4	2.480	89.8	0.002	89.9	15.45	-90.0
2	0.075	90.4	1.510	89.7	0.923	-90.2	0.047	-90.1	17.19	-90.0
3	0.825	89.7	0.508	89.5	1.189	-90.2	0.049	89.9	17.13	-90.0
4	0.172	89.1	1.454	-90.2	0.400	-90.2	0.006	-90.1	2.49	-90.0
5	0.954	-90.2	0.063	-90.9	0.144	-90.2	0.002	89.9	1.04	-90.0
T	0.075	-88.8	0.124	-89.3	0.176	-90.3	0.000	-88.7	53.30	-90.0

The residues of the experimental transfer functions are presented in Table 4-9 and they deserve a few comments. The first comment refers to the last row of the table, labelled 'T' (for total intensity). As mentioned in section 4.7.2, there is no fit for the total intensity, so we do not have residues either; however, we created a 'total intensity' by adding the complex residues of the individual modes and calculating the magnitude and the phase of the complex sum. While this row shows evidence of antiphase, the cancellation is not as good as the measured frequency response plot in Figure 4-23 would indicate (for example the resonance at 18.6 kHz is not visible in the plot, but quite substantial in the table).

Table 4-9 Residues of the experimental transfer functions

Freq.	13.26 kHz		18.60 kHz		25.50 kHz		34.60 kHz		96.06 kHz	
Mode	Mag.	Phase	Mag.	Phase	Mag.	Phase	Mag.	Phase	Mag.	Phase
1	0.719	89.7	0.206	80.8	0.698	106.5	1.365	91.4	19.97	-91.4
2	0.681	-89.1	0.108	-97.2	1.775	93.0	0.239	-86.3	12.72	-88.3
3	0.194	-84.0	0.073	-110.4	1.492	-91.9	0.738	95.5	12.07	-84.4
4	0.502	-94.1	0.177	87.5	1.081	-91.8	0.933	-92.9	12.04	-89.3
5	0.989	88.2	0.053	25.3	0.142	82.9	1.139	-91.1	11.97	-84.6
T	0.334	84.9	0.232	77.7	0.356	178.2	0.263	-126.8	68.69	-88.0

Another comment refers to the phase of the residues – they have been corrected with the value of the phase shifts introduced by the measurement system, which was shown in Figure 4-14. At the same time, the magnitudes have been scaled to give values comparable with those in the previous tables, for ease of representation. Finally, the residues for the relaxation oscillations frequency (96.06 kHz) should be considered with caution, as they are fitted from a region quite far from the location of the pole.

The tables of numbers presented above are useful, but they do not give a good 'feel' for the way the residues combine to achieve antiphase dynamics. Therefore, the information in the columns of the tables (each corresponding to a collective mode) is also presented in graphical form in the Figure 4-30 to Figure 4-34. In the previous two sections we presented in each figure the transfer function of an individual longitudinal mode or that of the total intensity (as a function of frequency or as a diagram in the complex frequency plane). In contrast, in this section we illustrate in each figure one of the normal modes of oscillation of the system (identified by its frequency). For each of them we display the residues of the transfer functions corresponding to individual longitudinal modes and to total intensity. For example, in Figure 4-30 we present the residues corresponding to the lowest resonant frequency. The residues of the theoretical transfer functions are either 'up' or 'down', so we can represent them in charts by displaying the magnitude with the appropriate sign (which explains the labelling of the vertical axis). For the experimental transfer function, most of the phase angles are sufficiently close to +90° or -90° to justify the hypothesis of clustering, so we consider the departures to be experimental errors. However, in addition to the 'up-down' chart (which shows the proper magnitude forced either up or down), we also present the residues with magnitude and orientation in the round diagram titled 'Residues of the 13.3 kHz Pole'. In this diagram the residues are scaled to the largest of them, while the total intensity is not represented.

The 'up-down' charts are useful for understanding the make-up of the clusters and for relative comparisons between the collective modes, while the round diagrams give a good indication of the degree of clustering in the experimental data. For example, the round diagram in Figure 4-31 shows one residue (corresponding to the longitudinal mode 5) that is neither 'up', nor 'down'. However, if we look at the 'up-down' chart on the left of this diagram, we see that the residues are quite small (compared with those for the other collective modes). It is plausible then that the fitting errors for these residues are greater and that the phases are less clustered.

Before interpreting the results, we would like to draw attention to the correspondence between the intensities of the longitudinal modes (from Table 4-2 and Table 4-4) and the magnitude of the residues corresponding to the collective mode of the highest frequency (the second to last column of Table 4-7 and Table 4-8, respectively). The ratios of residue magnitude to modal intensity are about the same (within ±8%) for both models. This is intuitively plausible, as the relaxation oscillations resonance is far from the low frequency zeros produced by the details of the mode-to-mode interaction.

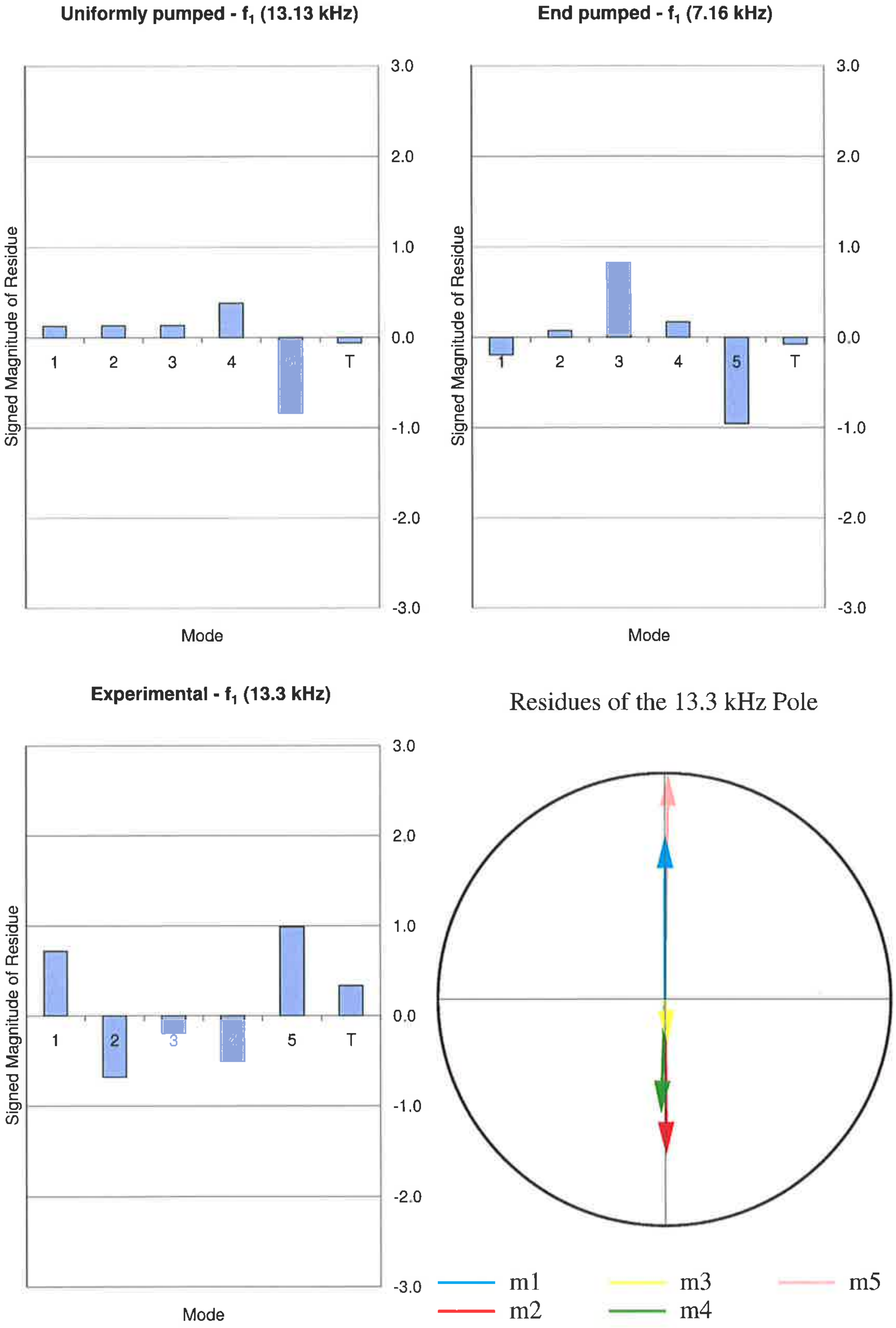

Figure 4-30 Calculated and measured residues for the collective mode I

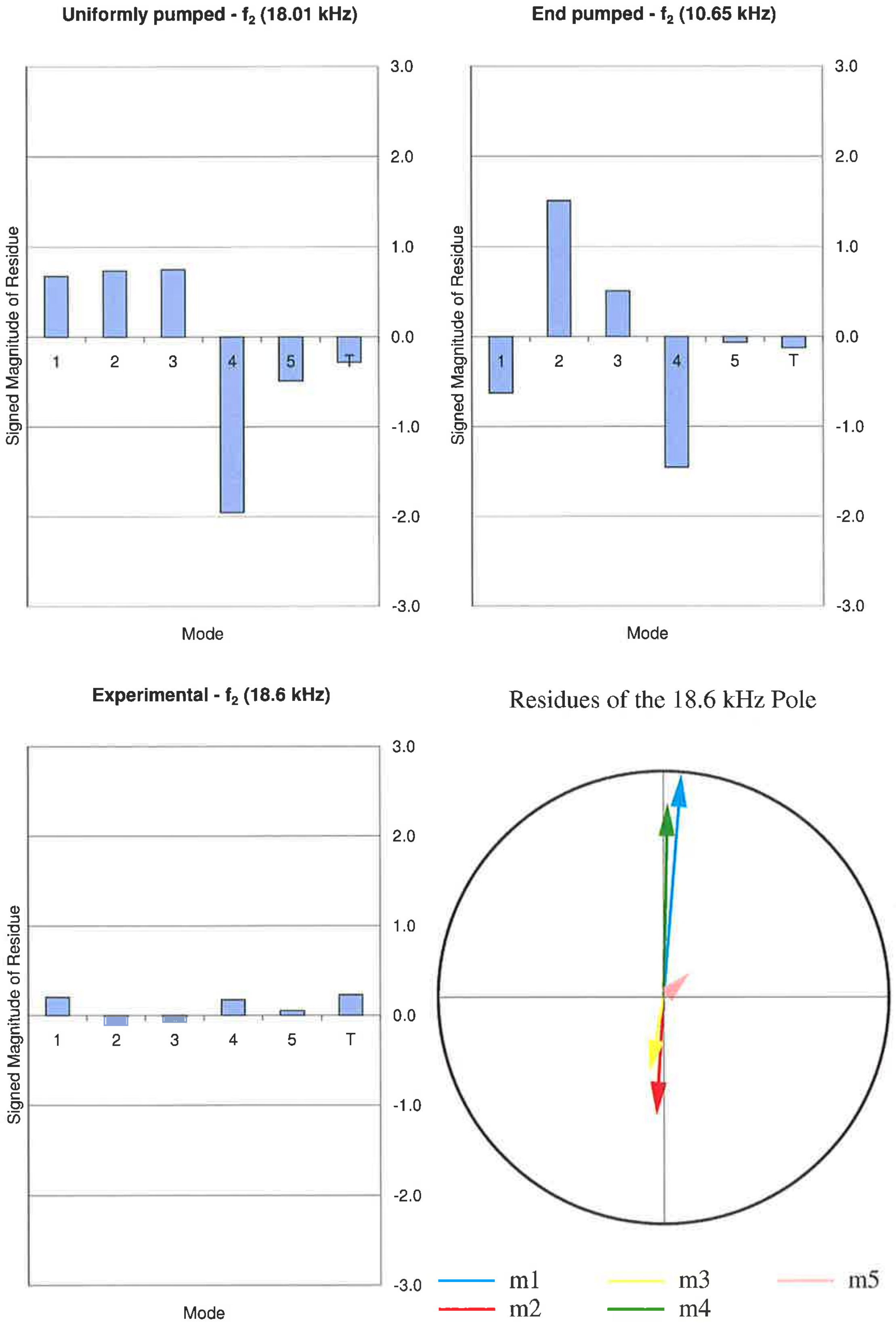

Figure 4-31 Calculated and measured residues for the collective mode II

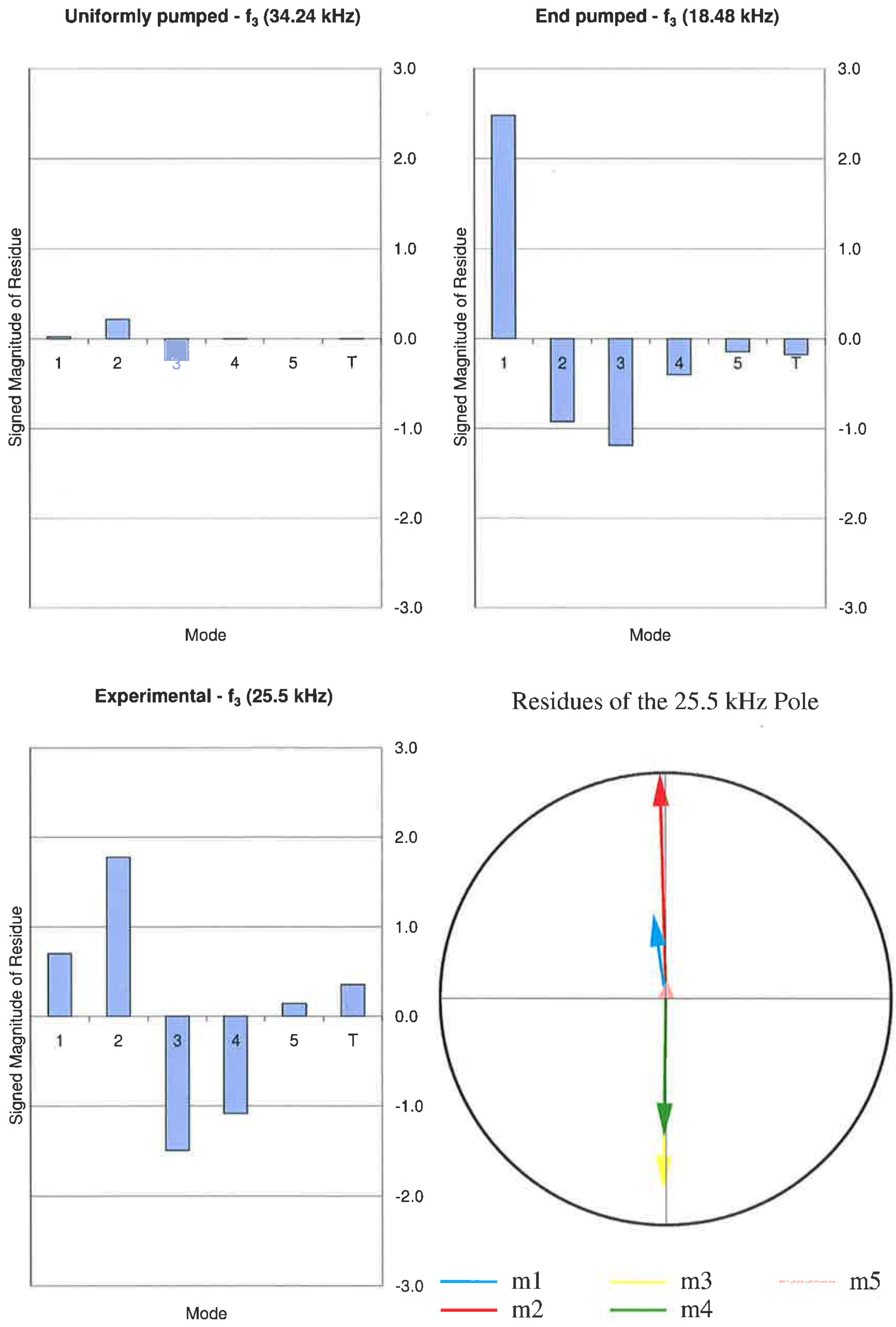
Uniformly pumped - f_3 (34.24 kHz)

End pumped - f_3 (18.48 kHz)

Experimental - f_3 (25.5 kHz)

Residues of the 25.5 kHz Pole

Figure 4-32 Calculated and measured residues for the collective mode III

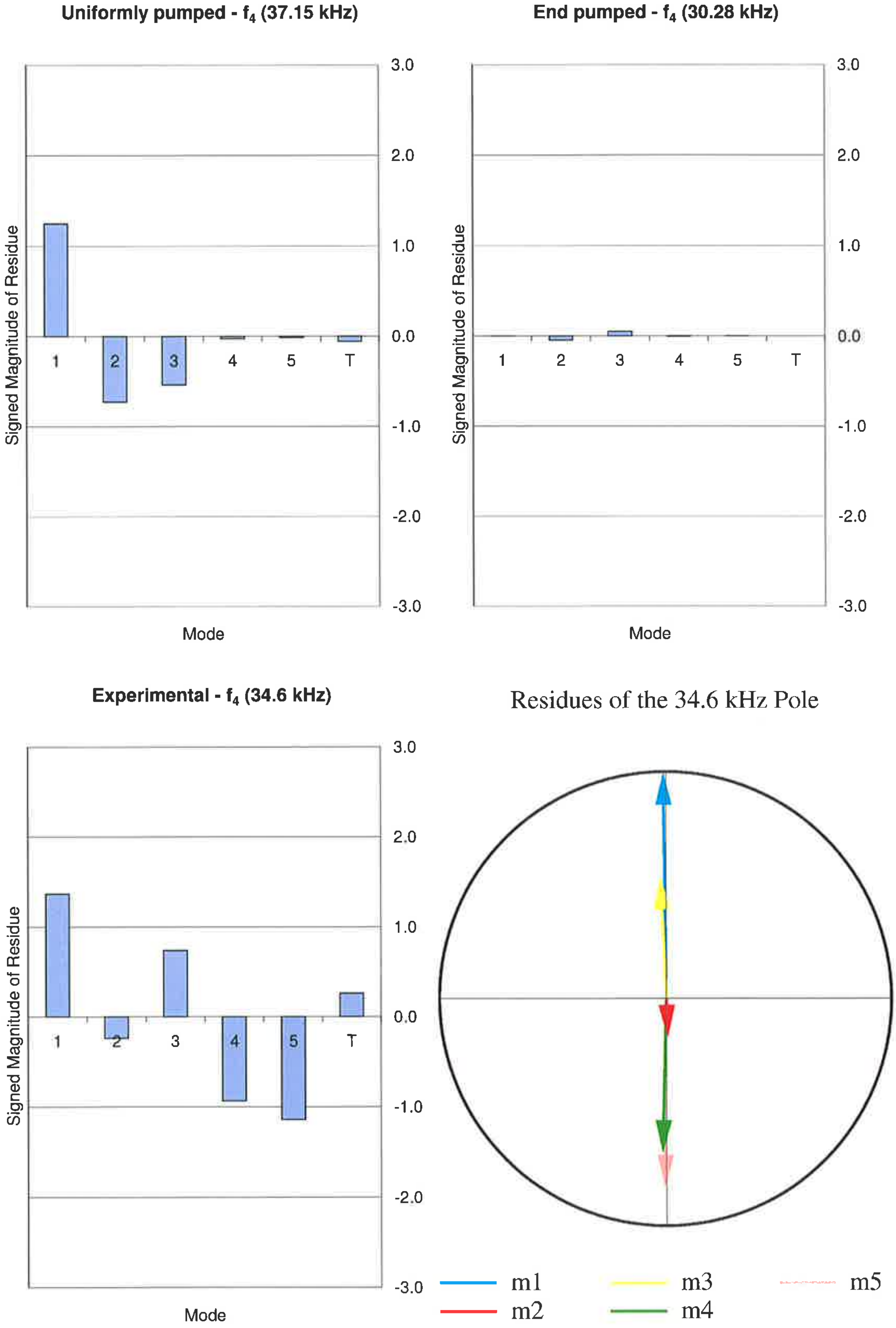

Figure 4-33 Calculated and measured residues for the collective mode IV

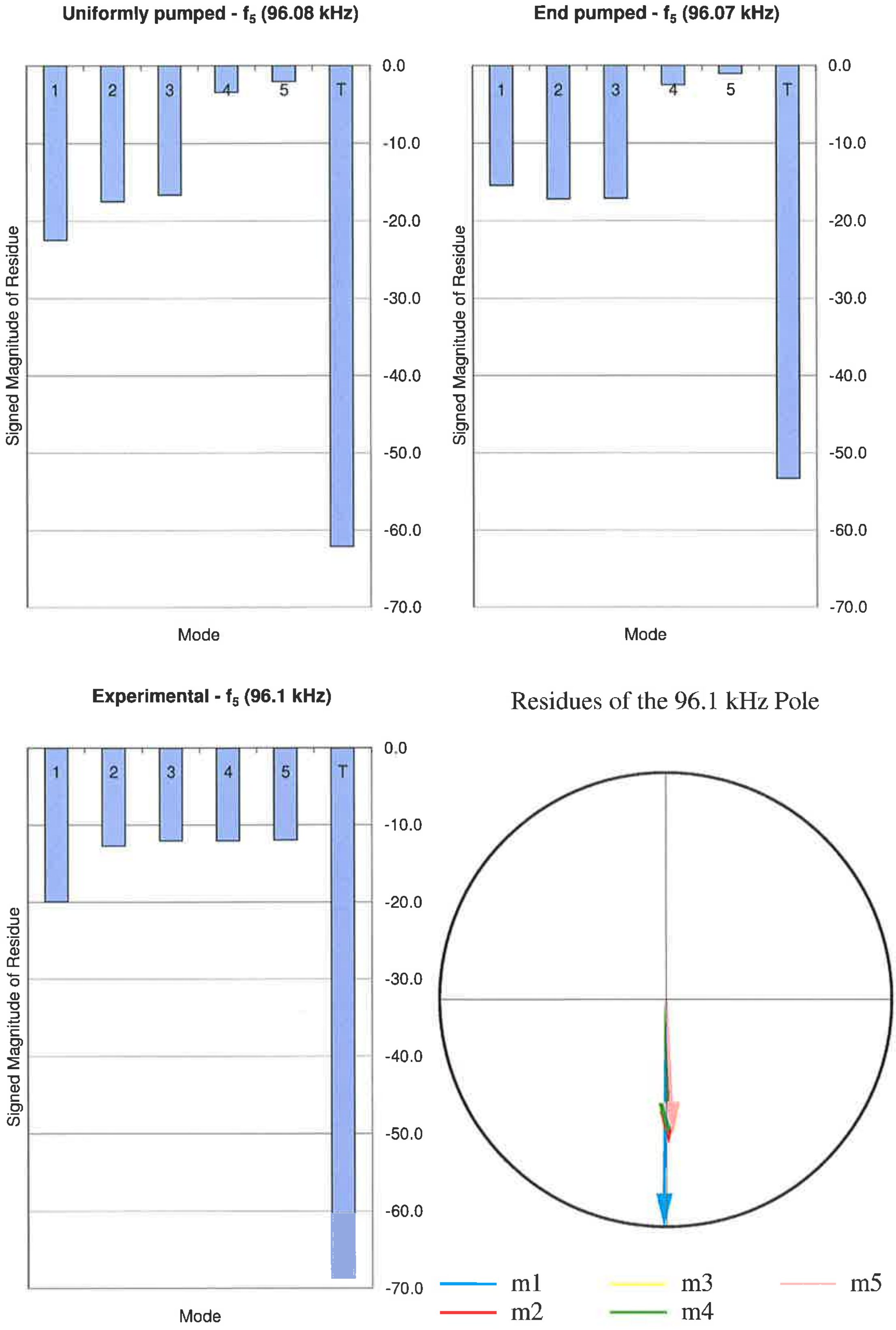

Figure 4-34 Calculated and measured residues for the collective mode V

If we assume that the above-mentioned proportionality also holds for the experiment, then Figure 4-34 indicates that there are discrepancies between models and experiment. The uniformly pumped model has normal mode ordering (the first mode is the most intense, followed by the second which is just a bit stronger than the third etc). With the selected value for q (the dimensionless absorption parameter), the end pumped model exhibits abnormal mode ordering, as described in the previous chapter (the intensity of the first mode is less than that of the second and the third etc). The residues suggest that the experiment is neither of these: the first mode is stronger then the other modes (as in the case of uniform pump), but those other four modes are of almost equal intensity (a situation more likely to occur for end pump). We cautioned before about the reliability of the residues corresponding to the 96 kHz pole, so these comments are rather speculative. However, they highlight the fact that quantitative agreement is not yet accessible and with the current models and limited knowledge of laser parameters only a qualitative description can be contemplated.

If we settle for qualitative agreement between theory and experiment, then the first and the most important conclusion that can be drawn from Figure 4-30 to Figure 4-33 is that for both experiment and theory the residues demonstrate clearly the existence of antiphase dynamics. They also identify the type of antiphase dynamics: clustering and not staggered phase. The residues correctly recognize the in phasing corresponding to the collective mode with the highest frequency (Figure 4-34).

A second conclusion that can be extracted from the residue tables and figures is that, for a subtle detail, the end pumped model seems to be closer to the experiment. The detail in question is related to the way the composition of the clusters changes as we go from one normal mode to the other. If we consider the 'up-down' charts for the uniformly pumped model, at f_1 the residues of all modes but mode 5 are up (Figure 4-30). At f_2 the residues of all modes but 4 and 5 are up (Figure 4-31). As we go higher in frequency, the residues of the modes flip in turn from 'up' to 'down' until at f_5 all the residues are 'down' (Figure 4-34). This order of change can be described in Table 4-10, where + means 'up' and – means 'down'. The row at the top identifies the normal modes of the coupled system by their frequencies and the left column identifies the longitudinal modes of the laser cavity.

Table 4-10 Phase ordering for the uniformly pumped model

Mode	f_1	f_2	f_3	f_4	f_5
1	+	+	+	+	–
2	+	+	+	–	–
3	+	+	–	–	–
4	+	–	–	–	–
5	–	–	–	–	–

This type of ordering has been described in several articles using the Tang Statz deMars equations and it appears to be a characteristic of the uniformly pumped model [47], [59].

Neither the end pumped model (Table 4-11) nor the experimental data (Table 4-12) show this rigid type of ordering. They are different from each other and do not seem to show any regularity in the make up of the clustering. It could be assumed that the clusters combine in a way that minimises the response of the total intensity, but this remains to be proven.

Table 4-11 Phase ordering for the end pumped model

Mode	f_1	f_2	f_3	f_4	f_5
1	–	–	+	+	–
2	+	+	–	–	–
3	+	+	–	+	–
4	+	–	–	–	–
5	–	–	–	+	–

Table 4-12 Phase ordering for the experiment

Mode	f_1	f_2	f_3	f_4	f_5
1	+	+	+	+	–
2	–	–	+	–	–
3	–	–	–	+	–
4	–	+	–	–	–
5	+	+	+	–	–

4.8 Conclusions

We have shown that the transfer function method, well known in engineering, can be successfully applied to model the antiphase dynamics of a multimode solid state laser in the small signal regime. It complements the analytic methods and allows us to analyse the behaviour of the modulated laser when the equations and the typical values for parameters are available. The transfer functions can also be measured experimentally, most easily with dedicated equipment (dynamic spectrum analyser or similar). Both the theoretical and the experimental transfer functions can be presented as frequency response plots, pole-zero diagrams or pole-residue plots, each representation offering specific advantages. They permit to identify the normal modes of oscillation of the laser and the relative contributions of the longitudinal modes to the total intensity as functions of frequency. The transfer functions have been used to describe the response of the lasers to modulation, but to our knowledge [8] is the first time when the phase information was used to get insight into the antiphase dynamics.

Using the transfer functions we compared the experimental data with the two models introduced in Chapter 3. We conclude that while neither model can match the measurements quantitatively, the end pumped model has a few features in common with the experiment that the model for uniform pump is lacking. These features include total phase change of more than 180° for some modes, zeros in the right-hand side of the complex frequency plane for those modes and the lack of rigid ordering for the phase clustering.

For the experimental measurements the temperature drift and the noise were the most significant problems. Of these two, the noise can be converted from adversary into ally, as it will be shown in the next chapter.

Chapter 5 Noise

5.1 Introduction

The study of noise in solid state lasers is important for both theoretical and practical reasons. From a theoretical point of view, the effect of the noise on the multimode laser is interesting because the system is non-linear and exhibits antiphase dynamics. The theoretical predictions can be compared relatively easily with the experiment and the noise becomes a tool for probing the dynamics of the system rather then being a nuisance. From a practical point of view, it is desirable to be able to construct lasers that are as quiet as possible. In some experiments output power is more important than a high degree of coherence, so a multimode laser can be a good choice; in other experiments, multimode operation is a mandatory requirement. In all these cases, having a model for the noise and the way it affects the operation of the multimode laser is an essential prerequisite for controlling it.

There are several possible approaches to the experimental investigation of noise in the output of a laser. The simplest is to use a single detector to measure the intensity fluctuations of a selected longitudinal mode or total intensity and transform to the frequency domain with a spectrum analyser. It can be shown [34] that this arrangement yields the spectrum of the intensity correlation superposed on shot noise and internal detector noise. A more complicated approach is that first used by Hanbury Brown and Twiss [65], where the outputs of two detectors are correlated in a linear multiplier and its averaged output directly gives the intensity correlation function. In this case, both the shot noise and the individual detector noise average to zero because they are not correlated between the two detectors.

We employed both approaches, the experimental set-up for the first being very similar to that used for measuring transfer functions, but without modulation. The second set-up was in the spirit of the Hanbury Brown and Twiss arrangement, with the difference that we were mostly interested in the correlation between different longitudinal modes. Another difference, at the technical level, is that instead of using a correlator at the outputs of the two detectors, we employed a dynamic spectrum analyser to calculate the cross-spectrum between the two detectors. We used a Fabry-Perot optical spectrum analyser in front of each detector to select the desired longitudinal mode. This way, we were able to measure either the power spectrum of each mode (by selecting the same mode for both detectors) or cross-spectra between pairs of modes.

The noise measured in the laser output represents the response of the laser to various sources of noise, which can be classified as either internal or external. In this classification the internal noise is the quantum noise that is ultimately attributable to the coupling between the laser system (atoms and fields) and their respective reservoirs. The external noise is the result of fluctuations in the pump power and the parameters of the system (through mechanical vibrations, temperature fluctuations, air currents etc).

In this context we are only concerned with the low frequency fluctuations of modal and total intensities (from zero to a fraction above the relaxation oscillations frequency). It is known that above the threshold the manifestation of the quantum noise is greatly reduced by the non-linear gain saturation. Since we did not take extensive measures to limit the external noise sources, it is quite likely that in the experimental situation they will dominate. Nevertheless, it is instructive to examine the effects and estimate the magnitude of the quantum noise in the total and modal intensities. Another reason for considering quantum noise is that, as far as the numerical modelling is concerned, it can be estimated from the knowledge of system parameters, while the external noise sources are quite difficult to characterise.

We start the discussion about noise with considerations regarding the quantum noise in the single-mode laser without spatial effects. For typical parameter values we compare the statistics of the photon number and intensity in the frequency domain. The reader familiar with the notations and the material presented in [34] and [39] can go directly to the conclusion of section 5.3.3 and then to the following sections. Based on the conclusions of this comparison,we then incorporate noise in the Tang Statz deMars equations and calculate the response of the linearised laser model to different scenarios for the input noise. Because we are interested in the manifestation of antiphase in the noise response of the laser, we need to have more than one longitudinal mode active. We choose three modes, because this is a number of modes that gives a good compromise between complexity and interesting behaviour. We then present the experimental technique for measuring the noise of the laser and make a few comments regarding the similarities and differences between calculations and measurements.

The experimental results presented in this chapter represented only a test of this technique to investigate laser dynamics; further investigations of the laser were carried out by Tim Hill as part of his thesis and the results published in [10] and [11].

5.2 Correlation Functions

The intensity correlation and photon coincidence experiments performed in the 1950's ([65], [66] and many others) have stimulated discussions [67] and the reconsideration of the optical coherence description [68]. The highly coherent output of the masers and lasers required the introduction of the concept of coherent states [69], the quantum mechanical states that are closest to the classical fields [70]. These and other theoretical advances have shown both the similarities and the differences between the quantum and classical treatment of optics. The similarities allowed the use of a number of semi-classical models for laser-like systems, with the accompanying simplifications in calculations, while the differences lead to developments that have no classical equivalent (squeezed states, atom optics, quantum non-demolition measurements etc).

The notion of coherent electro-magnetic field has been extended from the first order correlation function involving the amplitude of the electric field (as in Young's experiment), to an infinite hierarchy of correlation functions [68]:

$$G^{(n)}(\mathbf{r}_1 t_1,\ldots,\mathbf{r}_n t_n;\mathbf{r}_{n+1}t_{n+1},\ldots,\mathbf{r}_{2n}t_{2n})=tr\left(\rho E^{(-)}(\mathbf{r}_1 t_1)\ldots E^{(-)}(\mathbf{r}_n t_n)E^{(+)}(\mathbf{r}_{n+1}t_{n+1})\ldots E^{(+)}(\mathbf{r}_{2n}t_{2n})\right), \tag{5-1}$$

where $tr()$ represents the trace operation, ρ is the density operator, $E^{(-)}(\mathbf{r}t)$ and $E^{(+)}(\mathbf{r}t)$ are the photon creation and destruction operators. For our purposes, the second order correlation function is of interest:

$$G^{(2)}(\mathbf{r}_1 t_1,\mathbf{r}_2 t_2;\mathbf{r}_3 t_3,\mathbf{r}_4 t_4)=tr\left(\rho E^{(-)}(\mathbf{r}_1 t_1)E^{(-)}(\mathbf{r}_2 t_2)E^{(+)}(\mathbf{r}_3 t_4)E^{(+)}(\mathbf{r}_4 t_4)\right) \tag{5-2}$$

and, since we are measuring the correlation between separate intensity detectors, we restrict ourselves to the subset of the form:

$$G_{\text{int}}^{(2)}(\mathbf{r}_1 t_1,\mathbf{r}_2 t_2;\mathbf{r}_2 t_2,\mathbf{r}_1 t_1)=tr\left(\rho E^{(-)}(\mathbf{r}_1 t_1)E^{(-)}(\mathbf{r}_2 t_2)E^{(+)}(\mathbf{r}_2 t_2)E^{(+)}(\mathbf{r}_1 t_1)\right). \tag{5-3}$$

We assume that our experimental system is stationary and ergodic, so the ensemble average (5-3) can be replaced by a time average:

$$C_I(\tau)=\langle I_1(t+\tau)I_2(t)\rangle_t\,. \tag{5-4}$$

Because we are interested in the correlation of the noise and not in that of the DC terms present in (5-4), we subtract the value of (5-4) in the limit of infinitely long correlation times:

$$\Delta C_I(\tau)=C_I(\tau)-\langle I_1(t)\rangle_t\langle I_2(t)\rangle_t\,. \tag{5-5}$$

The Fourier transform of (5-5) translates the correlation information in the frequency domain, which is easier to interpret in terms of resonant frequencies and phase relationships:

$$S_I(\omega)=\int_{-\infty}^{+\infty}\Delta C_I(\tau)\mathrm{e}^{i\omega\tau}\,d\tau\,. \tag{5-6}$$

When a certain longitudinal mode is measured with a single square law detector, the autocorrelation function obtained corresponds to the following operator ordering [34], [39], [70]:

$$F(\mathbf{r},t_1,t_2)=tr\left(\rho E^{(-)}(\mathbf{r}t_1)E^{(+)}(\mathbf{r}t_1)E^{(-)}(\mathbf{r}t_2)E^{(+)}(\mathbf{r}t_2)\right), \tag{5-7}$$

which can be estimated, under the above mentioned conditions, from the time average:

$$C_P(\tau)=\langle P(t+\tau)P(t)\rangle_t\,. \tag{5-8}$$

As above, we subtract the DC terms to obtain:

$$\Delta C_P(\tau)=C_P(\tau)-\langle P(t)\rangle_t^2 \tag{5-9}$$

and take the Fourier transform to obtain the power spectrum:

$$S_P(\omega)=\int_{-\infty}^{+\infty}\Delta C_P(\tau)\mathrm{e}^{i\omega\tau}\,d\tau\,.$$

The operators $E^{(-)}(\mathbf{r}t)$ and $E^{(+)}(\mathbf{r}t)$ do not commute, so there is a difference between the correlation functions (5-3) and (5-7) or (5-5) and (5-9). The variances of the photon number and the intensity differ by:

$$\Delta C_P(0)-\Delta C_I(0)=\langle P\rangle_t\,, \tag{5-10}$$

which confirms that single detector measurements have superposed shot noise. In the following section we review the application of these concepts to the simpler case of a single-mode laser.

From the definitions (5-4), (5-8) of the autocorrelation functions it follows that the variance of the fluctuations is equal to the autocorrelation evaluated at zero time delay. This value can be in turn related to the integral of the power spectrum over all frequencies:

$$\langle \Delta I^2 \rangle = \Delta C_I(0) = \frac{1}{2\pi}\int_{-\infty}^{+\infty} S_I(\omega)d\omega$$

$$\langle \Delta P^2 \rangle = \Delta C_P(0) = \frac{1}{2\pi}\int_{-\infty}^{+\infty} S_P(\omega)d\omega.$$

(5-11)

5.3 Noise in the Single-Mode Laser without Spatial Hole Burning

In Chapter 3 we introduced the Langevin rate equations (3-1) and (3-2) for a homogeneously broadened, four level, single-mode laser without spatial hole burning. The previously discarded noise terms are now considered and we discuss the results obtained in [34] and [39] for the correlation functions and the associated power spectra due to quantum noise. McCumber based his work on the method developed in [71], while M. Lax applied previous results [72] to the situation where the atomic polarisation could be adiabatically eliminated. In [73], which provides proof for a few results used in [39], the density operator was associated with a classical function obeying a Fokker-Planck equation. This latter equation is used to obtain the drift vectors and the diffusion constants of the Langevin equations in both representations (photon number or intensity). It turns out that in either representation the drift vectors are the same (if one identifies the photon number with the intensity $P \equiv I$), but the diffusion constants are different [39].

5.3.1 Langevin Rate Equations in the (*N*, *P*) Representation

The rate equations mentioned above were given in the population difference (*N*) and photon number (*P*) representation. We repeat them below for convenience, with the added difference that the random forcing terms (the noise sources) have subscripts indicating the representation:

$$\frac{\mathrm{d}N_2(t)}{\mathrm{d}t} = W(t) - \Gamma_2 N_2(t) - \pi[1 + P(t)]N_2(t) + r_P(t)$$

(5-12)

$$\frac{\mathrm{d}P(t)}{\mathrm{d}t} = \pi[1 + P(t)]N(t) - \gamma P(t) + s_P(t).$$

(5-13)

The following parameters are as defined in both [34] and [39] and used to simplify the subsequent formulae:

$$\overline{\Gamma}_2 = \Gamma_2 + \pi(1 + \overline{P}),\ \overline{\gamma} = \gamma - \pi\overline{N}_2 = \frac{\gamma}{1 + \overline{P}}.$$

(5-14)

The diffusion constants are given by:

$$2D_{NN} = \overline{W} + \Gamma_2\overline{N}_2 + \pi(1 + \overline{P})\overline{N}_2 = \Delta_{RR}'$$
$$2D_{NP} = 2D_{PN} = -\pi(1 + \overline{P})\overline{N}_2 = \Delta_{RS}'$$
$$2D_{PP} = \pi(1 + \overline{P})\overline{N}_2 + \gamma\overline{P} = \Delta_{SS}'.$$

(5-15)

The $2D$ are the notations used by M. Lax, while the Δ' are those used by McCumber and, in this representation, they agree with each other. Linearising the rate equations about the steady state, applying the Fourier transform and solving for the power spectrum of the photon number fluctuations gives:

$$S_P(\omega)=\frac{\pi^2\left(1+\bar{P}\right)^2(2D_{NN})+2\pi\left(1+\bar{P}\right)\bar{\Gamma}_2(2D_{NP})+\left(\bar{\Gamma}_2^2+\omega^2\right)(2D_{PP})}{\left(\overline{\gamma\Gamma}_2+\pi\overline{\gamma P}-\omega^2\right)^2+\omega^2\left(\bar{\gamma}+\bar{\Gamma}_2\right)^2}. \tag{5-16}$$

The power spectrum of the laser can be seen as the response of the system to white noise sources whose strengths are equal to the diffusion constants (5-15). These diffusion constants are in fact the power spectra of the δ-correlated functions $r_P(t)$ and $s_P(t)$ and is important to note that they can be written by inspection from the rate equations (5-12) and (5-13). For example, the power spectrum $2D_{NN}$ of $r_P(t)$ is the sum of the absolute values of all the terms on the right hand side of (5-12), while the cross-spectrum of $r_P(t)$ and $s_P(t)$ is given by the terms which are common and with opposite signs in (5-12) and (5-13).

In this representation, the noise can be viewed as being generated by the discrete variations of the number of inverted atoms and photons in the cavity [34], [74]. Every time an inverted atom is created through the action of the pump or an inverted atom decays spontaneously or under the influence of the electric field in the cavity, noise is generated in the equation for $N_2(t)$ – the term $r_P(t)$in the equation (5-12). Similarly, every time a photon is created through stimulated emission from an inverted atom or lost at the end-mirrors or through absorption in the cavity, noise is generated in the corresponding equation for $P(t)$ – the term $s_P(t)$ in the equation (5-13).

Substitution of (5-15) into (5-16) gives:

$$S_P(\omega)=\frac{2\overline{\gamma P}\left(\bar{\Gamma}_2^2+\omega^2\right)}{\left(\overline{\gamma\Gamma}_2+\pi\overline{\gamma P}-\omega^2\right)^2+\omega^2\left(\bar{\gamma}+\bar{\Gamma}_2\right)^2} \tag{5-17}$$

and the variance of the fluctuations is:

$$\left\langle\Delta P^2\right\rangle=\Delta C_P(0)=\frac{\overline{\gamma P}\left[\bar{\Gamma}_2\left(\bar{\gamma}+\bar{\Gamma}_2\right)+\pi\overline{\gamma P}\right]}{\left(\bar{\gamma}+\bar{\Gamma}_2\right)\left(\overline{\gamma\Gamma}_2+\pi\overline{\gamma P}\right)}. \tag{5-18}$$

5.3.2 Langevin Rate Equations in the (*N*, *I*) Representation

The rate equations in the population difference (*N*) and intensity (*I*) representation are the same as those in the (*N*, *P*) representation, if we replace *P* with *I*:

$$\frac{\mathrm{d}N_2(t)}{\mathrm{d}t}=W(t)-\Gamma_2N_2(t)-\pi[1+I(t)]N_2(t)+r_I(t) \tag{5-19}$$

$$\frac{\mathrm{d}I(t)}{\mathrm{d}t}=\pi[1+I(t)]N(t)-\gamma I(t)+s_I(t). \tag{5-20}$$

The diffusion constants are given in [39] by:

$$\begin{aligned} 2D_{NN} &= \overline{W} + \Gamma_2 \overline{N}_2 + \pi\left(1+\bar{I}\right)\overline{N}_2 \\ 2D_{NI} &= 2D_{IN} = -\pi\left(1+2\bar{I}\right)\overline{N}_2 \\ 2D_{II} &= 2\pi\overline{N}_2\bar{I}\,. \end{aligned} \tag{5-21}$$

while in [34] they are given by:

$$\begin{aligned} \Delta_{RR} &= 0 \\ \Delta_{RS} &= \Delta_{SR} = -\pi\overline{N}_2\bar{I} \\ \Delta_{SS} &= 2\pi\overline{N}_2\bar{I}\,. \end{aligned} \tag{5-22}$$

In the (*N*, *I*) representation the variances (5-21) or (5-22) of the noise sources cannot be given a simple physical interpretation as was the case for the (*N*, *P*) representation. There are ways to transform the diffusion coefficients from one representation to the other [75], but the calculations are rather cumbersome.

Because the drift vectors in the Langevin equations (5-19) and (5-20) are the same as in (5-12) and (5-13), the power spectrum is given by the same formula as (5-16):

$$S_I(\omega) = \frac{\pi^2\left(1+\bar{I}\right)^2(2D_{NN}) + 2\pi\left(1+\bar{I}\right)\overline{\Gamma}_2(2D_{NI}) + \left(\overline{\Gamma}_2^2+\omega^2\right)(2D_{II})}{\left(\bar{\gamma}\overline{\Gamma}_2 + \pi\bar{\gamma}\bar{I} - \omega^2\right)^2 + \omega^2\left(\bar{\gamma}+\overline{\Gamma}_2\right)^2}. \tag{5-23}$$

It is interesting to observe that substituting either (5-21) or (5-22) in (5-23) leads to the same result:

$$S_I(\omega) = \frac{2\bar{\gamma}\bar{I}\left(\overline{\Gamma}_2^2+\omega^2\right) - 2\pi\bar{\gamma}\overline{\Gamma}_2\bar{I}^2}{\left(\bar{\gamma}\overline{\Gamma}_2 + \pi\bar{\gamma}\bar{I} - \omega^2\right)^2 + \omega^2\left(\bar{\gamma}+\overline{\Gamma}_2\right)^2} \tag{5-24}$$

and the variance of the fluctuations is:

$$\left\langle \Delta I^2 \right\rangle = \Delta C_I(0) = \frac{\bar{\gamma}\bar{I}^2\left[\overline{\Gamma}_2\left(\bar{\gamma}+\Gamma_2\right) + \pi\bar{\gamma}\bar{I}\right]}{\left(\bar{\gamma}+\overline{\Gamma}_2\right)\left(\bar{\gamma}\overline{\Gamma}_2 + \pi\bar{\gamma}\bar{I}\right)}. \tag{5-25}$$

5.3.3 Comparison Between the Photon Number and Intensity Representations

We now compare the two representations in terms of power spectra and variances using parameters specific to our laser (see section 3.2.2). We consider three situations: under, at and above threshold, the corresponding steady state values being indicated in Table 5-1. Also included in the table are the variances of the photon number (5-18) and intensity fluctuations(5-25), representing the integrated power spectra, as indicated in (5-11).

It should be mentioned that the quasi-linear approximations used in both [34] and [39] are not justified in the vicinity of the threshold. However, the approximate results are not too far from the exact calculations, so we include them to facilitate the comparisons. In fact, we are mostly interested in the case where the laser is above the threshold, because we need to know how different are the power spectra of the photon number and intensity.

Table 5-1 Single-mode laser characteristics at three power levels

Variable	Under threshold	At threshold	Above threshold
Relative pump, w	0.9644	1.0000	1.0370
Population inversion, $\overline{N}_2$	$4.433 \cdot 10^{13}$	$4.597 \cdot 10^{13}$	$4.597 \cdot 10^{13}$
Photon number or intensity, $\overline{P} \equiv \overline{I}$	27	18,479	12,634,694
Photon number variance, $\left\langle \Delta P^2 \right\rangle = \Delta C_P(0)$	761	$3.2088 \cdot 10^8$	$1.62383 \cdot 10^{12}$
Intensity variance, $\left\langle \Delta I^2 \right\rangle = \Delta C_I(0)$	734	$3.2086 \cdot 10^8$	$1.62382 \cdot 10^{12}$

It can be seen that the last three rows of Table 5-1 verify relation (5-10) and that the photon number variance and intensity variance are significantly different in relative terms only below the threshold. However, knowing that the integrated values of the spectra are almost the same, does not guarantee that the whole spectra are similar. Therefore, we also have to compare the power spectra (5-17) and (5-24), for our choice of parameters.

The photon number and intensity fluctuations spectra, calculated with (5-17) and (5-24), are shown in Figure 5-1. There is no scaling or normalisation of the spectrum and the vertical axis is marked in decibel ($10 \cdot \log_{10}[S(\omega)]$). The two graphs are almost identical and, as expected, a noticeable difference between them can only be seen for the curves corresponding to operation below threshold.

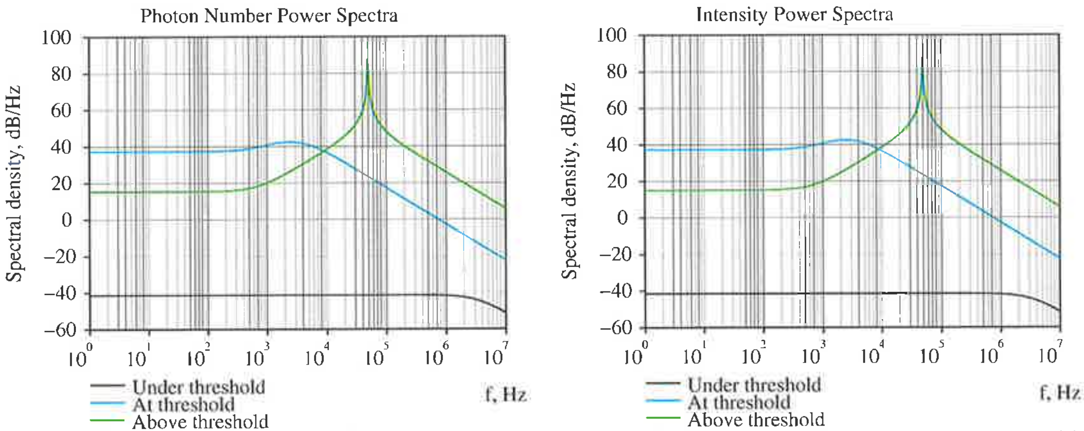

Figure 5-1 Power spectrum of fluctuations in the photon number and intensity

These are shown in Figure 5-2 and it can be observed that even in this case, when the magnitudes are different, the shapes of the curves are still very similar.

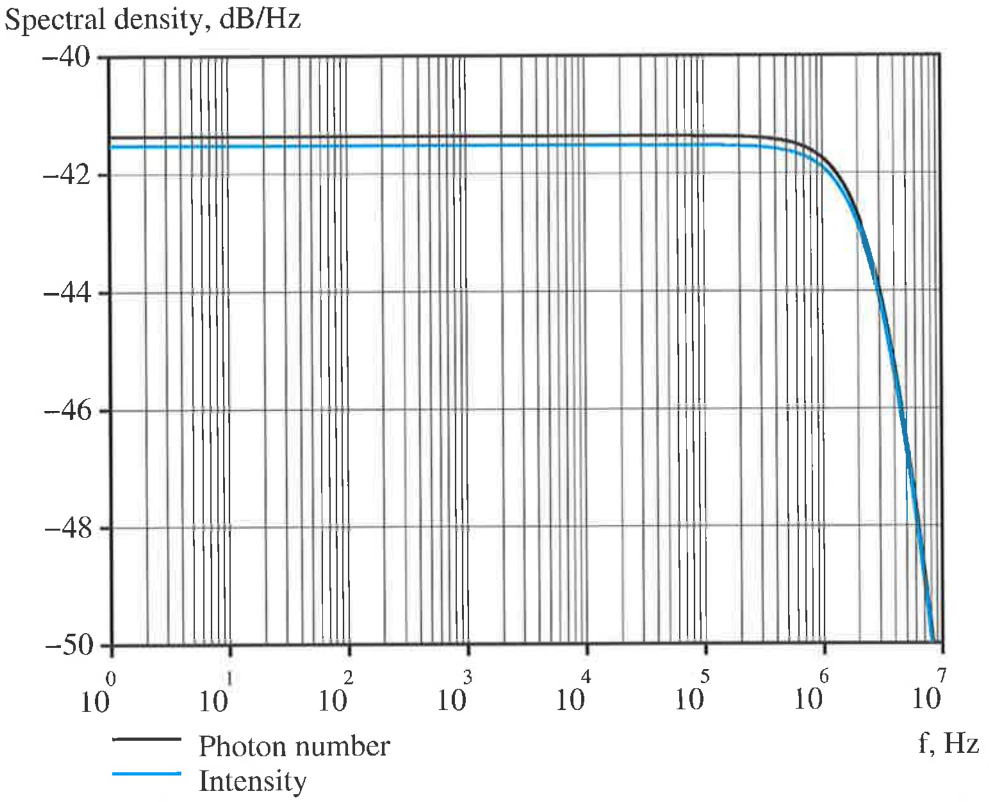

Figure 5-2 Comparison between photon number and intensity power spectra below threshold

We conclude that, while the photon number and the intensity fluctuations require quite different theoretical treatments, in practical terms the difference between their calculated spectra can be neglected above the threshold. We will assume that this conclusion for the single-mode laser is also true for the multimode laser with spatial hole burning. This will allow us to compare measured intensity fluctuation spectra with calculated photon number spectra. We prefer to work in the population inversion and photon number representation because the noise sources can be written by inspection from the Langevin equations. The lack of a rigorous proof for this assumption is a weakness of this work, but we hope that obtaining good agreement between theory and experiment will motivate further work on the theoretical side.

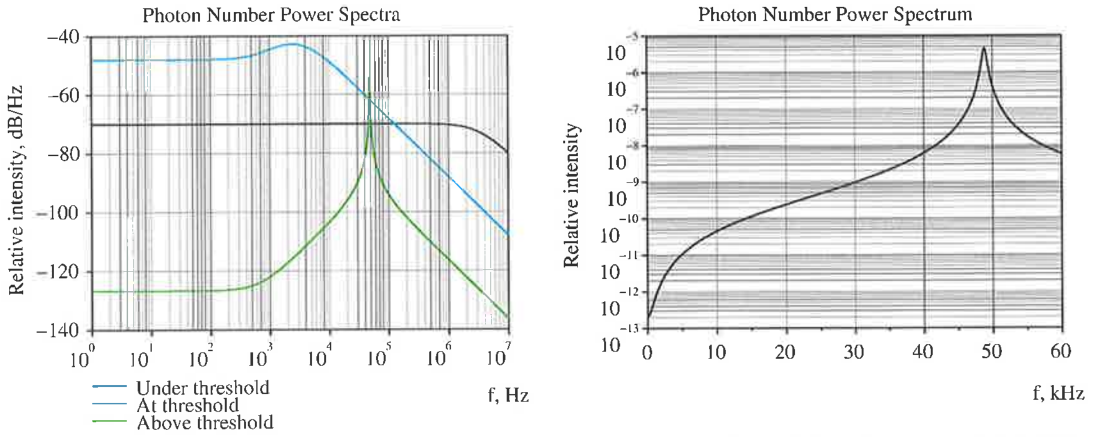

Figure 5-3 Alternative representations of the photon number power spectra

Before quitting the subject of the single-mode laser, we would like to consider alternative modes of displaying the spectra. The left-hand side graph of Figure 5-3 is a normalised version of the left-hand side graph of Figure 5-1. The normalisation has been achieved by dividing each spectrum by the square of the steady state value of the photon number. Finally, in the right-hand side graph of Figure 5-3, we present the power spectrum of the laser above the threshold for the range of frequencies relevant to the following sections. It will be useful to refer back to this graph when commenting on the spectra obtained for the multimode laser (vertical range, overall characteristic etc).

5.4 Tang Statz deMars Equations with Noise

In this section we will modify the Tang Statz deMars equations to include noise. Similar to Chapter 3, we extend the Langevin rate equations (5-12) and (5-13) to the multimode case and allow the population inversion to be a function of position, to be able to deal with the spatial hole burning. To simplify the notations we drop the indices from the population inversion $N_2(z,t)=N(z,t)$, and the noise terms $r_P(t)$ and $s_P(t)$. We also use the decay time constants τ_f and τ_c instead of the rates Γ_2 and γ.

Following the arguments presented in [75] and taking into account the high reflectivity of the mirrors used in our cavity, we conclude that enhanced spontaneous emission is unlikely to occur. Since the laser will be operated above threshold (*P*>>1), we choose to neglect the spontaneous emission – the 1 in (1+*P*); however, the noise associated with it is included in the noise sources [39]. Given that we use shot noise in our model, the absolute values of the numbers are important and it is preferable not to normalise the rate equations:

$$\frac{\partial N(z,t)}{\partial t}=\frac{W(t)}{L_{optic}}-\frac{N(z,t)}{\tau_f}-\pi\sum_{j=1}^{M} g_j N(z,t)P_j(t)\left[1-\cos(2k_j z)\right]+\frac{r(z,t)}{L_{optic}}$$

(5-26)

$$\frac{\mathrm{d}P_j(t)}{\mathrm{d}t}=\pi g_j P_j(t)\int_0^{L_{optic}} N(z,t)\left[1-\cos(2k_j z)\right]dz-\frac{P_j(t)}{\tau_c}+s_j(t).$$

(5-27)

We assume the level of noise to be sufficiently small so the average values of the number of inverted atoms and photons in the modes do not depart significantly from the steady state solution of the equation (5-26) without noise:

$$\frac{\overline{W}(t)}{L_{optic}}=\frac{\overline{N}(z,t)}{\tau_f}+\pi\sum_{j=1}^{M} g_j \overline{N}(z,t)\overline{P}_j(t)\left[1-\cos(2k_j z)\right].$$

(5-28)

From the above equation we can see that although the two terms on the right hand side of the equation (5-28) depend on *z*, their sum is constant along the axis of the laser [76]. As $r(z,t)$ is the sum of the variances of all the above terms, it means that it will not depend on *z* either. Similarly to the Tang Statz deMars equations without noise, we can write the number of inverted atoms as:

$$N(z,t)=\frac{N_0(t)}{L_{optic}}+\sum_{j=1}^{M}\frac{N_j(t)}{L_{optic}}\cos(2k_j z)$$

(5-29)

and substitute into the equations (5-26) and (5-27):

$$\frac{\mathrm{d}N_0(t)}{\mathrm{d}t}+\sum_{j=1}^{M}\frac{\mathrm{d}N_j(t)}{\mathrm{d}t}\cos(2k_j z)=W(t)-\frac{N_0(t)}{\tau_f}-\frac{1}{\tau_f}\sum_{j=1}^{M}N_j(t)\cos(2k_j z)-$$
$$-\pi\sum_{k=1}^{M}g_k\left[N_0(t)+\sum_{j=1}^{M}N_j(t)\cos(2k_j z)\right]P_k(t)[1-\cos(2k_k z)]+r(t)$$

(5-30)

$$\frac{\mathrm{d}P_j(t)}{\mathrm{d}t}=\pi g_j P_j(t)\frac{N_0(t)}{L_{optic}}\int_0^{L_{optic}}[1-\cos(2k_j z)]dz+$$
$$+\pi g_j P_j(t)\sum_{k=1}^{M}\frac{N_k(t)}{L_{optic}}\int_0^{L_{optic}}\cos(2k_k z)[1-\cos(2k_j z)]dz-\frac{P_j(t)}{\tau_c}+s_j(t).$$

(5-31)

The detailed calculations are very similar to the Tang Statz deMars equations without noise and are shown in Appendix A5.1. We obtain:

$$\frac{\mathrm{d}N_0(t)}{\mathrm{d}t}=W(t)-\frac{N_0(t)}{\tau_f}-\pi\sum_{j=1}^{M}g_j[N_0(t)-1/2N_j(t)]P_j(t)+r(t)$$

(5-32)

$$\frac{\mathrm{d}N_j(t)}{\mathrm{d}t}=\pi g_j N_0(t)P_j(t)-N_j(t)\left[\frac{1}{\tau_f}+\pi\sum_{k=1}^{M}g_k P_k(t)\right],\quad j=1\ldots N$$

(5-33)

$$\frac{\mathrm{d}P_j(t)}{\mathrm{d}t}=\pi g_j[N_0(t)-1/2N_j(t)]P_j(t)-\frac{P_j(t)}{\tau_c}+s_j(t),\quad j=1\ldots N.$$

(5-34)

It is important to note that there are noise sources in the equation for the population inversion average (5-32) and the equations for the modal intensities (5-34), but not in those giving the population inversion components(5-32).

These equations can be linearised around the steady state solutions of the equations without noise, given by formulae similar to (3-44), (3-47) and (3-49):

$$\overline{N}_j=2\overline{N}_0-\frac{2}{\tau_c g_j\pi}$$

(5-35)

$$\overline{P}_j=\frac{\overline{N}_0-\dfrac{1}{\tau_c\pi g_j}}{\pi g_j\tau_f\left[\dfrac{1}{\tau_c\pi}\displaystyle\sum_{k=1}^{M}\frac{1}{g_j}-\overline{N}_0(M-1/2)\right]}$$

(5-36)

$$\overline{N}_0 = \frac{\tau_f \overline{W}}{2} + \frac{\sum_{j=1}^{M} \frac{1}{g_j}}{\tau_c \pi (M - 1/2)} - \sqrt{\left(\frac{\tau_f \overline{W}}{2}\right)^2 + \left[\frac{\sum_{j=1}^{M} \frac{1}{g_j}}{\tau_c \pi (M - 1/2)}\right]^2 - \frac{\sum_{j=1}^{M} \frac{1}{g_j^2}}{(\tau_c \pi)^2 (M - 1/2)}} .$$

(5-37)

The Jacobian matrix of the Tang Statz deMars equations without noise is:

$$\mathbf{A} = \left(\frac{\partial \mathbf{F}(\mathbf{Z})}{\partial \mathbf{Z}}\right)\Bigg|_{\mathbf{Z}=\overline{\mathbf{Z}}} ,$$

(5-38)

where $\overline{\mathbf{Z}}$ represents the vector of steady state solutions given by (5-35), (5-36) and (5-37). The linearised Tang Statz deMars equations with noise can be written as:

$$\frac{\mathrm{d}\tilde{\mathbf{Z}}}{\mathrm{d}t} = \mathbf{A}\tilde{\mathbf{Z}} + \mathbf{X} ,$$

(5-39)

where **X** is the vector describing the noise sources in the Tang Statz deMars equations:

$$\mathbf{X} = \begin{bmatrix} r(t) \\ 0 \\ \vdots \\ 0 \\ s_1(t) \\ \vdots \\ s_M(t) \end{bmatrix} .$$

(5-40)

5.5 The Response of a Linear System to Noise

Since the system we deal with from now on is linear, the theory of Chapter 4 applies, with the difference that the input now consists of noise, either generated by the laser itself or applied externally. We shall assume that the system is in zero state at the moment $t = 0$ ($\tilde{\mathbf{Z}}(0) = \mathbf{0}$) and that the noise is applied to the system from that moment onwards ($\mathbf{X}(t) = \mathbf{0}, t < 0$). The output of the system is a convolution between the input into the system and the impulse response matrix of the system [77]:

$$\mathbf{Y}(t) = \int_0^{\infty} \mathbf{H}(\tau)\mathbf{X}(t - \tau) d\tau .$$

(5-41)

The Laplace transform of the impulse response matrix is the transfer function of the system:

$$\mathbf{H}(s) = (s\mathbf{I} - \mathbf{A})^{-1} .$$

(5-42)

We assume the input to the system to be a wide-sense stationary process (the white noise is an example of such a process), the power spectrum of which is a square matrix $\mathbf{S}_{xx}(s)$. The cross-spectrum between input and output can be written as:

$$\mathbf{S}_{xy}(s)=\mathbf{S}_{xx}(s)\mathbf{H}^{\dagger}(s) \tag{5-43}$$

and the output power spectrum becomes:

$$\mathbf{S}_{yy}(s)=\mathbf{H}(s)\mathbf{S}_{xy}(s). \tag{5-44}$$

Relations (5-43) and (5-44) can be condensed into:

$$\mathbf{S}_{yy}(s)=\mathbf{H}(s)\mathbf{S}_{xx}(s)\mathbf{H}^{\dagger}(s). \tag{5-45}$$

This allows us to calculate the power spectrum of each mode and the cross-spectra between the modes if we know the power spectrum and the cross-spectrum of the sources. The noise input into the system does not necessarily have to be of quantum mechanical nature: either internal or external noise can be considered, as long as it is well defined. Because the external noise is difficult to characterise, we concentrate on the internal noise, which can be expressed as function of the laser parameters, even though our system might be dominated by external noise.

For the Tang Statz deMars equations, similar to (5-15), we assume the following auto- and cross-correlation functions between the internal noise sources:

$$\begin{aligned}\langle r(t+\tau)r(t)\rangle &= 2\overline{W}\delta(\tau)\\ \langle r(t+\tau)s_j(t)\rangle &= -\frac{2\overline{P}_j}{\tau_c}\delta(\tau)\\ \langle s_j(t+\tau)s_k(t)\rangle &= \frac{2\overline{P}_j\delta_{jk}}{\tau_c}\delta(\tau).\end{aligned} \tag{5-46}$$

The Kroneker symbol δ_{jk} in the last formula indicates that the noise sources in different longitudinal modes are uncorrelated. The delta function $\delta(t)$ in the above auto- and cross-correlation functions implies uniform power spectral density (white noise), with infinite total power; however, in the high frequency limit (above the relaxation oscillations frequency) the laser behaves like a second order low-pass filter, so the integrated output spectrum is finite.

5.6 Investigation of the Tang Statz deMars Equations with Noise

As mentioned in the section 5.1, we have chosen a model with three longitudinal modes, because this is the minimum number of modes to display non-trivial antiphase dynamics. Even so, the number of equations is 7 ($2M+1$, with $M=3$), so we are dealing with 7 x 7 matrices. This means that, in principle, there are 49 numbers for the noise input (assuming white noise, when the input spectrum is independent of frequency) and 49 rational fractions describing the output spectra. In reality, the problem is first simplified by the fact that, for internal noise, there are only 7 independent elements of the matrix describing the input spectrum $\mathbf{S}_{xx}(s)$, according to (5-46). Secondly, we are mostly interested in the spectra of the longitudinal modes and this reduces the output to 3 power spectra (magnitude only) and 3 cross-spectra (magnitude and phase). However, we are also interested in the total intensity spectrum, because comparisons between this spectrum and those of individual modes reveal antiphase behaviour. The power spectrum for the total intensity can be calculated [76] by adding both the power- and the cross-spectra (and not only the power spectra) of the modes:

$$S_T(s)=\sum_{i=1}^{3}S_i(s)+\sum_{j,k=1,j\neq k}^{3}S_{jk}(s) \tag{5-47}$$

where the power spectra $S_i(s)$ and the cross-spectra $S_{jk}(s)$ are elements of the output power spectrum matrix $\mathbf{S}_{yy}(s)$. For an input such as that specified by (5-46), the imaginary parts in the second sum cancel out, leaving the power spectrum $S_T(s)$ a real quantity, as expected.

The laser parameters and the pump level ($w=1.0370$) are the same as for the 'Above threshold' column of Table 5-1 in section 5.3.3. The offset of the first mode with respect to the centre of the cavity (see section 3.3.4) was chosen to be $offset=0.15$. With these choices, the steady state value of the total photon number (Table 5-2) is about 79% of that of the single-mode laser without spatial hole burning (Table 5-1). This is due to the fact that in this case the population inversion located around the nodes of the electric field in the cavity does not contribute to stimulated emission.

Table 5-2 Three-mode laser steady state

Variable	Population inversion	Photon number
Mode 1	$0.7227\cdot10^{12}$	5,481,381
Mode 2	$0.4222\cdot10^{12}$	3,212,758
Mode 3	$0. 1646 \cdot10^{12}$	1,256,367
Average/Total	$46.330\cdot10^{12}$	9,950,506

With these steady state values, the Jacobian matrix can be calculated and the resonant frequencies of the system found. There values are:

$$f_1=12.16\,kHz$$
$$f_2=19.45\,kHz$$
$$f_3=47.75\,kHz\,.$$

One problem related to the dimension of the matrices used for the calculations is that of the numerical accuracy. The characteristic equation of the Jacobian matrix if a polynomial of the 7th degree; the calculations implied in (5-45) lead to a squaring of this polynomial, so the degree of the denominator of $\mathbf{S}_{yy}(s)$ is 14. For a frequency range of 100 Hz to 60 kHz, this requires a dynamic range of about $8\cdot10^{38}$, significantly more than 1 over the machine epsilon ($4.5\cdot10^{15}$). The solution to this problem is a careful scaling of the time constants, followed by a scaling of the frequency with the opposite effect. Monitoring the phase of the diagonal elements of $\mathbf{S}_{yy}(s)$ (the power spectra) is a good consistency check for the calculations; in general, the phase of these elements was $0\pm(10^{-14}$ to $10^{-15})$ degrees.

All spectra presented below were normalised by dividing them to the square of the total photon number. This way, the output noise is the relative intensity noise (RIN) used in some publications.

5.6.1 Noise in the Population Inversion

We start our study with noise injected in the population inversion only, its magnitude being given by the first formula in (5-46):

$$\mathbf{S}_{xx}(s)=\begin{bmatrix} 82.904 & 0 & 0 & 0 & 0 & 0 & 0 \\ 0 & 0 & 0 & 0 & 0 & 0 & 0 \\ 0 & 0 & 0 & 0 & 0 & 0 & 0 \\ 0 & 0 & 0 & 0 & 0 & 0 & 0 \\ 0 & 0 & 0 & 0 & 0 & 0 & 0 \\ 0 & 0 & 0 & 0 & 0 & 0 & 0 \\ 0 & 0 & 0 & 0 & 0 & 0 & 0 \end{bmatrix}\cdot 10^{16}\,\mathrm{Hz}^{-1}.$$

The output results are plotted in Figure 5-4 to Figure 5-6 and there are a few interesting things to note. One of them is the manifestation of antiphase dynamics at low frequencies, visible in Figure 5-4: some individual modes oscillate with higher amplitude than the total intensity. This makes the graph for the total intensity look rather similar in shape to that of the single-mode laser of Figure 5-3. However, the power spectrum of total intensity due to population inversion noise is significantly smaller in magnitude than that of the single-mode laser.

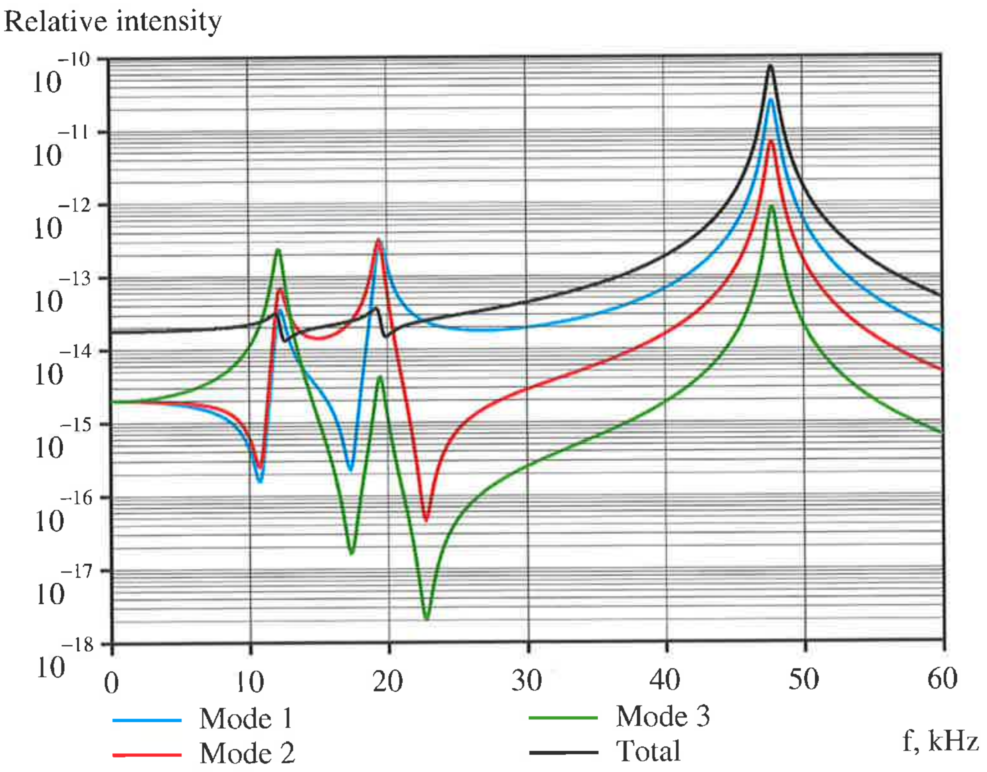

Figure 5-4 Power spectra of the modes and of the total intensity for noise in the population inversion

Another thing that is worth noting is that the power spectra for the modal and total intensities are rather similar to the transfer functions. This is not very surprising, since the transfer functions are obtained by modulating the pump power with sinusoidal signals. The situation studied here represents, in a sense, the modulation of the pump power with white noise, so the result is likely to be similar.

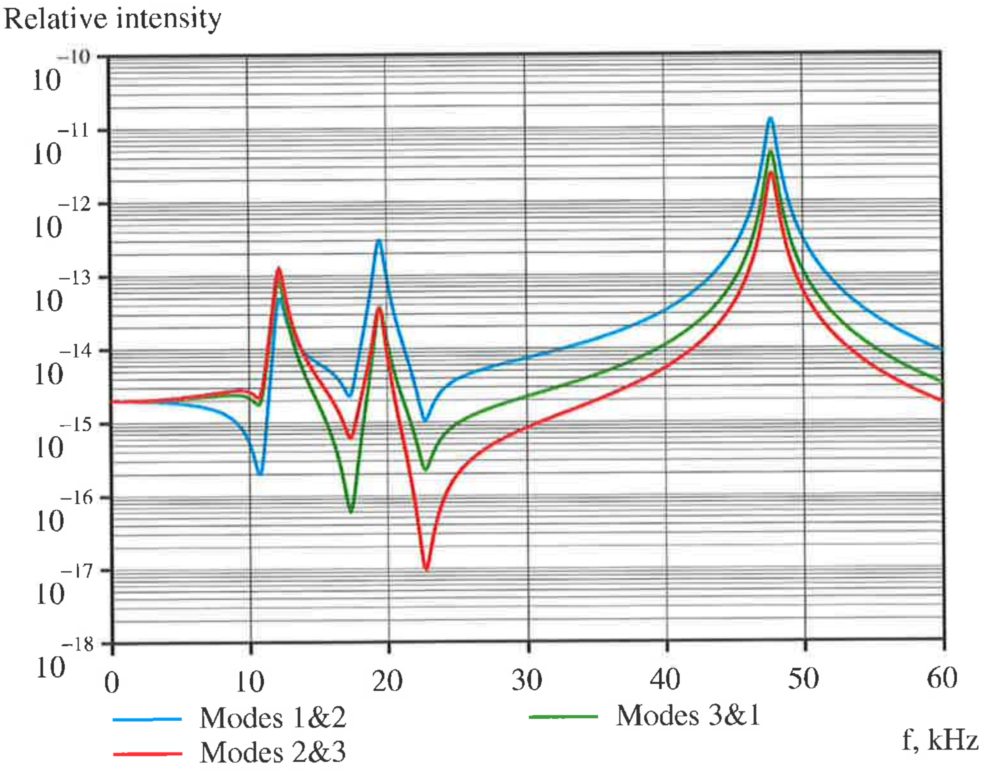

Figure 5-5 Magnitude of cross-spectra between pairs of modes for noise in the population inversion

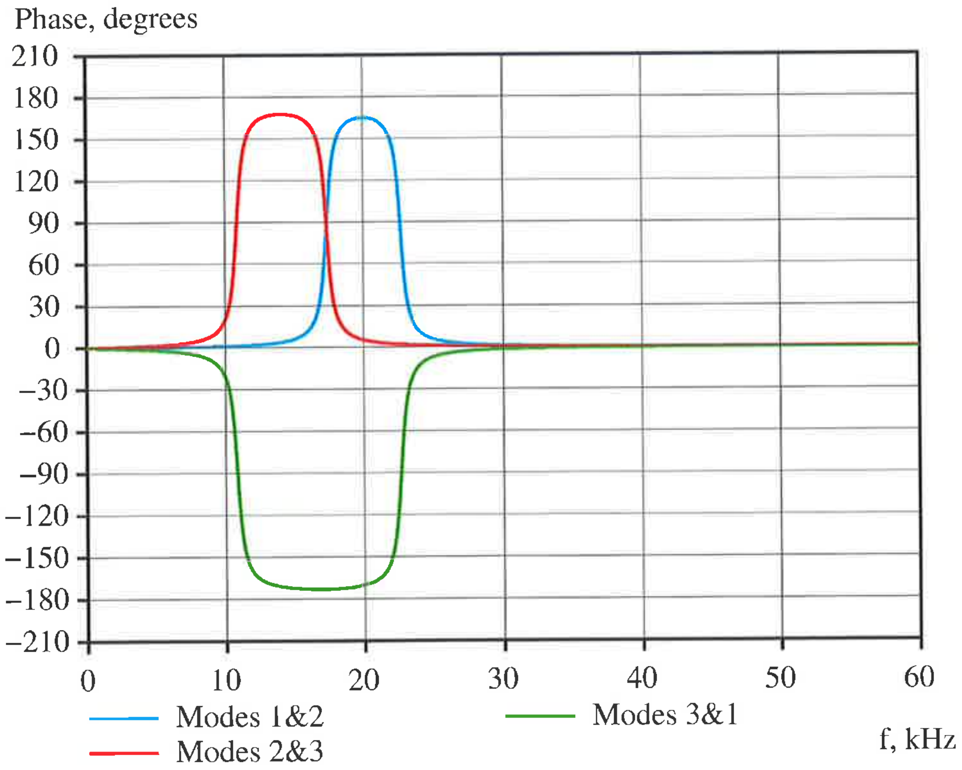

Figure 5-6 Phase of cross-spectra between pairs of modes for noise in the population inversion

The way the cancellation occurs is unravelled by Figure 5-6: at the resonant frequency f_1, modes 1 and 2 are approximately in phase with each other and in anti-phase with mode 3, at f_2, modes 2 and 3 are approximately in phase with each other and in anti-phase with mode 1 and at f_3, they are all in phase. The phases are such the their sum is always zero. At DC the modes are all in phase, and this can be understood as slow increases and decreases in the population inversion lead to simultaneous variations in the modal intensities – so they are all in phase.

5.6.2 Noise in the Mode 1

Another possibility for noise injection is to select one of the laser modes. In this case, we chose mode 1 and, as before, we select the magnitude of the noise according to the last of the formulae (5-46), with the indices j and k both equal to 1:

$$\mathbf{S}_{xx}(s)=\begin{bmatrix}0&0&0&0&0&0&0\\0&0&0&0&0&0&0\\0&0&0&0&0&0&0\\0&0&0&0&0&0&0\\0&0&0&0&1.283&0&0\\0&0&0&0&0&0&0\\0&0&0&0&0&0&0\end{bmatrix}\cdot 10^{16}\,\mathrm{Hz}^{-1}.$$

The graphs corresponding to this type of input noise (quite difficult to obtain experimentally) are shown in Figure 5-7 to Figure 5-9.

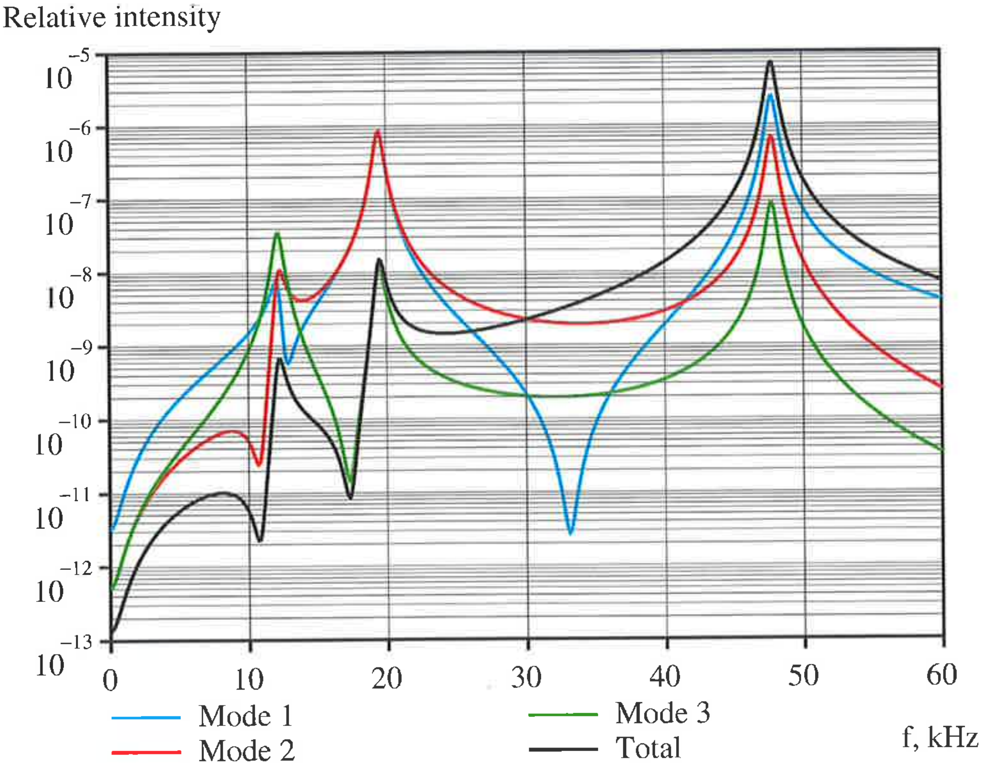

Figure 5-7 Power spectra of the modes and of the total intensity for noise in mode 1

The power spectra in Figure 5-7 reveal that, despite the reduced intensity of the input spectrum (compared to the situation discussed in section 5.6.1), the power spectrum of total intensity is comparable to the single-mode case. This means that there is considerably more 'gain' from the mode 1 input than from N_0 input.

We notice the antiphase again, with the low frequency peaks of total intensity lower than or equal to those of the individual modes. For example, at f_2 modes 1 and 2 are oscillating in opposition and the response is basically that of mode 3.

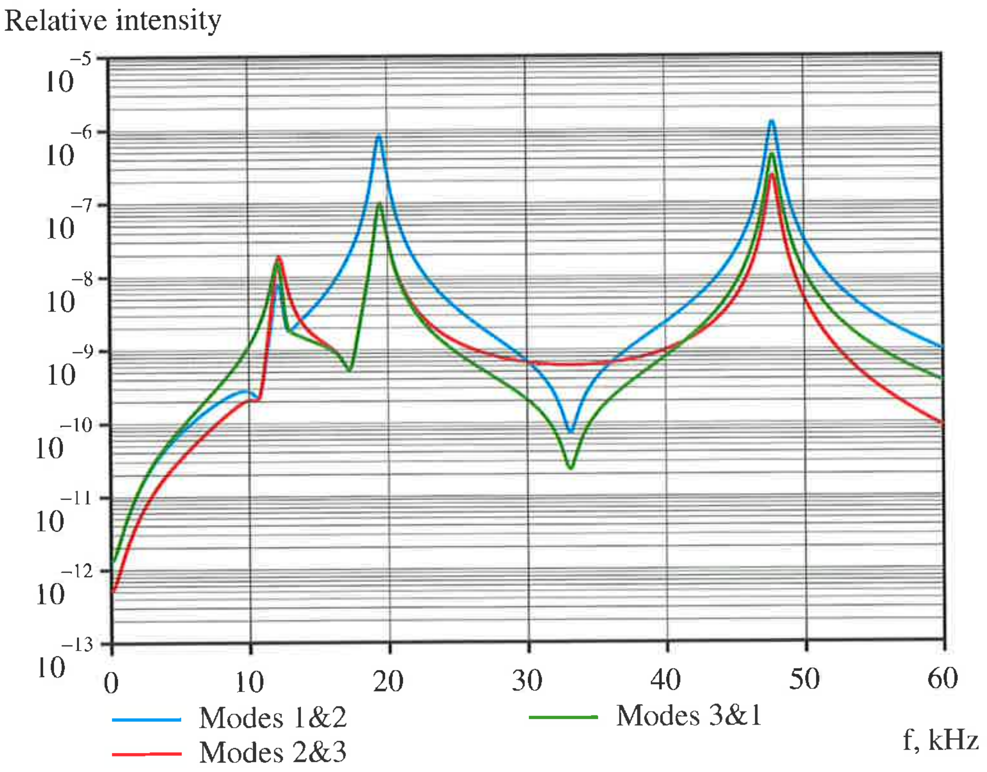

Figure 5-8 Magnitude of cross-spectra between pairs of modes for noise in mode 1

At the frequency f_1 however, there is some degree of antiphasing, but the modal intensities oscillate with the following phase relationships (Figure 5-9):

$$\varphi_{12} = 48.3^\circ, \varphi_{23} = 160.8^\circ, \varphi_{31} = 150.9^\circ .$$

This is more like a splay state type of antiphase, rather than the usual 0°/180° phase relationship between the laser modes. At DC mode 1 is in antiphase with modes 2 and 3. Since the noise is injected directly into mode 1, a slow increase of its intensity leads to corresponding decreases in the intensities of modes 2 and 3.

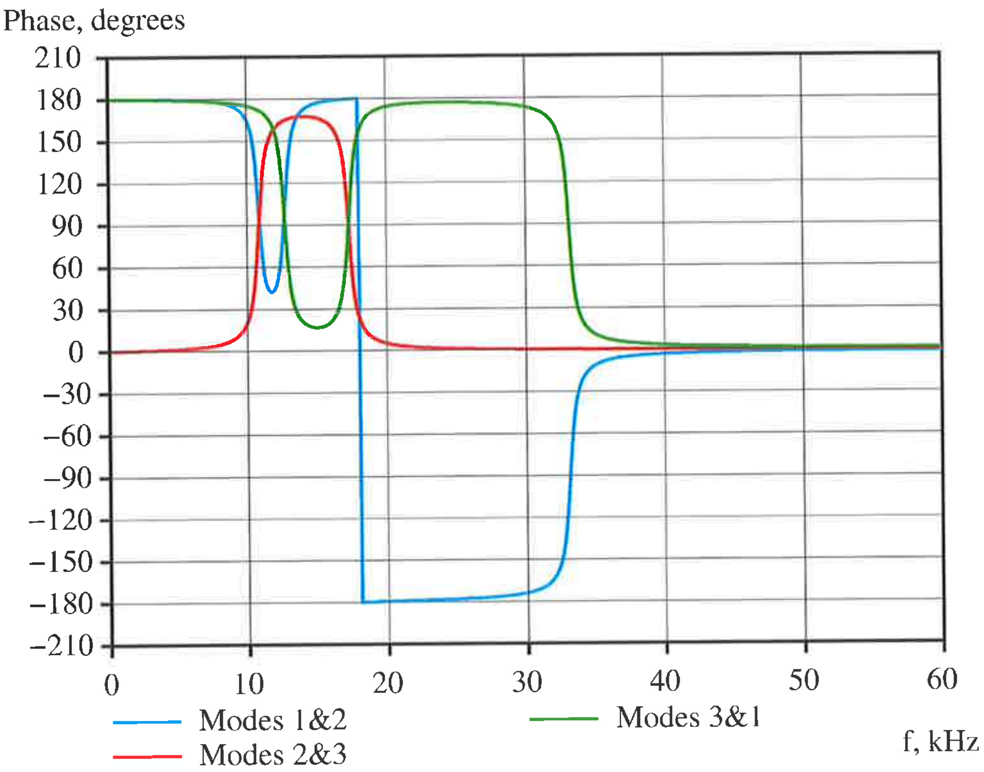

Figure 5-9 Phase of cross-spectra between pairs of modes for noise in mode 1

5.6.3 Correlated Noise in the Population Inversion and in the Modes

The final situation considered is that where all noise sources considered in (5-46) are included:

$$\mathbf{S}_{xx}(s)=\begin{bmatrix} 82.904 & 0 & 0 & 0 & -0.642 & -0.376 & -0.147 \\ 0 & 0 & 0 & 0 & 0 & 0 & 0 \\ 0 & 0 & 0 & 0 & 0 & 0 & 0 \\ 0 & 0 & 0 & 0 & 0 & 0 & 0 \\ -0.642 & 0 & 0 & 0 & 1.283 & 0 & 0 \\ -0.376 & 0 & 0 & 0 & 0 & 0.752 & 0 \\ -0.147 & 0 & 0 & 0 & 0 & 0 & 0.294 \end{bmatrix}\cdot 10^{16}\,\mathrm{Hz}^{-1}.$$

The corresponding results are what we would expect to see in a laser with no external noise input (the natural noise of the laser) and are shown in Figure 5-10 to Figure 5-12. The power spectra display the now usual characteristics: in-phase at f_3 and antiphase at f_1 and f_2. The magnitude of the total intensity power spectrum is comparable to that of the single-mode laser and the shape is similar, except for the low frequency remnant peaks.

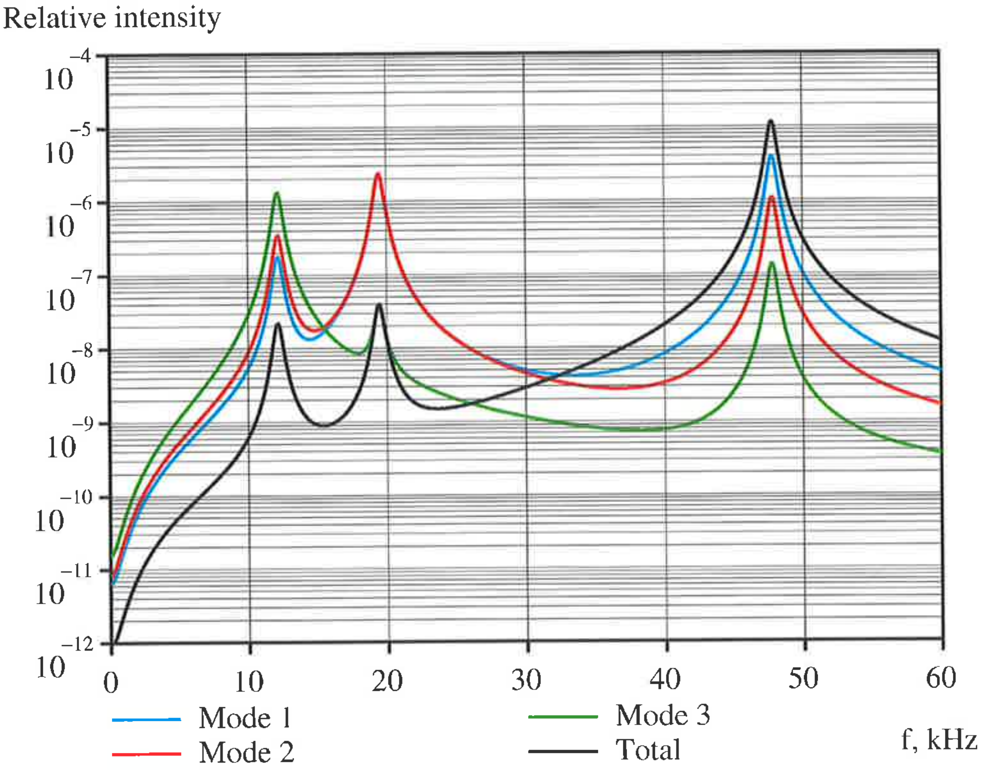

Figure 5-10 Power spectra of the modes and of the total intensity for correlated noise

The magnitude of the cross-spectra (Figure 5-11) show quite deep nulls and there are sudden phase changes (Figure 5-12), corresponding to these nulls.

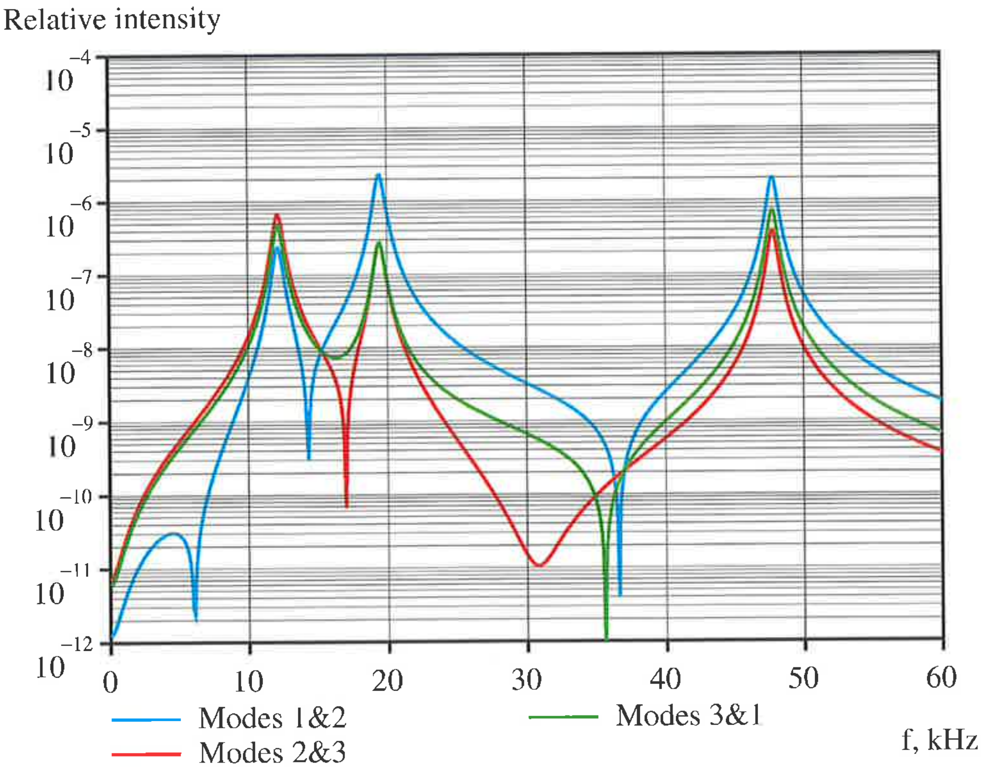

Figure 5-11 Magnitude of cross-spectra between pairs of modes for correlated noise

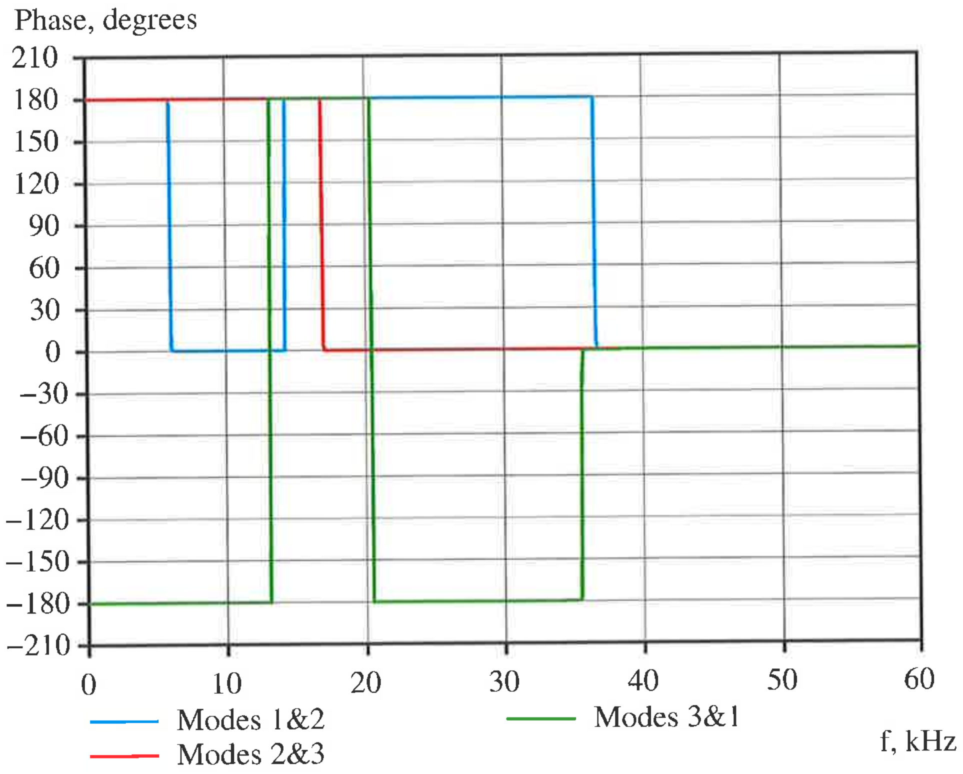

Figure 5-12 Phase of cross-spectra between pairs of modes for correlated noise

The phase of the cross-spectra has, in this case, a behaviour that is quite different from that of the previous ones (sections 5.6.1 and 5.6.2). The values of the phase are 0°, 180° or -180° for most of the frequency response, with very little rounding at the transitions.

Because the phase relationship between modes at the resonant frequencies is one of 2 possible values (+180° and –180° are the same thing), we can construct a table of relative contributions to the system dynamics (Table 5-3). Here we choose mode 1 as the reference and indicate with the + sign when the modes have the same phase as mode 1 and with the – sign when they have opposite phase.

Table 5-3 Relative phases of the modes

Mode	f_1	f_2	f_3
1	+	+	+
2	+	–	+
3	–	–	+

While at the resonant frequencies the relative phases of the modes have reasonable values, there are frequency ranges where the values are hard to reconcile. For example, around 15 kHz all pairs of modes are in antiphase (180°). One would expect that if modes 1&2 are in antiphase and modes 2&3 are also in antiphase, then modes 1&3 should be in phase. How can we explain this?

One possibility is that our results are incorrect, due to either the theoretical treatment or the numerical calculations. It is quite difficult to prove that the results are correct, but we are encouraged by the fact that power spectra of the individual modes have vanishing imaginary parts across the whole frequency range. The same can be said about the power spectrum of the total intensity, calculated with (5-47). It is hard to imagine mistakes compensating to such degree of accuracy.

Another possibility is that the simple picture where the modes are either all in phase (as at the relaxation oscillations frequency) or two in phase with each other and in antiphase with the third is valid only when there is a single dominant source of noise. When several noise sources excite the system, the output noise in each longitudinal mode has components from each source. Since the system is linear, these components are the responses from each input source, acting alone (the superposition principle). However, the strength of the response produced by each input at a particular output is a function of frequency and these functions are different for each mode. Therefore, it is conceivable that when the cross-spectra between pairs of modes are calculated, the changes from in phase to antiphase to occur at different frequencies for different pairs. This leaves open the possibility for the anomaly described above.

One might ask: how is possible to imagine signals with such a property? For example, let us imagine that it we could simultaneously detect the intensities of the three longitudinal modes. If we used electronic filters to select oscillations of the modal intensities in narrow band around 15 kHz, would we see three waveforms in antiphase with each other at all times? We think that the answer to this question is negative, because the signals are not deterministic. Acquiring cross-spectra involves averaging and this means that when we average the product of the signals 1&2 we eliminate any signals unrelated to their correlation. Those parts of the signal 1 and of the signal 2 conveying information about the correlation between 1&3, between 2&3 and those completely uncorrelated average to zero.

5.6.4 Discussion of Universal Relations in Power Spectra

There is a considerable amount of work [52], [53], [47] by Mandel and collaborators regarding the existence of 'universal relations' between the peaks of the modes and the corresponding peaks (if any) in the power spectrum of the total intensity. We would like to investigate the applicability of these relations to our theoretical results. To this end, we collected information from the above calculations about the relative phases and the magnitudes of the peaks of the modal intensities at the resonant frequencies of the laser. We then tried to predict the total intensity peaks by applying applied the following relation, written for a 3-mode laser [47]:

$$s_T\sqrt{S_T(f_i)} = s_1\sqrt{S_1(f_i)} + s_2\sqrt{S_2(f_i)} + s_3\sqrt{S_3(f_i)}, \tag{5-48}$$

where $s_j = \pm 1$ and $S_j(f_i)$ are the peak heights at the resonant frequencies.

We first apply these calculations to the situation were the noise is applied to the average population inversion. The results are shown in the last two rows of Table 5-4. The one labelled '*$S_T(f)$-pred*' contains the results of applying (5-48) with the signs chosen according to the relative phases φ_{ij}. The last row, labelled '*$S_T(f)$-calc*' has the values calculated at the same time with '*$S_j(f)$*', using (5-47).

Table 5-4 Universal relations for noise in the population inversion

Mode	f_1	f_2	f_3
$S_1(f)$	3.31	29.71	2447.8
$S_2(f)$	6.42	29.97	665.8
$S_3(f)$	23.29	0.415	84.8
φ_{12}	1.9°	164.0°	0.1°
φ_{23}	160.7°	7.1°	0.1°
φ_{31}	-162.6°	-171.1°	-0.2°
$S_T(f)$*-pred*	0.22	0.45	7138.2
$S_T(f)$*-calc*	2.38	2.78	7138.2

We can see that the results agree quite well for the last column, when the vectors are all in phase, but not so well in the first two columns.

Table 5-5 Universal relations for noise in mode 1

Mode	f_1	f_2	f_3
$S_1(f)$	644,480	81,152,414	240,284,150
$S_2(f)$	956,638	83,056,292	65,310,887
$S_3(f)$	3,471,331	1,150,605	8,320,855
φ_{12}	48.3°	-179.5°	-1.7°
φ_{23}	160.8°	7.1°	0.1°
φ_{31}	150.9°	172.4°	1.6°
$S_T(f)$*-pred*	6,769	1,387,028	700,512,980
$S_T(f)$*-calc*	61,414	1,411,837	700,370,590

The same pattern appears to manifest itself in Table 5-5: when the phases are significantly different from 0° or ±180°, the differences are larger. Thus, it comes to no surprise that the agreement is quite good in the case presented in Table 5-6.

Table 5-6 Universal relations for correlated noise in population inversion and modes

Mode	f_1	f_2	f_3
$S_1(f)$	17,616,720	228,866,030	389,187,450
$S_2(f)$	34,010,143	234,695,250	105,912,910
$S_3(f)$	130,633,864	3,633,839	13,516,670
φ_{12}	0.0°	180.0°	0.0°
φ_{23}	180.0°	0.0°	0.0°
φ_{31}	-180.0°	-180.0°	0.0°
$S_T(f)$*-pred*	1,961,311	4,400,391	1,134,687,400
$S_T(f)$*-calc*	2,179,848	3,946,702	1,135,402,700

The explanation resides in (5-47): when all phase angles are either 0° or ±180°, the cosine functions implicit in the cross-spectra are ±1 and this formula reduces to (5-48).

5.7 Experimental Set-up and Results

In this section we investigate experimental set-ups suitable for noise measurements and present examples of modal power- and cross-spectra. While the measurements discussed here are not appropriate for comparisons with the theoretical calculations, they demonstrate the potential of the technique and allow us to make a few comments about the salient features of the noise spectra.

The simplest arrangement, suitable only for power spectra, is that presented in Figure 4-13. This is the set-up used for measuring the transfer functions, but with the modulation turned off. The optical spectrum analyser FP serves to select the desired longitudinal mode, which is applied to the photodiode PDA1. The total intensity is detected with photodiode PDA2. The electric signals are analysed by the dynamic signal analyser (HP35670A). Results obtained with the laser operating in 5 modes, in exactly the same conditions as those used for measuring the transfer functions discussed in Chapter 4, are presented in Figure 5-13.

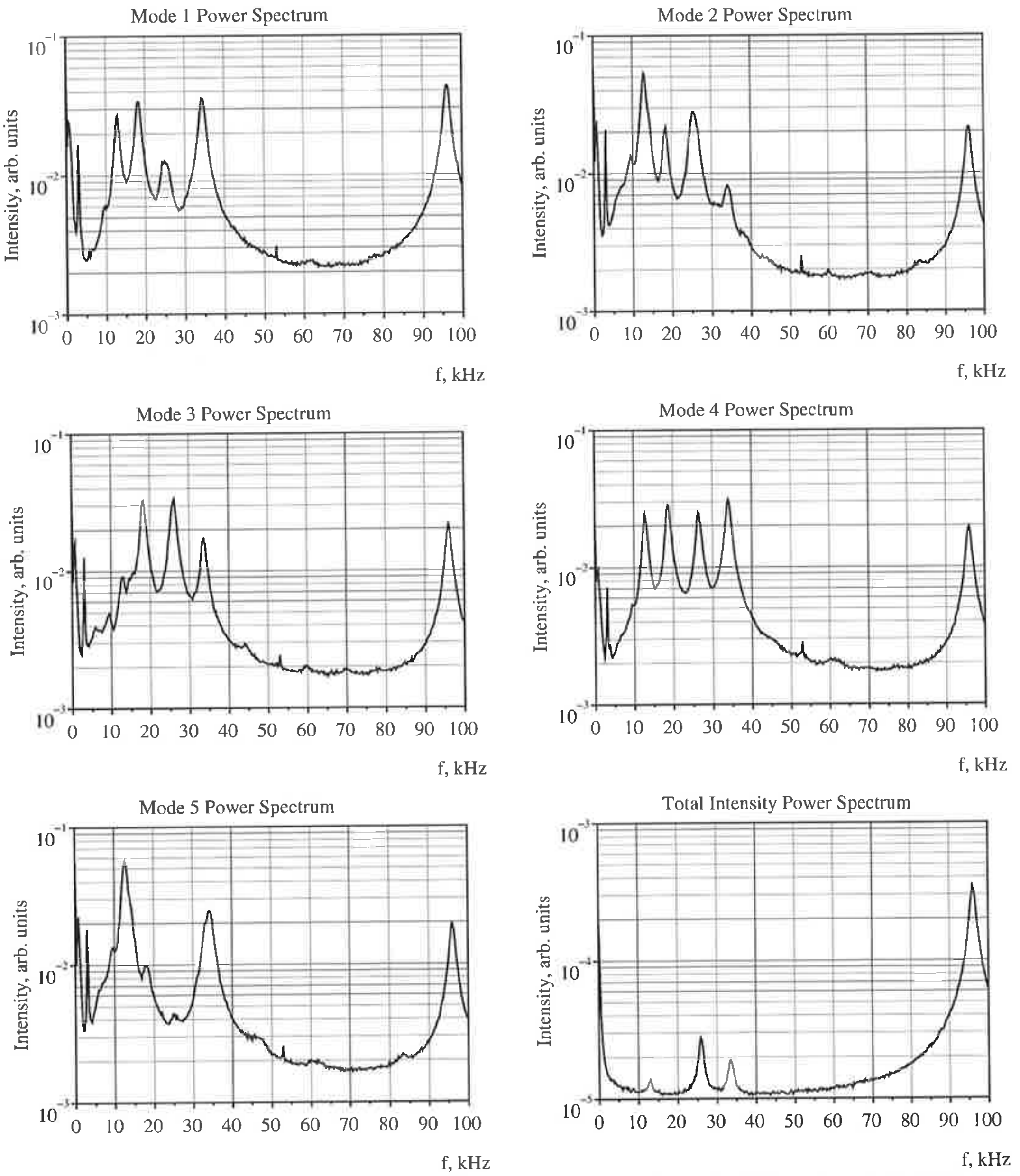

Figure 5-13 Power spectra of the 5 mode laser

The antiphase dynamics is quite obvious in these power-spectra: the total intensity of the laser resonates strongly only at the highest frequency (the relaxation oscillations peak at about 96 kHz), while the individual longitudinal modes have also significant collective motion at low frequencies. The low frequency compensation is not perfect, but it is significant: while individual modes have low frequency peaks sometimes higher than that of the relaxation oscillations, in the total intensity they are reduced by more than a factor of 10.

The power spectra of the modes and total intensity illustrate well the manifestation of antiphase dynamics and allow to infer some information about the way the modes combine their oscillations to achieve it [47]. However, the lack of direct information about the relative phases of the modes is both obvious and frustrating.

Measuring the complete noise spectrum of the laser output (both self- and cross-spectra) is a relatively simple procedure, compared to the transfer function measurements. There is no need for modulation, as long as one is content with the natural sources of noise (environmental, pump or, in the best case, of quantum nature). However it is necessary to have a reasonably good matching between the two detection channels (as discussed below) and to use low-noise electronics. With reference to Figure 5-14, the laser is powered up with the laser diode at the desired level and the output beam is split in half with the 50-50 non-polarising beam splitter BS. Each beam is processed through a channel consisting of:

- an optical isolator to prevent optical feedback into the laser;
- a Fabry-Perot optical spectrum analyser (FP1 or FP2) to select the mode of interest;
- a photodiode with the associated transconductance amplifier (PDA1 or PDA2) to detect the Fabry-Perot output.

The amplified electrical signals are applied to the inputs of the dynamic signal analyser (HP35670A), which is capable of calculating the power spectrum for each channel and the cross-spectrum between the two channels.

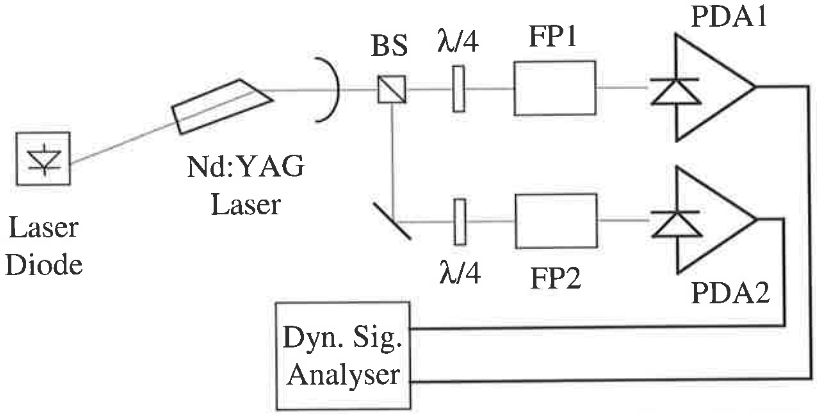

Figure 5-14 Noise measuring set-up

As mentioned in the previous chapter, when operating in dual channel mode (which is required for transfer functions and cross-spectra) the dynamic signal analyser is limited in frequency to 55.2 kHz. For the measurements reported here, this means that the relaxation oscillations peak is not visible, but the low frequency peaks are all included.

Before taking any cross-spectrum measurements it is important to check the correct operation of the system and to determine the amplitude and / or phase errors. This can be done quite easily by selecting the same longitudinal mode for both channels and comparing the responses. The result of this system check is shown in Figure 5-15 to Figure 5-18.

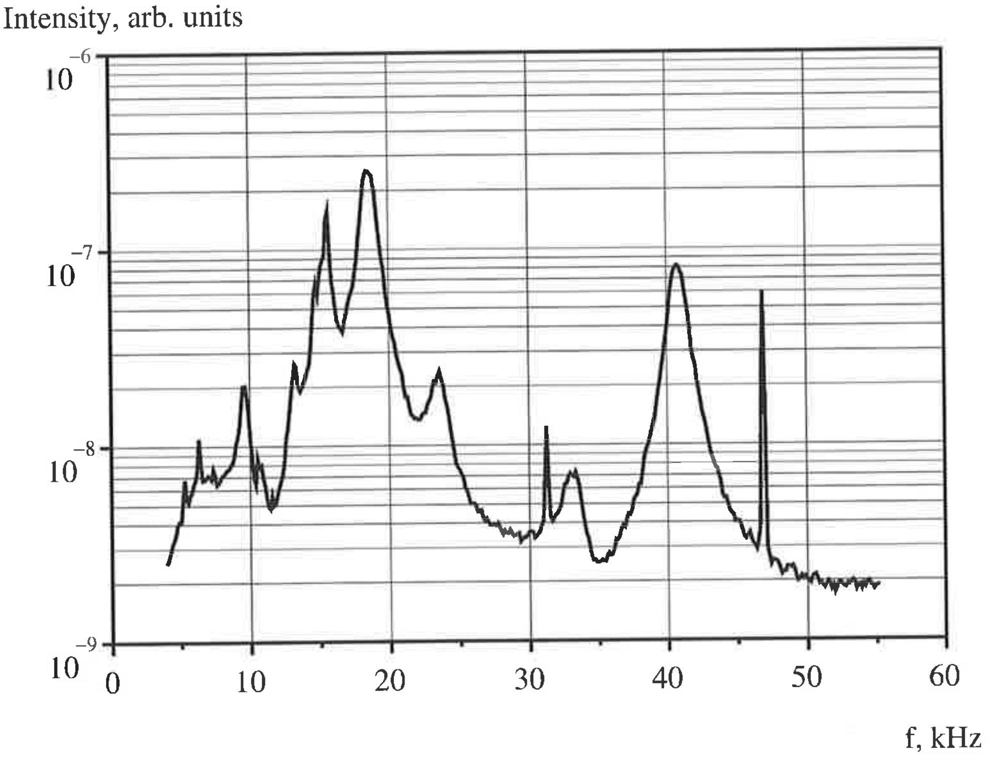

Figure 5-15 Power spectrum of a certain longitudinal mode measured through channel 1

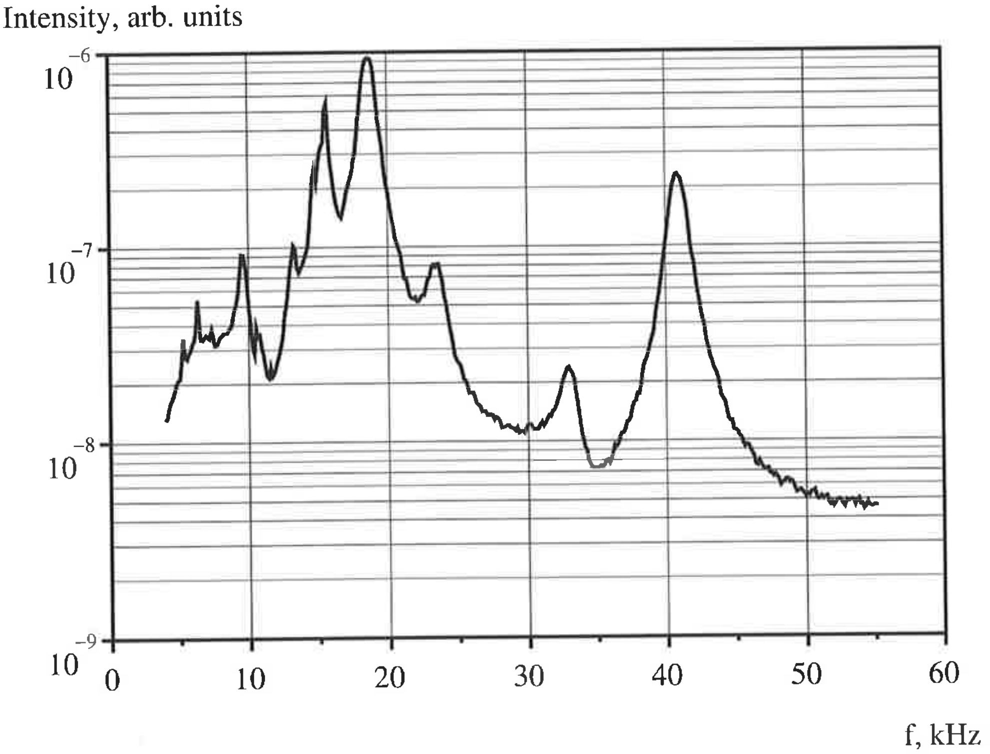

Figure 5-16 Power spectrum of the same longitudinal mode measured through channel 2

The first two spectra (Figure 5-15 and Figure 5-16) show the power spectrum of the selected longitudinal mode, as measured by each channel. It is visible that the same features appear in both spectra, except for a couple of interfering signals that are only present in channel 1. These parasitic signals are the harmonics of a TV monitor (multiples of the horizontal sweep frequency 15,625 Hz). It is also visible that the gains of the two channels are different, that of channel 2 being about 6dB higher than that of channel 1.

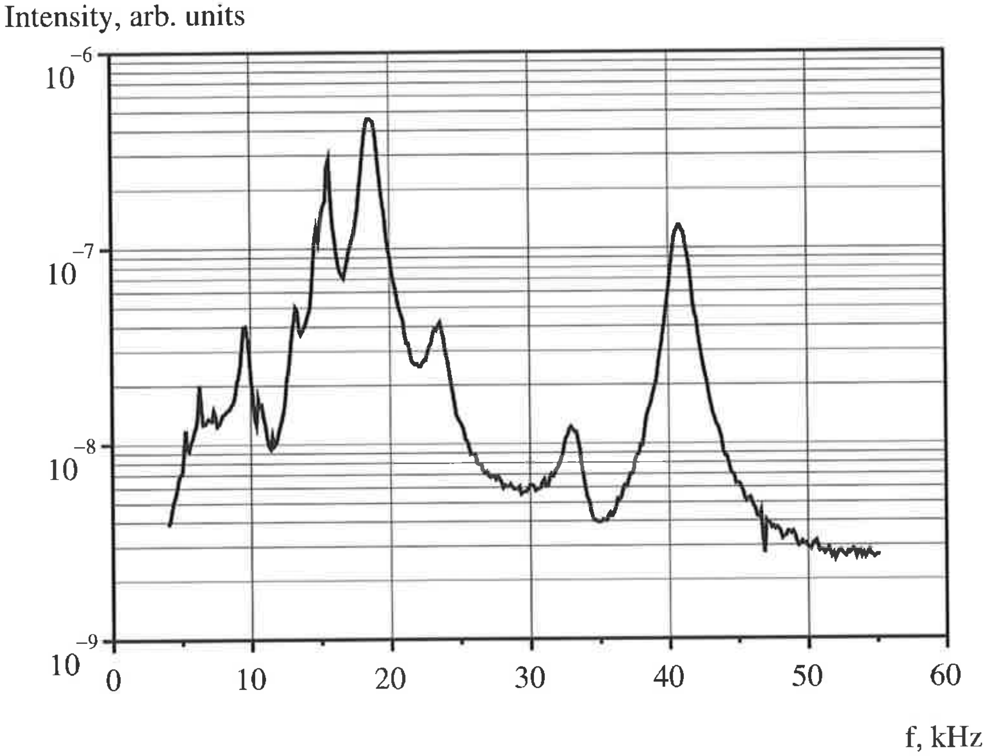

Figure 5-17 Magnitude of the cross-spectrum between channel 1 and channel 2 (the same longitudinal mode as in Figure 5-15 and Figure 5-16)

The cross-spectrum of the two channels is shown in Figure 5-17 (the magnitude) and in Figure 5-18 (the phase). One would expect the magnitude to be similar to the power spectra shown before and the phase to be zero. This is indeed the case, as far as the magnitude is concerned; the phase however, is closer to 180° than to 0° and varies with frequency. This indicates that one of the channels inverts the signal and that the phase characteristics of the two channels are not the same. Having this information about the phase characteristic is important, as it allows us to compensate the phase of the subsequent measurements.

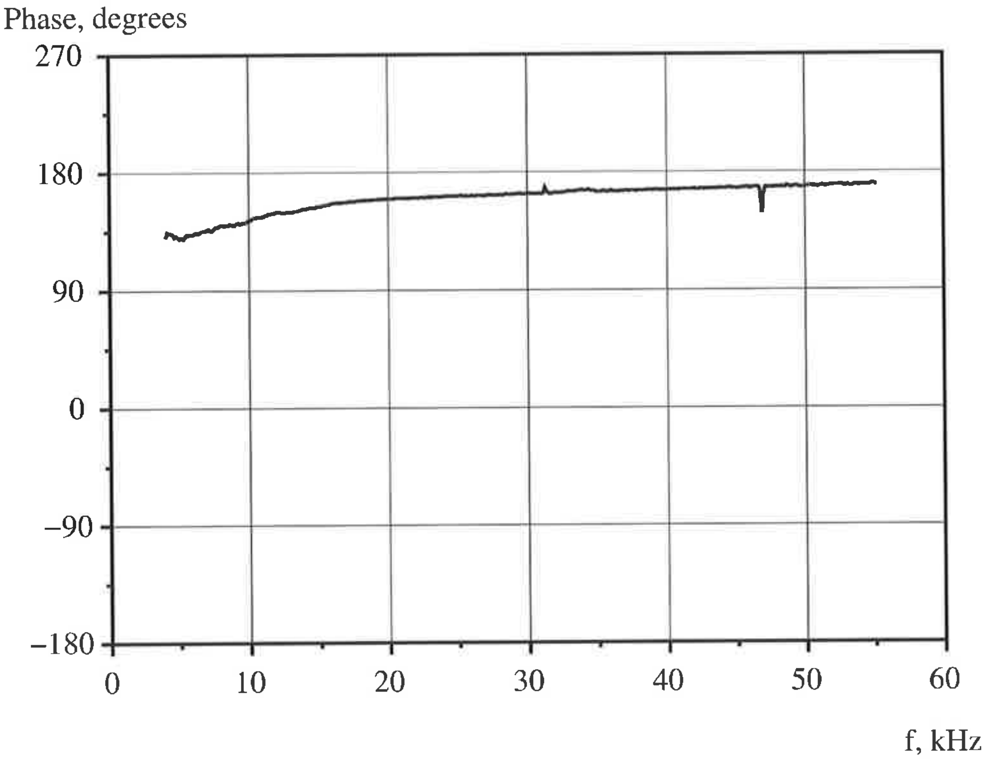

Figure 5-18 Phase of the cross-spectrum between channel 1 and channel 2 (the same longitudinal mode as in Figure 5-15 and Figure 5-16)

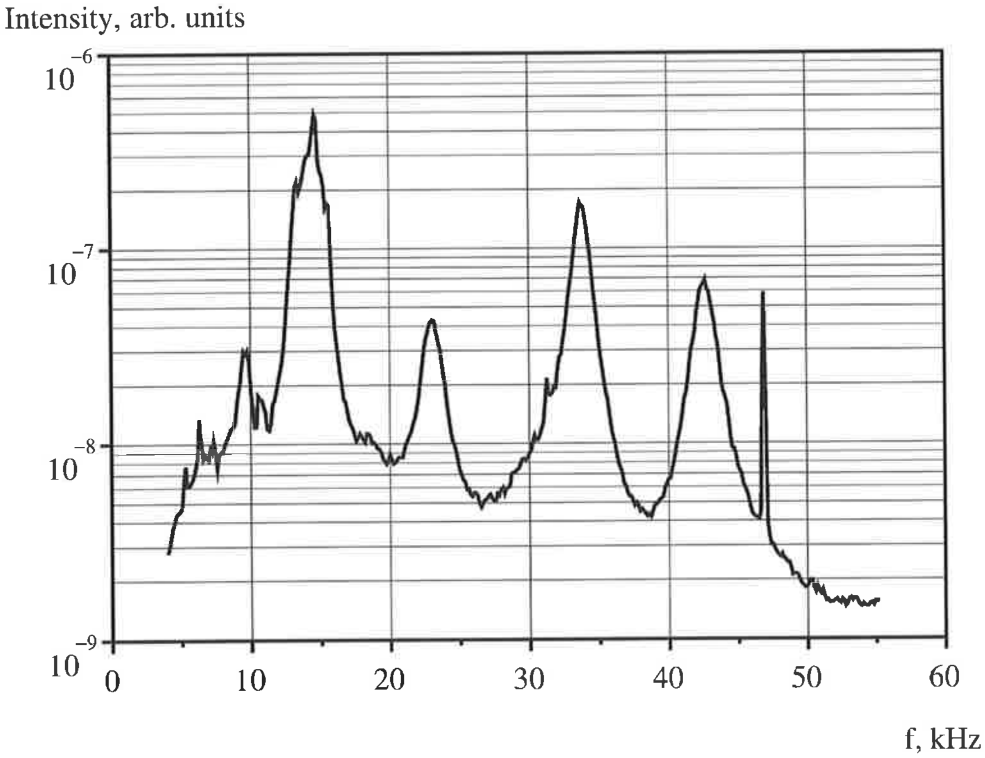

Figure 5-19 Power spectrum of mode 1, measured with channel 1

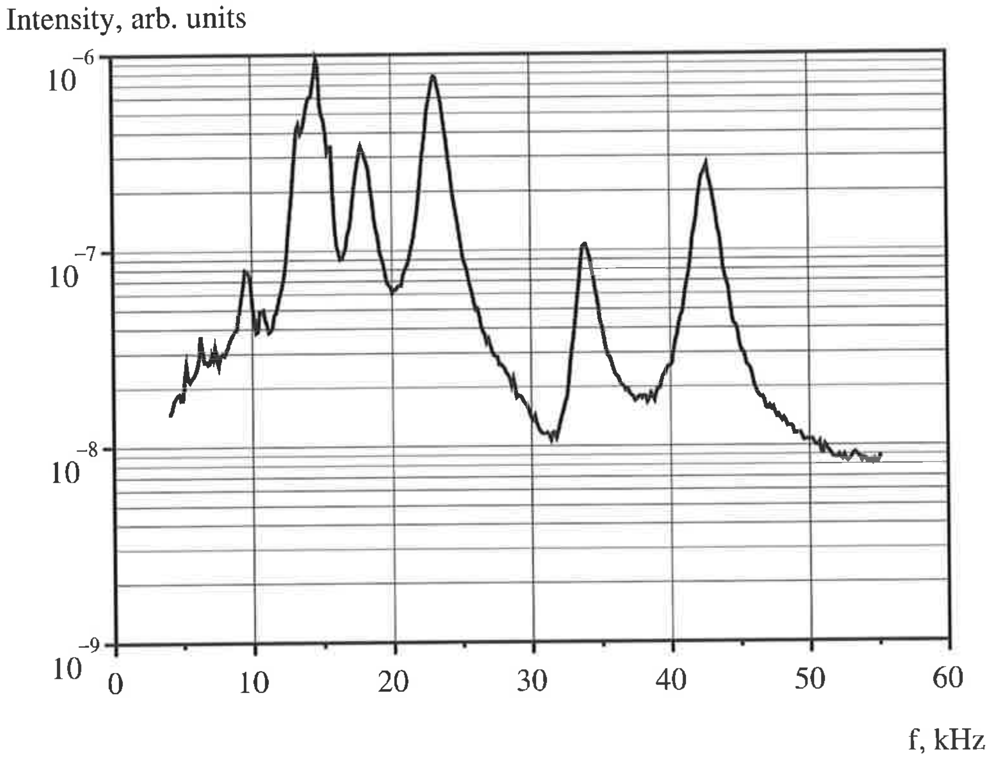

Figure 5-20 Power spectrum of mode 2, measured with channel 2

The power spectra of two different modes of the laser are shown in Figure 5-19 and Figure 5-20. There are 6 low frequency peaks, indicating that the laser was operating on 7 longitudinal modes (the seventh resonant frequency being the relaxation oscillation frequency, not visible in these spectra).

The magnitude of the cross-spectrum (Figure 5-21) is different from the power spectra in that it shows the presence of deep zeroes between the peaks. This appearance is similar to the case of correlated noise in the population inversion and modes (Figure 5-11 in section 5.6.3).

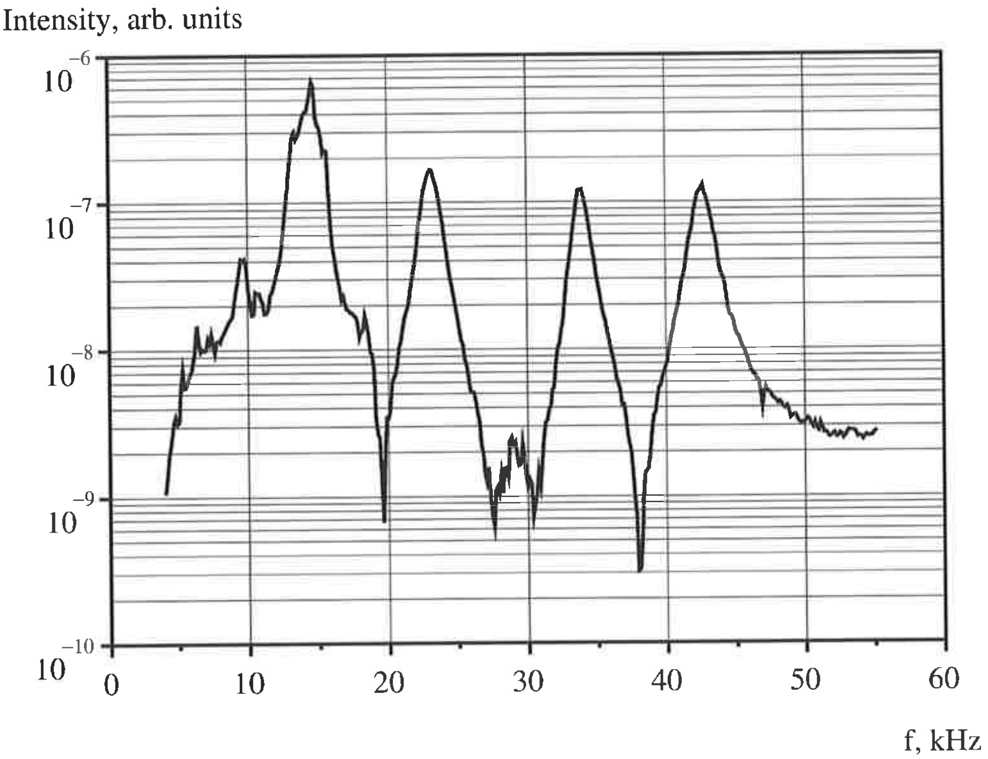

Figure 5-21 Magnitude of the cross-spectrum between modes 1 and 2

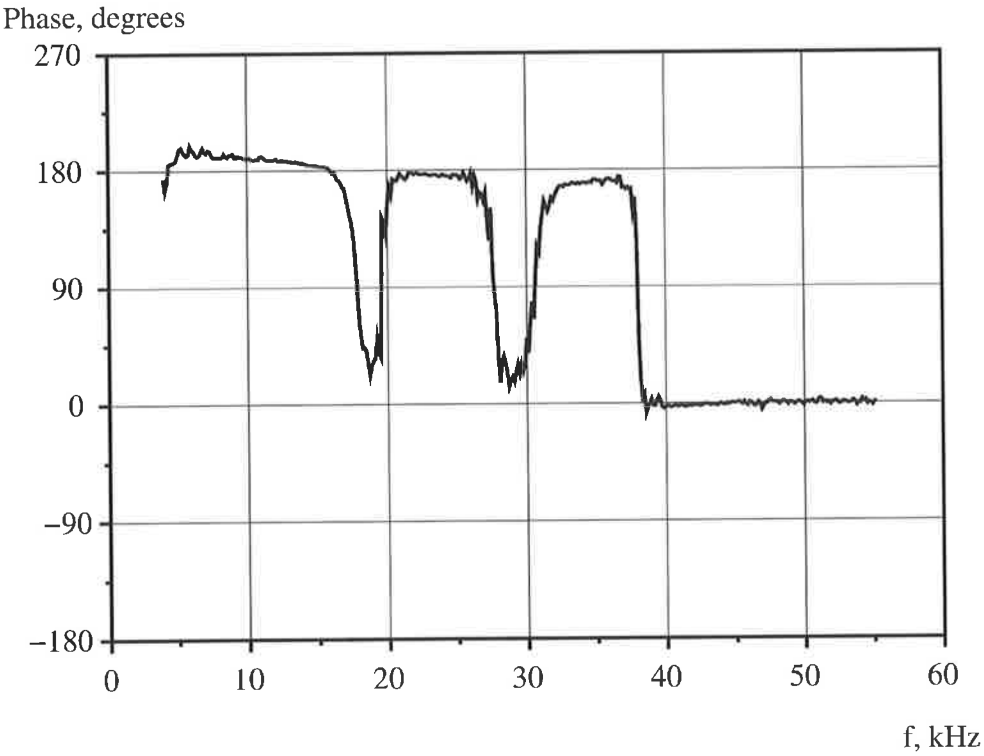

Figure 5-22 Phase of the cross-spectrum between modes 1 and 2

The phase of the measured cross-spectrum was corrected for the phase shift introduced by the electronics and is presented in Figure 5-22. The phase jumps almost all the way between 0°

and 180°, but it also shows some degree of rounding. If compared to the graphs in Figure 5-6 and Figure 5-9 on one hand and that of Figure 5-12 on the other hand, the measured phase is almost in the middle. The more careful measurements presented in [10] and [11] indicate that the phase has jumps rather than gradual changes. This reinforces the similarity between measurements and the correlated noise in population inversion and modal intensities. It is not possible to make any stronger connections based just on similarities, but it can be argued that noise in the pump alone is unlikely to produce this kind of cross-spectra.

5.8 Conclusions

In this chapter we presented arguments for using the noise to investigate the dynamics of the laser. From a theoretical point of view, the noise in lasers has quite profound significations and requires an elaborate mathematical apparatus to reduce the quantum mechanical equations for fields and atoms to the Langevin rate equations. We have explored the results of such calculations and tried to adapt them to our purposes, i.e. the Tang Statz deMars equations with noise. Using a matrix formalism for the calculation of output spectra, we investigated a few simple cases where the input noise was white and of known intensity. The antiphase dynamics of the laser was highlighted and links with other theoretical methods for investigating it were discussed.

Two experimental set-ups for measuring noise were presented and results from each of them were shown and compared to the previous theoretical results. The two detector arrangement permits the measurement of the cross-spectra, who's phase characteristic is particularly useful for the investigation of antiphase dynamics. This set-up was further improved and successfully used for taking complete sets of measurements by Tim Hill.

There are things related to the substance of this chapter that we would have liked to do and decided not to: apply noise to the Tang Statz deMars equations with exponential decay, compare these linearised results with numerical integration of the Langevin rate equations, apply stochastic realisation methods to estimate the laser parameters from measured time series etc. We hope that the work presented here can provide a starting point and stimulate curiosity for more advanced investigations.

Chapter 6 Conclusions

6.1 Summary of Results

This thesis has described the construction of a low-power end pumped Nd:YAG laser and the subsequent theoretical and experimental investigation of the antiphase dynamics exhibited by the laser.

The Nd:YAG laser was specifically designed for the study of non-linear dynamics under the influence of noise. It was pumped at 808 nm by a current and temperature controlled 40 mW single-mode laser diode. The pump beam produced by the laser diode could be modulated with an acousto-optic modulator up to almost 100 kHz. The Nd:YAG laser operated with an input threshold power as low as 9.2 mW and an output power of the order of 2 mW. With appropriate alignment the transverse profile was TEM_{00}, while simultaneously oscillating on up to 11 longitudinal modes. The length of the laser cavity could be finely adjusted with a piezoelectric element for longitudinal mode control and frequency modulation. The total laser output, individual longitudinal modes or pairs of modes (selected with Fabry-Perot filters) could be investigated with suitable detectors and analysing equipment.

The theoretical investigation of antiphase dynamics requires a good model for the laser. The fact that our laser readily oscillated on many frequencies, despite the fact that the material is homogeneously broadened, indicates that the spatial hole burning plays an important role. We used the classical model of Tang Statz deMars as a reference model and then we developed an extension of this model to take explicitly into account the effect of non-uniform (end) pumping. The measured threshold behaviour of the laser was used to test the two models and we found better qualitative agreement between the experiment and the prediction of the end pumped model. We consider that our model, specifically developed for end pumped lasers, is capable of a more accurate description of this type of lasers, compared to other models for longitudinally non-uniform pump.

A convenient method to excite the laser and thus observe antiphase dynamics is to modulate the amplitude of the pump beam. Of many possible test signals such as impulse or step functions, noise, sinusoidal signals, we have chosen the latter. If the modulation index is small enough to keep the response of the laser in the linear regime, the input-output relationship can be described in terms of transfer functions. The experimental technique for the measurement of the transfer functions is fairly straightforward as is the numerical modelling, if the differential equations governing the system dynamics are known. Making educated guesses about the parameters of the laser allowed us to calculate the transfer functions for both the uniformly pumped and the end pumped models, so we can compare them to the measurements.

The transfer function description of the laser, expressed in plots of magnitude and phase versus frequency for each longitudinal mode or total intensity, permits an immediate comparison between measurements and calculations. The pole-zero representation of the transfer functions gives a semi-quantitative explanation for the reduced response of total intensity to modulation in the low-frequency region, in stark contrast to that of the individual modes. When the transfer functions are converted to the pole-residue form, the antiphase dynamics can be understood in more quantitative terms. For example, for each collective mode it is possible to determine the phase and the amplitude of the contributions from each longitudinal mode. Both the numerical calculations and the processed measurements indicate that the antiphase dynamics in our laser is of the cluster type, with either in-phase or out-of phase contributions. To our knowledge, the methods presented here and in the articles we published represent the first case when knowledge of the phase of the transfer functions is used to investigate the antiphase dynamics.

An alternative method to investigate the laser dynamics makes use of the intrinsic noise of the laser. Whether of fundamental (quantum) nature or due to environmental factors, the noise excites the laser and produces a different response in each of the longitudinal modes and in the total intensity. Power spectra of the natural noise of the lasers have been measured and calculated before. What we believe is a new addition to the toolset for investigating antiphase dynamics is the use of cross-spectra between pairs of modes. The cross-spectra supplement the information provided by the power spectra because they convey not only magnitude but also phase information. This allows a better understanding of the mode-to-mode interaction details. Measuring cross-spectra is not difficult, if pairs of modes can be separated from the total intensity and measured simultaneously. However, interpreting the results is a more difficult task.

It is of great advantage to be able to model the response of the laser to noise and to investigate it numerically. This way, the noise can be selectively applied to individual dynamic variables or combinations of dynamic variables, with or without correlations. To this end, we applied to the Tang Statz deMars equations the concepts from the models for quantum noise in the single-mode laser without spatial hole burning. Although the intrinsic level of noise in our laser is much greater then the quantum noise, such a model is useful because it provides an interesting example and a lower limit to the noise level. The linearised model proved to be tractable from a numerical point of view and provided interesting insight into the way the laser responds to noise. It also showed that when multiple sources of noise contribute simultaneously, the notion of antiphase dynamics becomes more complex and power spectra alone are insufficient to capture this complexity. While our measurements were not sufficient for meaningful comparisons with the model, they stimulated further effort and refinement of the experimental set-up, processing methods and interpretation.

6.2 Areas of Further Work

There is no aspect of this work that could not be improved in one way or another: the construction of the laser, the models developed, the measurements taken. There are, however, a few areas were further effort could yield interesting results, most of them related to the last chapter.

Probably the most obvious is the need to check the apparently puzzling results regarding the antiphase between each pair of modes, when noise is applied to all laser modes. This would require an independent method and, most likely, the easiest way to achieve it would be through the direct numerical integration of the non-linear laser equations. Once this question is answered, modifying the end pumped model to include noise would be the next logical step. Given the differences between the results produced by the two models in the case of the transfer functions, we could expect similar things here as well.

To take things one step further, one could consider applying system identification methods to the time series produced by the laser. Of course, these methods could be tested by first applying them to data generated by numerical integration of the differential equations of one laser model or the other. Recovering the parameters used for generating the data with the Tang Statz deMars equations would be a good indication of success. The case of the end pumped model would pose more difficulty, because of the zeros in the right hand side plane. For this situation bi-spectra could be considered.

Appendix 1 Publications

A1.1 Journal Articles

L. Stamatescu and M. W. Hamilton, "Transfer function approach to collective mode dynamics in a Nd:YAG laser", Physical Review E **55**, R2115-R2118, 1997

T. Hill, L. Stamatescu and M. W. Hamilton, "Method for determining antiphase dynamics in a multimode laser", Physical Review E **61**, R4718-R4721, 2000

A1.2 Conference Presentations

L. Stamatescu and M. W. Hamilton, "Transfer function description of antiphase dynamics in a Nd:YAG laser", XX International Quantum Electronics Conference – IQEC'96, Sydney, Australia (1996)

L. Stamatescu, T. Hill and M. W. Hamilton, "The multimode laser as a non-linear oscillator array", XI Australian Optical Society Conference – XI AOS , Adelaide, Australia (1997)

M. W. Hamilton, T. Hill and L. Stamatescu, "Noisy excitation of non-linear oscillator arrays", Unsolved Problems of Noise and Fluctuations – UpoN'99: Second International Conference, Adelaide, Australia (1999)

Appendix 2 Electronic Circuits

A2.1 Current Controller Design

The power supply for the laser diode has undergone several modifications before arriving at the present configuration. The first attempt was to use an optical power controller, where the current through the laser diode was adjusted to maintain the optical output to a constant level. In this arrangement the monitor photodiode was included in the feedback path, as it gave a current proportional to the output power of the laser diode. Although this scheme worked quite well in steady state, it had several drawbacks: it was sensitive to back reflections, to open-circuits in the photodiode connections and the modulation of the output power was difficult to achieve. The second attempt was to use a current controller similar to that described in [78], with the modulation input acting through the feedback loop; this required fast operational amplifiers, leading to stability problems and having a rather high level of noise. The third attempt (illustrated in the Figure A6-1) was a simplified version of the second and employed a slow (DC) feedback controller with direct modulation of the laser diode.

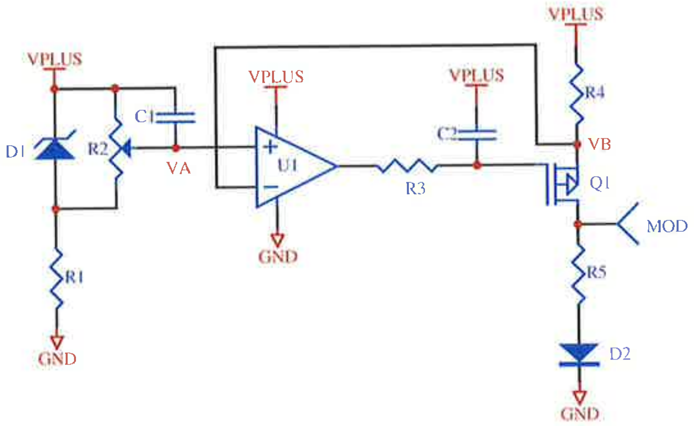

Figure A6-1 Current controller schematic

The operation of the circuit is relatively simple to understand: the voltage reference diode D_1, biased through the resistor R_1, maintains a constant voltage across the potentiometer R_2. With this potentiometer the user selects a certain voltage level (VA) with respect to VPLUS at the non-inverting input of the operational amplifier. The operational amplifier adjusts the gate-source voltage of Q_1, and thus the current through R_4, such that the voltage drop across the resistor (VPLUS - VB) is equal to the potential difference $VSET = VPLUS - VA$. In other words, when the feedback loop is in regulation, the current through R_4 is given by the relation:

$$I = \frac{VSET}{R_4}. \tag{A2-1}$$

Given that the insulation resistance between the gate and the channel of the P MOSFET is essentially infinite, all the current through R_4 must also flow through R_5 and the laser diode D_2. The low-pass filter R_3 - C_2 insures that the frequency response of the feedback loop is limited to very low frequency (DC). Modulation from an external source is applied to the MOD input, with the load seen by this source being about 50Ω (the resistance of R5 plus the incremental resistance of the laser diode).

The current noise of the circuit is dominated at very low frequency by the $1/f$ noise of the operational amplifier and of the FET. At medium and high frequencies the influence of the operational amplifier becomes negligible and the main noise sources are:

- the thermal current noise of the resistor R_4: $i_R = \sqrt{\frac{4kT}{R_4}} \cong 40.7\ \mathrm{pA}/\sqrt{\mathrm{Hz}}$;
- the voltage noise of the FET, transformed into a current and amplified by its own transconductance.

It is interesting to note that, unlike a bipolar transistor, the conducting FET does not have any junctions in the path of the current (the drain, the source and the channel are all p-type semiconductors), so it does not contribute with shot noise to the total noise of the circuit. Also, since the FET acts as a constant current source for the laser diode D_2, it suppresses the shot noise of the junction. For the same reason, the thermal noise of the resistor R_5 does not influence the current through the laser diode. However, at high frequency the output capacitance of the FET short-circuits the internal constant current generator, allowing both the shot noise of the diode and the thermal noise of the resistor to contribute to the current total noise.

A2.2 Temperature Controller Design

The considerations taken into account in the design of the temperature controller were of both electronic and mechanical / thermal nature. While the electronic design was a simple modification of the circuit presented in the Figure 3 of [79], the mechanical / thermal design presented an interesting challenge.

When the electronic circuit was constructed and connected to the heat sink equipped with the thermistor and the heat pump, it turned out that the temperature would oscillate with large amplitude, no matter what settings were chosen for the gains of the integral and proportional stage. The only way to stabilise the system was to reduce the overall gain of the feedback loop to the point where the regulation was almost non-existent. The reason for this behaviour can be understood by comparing the two versions of the laser diode heat sink, shown in Figure A6-2. In the first one, the thermistor is located far away from the heat pump, in the hope that having the laser diode between the two elements would improve the temperature stability. However, the time delay introduced by the distance between the thermistor and the heat pump proved to be fatal for this arrangement. The second arrangement was better, but when the ambient temperature was substantially different from that of the heat sink (generally maintained around 25°C), there was a significant temperature gradient along the heat sink. This meant that despite the good stability of the temperature at the point where the thermistor was, the temperature of the laser diode would be different and would vary with the ambient temperature.

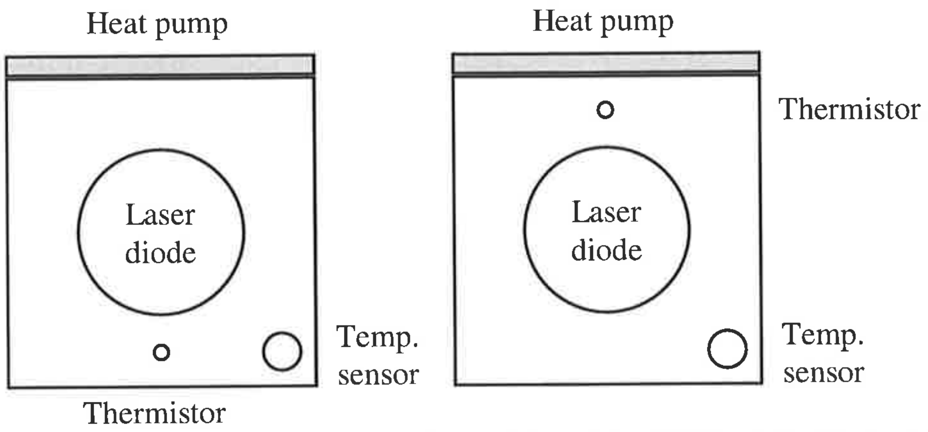

Figure A6-2 Alternative positions of the thermistor with respect to the heat pump

A partial solution to the temperature gradient problem was to use two heat pumps on the opposite sides of the heat sink, as shown in Figure A6-3. This way, due to the symmetry of heat sink, the temperature gradient is stronger side-ways but reduced between the centre (laser diode) and the heat pumps. Electrically, the heat pumps are connected in series and since the thermistor is close to one of them, the stability of the system is still good.

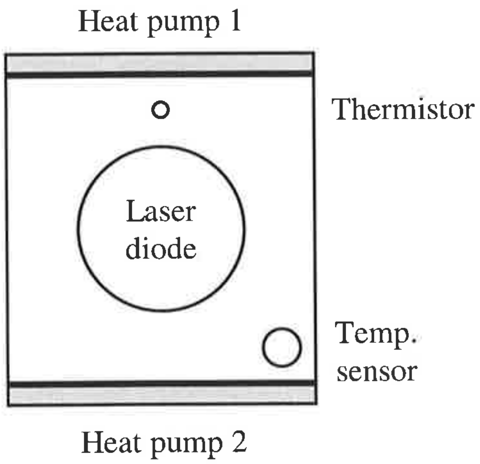

Figure A6-3 Final placement of the temperature control elements

The heat sink (an aluminium cube with 20mm sides) forms the mounting base of the collimator and has mounting holes for the thermistor and a temperature sensor. The latter is an integrated circuit (LM35DZ), which generates a voltage proportional to the temperature of the diode (10 mV/°C); this voltage is directed to the front panel display of the temperature controller where it can be used to display either the laser diode temperature or the error signal in the feedback loop.

A2.3 Photodiode Amplifier Design

When light falls on the photodiode, electron-hole pairs are generated within the depleted region of the *p-n* junction if the energy of the photons is higher than the band-gap of the semiconductor. These pairs are quickly separated by the intense electric field present in the reverse-biased junction. Thus, the current I_{photo} appearing through the photodiode is proportional to the intensity of light and the photodiode behaves like a light controlled current generator in parallel with a semiconductor junction [17]:

$$I = -I_{photo} + I_{dark}\left(e^{qV/kT} - 1\right),$$

(A2-2)

where I_{dark} is the dark current, q is the charge of an electron, k is Boltzman's constant, T is the absolute temperature and V is the voltage across the photodiode. When this voltage is negative and much larger than the thermal voltage $V_T = kT/q$ (about 26 mV at room temperature), the current through the photodiode is:

$$I \cong -I_{photo} - I_{dark}.$$

(A2-3)

The topology chosen for the photodiode amplifiers used in experiments is that of a transimpedance amplifier. This type of amplifier transforms an input current into an output voltage, because the best linearity of the photodiodes is obtained when the current rather than the generated voltage is measured. A simplified schematic of the transimpedance configuration is shown in Figure A6-4.

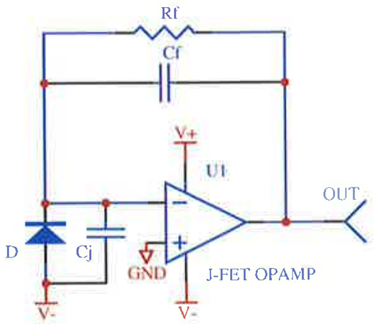

Figure A6-4 Photodiode amplifier schematic

Since the inverting input of the operational amplifier is a virtual ground, the photodiode is reverse biased with a voltage equal to the negative supply *V-*. This has the effect of reducing the capacitance of the junction and thus improves the frequency response of the circuit. When light is shone on the photodiode, the photodiode current tends to pull the inverting input of the operational amplifier below ground level, so the output of the amplifier moves towards the positive supply *V+* sufficiently to produce a current through the resistor R_f equal to the current of the photodiode (no current flows in or out of the J-FET operational amplifier inputs, since they have extremely high impedance). Thus, the output voltage is positive and equal to:

$$V_{out} = -IR_f = \left(I_{photo} + I_{dark}\right)R_f.$$

(A2-4)

The frequency response of the photodiode amplifier depends on the capacitance of the photodiode C_j and the required gain of the system. We can assume that the operational amplifier has a single-pole open loop gain, which can be expressed as:

$$G(s) = \frac{2\pi GBW}{s + p}.$$

(A2-5)

Here *GBW* is the gain-bandwidth product and *p* is the pole of the amplifier (generally situated at very low frequency). The transfer function of the transimpedance amplifier can be written as [17]:

$$\frac{V_0(s)}{I(s)} = \frac{\omega_0^2}{s^2 + 2\zeta\omega_0 s + \omega_0^2} R_f .$$

(A2-6)

This second order system has a natural frequency ω_0 given by:

$$\omega_0{}^2 = \frac{2\pi GBW}{R_f\left(C_j + C_f\right)}$$

(A2-7)

and the damping ζ given by:

$$\zeta = C_f \sqrt{\frac{\pi GBW R_f}{2\left(C_j + C_f\right)}} .$$

(A2-8)

In order to obtain a frequency response as flat as possible, one would use critical damping ($\zeta = 1$) and the required feedback capacitance is:

$$C_f = \frac{1 + \sqrt{1 + 2\pi GBW R_f C_j}}{2\pi GBW R_f} .$$

(A2-9)

As an example, we design a photodiode amplifier for detecting the total intensity of the Nd:YAG laser. Since the output power of the laser is less than 2 mW and the power density should be kept below 10 mW/cm^2 to avoid saturation of the photodiode, the minimum junction area should be about 20 mm^2. The PIN-6DI photodiode manufactured by UDT Sensors, Inc has the required area and, having a responsivity of about 0.2 A/W at 1064 nm, we can expect a maximum current of 0.4 mA. A feedback resistor $R_f = 20\ \text{k}\Omega$ would give a maximum output voltage of about 8V, which is within the range of an operational amplifier supplied with ±12V. A suitable device is AD745 from Analog Devices, a fast JFET input, ultra low noise operational amplifier. As its gain-bandwidth is 20 MHz, the feedback capacitance can be calculated according to the relation (A2-9), knowing that the capacitance of the junction at 10V reverse bias is 60 pF and the input capacitance of the operational amplifier is 20 pF (the two appear in parallel, so $C_j = 80$ pF). The result is $C_f = 6$ pF and the natural frequency calculated with (A2-7) is $f_0 = 1.36$ MHz.

A Spice simulation of the circuit has shown that the calculated value of the feedback capacitance gives some peaking, while $C_f = 7.5$ pF gives a flat response with a -3 dB frequency of 1.716 MHz. This deviation from the calculated values is not surprising, as the operational amplifier has a several poles and zeroes in the vicinity of the cut-off frequency.

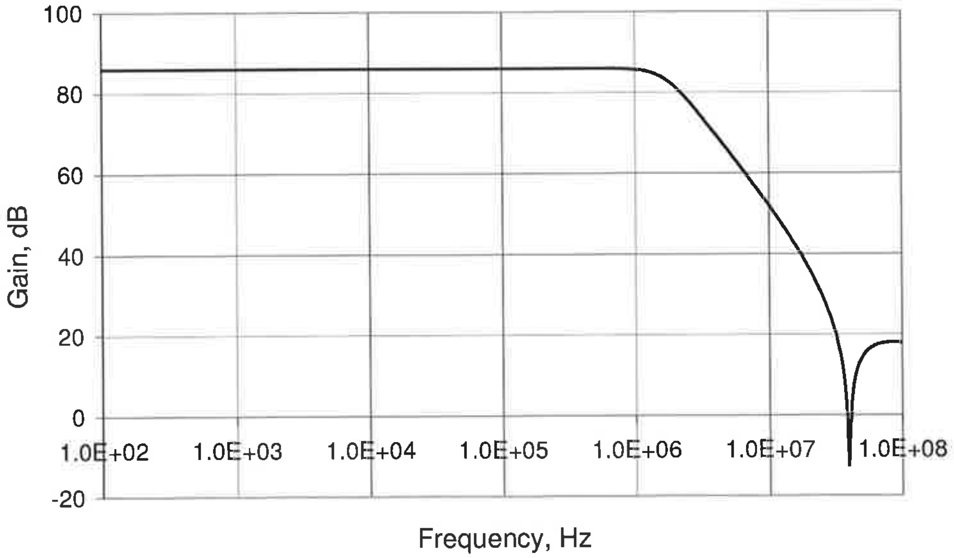

Figure A6-5 Simulation of the transconductance amplifier frequency response (magnitude)

The frequency response of the photodiode amplifier is shown in Figure A6-5 (the gain) and Figure A6-6 (the phase). It is visible that while the gain is flat to above 1 MHz, the phase starts deviating from zero between 10 and 100 kHz.

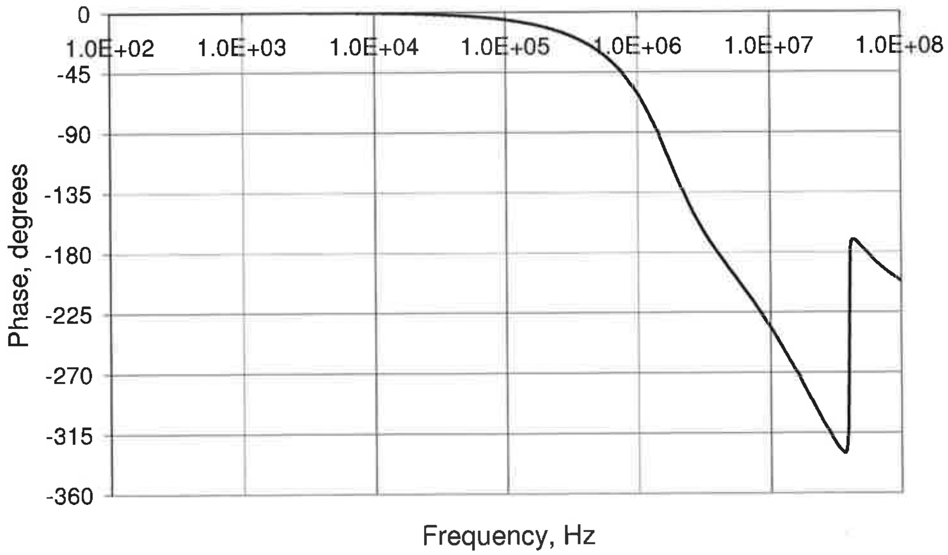

Figure A6-6 Simulation of the transconductance amplifier frequency response (phase)

The output noise of the photodiode amplifier (without the contribution from the photodiode) is shown in Figure A6-7. At medium frequencies (around 10 kHz) the noise is the result of the uncorrelated contributions of the following sources:

- thermal noise of the resistor: $\tilde{N} = \sqrt{4kTR_f} \cong 18.2\,\mathrm{nV}/\sqrt{\mathrm{Hz}}$;
- voltage noise of the operational amplifier: $e_n = 2.9\,\mathrm{nV}/\sqrt{\mathrm{Hz}}$;
- current noise of the operational amplifier times feedback resistor: $i_n R_f = 0.14\,\mathrm{nV}/\sqrt{\mathrm{Hz}}$.

The total output noise is given by:

$$v_n = \sqrt{\tilde{N}^2 + e_n^{\,2} + i_n^{\,2} R_f^{\,2}} \cong 18.4\,\mathrm{nV}/\sqrt{\mathrm{Hz}}\,,$$

(A2-10)

which translates into $0.922\,\mathrm{pA}/\sqrt{\mathrm{Hz}}$ equivalent current noise (referred to input). For comparison, the shot noise corresponding to the maximum photocurrent (0.4 mA) is about $11.3\,\mathrm{pA}/\sqrt{\mathrm{Hz}}$.

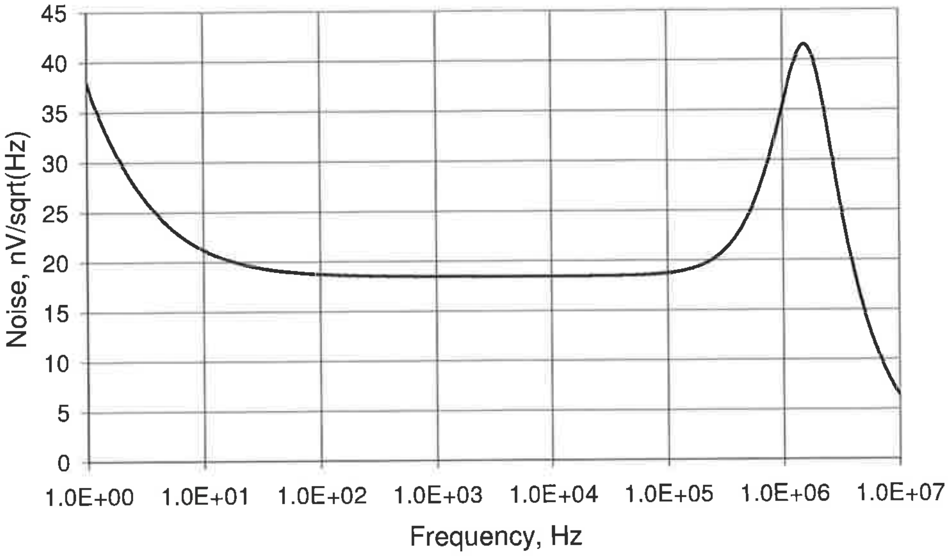

Figure A6-7 Output noise of the photodiode amplifier

At lower frequencies (below 100 Hz) the noise increases due to the flicker noise of the operational amplifier, while at high frequency the increase is due to the noise gain of the amplifier – at high frequency the amplifier is no longer a voltage follower, it has a gain given by the ratio of the reactance of C_f over that of C_j. However, as the frequency increases, the gain of the amplifier rolls off and the output noise decreases accordingly.

A complete schematic of the photodiode amplifier, including the decoupling components, the nulling circuit and a test input is shown in the Figure A6-8.

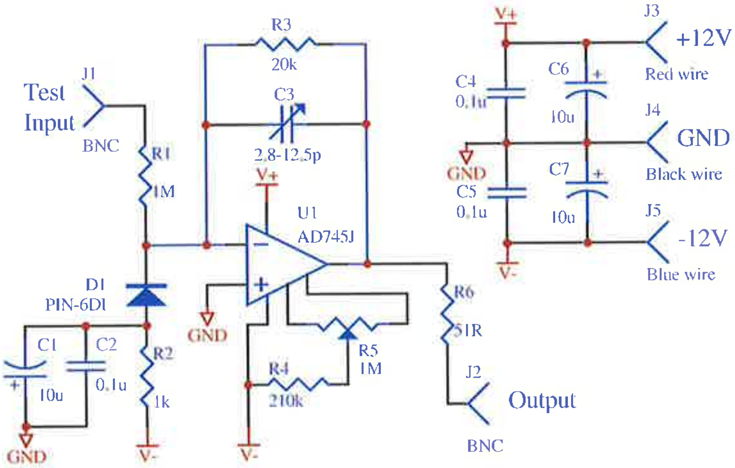

Figure A6-8 Photodiode amplifier schematic

The amplitude and the phase response of the circuit can be measured by applying a sinusoidal signal at the test input and sweeping the frequency.

Appendix 3 Model Calculations

A3.1 Deduction of the Tang Statz deMars Equations

We start from the equations (3-36) and (3-37), reproduced here for convenience:

$$\frac{\mathrm{d}n_0(t)}{\mathrm{d}t}+\sum_{i=1}^{N}\frac{\mathrm{d}n_i(t)}{\mathrm{d}t}\cos(2k_iz)=\frac{1}{\tau_f}\left\{w(t)-n_0(t)-\sum_{i=1}^{N}n_i(t)\cos(2k_iz)-\right.$$
$$\left.-\sum_{k=1}^{N}g_k\left[n_0(t)+\sum_{i=1}^{N}n_i(t)\cos(2k_iz)\right]i_k(t)(1-\cos 2k_kz)\right\}$$

(A3-11)

$$\frac{\mathrm{d}i_j(t)}{\mathrm{d}t}=\frac{1}{\tau_c}\left[g_ji_j(t)n_0(t)\int_0^{L_{optic}}(1-\cos 2k_jz)dz+\right.$$
$$\left.+g_ji_j(t)\sum_{k=1}^{N}n_k(t)\int_0^{L_{optic}}\cos 2k_kz(1-\cos 2k_jz)dz-i_j(t)\right].$$

(A3-12)

The first equation can be integrated over the whole length of the cavity:

$$\int_0^{L_{optic}}\frac{\mathrm{d}n_0(t)}{\mathrm{d}t}\mathrm{d}z+\sum_{i=1}^{N}\int_0^{L_{optic}}\frac{\mathrm{d}n_i(t)}{\mathrm{d}t}\cos(2k_iz)\,\mathrm{d}z=\frac{1}{\tau_f}\left[\int_0^{L_{optic}}w(t)\,\mathrm{d}z-\int_0^{L_{optic}}n_0(t)\,\mathrm{d}z-\right.$$
$$-\sum_{i=1}^{N}\int_0^{L_{optic}}n_i(t)\cos(2k_iz)\mathrm{d}z-\sum_{k=1}^{N}\int_0^{L_{optic}}g_kn_0(t)i_k(t)\mathrm{d}z+\sum_{k=1}^{N}\int_0^{L_{optic}}g_kn_0(t)i_k(t)\cos(2k_kz)\mathrm{d}z-$$
$$-\sum_{i=1}^{N}\sum_{k=1}^{N}\int_0^{L_{optic}}g_kn_i(t)i_k(t)\cos(2k_iz)\mathrm{d}z+\sum_{i=1}^{N}\sum_{k=1}^{N}\int_0^{L_{optic}}g_kn_i(t)i_k(t)\cos(2k_iz)\cos(2k_kz)\mathrm{d}z.$$

(A3-13)

As the variables w, n_0, n_i, i_k are only functions of time, the integrals can be evaluated without too much difficulty. We need to calculate a few integrals that appear repeatedly and this can be done based on the assumptions mentioned in section 3.3.2, in particular on (3-30):

$$\int_0^{L_{optic}}\mathrm{d}z=L_{optic}$$

(A3-14)

$$\int_0^{L_{optic}}\cos(2k_iz)\,\mathrm{d}z=0$$

(A3-15)

$$\int_0^{L_{optic}}\cos(2k_iz)\cos(2k_kz)\,\mathrm{d}z=\frac{1}{2}\delta_{ik}L_{optic}.$$

(A3-16)

Using these results, we obtain the first of the Tang Statz deMars equations:

$$\frac{\mathrm{d}\,n_0(t)}{\mathrm{d}\,t}=\frac{1}{\tau_f}\left\{w(t)-n_0(t)-\sum_{k=1}^{N} g_k\left[n_0(t)-1/2\,n_k(t)\right]i_k(t)\right\}.$$

(A3-17)

The first equation can also be multiplied by $\cos(2k_j z)$ and integrated over the whole length of the cavity:

$$\int_0^{L_{optic}}\frac{\mathrm{d}\,n_0(t)}{\mathrm{d}\,t}\cos(2k_j z)\,\mathrm{d}\,z+\sum_{i=1}^{N}\int_0^{L_{optic}}\frac{\mathrm{d}\,n_i(t)}{\mathrm{d}\,t}\cos(2k_i z)\cos(2k_j z)\,\mathrm{d}\,z=$$
$$=\frac{1}{\tau_f}\left[\int_0^{L_{optic}} w(t)\cos(2k_j z)\,\mathrm{d}\,z-\int_0^{L_{optic}} n_0(t)\cos(2k_j z)\,\mathrm{d}\,z-\right.$$
$$-\sum_{i=1}^{N}\int_0^{L_{optic}} n_i(t)\cos(2k_i z)\cos(2k_j z)\mathrm{d}\,z-\sum_{k=1}^{N}\int_0^{L_{optic}} g_k n_0(t) i_k(t)\cos(2k_j z)\mathrm{d}\,z+$$
$$+\sum_{k=1}^{N}\int_0^{L_{optic}} g_k n_0(t) i_k(t)\cos(2k_k z)\cos(2k_j z)\mathrm{d}\,z-\sum_{i=1}^{N}\sum_{k=1}^{N}\int_0^{L_{optic}} g_k n_i(t) i_k(t)\cos(2k_i z)\cos(2k_j z)\mathrm{d}\,z+$$
$$\left.+\sum_{i=1}^{N}\sum_{k=1}^{N}\int_0^{L_{optic}} g_k n_i(t) i_k(t)\cos(2k_i z)\cos(2k_k z)\cos(2k_j z)\mathrm{d}\,z\right].$$

(A3-18)

Following the same arguments as above, we can separate the temporal and spatial variables and calculate the integral:

$$\int_0^{L_{optic}}\cos(2k_i z)\cos(2k_k z)\cos(2k_j z)\,\mathrm{d}\,z=0.$$

(A3-19)

Using this result, (A3-15) and (A3-16), we can obtain the second of the Tang Statz deMars equations:

$$\frac{\mathrm{d}\,n_j(t)}{\mathrm{d}\,t}=\frac{1}{\tau_f}\left\{g_j n_0(t) i_j(t)-n_j(t)\left[1+\sum_{k=1}^{N} g_k i_k(t)\right]\right\}.$$

(A3-20)

The third of the Tang Statz deMars equations can be obtained immediately by integrating the equation corresponding to the modal intensity:

$$\frac{\mathrm{d}\,i_j(t)}{\mathrm{d}\,t}=\frac{1}{\tau_c}\left\{g_j\left[n_0(t)-1/2\,n_j(t)\right]-1\right\}i_j(t).$$

(A3-21)

A3.2 Deduction of the Tang Statz deMars Equations with Exponential Decay

We start from the equations (3-63) and (3-64), reproduced here for convenience:

$$\frac{\mathrm{d}n_0(t)}{\mathrm{d}t}+\sum_{i=1}^{N}\frac{\mathrm{d}n_i(t)}{\mathrm{d}t}\cos(2k_iz)=\frac{1}{\tau_f}\Bigg\{w(t)-n_0(t)-\sum_{i=1}^{N}n_i(t)\cos(2k_iz)-$$
$$-\sum_{k=1}^{N}g_k\left[n_0(t)+\sum_{i=1}^{N}n_i(t)\cos(2k_iz)\right]i_k(t)(1-\cos 2k_kz)\Bigg\}$$

(A3-22)

$$\frac{\mathrm{d}i_j(t)}{\mathrm{d}t}=\frac{1}{\tau_c}\Bigg[g_ji_j(t)n_0(t)\mu\int_0^{L_{optic}}(1-\cos 2k_jz)\exp(-\mu z)dz+$$
$$+g_ji_j(t)\sum_{k=0}^{N}n_k(t)\mu\int_0^{L_{optic}}\cos(2k_kz)(1-\cos 2k_jz)\exp(-\mu z)dz-i_j(t)\Bigg].$$

(A3-23)

As in Appendix A3.1, from the first equation we obtain equations for the time derivatives of the average and the components of the population inversion:

$$\frac{\mathrm{d}n_0(t)}{\mathrm{d}t}=\frac{1}{\tau_f}\left\{w(t)-n_0(t)-\sum_{k=1}^{N}g_k\left[n_0(t)-1/2\,n_k(t)\right]i_k(t)\right\}$$

(A3-24)

$$\frac{\mathrm{d}n_j(t)}{\mathrm{d}t}=\frac{1}{\tau_f}\left\{g_jn_0(t)i_j(t)-n_j(t)\left[1+\sum_{k=1}^{N}g_ki_k(t)\right]\right\}.$$

(A3-25)

For the second equation, we need the following integrals:

$$\mu\int_0^{L_{optic}}\exp(-\mu z)\,\mathrm{d}z=-\exp(-\mu z)\Big|_0^{L_{optic}}\approx 1$$

(A3-26)

$$\mu\int_0^{L_{optic}}\cos(2k_jz)\exp(-\mu z)\,\mathrm{d}z=\mu\frac{\left(2k_j\sin 2k_jz-\mu\cos 2k_jz\right)\exp(-\mu z)}{\left(\mu^2+4k_j^2\right)}\Bigg|_0^{L_{optic}}\approx$$
$$\approx\frac{\mu^2}{\left(\mu^2+4k_j^2\right)}\approx 0$$

(A3-27)

$$\mu\int_0^{L_{optic}}\cos(2k_kz)\cos(2k_jz)\exp(-\mu z)\,\mathrm{d}z=$$
$$=\frac{\mu}{2}\int_0^{L_{optic}}\cos\left[2\left(k_k+k_j\right)z\right]\exp(-\mu z)\,\mathrm{d}z+\frac{\mu}{2}\int_0^{L_{optic}}\cos\left[2\left(k_k-k_j\right)z\right]\exp(-\mu z)\,\mathrm{d}z=$$
$$=\mu\frac{\left\{2\left(k_k+k_j\right)\sin\left[2\left(k_k+k_j\right)z\right]-\mu\cos\left[2\left(k_k+k_j\right)z\right]\right\}\exp(-\mu z)}{2\left[\mu^2+4\left(k_k+k_j\right)^2\right]}\Bigg|_0^{L_{optic}}+$$

$$+\mu \left. \frac{\left\{2(k_k-k_j)\sin\left[2(k_k-k_j)z\right]-\mu\cos\left[2(k_k-k_j)z\right]\right\}\exp(-\mu z)}{2\left[\mu^2+4(k_k-k_j)^2\right]} \right|_0^{L_{optic}} \approx$$

$$\approx \frac{\mu^2}{2\left[\mu^2+4(k_k+k_j)^2\right]}+\frac{\mu^2}{2\left[\mu^2+4(k_k-k_j)^2\right]} \approx$$

$$\approx \frac{1}{2\left[1+4\dfrac{\pi^2(m_k-m_j)^2}{\mu^2 L_{optic}^2}\right]}.$$

(A3-28)

Using these results, we can get the equations for the time derivatives of the modal intensities (3-67):

$$\frac{\mathrm{d}i_j(t)}{\mathrm{d}t}=\frac{1}{\tau_c}\left\{g_j\left[n_0(t)-1/2\sum_{k=1}^{N}\frac{n_k(t)}{1+4\dfrac{\pi^2(m_k-m_j)^2}{\mu^2 L_{optic}^2}}\right]-1\right\}i_j(t).$$

(A3-29)

Appendix 4 Jacobian Calculations

A4.1 Jacobian Matrix for the Tang Statz deMars Equations

We present here the results of the calculations for the Jacobian matrix of a system modelled with the Tang Statz deMars equations. The matrix is given by:

$$\mathbf{A}=\left(\frac{\partial\,\mathbf{F}(\mathbf{x})}{\partial\,\mathbf{x}}\right)\Bigg|_{\mathbf{x}=\mathbf{x}^0},\tag{A4-1}$$

where $\mathbf{F}(\mathbf{x})$ is the right hand side of the Tang Statz deMars equations, and $\mathbf{x}^0$ is the steady state solution around which the linearisation is required. For the convenience of the calculations, the Jacobian matrix can be divided into several blocks:

$$\mathbf{A}=\left|\begin{array}{c:cccc:ccc}
a_{1,1} & a_{1,2} & \cdots & a_{1,N+1} & a_{1,N+2} & \cdots & a_{1,2N+1} \\
\hdashline
a_{2,1} & a_{2,2} & \cdots & a_{2,N+1} & a_{2,N+2} & \cdots & a_{2,2N+1} \\
\vdots & \vdots & & \vdots & \vdots & & \vdots \\
a_{N+1,1} & a_{N+1,2} & \cdots & a_{N+1,N+1} & a_{N+1,N+2} & \cdots & a_{N+1,2N+1} \\
\hdashline
a_{N+2,1} & a_{N+2,2} & \cdots & a_{N+2,1N+1} & a_{N+2,N+2} & \cdots & a_{N+2,2N+1} \\
\vdots & \vdots & & \vdots & \vdots & & \vdots \\
a_{2N+1,1} & a_{2N+1,2} & \cdots & a_{2N+1,N+1} & a_{2N+1,N+2} & \cdots & a_{2N+1,2N+1}
\end{array}\right|.\tag{A4-2}$$

Using this division, the elements of the matrix can be expressed as:

$$a_{1,1}=-\frac{1+\sum_{k=1}^{N}g_k i_k}{\tau_f}$$

$$a_{1,j+1}=\frac{g_j i_j}{2\tau_f},\ j=1\cdots N$$

$$a_{1,j+N+1}=-\frac{1}{\tau_f},\ j=1\cdots N$$

$$a_{i+1,1}=\frac{g_i i_i}{\tau_f},\ i=1\cdots N$$

$$a_{i+1,j+1}=-\frac{1+\sum_{k=1}^{N}g_k i_k}{\tau_f}\delta_{i,j},\ i,j=1\cdots N$$

$$a_{i+1,j+N+1}=\frac{-g_j n_i+g_j n_0\delta_{i,j}}{\tau_f},\ i,j=1\cdots N$$

$$a_{i+N+1,1}=\frac{g_i i_i}{\tau_c},\ i=1\cdots N$$

$$a_{i+N+1,j+1}=-\frac{g_i i_i\delta_{i,j}}{2\tau_c},\ i,j=1\cdots N$$

$$a_{i+N+1,j+N+1}=0,\ i,j=1\cdots N.$$

(A4-3)

In the above equations, n_0, n_i and i_i, $i=1\cdots N$ represent the components of the steady state vector $\mathbf{x}^0$.

A4.2 Jacobian Matrix for the Tang Statz deMars Equations with Exponential Decay

We present here the results of the calculations for the Jacobian matrix of a system modelled with the Tang Statz deMars equations with exponential decay. This matrix is given by:

$$\mathbf{A}=\left.\left(\frac{\partial\,\mathbf{F}(\mathbf{x})}{\partial\,\mathbf{x}}\right)\right|_{\mathbf{x}=\mathbf{x}^0},$$

(A4-4)

where $\mathbf{F}(\mathbf{x})$ is the right hand side of the Tang Statz deMars equations with exponential decay, and $\mathbf{x}^0$ is the steady state solution around which the linearisation is required. For the convenience of the calculations, the Jacobian matrix can be divided into several blocks:

$$\mathbf{A}=\left|\begin{array}{c|ccc|ccc}
a_{1,1} & a_{1,2} & \cdots & a_{1,N+1} & a_{1,N+2} & \cdots & a_{1,2N+1}\\
\hline
a_{2,1} & a_{2,2} & \cdots & a_{2,N+1} & a_{2,N+2} & \cdots & a_{2,2N+1}\\
\vdots & \vdots & & \vdots & \vdots & & \vdots\\
a_{N+1,1} & a_{N+1,2} & \cdots & a_{N+1,N+1} & a_{N+1,N+2} & \cdots & a_{N+1,2N+1}\\
\hline
a_{N+2,1} & a_{N+2,2} & \cdots & a_{N+2,1N+1} & a_{N+2,N+2} & \cdots & a_{N+2,2N+1}\\
\vdots & \vdots & & \vdots & \vdots & & \vdots\\
a_{2N+1,1} & a_{2N+1,2} & \cdots & a_{2N+1,N+1} & a_{2N+1,N+2} & \cdots & a_{2N+1,2N+1}
\end{array}\right|.$$

(A4-5)

Using this division, the elements of the matrix can be expressed as:

$$a_{1,1}=-\frac{1+\sum_{k=1}^{N}g_k i_k}{\tau_f}$$

$$a_{1,j+1}=\frac{g_j i_j}{2\tau_f},\ j=1\cdots N$$

$$a_{1,j+N+1}=-\frac{g_j\left(n_0-1/2n_j\right)}{\tau_f},\ j=1\cdots N$$

$$a_{i+1,1}=\frac{g_i i_i}{\tau_f},\ i=1\cdots N$$

$$a_{i+1,j+1}=-\frac{1+\sum_{k=1}^{N}g_k i_k}{\tau_f}\delta_{i,j},\ i,j=1\cdots N$$

$$a_{i+1,j+N+1}=\frac{-g_j n_i+g_j n_0\delta_{i,j}}{\tau_f},\ i,j=1\cdots N$$

$$a_{i+N+1,1} = \frac{g_i i_i}{\tau_c},\ i = 1 \cdots N$$

$$a_{i+N+1,j+1} = -\frac{g_i i_i}{2\tau_c \left[1 + q^2 \left(m_j - m_i\right)^2\right]},\ i, j = 1 \cdots N$$

$$a_{i+N+1,j+N+1} = 0,\ i, j = 1 \cdots N.$$

(A4-6)

In the above equations, n_0, n_i and i_i, $i = 1 \cdots N$ represent the components of the steady state vector $\mathbf{x}^0$.

Appendix 5 Noise Calculations

A5.1 Deduction of the Tang Statz deMars Equations with Noise

We start from the equations (5-30) and (5-31):

$$\frac{\mathrm{d}\,N_0(t)}{\mathrm{d}\,t}+\sum_{j=1}^{M}\frac{\mathrm{d}\,N_j(t)}{\mathrm{d}\,t}\cos(2k_jz)=W(t)-\frac{N_0(t)}{\tau_f}-\frac{1}{\tau_f}\sum_{j=1}^{M}N_j(t)\cos(2k_jz)-$$
$$-\pi\sum_{k=1}^{M}g_k\left[N_0(t)+\sum_{j=1}^{M}N_j(t)\cos(2k_jz)\right]P_k(t)(1-\cos 2k_kz)+r(t)$$

(A5-1)

$$\frac{\mathrm{d}\,P_j(t)}{\mathrm{d}\,t}=\pi g_jP_j(t)\frac{N_0(t)}{L_{optic}}\int_0^{L_{optic}}(1-\cos 2k_jz)dz+$$
$$+\pi g_jP_j(t)\sum_{k=1}^{M}\frac{N_k(t)}{L_{optic}}\int_0^{L_{optic}}\cos 2k_kz(1-\cos 2k_jz)dz-\frac{P_j(t)}{\tau_c}+s(t).$$

(A5-2)

The first equation can be integrated over the whole length of the cavity:

$$\frac{\mathrm{d}\,N_0(t)}{\mathrm{d}\,t}\int_0^{L_{optic}}\mathrm{d}\,z+\sum_{j=1}^{M}\frac{\mathrm{d}\,N_j(t)}{\mathrm{d}\,t}\int_0^{L_{optic}}\cos(2k_jz)\mathrm{d}\,z=W(t)\int_0^{L_{optic}}\mathrm{d}\,z-\frac{N_0(t)}{\tau_f}\int_0^{L_{optic}}\mathrm{d}\,z-$$
$$-\frac{1}{\tau_f}\sum_{j=1}^{M}N_j(t)\int_0^{L_{optic}}\cos(2k_jz)\mathrm{d}\,z-\pi N_0(t)\sum_{k=1}^{M}g_kP_k(t)\int_0^{L_{optic}}\mathrm{d}\,z+$$
$$+\pi N_0(t)\sum_{k=1}^{M}g_kP_k(t)\int_0^{L_{optic}}\cos(2k_jz)\mathrm{d}\,z-\pi\sum_{k=1}^{M}\sum_{j=1}^{M}g_kN_j(t)P_k(t)\int_0^{L_{optic}}\cos(2k_jz)\mathrm{d}\,z+$$
$$+\pi\sum_{k=1}^{M}\sum_{j=1}^{M}g_kN_j(t)P_k(t)\int_0^{L_{optic}}\cos(2k_kz)\cos(2k_jz)\mathrm{d}\,z+r(t)\int_0^{L_{optic}}\mathrm{d}\,z\,.$$

(A5-3)

Using (A3-14), (A3-15) and (A3-16), the above equation can be reduced to:

$$\frac{\mathrm{d}\,N_0(t)}{\mathrm{d}\,t}=W(t)-\frac{N_0(t)}{\tau_f}-\pi\sum_{j=1}^{M}g_j[N_0(t)-1/2\,N_j(t)]P_j+r(t).$$

(A5-4)

Multiplying the first equation by $\cos(2k_iz)$ and integrating over the length of the cavity we get:

$$
\begin{aligned}
&\frac{\mathrm{d}\,N_0(t)}{\mathrm{d}\,t}\int_0^{L_{optic}}\cos(2k_i z)\,\mathrm{d}\,z+\sum_{j=1}^{M}\frac{\mathrm{d}\,N_j(t)}{\mathrm{d}\,t}\int_0^{L_{optic}}\cos(2k_j z)\cos(2k_i z)\,\mathrm{d}\,z=W(t)\int_0^{L_{optic}}\cos(2k_i z)\,\mathrm{d}\,z-\\
&\quad-\frac{N_0(t)}{\tau_f}\int_0^{L_{optic}}\cos(2k_i z)\,\mathrm{d}\,z-\frac{1}{\tau_f}\sum_{j=1}^{M}N_j(t)\int_0^{L_{optic}}\cos(2k_j z)\cos(2k_i z)\,\mathrm{d}\,z-\\
&\quad-\pi N_0(t)\sum_{k=1}^{M}g_k P_k(t)\int_0^{L_{optic}}\cos(2k_i z)\mathrm{d}\,z+\pi N_0(t)\sum_{k=1}^{M}g_k P_k(t)\int_0^{L_{optic}}\cos(2k_k z)\cos(2k_i z)\mathrm{d}\,z-\\
&\quad-\pi\sum_{k=1}^{M}\sum_{j=1}^{M}g_k N_j(t)P_k(t)\int_0^{L_{optic}}\cos(2k_j z)\cos(2k_i z)\mathrm{d}\,z+\\
&\quad+\pi\sum_{k=1}^{M}\sum_{j=1}^{M}g_k N_j(t)P_k(t)\int_0^{L_{optic}}\cos(2k_k z)\cos(2k_j z)\cos(2k_i z)\mathrm{d}\,z+r(t)\int_0^{L_{optic}}\cos(2k_i z)\mathrm{d}\,z\,.
\end{aligned}
\tag{A5-5}
$$

Using again (A3-14), (A3-15), (A3-16) and (A3-19) we obtain:

$$
\frac{\mathrm{d}\,N_i(t)}{\mathrm{d}t}=\pi g_i N_0(t)P_i(t)-N_i(t)\left[\frac{1}{\tau_f}-\pi\sum_{k=1}^{M}g_k P_k(t)\right].
\tag{A5-6}
$$

Finally, using (A3-14), (A3-15) and (A3-16) in (A5-2) we obtain:

$$
\frac{\mathrm{d}\,P_j(t)}{\mathrm{d}t}=\pi g_j\left[N_0(t)-1/2\,N_j(t)\right]P_j(t)-\frac{P_j(t)}{\tau_c}+s(t).
\tag{A5-7}
$$

Bibliography

1 H. D. I. Abarbanel, R. Brown and L. Sh. Tsimring, Reviews of Modern Physics **65**, 1331 (1993)
2 D. Maza, S. Boccaletti and H. Mancini, International Journal of Bifurcation and Chaos **10**, 829 (2000)
3 Y. Loewenstein, Y. Yarom and H. Sompolinsky, Proceedings of the National Academy of Sciences **98**, 8095 (2001)
4 P. Hadley and M. R. Beasly, Applied Physics Letters **50**, 621 (1987)
5 P. Hadley, M. R. Beasly and K Wiesenfeld, Physical Review B **38**, 8712 (1988)
6 K. Wiesenfeld, C. Bracikowski, G. James and R. Roy, Physical Review Letters **65**, 1749 (1990)
7 C. L. Tang, H. Statz and G. deMars, Journal of Applied Physics **34**, 2289 (1963)
8 L. Stamatescu and M. Hamilton, Physical Review E **55**, R2115 (1997)
9 Scilab 2.5 (free scientific software package), INRIA France (1999)
10 T. Hill, L. Stamatescu and M. Hamilton, Physical Review E **61**, R4718 (2000)
11 T. Hill, M. Hamilton, D. Pieroux and P. Mandel, Physical Review A **66**, 063803 (2002)
12 W. Koechner, Solid state Laser Engineering, Springer Series in Optical Sciences, Vol. 1, Springer-Verlag, NY, Heidelberg, Berlin (1976)
13 P. Nachman, J. Munch and R. Yee, IEEE Journal of Quantum Electronics **26**, 317 (1990)
14 D.L. Sipes, Applied Physics Letters **47**, 74 (1985)
15 N.P. Barnes, M.E. Storm, P.L. Cross and M.W. Skolaut, IEEE Journal of Quantum Electronics **26**, 558 (1990)
16 Laser Diode User's Manual, Sharp Corporation, Japan (1988)
17 Optics Guide 5, Melles Griot (1990)
18 Paraxia (laser resonator and beam propagation software), SCIOPT Enterprises, San Jose CA, 95160 USA.
19 F. L. Pedrotti and L. S. Pedrotti, Introduction to Optics (2nd ed.), Prentice-Hall, Upper Saddle River, New Jersey (1993)
20 A.E. Siegman, M.W. Sasnett and T.F. Johnston, IEEE Journal of Quantum Electronics **27**, 1098 (1991)
21 C.B. Roundy, G.E. Slobodzian, K. Jensen and D. Ririe, Laser Focus World **10**, 117 (1993)
22 R.W. Tkach and A.R. Chraplyvy, Journal of Lightwave Technology **4**, 1655 (1986)
23 L.N. Langley, K.A. Shore and J. Mørk, Optics Letters **19**, 2137 (1994)
24 J. Mørk, M. Semkow and B. Tromborg, Electronics Letters **26**, 609 (1990)
25 Acousto-Optic Products Catalog, Newport Electro Optics Systems (1995)
26 T. Kushida, H.M. Markos and J. E. Geusic, Physical Review **167**, 289 (1968)
27 R. K. Watts, Journal of the Optical Society of America **61**, 123 (1971)
28 R. Moncorgé, B. Chambon, J.Y. Rivoire, N. Garnier, E. Descroix, P. Laporte, H. Guillet, S. Roy, J. Mareschal, D. Pelenc and P. Farge, Optical Materials **8**, 109 (1997)
29 G.J. Kintz and T. Baer, IEEE Journal of Quantum Electronics **26**, 1457 (1990)
30 J. Berger, D.F. Welch, D.R. Scifres, W. Streifer and P.S. Cross, Applied Physics Letters **51**, 1212 (1987)
31 E. Lacot and F. Stoeckel, Journal of the Optical Society of America B **13**, 2034 (1996)
32 C. Serrat and N.B. Abraham, Quantum and Semiclassical Optics **10**, 197 (1998)
33 M. Hercher, Applied Optics **7**, 951 (1968)
34 D. E. McCumber, Physical Review **141**, 306 (1966)
35 K. J. Weingarten, B. Braun and U. Keller, Optics Letters **19**, 1140 (1994)
36 A.E. Siegman, Lasers, University Science Books, Mill Valley California (1986)

37 K. Otsuka, R. Kawai, Y. Asakawa, P. Mandel and E.A.Viktorov, Optics Letters **23**, 201 (1998)
38 M. Lax, Physical Review **145**, 110 (1966)
39 M. Lax, IEEE Journal of Quantum Electronics **QE-3**, 37 (1967)
40 D. Pieroux and P. Mandel, Optics Communications **107**, 245 (1994)
41 O.N. Evdokimova and L.N. Kaptsov, Kvantovaya Elektron. **16**, 1557 (1989), Soviet Journal of Quantum Electronics **19**, 1001 (1989)
42 D. Pieroux and P. Mandel, Quantum and Semiclassical Optics **9**, L17 (1997)
43 P.A. Khandokhin, E.A. Ovchinnikov and E. Yu. Shirokov, Physical Review A **61**, 053807 (2000)
44 N.B. Abraham, L. Sekaric, L. L. Carson, V. Seccareccia, P.A. Khandokhin, Ya. I. Khanin, I. V. Koryukin and V. G. Zhislina, Physical Review A **62**, 013810 (2000)
45 T.Y. Fan and R.L. Byer, IEEE Journal of Quantum Electronics **23**, 605 (1987)
46 P. Laporta and M. Brussard, Optics Communications **85**, 47 (1991)
47 P. Mandel, B. A. Nguyen and K. Otsuka, Quantum and Semiclassical Optics **9**, 365 (1997)
48 K. Otsuka, P. Mandel, S. Bielawaski, D. Derozier and P. Glorieux, Physical Review A **46**, 1692 (1992)
49 P. Mandel, M. Georgiou, K. Otsuka, and D. Pieroux, Optics Communications **100**, 341 (1993)
50 B. A. Nguyen and P. Mandel, Optics Communications **138**, 81 (1997)
51 K. Otsuka, M. Georgiou and P. Mandel, Japanese Journal of Applied Physics **31**, L1250 (1992)
52 P. Mandel and J.-Y. Wang, Physical Review Letters **75**, 1923 (1995)
53 P. Mandel, K. Otsuka, J.-Y. Wang and D. Pieroux, Physical Review Letters **76**, 2694 (1996)
54 M. Georgiou, P. Mandel and K. Otsuka, IEEE Journal of Quantum Electronics **30**, 854 (1994)
55 A. A. Mak, O. A. Orlov and V. I. Ustyugov, Soviet Journal of Quantum Electronics **12**, 1574 (1982)
56 Yu. D. Golyaev and S. V. Lantratov, Soviet Journal of Quantum Electronics **9**, 1390 (1979)
57 B. A. Nguyen and P. Mandel, Optics Communications **112**, 235 (1994)
58 K. Otsuka, D. Pieroux and P. Mandel, Optics Communications **108**, 265 (1994)
59 D. Pieroux, P. Mandel and K. Otsuka, Optics Communications **108**, 273 (1994)
60 P. Khandokhin, Ya. Khanin, J.-C. Celet, D. Dangoisse and P. Glorieux, Optics Communications **123**, 372 (1996)
61 R. C. Dorf, R. H. Bishop, Modern control systems, (7th Ed.) Addison-Wesley (1995)
62 P. F. Blackman, Introduction to State-variable Analysis, The Macmillan Press Ltd (1977)
63 B. A. Nguyen and P. Mandel, Physical Review A **54**, 1638 (1996)
64 HP 35670A Operator's Guide, HP 35670-90024, Hewlett-Packard Company (1994)
65 R. Hanbury Brown and R. Q. Twiss, Nature **177**, 27 (1956)
66 G. A. Rebka and R. V. Pound, Nature **180**, 1035 (1957)
67 E. M. Purcell, Nature **178**, 1449 (1956)
68 R. J. Glauber, Physical Review **130**, 2529 (1963)
69 R. J. Glauber, Physical Review B **1**, 2766 (1963)
70 D. F. Walls and G. J. Milburn, Quantum Optics (1st Ed.) Springer-Verlag (1995)
71 K. Shimoda, H. Takahasi and C. H. Townes, Journal of the Physical Society of Japan **12**, 686 (1957)
72 M. Lax, Physical Review **145**, 110 (1966)

73 M. Lax, Physical Review **157**, 213 (1967)
74 S. O. Rice, Bell Telephone Technical Journal **23**, 282 (1944)
75 C. H. Henry, Chapter 2 in Coherence, Amplification and Quantum Effects in Semiconductor Lasers (Y. Yamamoto, Ed.), John Wiley (1991)
76 V. V. Azarova, N. M. Galaktionova, A. A. Mak, O. A. Orlov and V. I. Ustyugov, Soviet Journal of Quantum Electronics **9**, 1378 (1979)
77 A. Papoulis, Probability, Random Variables and Stochastic Processes (3rd Ed.), McGraw-Hill (1991)
78 K. G. Libbrecht, J. L. Hall, Review of Scientific Instrumentation **64**, 2133 (1993)
79 C. C. Bradely, J. Chen, R. G. Hulet, Review of Scientific Instrumentation **61**, 2097 (1990)